DE GRUYTER

Rasmus Fehrmann, Catherine Santini (Eds.)

IONIC LIQUIDS

SYNTHESIS, PROPERTIES, TECHNOLOGIES AND APPLICATIONS

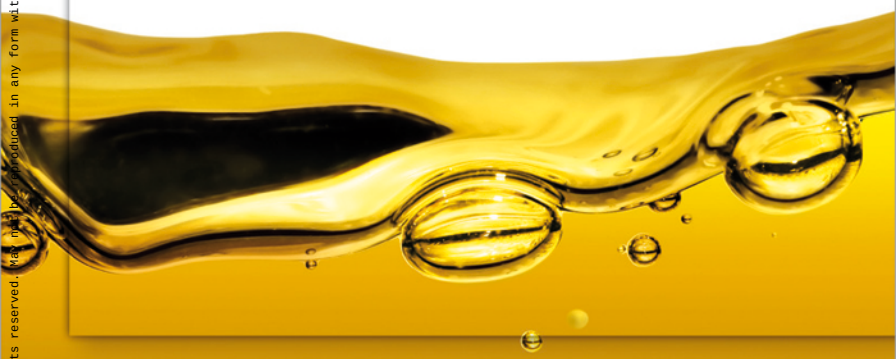

Ionic Liquids

Also of Interest

Green Chemistry in Industry.
Benvenuto, Plaumann (Eds.), 2018
ISBN 978-3-11-056113-5, e-ISBN 978-3-11-056278-1

Green Chemistry and Technologies.
Zhang, Gong, Bin (Eds.), 2018
ISBN 978-3-11-047861-7, e-ISBN 978-3-11-047931-7

Ionic Surfactants and Aqueous Solutions.
Biomolecules, Metals and Nanoparticles
Vera, Wilczek-Vera (Eds.), 2018
ISBN 978-3-11-056336-8, e-ISBN 978-3-11-056480-8

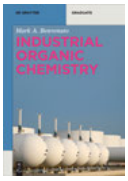

Industrial Organic Chemistry.
Benvenuto, 2017
ISBN 978-3-11-049446-4, e-ISBN 978-3-11-049447-1

Ionic Liquids

Synthesis, Properties, Technologies and Applications

Edited by
Rasmus Fehrmann and Catherine Santini

DE GRUYTER

Editors
Prof. Rasmus Fehrmann
Technical University of Denmark
Department of Chemistry
Centre for Catalysis and Sustainable Chemistry
2800 Lyngby
Denmark
rf@kemi.dtu.dk

Catherine Santini
Laboratory of Chemistry, Catalysis, Polymers and Process
CNRS 5265
43 Boulevard du 11 Novembre 1918
69616 Villeurbanne
France
Catherine.SANTINI@univ-lyon1.fr

ISBN 978-3-11-058201-7
e-ISBN (PDF) 978-3-11-058363-2
e-ISBN (EPUB) 978-3-11-058212-3

Library of Congress Control Number: 2018953428

Bibliographic information published by the Deutsche Nationalbibliothek
The Deutsche Nationalbibliothek lists this publication in the Deutsche Nationalbibliografie; detailed bibliographic data are available on the Internet at http://dnb.dnb.de.

Typesetting: Integra Software Services Pvt. Ltd.
Printing and binding: CPI books GmbH, Leck
Cover image: Zffoto/iStock/Getty Images Plus

www.degruyter.com

Preface

The objective of the COST Action CM 1206 EXIL (Exchange on Ionic Liquids) Action was to *coordinate European research activities and knowledge exchange* on ionic liquids and to explore their full potential in the context of fundamental and applied chemistry, materials science and engineering. It provided a coordinated forum for an efficient intra- and interdisciplinary knowledge and expertise exchange, networking and dissemination of information and results, training and initiating collaborations. Through 99 short-team scientific missions (STSM) of PhD students in 21 different countries, one summer school, workshops, and joint publications, this network supplied the scientific community with systematic high-quality information on ILs and their applications through new and improved technologies and materials, through cleaner and safer production techniques. The Action aims to combat misinformation as well as to contradict data and reports.

This book provides an interesting snapshot of some of the main lines of current and new research regarding the properties and applications of ionic liquids. The chapters reflect the growing theoretical and computational work leading to new predictive properties of ionic liquids.

The accurate experimental determination of these properties (Villaneuva – thermal stability) and their mixtures with solvents (Bendova – liquid–liquid equilibria) or solute (Dinis – aqueous biphasic systems with mixtures of polymers) are firstly developed. Then, the modeling of ionic liquids and their mixtures (Wang – multi-granular modeling) is described. The impact of solid–liquid interfaces for energy applications (Costa – advanced energy applications), and solid liquids interface for the synthesis of nanomaterials (Minofar – silver nanoparticles in $EMIMPF_6$), and surface treatments (Verpoort – surface treatment) are discussed.

We would like to heartly thank all 400 participants of the EXIL from 21 differents countries, particularly group leaders, MC members, STSM responsibles, and grant holders and the 99 PhD students who participated in the exchange program through STSMs.

Chair of the Action: Prof Rasmus FEHRMANN (DK)
Vice Chair of the Action: Dr Catherine SANTINI (FR)

https://doi.org/10.1515/9783110583632-201

Contents

List of contributors

Luís Barbosa
CICECO – Aveiro Institute of Materials
Department of Chemistry
University of Aveiro
Campus Universitário de Santiago
3810-193 Aveiro
Portugal

M. Bendová
Department of Aerosol Chemistry and Physics
Institute of Chemical Process Fundamentals
of the CAS, v. v. i.
Rozvojová 135/1
165 02 Prague 6
Czech Republic

Renata Costa
CIQUP – Physical Analytical Chemistry and
Electrochemistry group
Faculdade de Ciências
Universidade do Porto
Departamento de Química e Bioquímica
Rua do Campo Alegre
4169-007 Porto
Portugal

João A.P. Coutinho
CICECO – Aveiro Institute of Materials
Department of Chemistry
University of Aveiro
Campus Universitário de Santiago
3810-193 Aveiro
Portugal

A. De Cleene
OCAS N.V.
Pres. J.F. Kennedylaan 3
B-9060 Zelzate
Belgium

J. De Strycker
OCAS N.V.
Pres. J.F. Kennedylaan 3
B-9060 Zelzate
Belgium

Teresa B.V. Dinis
CICECO – Aveiro Institute of Materials
Department of Chemistry
University of Aveiro
Campus Universitário de Santiago
3810-193 Aveiro
Portugal

Mara G. Freire
CICECO – Aveiro Institute of Materials
Department of Chemistry
University of Aveiro
Campus Universitário de Santiago
3810-193 Aveiro
Portugal
maragfreire@ua.pt

Mikhail Golets
AkzoNobel Surface Chemistry AB
Hamnvägen 2
SE-444 85 Stenungsund
Sweden

Aatto Laaksonen
Division of Physical Chemistry
Department of Materials and Environmental
Chemistry
Arrhenius Laboratory
Stockholm University
SE-10691 Stockholm
Sweden
aatto@mmk.su.se

https://doi.org/10.1515/9783110583632-202

Zhong-Yuan Lu
State Key Laboratory of Supramolecular Structure and Materials
Institute of Theoretical Chemistry
Jilin University
Changchun 130023
China

Babak Minofar
Faculty of Science
University of South Bohemia
Branišovská 1760
37005 České Budějovice
Czech Republic
minofar@nh.cas.cz

Francesca Mocci
Department of Chemical and Geological Sciences
University of Cagliari
I-09042 Monserrato
Italy

Catarina M.S.S. Neves
CICECO – Aveiro Institute of Materials
Department of Chemistry
University of Aveiro
Campus Universitário de Santiago
3810-193 Aveiro
Portugal

J.J. Parajó
Grupo Nafomat
Departamento de Física Aplicada
Facultade de Física
Universidade de Santiago de Compostela
15782 Santiago de Compostela
Spain

Carlos M. Pereira
CIQUP – Physical Analytical Chemistry and Electrochemistry group
Faculdade de Ciências
Universidade do Porto
Departamento de Química e Bioquímica
Rua do Campo Alegre
4169-007 Porto
Portugal

J. Rotrekl
Department of Aerosol Chemistry and Physics
Institute of Chemical Process Fundamentals of the CAS, v. v. i.
Rozvojová 135/1
165 02 Prague 6
Czech Republic

J. Salgado
Grupo Nafomat
Departamento de Física Aplicada
Facultade de Física
Universidade de Santiago de Compostela
15782 Santiago de Compostela
Spain

Sten Sarman
Division of Physical Chemistry
Department of Materials and Environmental Chemistry
Arrhenius Laboratory
Stockholm University
SE-10691 Stockholm
Sweden

A. Fernando Silva
CIQUP – Physical Analytical Chemistry and Electrochemistry group
Faculdade de Ciências
Universidade do Porto
Departamento de Química e Bioquímica
Rua do Campo Alegre
4169-007 Porto
Portugal

Farid Taherkhani
Department of Chemistry
Sharif University of Technology
Tehran 11365-11155
Iran *and*
Center for Nanobiology and Structural Biology
Institute of Microbiology
Academy of Sciences of the Czech Republic
Nové Hrady
Czech Republic
faridtaherkhani@gmail.com

P. Verpoort
OCAS N.V.
Pres. J.F. Kennedylaan 3
B-9060 Zelzate
Belgium
philippe.verpoort@ocas.be

M. Villanueva
Grupo Nafomat
Departamento de Física Aplicada
Facultade de Física
Universidade de Santiago de Compostela
15782 Santiago de Compostela
Spain
maria.villanueva@usc.es

Z. Wagner
Department of Aerosol Chemistry and Physics
Institute of Chemical Process Fundamentals
of the CAS, v. v. i.
Rozvojová 135/1
165 02 Prague 6
Czech Republic

Yong-Lei Wang
Division of Physical Chemistry
Department of Materials and Environmental
Chemistry
Arrhenius Laboratory
Stockholm University
SE-10691 Stockholm
Sweden
and
Department of Chemistry
Stanford University
Stanford
California 94305
United States
wangyonl@gmail.com

J.J. Parajó, M. Villanueva, J. Salgado

1 Thermal stability of ionic liquids

Abstract: Thermal stability of 50 ionic liquids (ILs) has been analyzed using a Perkin Elmer thermogravimetric device. Several families with fixed anions and different cations and vice versa were chosen to provide a comprehensive knowledge of thermal properties of ILs against structure. For all the selected ILs, dynamic scans were performed under air atmosphere and a heating rate of 10 $K \cdot min^{-1}$ to estimate the short-term thermal stability. Isothermal studies were also carried out for some of the above compounds, at temperatures lower than onset temperature (T_{onset}), in order to evaluate the long-term thermal stability.

One of the most used parameters to characterise the long-term thermal stability of an IL is Maximum Operation Temperature (MOT). Because the estimation of this parameter involves the calculation of the activation energy of the degradation process, the kinetics of some of the ILs was analyzed by using different dynamic kinetic methods (Kissinger, Kissinger–Akahira–Sunose (KAS), Flynn–Wall–Ozawa (FWO) and Friedman), and the obtained energy values were compared to those obtained through isothermal methods. There was relatively good concordance in the values of MOT using different criteria.

Keywords: thermogravimetry, onset temperature, long-thermal stability, maximum operation temperature, activation energy

1.1 Introduction

Ionic liquids (ILs) have been considered "designer-solvents" [1] and proposed for medical, industrial, cosmetic and food applications [2] due to their intrinsic properties. These include nonvolatility, nonflammability, high thermal stability, high polarity, large electrochemical window and high thermal conductivity, among others.

The thermal stability of a compound, which should be determined from the maximum temperature of operation, can change depending on the use and conditions that this compound is submitted to. For example, a system with low oxidation stability and relative evaporation capacity, which was firstly classified as slightly stable, might be used without problems in application under an inert atmosphere and in a closed system. Due to these dependences and possibilities, the definition of thermal stability and maximum operation temperature for ILs is nowadays an open question [3, 4].

J.J. Parajó, M. Villanueva, J. Salgado, Departamento de Física Aplicada, Universidade de Santiago de Compostela, Spain

https://doi.org/10.1515/9783110583632-001

Additionally, thermal stability of ILs is currently being evaluated using thermogravimetric (TG) analysis at a single linear heating rate in controlled atmosphere. The onset and peak decomposition temperatures obtained from these experiments often overestimate the long-term thermal stabilities of ILs due to the scanning nature of this test, and isothermal studies [5, 6] at temperatures significantly lower than those exhibit appreciable decomposition [7, 8].

Thus, in order to establish a more realistic thermal degradation temperature, some parameters have been defined in the literature; for instance the temperature $T_{0.01/10h}$, (temperature at which the decomposition of ILs reaches 1% in 10 h) [4, 9, 10].

This work summarizes the main analysis and conclusions with regard to the thermal stability of ILs obtained from previous works by our group. The comparison presented here is especially important since all the results are obtained in similar experimental conditions, using the same technique and apparatus, providing a large database of thermal stability results for ILs.

1.2 Materials and methodology

The selected ILs have different origin; some were kindly provided by Merck KGaA, others were purchased from different companies as Sigma Aldrich and Iolitec and some of them were synthetized by co-workers; the specified fraction purity was higher than 0.95 in all the cases. The 50 ILs analyzed in this work are listed in Table 1.1, and the cations and anions moieties structures of these ILs are shown in Figure 1.1.

ILs were used, in the main part of this work, without further purification, because, in many potential industrial applications, contact with air does not allow to avoid the residual water content, which is the main impurity. Nevertheless, and taking into account that the influence of water content on thermal stability has not been deeply studied, thermal stability of some ILs purified and saturated of water has also been analyzed.

Thermogravimetry is the most commonly used technique to analyze the thermal stability of fluids operating in dynamic and isothermal modes. Dynamic experiments were performed at temperatures from 373 to 1,073 K with a heating rate of 10 $K \cdot min^{-1}$ and a purge gas flow of 20 $cm^3 \cdot min^{-1}$. From the experimental curve, TG, and the corresponding derivative, DTG, onset and endset temperatures were determined as it is shown in Figure 1.2. Additionally, temperature at which the 1%, 2%, 5% and 10% of mass loss appears $T_{1\%}$, $T_{2\%}$, $T_{5\%}$ and $T_{10\%}$, respectively, the remaining mass at onset temperature (W_{onset}), as well as the temperature of the minimum of the DTG peaks (T_{1st} and T_{2nd}) can also be determined from these curves.

Like almost all the thermal analysis techniques, experimental conditions have a strong influence on the results, and readers must pay attention to it before to perform comparisons between different fluids. In the paper of Villanueva et al. [6], the

Table 1.1: Selected ILs, short name, CAS number, mass fraction purity and provenance.

Name	AbbreviationCAS number	Mass fraction purity (%)	Provenance
1-butyl-2,3-dimethyl imidazolium tris(pentafluoroethyl) trifluorophosphate	$[C_4C_1C_1Im][(C_2F_5)_3PF_3]$1350559-92-0	≥ 98	Merck KGaA
1-butyl-2,3-dimetilimidazolium bis(trifluoromethylsulfonyl)imide	$[C_4C_1C_1Im][NTf_2]$350493-08-2	≥ 99	Merck KGaA
1-butyl-2,3-dimethylimidazolium trifluoromethanesulfonate	$[C_4C_1C_1Im][OTf]$765910-73-4	≥ 98	Merck KGaA
1,3-Dimethylimidazolium dimethylphosphate	$[C_1C_1Im][C_1C_1PO_4]$654058-04-5	≥ 99.3	Merck KGaA
1-ethyl-3-methylimidazolium n-hexylsulfate	$[C_2C_1Im][C_6SO_4]$942916-86-1	≥ 98.4	Merck KGaA
1-butyl-3-methylimidazolium bis(trifluoromethylsulfonyl)imide	$[C_4C_1Im][NTf_2]$174899-83-3	≥ 99.7	Aldrich
1-ethyl-3-methylimidazolium bis(trifluoromethylsulfonyl)imide	$[C_2C_1Im][NTf_2]$174899-82-2	> 99.4	Aldrich
1-butyl-3-methylimidazolium trifluoromethanesulfonate	$[C_4C_1Im][OTf]$174899-66-2	> 99	IoLiTec
1-propyl-3-methyl imidazolium bis(trifluoromethyllsulfonyl)imide	$[C_3C_1Im][NTf_2]$216299-72-8	> 98	Aldrich
1-ethyl-3-methylimidazolium trifluoromethanesulfonate	$[C_2C_1Im][OTf]$145022-44-2	> 99	IoLiTec
1-ethyl-3-methylimidazolium bis(tperfluoroethyllsulfonyl)imide	$[C_2C_1Im][BETI]$216299-76-2	> 99	IoLiTec
1-butyl-1-methylpyrrolidinium tris(pentafluoroethyl) trifluorophosphate	$[C_4C_1Pyrr][(C_2F_5)_3PF_3]$851856-47-8	≥ 99	Merck KGaA

(continued)

Table 1.1 (continued)

Name	AbbreviationCAS number	Mass fraction purity (%)	Provenance
1-butyl-1-methylpyrrolidinium bis(trifluoromethylsulfonyl)imide	$[C_4C_1Pyrr][NTf_2]$223437-11-4	≥ 99.9	Merck KGaA
1-butyl-1-methylpyrrolidinium trifluoromethanesulfonate	$[C_4C_1Pyrr][OTf]$367522-96-1	≥ 98	Merck KGaA
1-butyl-1-methylpyrrolidinium tetracyanoborate	$[C_4C_1Pyrr][B(CN)_4]$1266721-18-9	≥ 99	Merck KGaA
1-butyl-1-methylpyrrolidinium tris(nonafluorobutyl) trifluorophosphate	$[C_4C_1Pyrr][(C_4F_9)_3PF_3]$	≥ 98	Merck KGaA
1-butyl-1-methylpyrrolidinium tris(perfluorooctyl) trifluorophosphate	$[C_4C_1Pyrr][(C_8F_{17})_3PF_3]$—	> 98	Merck KGaA
1-(2-Methoxyethyl)-1-methyl-pyrrolidinium bis(trifluoromethylsulfonyl)imide	$[C_1OC_2C_1Pyrr][NTf_2]$757240-24-7	> 99.3	Merck KGaA
1-(2-Methoxyethyl)-1-methyl-pyrrolidinium tris(pentafluoroethyl)trifluorophosphate	$[C_1OC_2C_1Pyrr][(C_2F_5)_3PF_3]$1195983-48-2	> 98	Merck KGaA
Trihexyl(tetradecyl)phosphonium tris(pentafluoroethyl) trifluorophosphate	$[P_{6,6,6,14}][(C_2F_5)_3PF_3]$883860-35-3	> 99	Merck KGaA
Tri(butyl)ethylphosphonium diethylphosphate	$[P_{4,4,4,2}][C_2C_2PO_4]$20445-94-7	> 96.3	CytecIndustries Inc.
1-butyl-3-methylpiperidinium trifluoromethanesulfonate	$[C_4C_1pip][OTf]$174899-66-2	> 99	IoLiTec
1-butyl-3-methylpiperidinium bis(trifluoromethylsulfonyl)imide	$[C_4C_1pip][NTf_2]$344790-86-9	> 99	IoLiTec

Ethyl-(2-hydroxyethyl)-dimethylammonium bis(trifluoromethylsulfonyl)imide	$[C_2C_1C_1NC_2OH][NTf_2]$	> 98.5	Synthesised [7]
Ethyl-di-(2-hydroxyethyl)-dimethylammoniumbis (trifluoromethylsulfonyl)imide	$[C_2C_1N(C_2OH)_2][NTf_2]$	> 98.5	
Ethyl-(2-hydroxyethyl)-dimethylammonium trifluoromethanesulfonate	$[C_2C_1C_1NC_2OH][OTf]$	> 98.5	
Ethyl-di-(2-hydroxyethyl)-dimethylammonium trifluoromethanesulfonate	$[C_2C_1N(C_2OH)_2][OTf]$	> 98.5	
Ethyl-(2-hydroxyethyl)-dimethylammonium tris(pentafluoroethyl)trifluorophosphate	$[C_2C_1C_1NC_2OH][(C_2F_5)_3PF_3]$	> 98.5	
Ethyl-di-(2-hydroxyethyl)-dimethylammonium tris(pentafluoroethyl)trifluorophosphate	$[C_2C_1N(C_2OH)_2][(C_2F_5)_3PF_3]$	> 98.5	
Ethyl-(2-hydroxyethyl)-dimethylammonium dicyanamide	$[C_2C_1C_1NC_2OH][DCA]$	> 98.5	
Ethyl-di-(2-hydroxyethyl)-dimethylammonium dicyanamide	$[C_2C_1N(C_2OH)_2][DCA]$	> 98.5	
Methyl-diethylammonium methanesulfonate	$[C_2C_2C_1N][C_1SO_3]$945715-44-6	> 99	IoLiTec
Methyl-diethylammonium trifluoromethanesulfonate	$[C_2C_2C_1N][OTf]$945715-39-9	> 98	IoLiTec
Ethylammonium nitrate	$[C_2N][NO_3]$22113-86-6	> 97	IoLiTec
Propylammonium nitrate	$[C_3N][NO_3]$22113-88-8	> 97	IoLiTec
Butylammonium nitrate	$[C_4N][NO_3]$58888-50-9	> 95	Synthesised [11]
Choline acetate	[Chol][Ac]14586-35-7	> 98	IoLiTec
Choline dicyanamide	[Chol][DCN]1043576-49-3	> 97	IoLiTec
Choline tosylate	[Chol][tosy]55357-38-5	> 97	IoLiTec
Choline dihydrogenphosphate	$[Chol][H_1H_1PO_4]$83846-92-8	> 98	IoLiTec
Choline bis(trifluoromethylsulfonyl)imide	$[Chol][NTf_2]$827027-25-8	> 99	IoLiTec
1-ethylpyridinium bis(trifluoromethylsulfonyl)imide	$[C_2Py][NTf_2]$712354-97-7	> 99	IoLiTec
1-ethylpyridinium methanesulfonate	$[C_2Py][C_1SO_3]$681481-41-4	> 95	IoLiTec
1-ethylpyridinium trifluoromethanesulfonate	$[C_2Py][OTf]$3878-80-6	> 99	IoLiTec
Ethylpyridinium tosylate	$[C_2Py]$[tosy]95982-69-7	> 97	IoLiTec

(continued)

Table 1.1 (continued)

Name	AbbreviationCAS number	Mass fraction purity (%)	Provenance
1-ethyl-3,5-dimethyl-2-pentylpyridinium bis(trifluoromethylsulfonyl)imide	$[C_2C_1C_1C_5py][NTf_2]$	> 99	Synthesised [12]
1-butyl-3,5-dimethyl-2-pentylpyridinium bis(trifluoromethylsulfonyl)imide	$[C_4C_1C_1C_5py][NTf_2]$	> 99	
1-hexyl-2,3,5-trimethylpyridinium bis(trifluoromethylsulfonyl)imide	$[C_6C_1C_1C_1py][NTf_2]$	> 99	
2-ethyl-1-hexyl-3,5-dimethylpyridinium bis(trifluoromethylsulfonyl)imide	$[C_2C_6C_1C_1py][NTf_2]$	> 99	
1-hexyl-3,5-dimethyl-2-pentylpyridinium bis(trifluoromethylsulfonyl)imide	$[C_6C_1C_1C_5py][NTf_2]$	> 99	

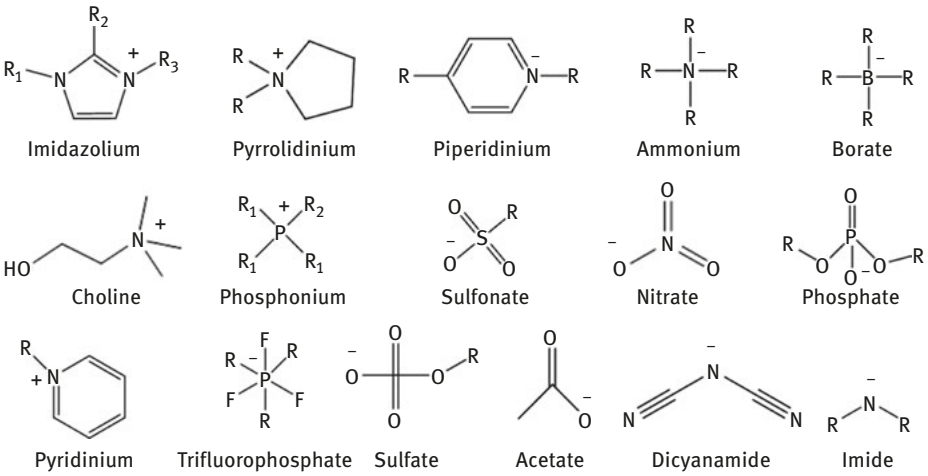

Figure 1.1: Chemical structure of cations and anions used in this work.

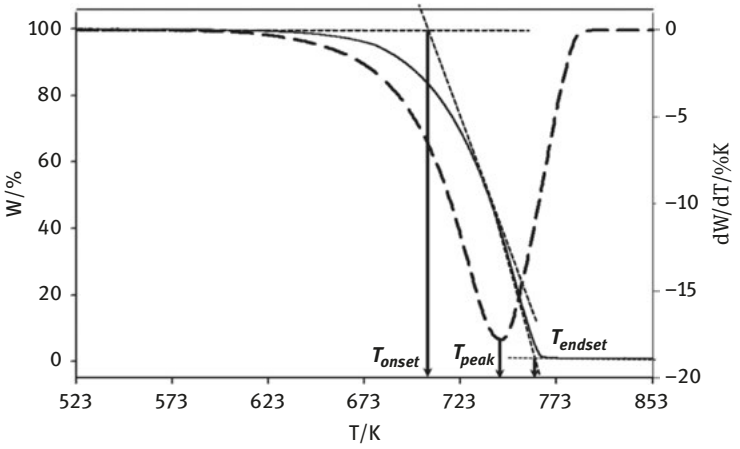

Figure 1.2: TG (continuous) and DTG (dashed) curves of the IL $[C_4C_1Im][NTf_2]$. Determination of onset, endset and peak temperatures.

influence of atmosphere, scanning rate and mass sample on the results of dynamic scans of $[C_2C_1Im][NTf_2]$ were analyzed. It was observed that degradation temperatures increased with the heating rate; in particular, onset temperature increased by approximately 100 K when the rate grew from 1 to 20 K · min^{-1}. Additionally, result of this work also showed that inert atmosphere experienced with this IL imply higher thermal stability, although, in a recent study [5] it was observed that the influence of the atmosphere depends on the fluid, since the IL $[P_{6,6,6,14}][(C_2F_5)_3PF_3]$ presents differences on starting degradation up to 100 K between air and nitrogen, whereas

in $[C_1OC_2C_1Pyrr][(C_2F_5)_3PF_3]$ the beginning of degradation curve scarcely differs in 20 K. In any case, the common characteristic is that thermal stability is higher in nitrogen than in air atmospheres.

In the abovementioned work [5], the water influence is also studied frequently due to bibliographic references that indicate the important effect that impurities, such as water, have on the thermophysical properties of ILs [13–16]; nevertheless, scarce data about the changes in thermal stability as consequence of impurities can be found. As it was mentioned above, in order to analyze how water affects to this property, a comparison between the TG-dynamic scans of some ILs was performed in two different conditions of water content (as supplied and saturated). Saturated samples were obtained keeping the selected ILs in an open bottle, weighing samples every 24 h, reaching up to a constant mass (approximately 10 days). Water contents of the pure and water-saturated samples were measured with a Karl Fischer coulometric titrator (Metler Toledo DL32) and results showed, as examples, an increase from 174 to 3,700 ppm for $[C_1OC_2C_1Pyrr][NTf_2]$ and from 139 to 1,028 ppm for $[C_1OC_2C_1Pyrr][(C_2F_5)_3PF_3]$ after saturation, whereas neither TG and DTG curves nor the onset temperature change significantly.

Moreover, in the work of Lorenzo et al. [7], the thermal stability of some ammonium ILs related with choline was analyzed. In particular, TG curves corresponding to the ILs incorporating $[OTf]^-$ anion exhibit three degradation steps. The first one could be attributed to the loss of tied water, which is difficult to eliminate even drying under vacuum, being necessary a preheating at similar temperatures than onset ones to eliminate this water.

In summary, to make comparable results, it is important to take into account the influence of experimental conditions and the peaks nature. Thus, this chapter collects results obtained with the thermogravimetric analyzer equipment (TGA7-Perkin Elmer) with the same experimental conditions, namely samples of similar weight (3–5mg) placed in an open platinum pan, same heating rate and same atmospheric nature and flow for a database of 50 ILs.

1.3 Results

1.3.1 Short-term thermal stability

TG and DTG curves of all the ILs under dry air atmosphere and 10 $K \cdot min^{-1}$ in a temperature interval from 373 to 1,073 K were obtained.

Four different behaviours can be essentially observed from the comparison of the shapes of DTG curves, as is presented in Figure 1.3.

A unique degradation step, as observed for $[C_1OC_2C_1Pyrr][NTf_2]$, characterized by no relevant residual mass detected at the end of the experiment.

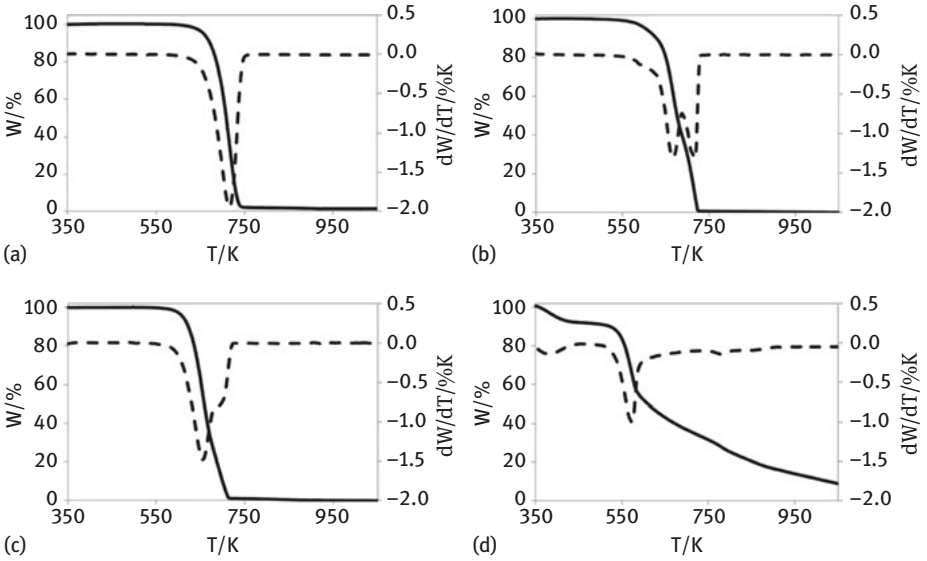

Figure 1.3: TG and DTG curves of (a) $[C_1OC_2C_1Pyrr][NTf_2]$, (b) $[P_{6,6,6,14}][(C_2F_5)_3PF_3]$, (c) $[C_1OC_2C_1Pyrr][(C_2F_5)_3PF_3]$ and (d) $[C_1C_1Im][C_1C_1PO_4]$.

(a) Two resolved peaks corresponding to two different degradation processes in the sample, as detected for $[P_{6,6,6,14}][(C_2F_5)_3PF_3]$.
(b) One resolved peak followed by a shoulder, as for $[C_1OC_2C_1Pyrr][(C_2F_5)_3PF_3]$.
(c) A resolved degradation step with a significant residue of the initial mass, as observed for $[C_1C_1Im][C_1C_1PO_4]$ (approximately 20%), that can also present some other small peaks or shoulders.

Onset temperatures of the 50 selected ILs, obtained from the TG and DTG curves in dry air atmosphere, are presented in Figure 1.4. These values range between 485 and 709 K, and it can be clearly seen that the anion influence on the thermal stability of ILs is higher than the cation one, ILs with $[NTf_2]^-$ and $[OTf]^-$ anions being the most stable; meanwhile, dicyanamide, nitrate- and acetate-based ILs were the least stable, agreeing with the main observations for thermal stability of ILs in literature [17–20].

Although cation influence is lower than that of the anion [5–8, 21–23], results show that the sequence with the cation family for the common anion $[NTf_2]^-$ is Imidazolium > Pyrrolidinium > Piridinium ≈ Piperidinium > Choline ≈ Ammonium, and for the common anion $[OTf]^-$ is Imidazolium > Piperidinium ≈ Pyrrolidinium > Piridinium > Choline ≈ Ammonium.

Other temperatures determined from the dynamic TG–DTG curves, as T_{peak} and T_{endset} presented similar trends for these ILs.

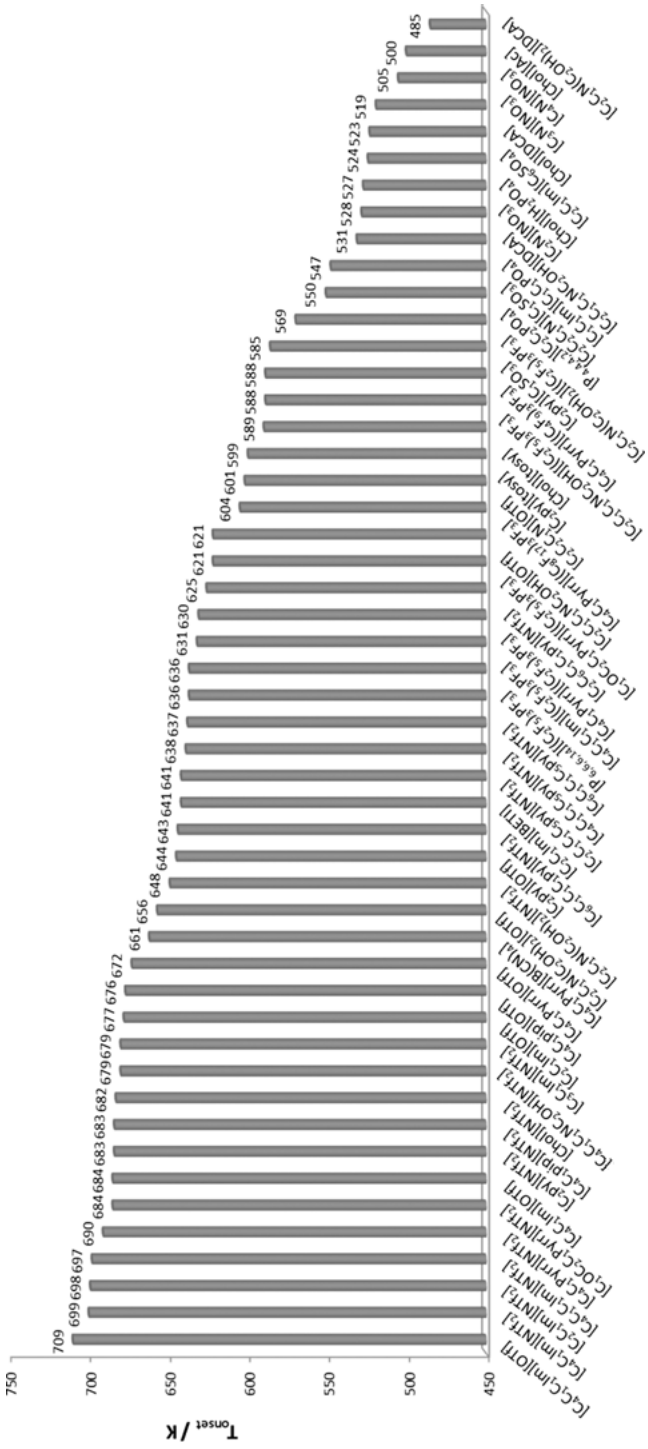

Figure 1.4: Onset temperatures of the selected ILs determined in dynamics scans of 10 K · min^{-1} in dry air atmosphere.

1.3.2 Long-term thermal stability

To make a more realistic description of the thermal stability of the ILs, isothermal TG analysis was used to determine its long-term thermal stability. This study provides rates of decomposition at a given temperature after a given isothermal-heating time. Figure 1.5 shows, as examples, isothermal scans corresponding to four ILs with different cations. In all cases, six temperatures lower than T_{onset} were selected for these scans. The lowest isothermal temperature was chosen when the mass loss was lower than 1% in 5 h.

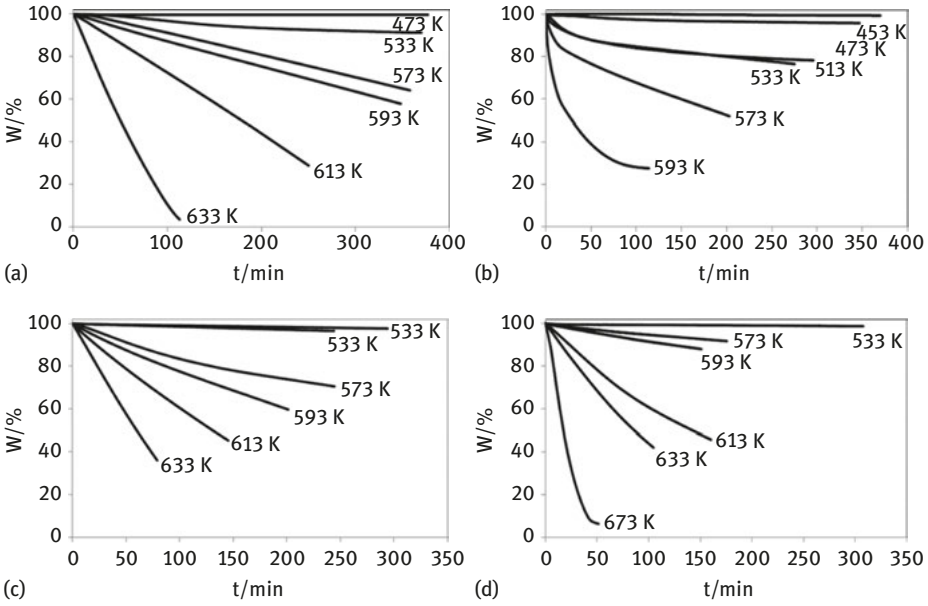

Figure 1.5: (a) $[C_1OC_2C_1Pyrr][NTf_2]$, (b) $[P_{6,6,6,14}][(C_2F_5)_3PF_3]$, (c) $[C_2Py][NTf_2]$ and (d) $[C_4C_1C_1Im][OTf]$

Fast degradation at the highest temperatures, close to T_{onset}, can be observed for all the studied ILs, confirming that the onset temperature cannot be considered as the maximum temperature of operation in any case. Furthermore, the shape of the isothermal degradation curve depends on the IL considered, although there is a common feature that is at the beginning of the curve, usually until 10%–15% of mass loss, there is a linear behaviour.

1.3.3 Maximum operation temperature

Till now, a clear criterion on the degradation level allowed in different applications does not exist, finding in literature a wide range, from the temperature corresponding

to a 1% of mass loss in 1 year [24] to the temperature corresponding to a 10% of mass loss in 10 h [25]. Indeed, one of the main reasons is that the criterion should depend on the degradation level allowed by the application, as well as on the mechanism of mass loss. Taking the previous consideration into account, a parameter that permits characterizing the thermal stability for different degradation levels was necessary. For this reason, the maximum operation temperature (MOT) was introduced in the last years, although there are, also, different criteria to determine it. Some examples are presented as follows:

(a) Wooster et al. [10] and Baranyai et al. [26] suggested that the temperature at which 1% degradation occurs in 10 h ($T_{0.01/10\ h}$) is a good indicator of thermal stability, stablishing a method to estimate $T_{0.01/10\ h}$ from dynamic scans by using eq. (1.1):

$$T_{0.01/10h} = 0.82T_{(dW/dt \neq 0)} \tag{1.1}$$

$T_{(dW/dt)\neq 0}$ being the temperature in Kelvin at which the first appreciable weight loss occurs.

(b) Efimova et al. [9] followed the criterion of Seeberger et al. [24] who took into account short-term non-isothermal conditions at different heating rates and a maximum level of degradation of 1%. They proposed the use of eq. (1.2) to calculate the MOT for a defined time of operation (t_{max}):

$$MOT = \frac{E_a/R}{4.6 + ln(A \cdot t_{max})} \tag{1.2}$$

where E_a is the activation energy of degradation process and t_{max} is the maximum time of exposition.

Calculation of the E_a and A parameters can be done following different kinetic methodologies. There are many works focused on the determination of the activation energy of the degradation process of a specific material, which can be classified into two categories, namely isothermal and dynamic methods. As the name suggests, the first group uses isothermal TG curves [21], and activation energy is calculated by application of Arrhenius equation [8, 25], whereas the second method makes calculations from data of dynamic TG and DTG curves, as is the case of Efimova et al. [9], who used the Kissinger–Akahira–Sunose equation. Despite these kinetic methods being widely used, scarce references applying them to ILs have been found [4].

The most common dynamic methods used in the bibliography are: Kissinger, Flynn–Wall–Ozawa (FWO), Kissinger–Akahira–Sunose (KAS) and Friedman methods. The first one, Kissinger method, is a dynamic method that uses the peak temperature of the DTG curve to determine the activation energy. The other ones are isoconversional methods, that is, they are based on the isoconversional principle [27–29], and the activation energy is calculated as the mean value of those obtained for all the considered conversion values. In a recent work [4], a deep study of the degradation

kinetics of four imidazolium ILs with common anions ($[C_2C_1Im][NTf_2]$, $[C_3C_1Im][NTf_2]$, $[C_4C_1Im][NTf_2]$ and $[C_4C_1C_1Im][NTf_2]$) was done, using isothermal and dynamic methods. It was checked that, at least for these ILs, obtained activation energies through the different methods are similar, so in order to determine the MOT, it does not matter whatever the kinetic method is selected to estimate the activation degradation energy. Nevertheless, this must be taken with caution, especially in cases where several steps are overlapped on degradation process, as for example, $[P_{6,6,6,14}][(C_2F_5)_3PF_3]$ (see Figure 1.3).

(c) In previous works of our group [5, 8], the MOT at which an IL could be used was estimated from the fit of four possible conversion degrees, or degradation levels 1%, 2%, 5% and 10%, with the temperatures of isothermal scans, that is, the time that each IL takes to decompose in the above percentages was determined from isothermal scans. A decreasing exponential function of the temperature (eq. 1.3) was used to correlate these data of time and temperature:

$$t' = B\ e^{-C(T-273)} \tag{1.3}$$

t' being the time in minutes, T the temperature in K, and B and C the fitting coefficients. Knowledge of these fitting parameters allows the estimation of the MOT.

Obviously, the stricter the criterion, the lower the MOT is. Taking into account that in all of these calculations, an important loss of accuracy can appear (10%–15%), to assess these criteria operation, temperatures should not overcome these MOT temperatures in any case.

As example, Table 1.2 shows onset temperatures determined from dynamic scans and the MOT values of three ILs, calculated as the temperature that each degradation level takes place in 10 h. In all the cases, the MOT corresponding to the highest degree of conversion is around 150 K lower than T_{onset}.

Table 1.2: MOT for different degradation levels (1%, 5% and 10% in 10 h) and onset temperatures.

	$T_{0.01/10h}$/K	$T_{0.05/10h}$/K	$T_{0.10/10h}$/K	T_{onset}/K
$[C_1OC_2C_1Pyrr][NTf_2]$	474	496	525	684
$[C_1OC_2C_1Pyrr][(C_2F_5)_3PF_3]$	416	458	492	625
$[P_{6,6,6,14}][(C_2F_5)_3PF_3]$	430	469	485	636

Table 1.3 summarizes the $T_{0.01/10h}$ values (expressed in Kelvin) predicted by the three abovementioned methods. The highest values of MOT correspond to the dynamic method used by Wooster et al. [10], as it was also observed in a previous work [23]. The lowest values of MOT are those obtained from Efimova et al. [9] and Seeberger et al. [24] method. Up to our knowledge, no previous data have been published about this parameter for the selected compounds.

Table 1.3: Comparison between temperature values corresponding to the mass loss of 1% in 10 h obtained from isothermal studies and those estimated according to Wooster et al. [10] and Efimova et al. [9].

	$T_{0.01/10h}$/ KIsothermal study	$T_{0.01/10h}$/KDynamic study [10]	$T_{0.01/10h}$/K [9]
$[C_1OC_2C_1Pyrr][NTf_2]$	474	531	434
$[C_1OC_2C_1Pyrr][(C_2F_5)_3PF_3]$	416	453	401
$[P_{6,6,6,14}][(C_2F_5)_3PF_3]$	430	469	424

Taking into account the data obtained from the isothermal study, the observed trend, from higher to lower thermal stability, is $[C_1OC_2C_1Pyrr][NTf_2]$ > $[C_1OC_2C_1Pyrr][(C_2F_5)_3PF_3]$ > $[P_{6,6,6,14}][(C_2F_5)_3PF_3]$, which is the same as those tendencies obtained in other works with the E_a and T_{onset} values [5]. It can be seen again that ILs with $[NTf_2]^-$ anions show higher values of thermal stability [4, 6–8, 21, 23], whatever the parameter studied and the criterion used are.

1.4 Main conclusions

Thermal stability of 50 ILs has been analyzed using dynamic thermogravimetric analysis. Short-term thermal stability was characterized through onset temperatures. The first conclusion is that the anion influence on the thermal stability of ILs is higher than the cation one, ILs with $[NTf_2]^-$ and $[OTf]^-$ anions being the most stable, while, dicyanamide-, nitrate- and acetate-based ILs were the least stable.

Two very similar sequences with the cation family for the common anion $[NTf_2]^-$ and for the common anion $[OTf]^-$ (which are the most used in the literature) were obtained:

- For $[NTf_2]^-$: Imidazolium > Pyrrolidinium > Piridinium ≈ Piperidinium > Choline ≈ Ammonium.
- For $[OTf]^-$: Imidazolium > Piperidinium ≈ Pyrrolidinium > Piridinium > Ammonium.

Long-term stability was checked for several of the selected ILs using thermogravimetric isothermal analysis. The observed trend was the same than that obtained with T_{onset} values. Maximum operation temperature was also estimated by the application of three different criteria obtaining good concordance between them and with previous bibliographic results.

Acknowledgments: This work was supported by Spanish Ministry of Economy and Competitiveness and FEDER Program through the CTQ2011-23925, MAT2014-57943-C3-1-P, MAT2017-89239-C2-1-P and MAT2017-89239-C2-2-P projects as well as by

Xunta de Galicia through the EM2013/031, AGRUP2015/11 and GRC ED431C 2016/001 projects and the Galician Network of Ionic Liquids (ReGaLIs) ED431D 2017/06.

References

[1] M. Cvjetko Bubalo, S. Vidović, I. Radojčić Redovniković, S. Jokić, Green solvents for green technologies, J. Chem. Technol. Biotechnol. 90 (2015) 1631–1639. doi:10.1002/jctb.4668.

[2] A.A.C. Toledo-Hijo, G.J. Maximo, M.C. Costa, E.A.C. Batista, A.J.A. Meirelles, Applications of ionic liquids in the food and bioproducts industries, ACS Sustain. Chem. Eng. 4 (2016) 5347–5369. doi:10.1021/acssuschemeng.6b00560.

[3] J.C.O. Santos, I.M.G. Santos, a. G. Souza, Thermal degradation process of synthetic lubricating Oils: Part I—spectroscopic study, Pet. Sci. Technol. 33 (2015) 1238–1245. doi:10.1080/10916466.2015.1047031.

[4] J.J. Parajó, T. Teijeira, J. Fernández, J. Salgado, M. Villanueva, Thermal stability of some imidazolium [NTf2] ionic liquids: Isothermal and dynamic kinetic study through thermogravimetric procedures, J. Chem. Thermodyn. 112 (2017) 105–113. doi:10.1016/j.jct.2017.04.016.

[5] J.J. Parajó, M. Villanueva, I. Otero, J. Fernández, J. Salgado, Thermal stability of aprotic ionic liquids as potential lubricants. Comparison with synthetic oil bases, J. Chem. Thermodyn. 116 (2018) 185–196. doi:https://doi.org/10.1016/j.jct.2017.09.010.

[6] M. Villanueva, A. Coronas, J. García, J. Salgado, Thermal stability of ionic liquids for their application as new absorbents, Ind. Eng. Chem. Res. 52 (2013) 15718–15727. doi:dx.doi.org/10.1021/ie401656e.

[7] M. Lorenzo, M. Vilas, P. Verdía, M. Villanueva, J. Salgado, E. Tojo, Long-term thermal stabilities of ammonium ionic liquids designed as potential absorbents of ammonia, RSC Adv. 5 (2015) 41278–41284. doi:10.1039/C5RA03192C.

[8] M. Villanueva, J.J. Parajó, P.B. Sánchez, J. García, J. Salgado, Liquid range temperature of ionic liquids as potential working fluids for absorption heat pumps, J. Chem. Thermodyn. 91 (2015) 127–135. doi:10.1016/j.jct.2015.07.034.

[9] A. Efimova, L. Pfützner, P. Schmidt, Thermal stability and decomposition mechanism of 1-ethyl-3-methylimidazolium halides, Thermochim. Acta. 604 (2015) 129–136. doi:10.1016/j.tca.2015.02.001.

[10] T.J. Wooster, K.M. Johanson, K.J. Fraser, D.R. MacFarlane, J.L. Scott, Thermal degradation of cyano containing ionic liquids, Green Chem. 8 (2006) 691–696. doi:10.1039/b606395k.

[11] S. Bouzón- Capelo, T. Méndez-Morales, J. Carrete, E. López Lago, J. Vila, O. Cabeza, J.R. Rodríguez, M. Turmine, L.M. Varela, Effect of temperature and cationic chain length on the physical properties of ammonium nitrate-based protic ionic liquids, J. Phys. Chem. B. 116 (2012) 11302–11312. doi:10.1021/jp3066822.

[12] P. Verdía, M. Hernaiz, E.J. González, E.A. Macedo, J. Salgado, E. Tojo, Effect of the number, position and length of alkyl chains on the physical properties of polysubstituted pyridinium ionic liquids. J. Chem. Thermodyn. 69 (2014) 19–26.

[13] P.B. Sánchez, M.R. Currás, M.M. Mato, J. Salgado, J. García, Density and viscosity study of pyridinium based ionic liquids as potential absorbents for natural refrigerants: Experimental and modelling, Fluid Phase Equilib. 405 (2015) 37–45. doi:10.1016/j.fluid.2015.06.043.

[14] H. Rodríguez, J. Brennecke, Temperature and composition dependence of the density and viscosity of binary mixtures of water+ ionic liquid, J. Chem. Eng. Data. 51 (2006) 2145–2155. doi:10.1021/je0602824.

[15] J. Jacquemin, P. Husson, A.A.H. Padua, V. Majer, Density and viscosity of several pure and water-saturated ionic liquids, Green Chem. 8 (2006) 172. doi:10.1039/b513231b.
[16] E.J. González, Á. Domínguez, E.A. Macedo, Physical and excess properties of eight binary mixtures containing water and ionic liquids, J. Chem. Eng. Data. 57 (2012) 2165–2176. doi:10.1021/je201334p.
[17] A.F. Ferreira, P.N. Simões, A.G.M. Ferreira, Quaternary phosphonium-based ionic liquids: Thermal stability and heat capacity of the liquid phase, J. Chem. Thermodyn. 45 (2012) 16–27. doi:10.1016/j.jct.2011.08.019.
[18] C. Maton, N. De Vos, C. V. Stevens, Ionic liquid thermal stabilities: decomposition mechanisms and analysis tools, Chem. Soc. Rev. 42 (2013) 5963. doi:10.1039/c3cs60071h.
[19] M.T. Clough, K. Geyer, P. A. Hunt, J. Mertes, T. Welton, Thermal decomposition of carboxylate ionic liquids: Trends and mechanisms, Phys. Chem. Chem. Phys. 15 (2013) 20480–20495. doi:10.1039/c3cp53648c.
[20] M. Götz, R. Reimert, S. Bajohr, H. Schnetzer, J. Wimberg, T.J.S. Schubert, Long-term thermal stability of selected ionic liquids in nitrogen and hydrogen atmosphere. Thermochim Acta. 600 (2015) 82–88. doi:10.1016/j.tca.2014.11.005.
[21] J. Salgado, M. Villanueva, J.J. Parajó, J. Fernández, Long-term thermal stability of five imidazolium ionic liquids, J. Chem. Thermodyn. 65 (2013) 184–190. doi:http://dx.doi.org/10.1016/j.jct.2013.05.049.
[22] I. Otero, E.R. López, M. Reichelt, M. Villanueva, J. Salgado, J. Fernández, Ionic liquids based on phosphonium cations As neat lubricants or lubricant additives for a steel/steel contact, ACS Appl. Mater. Interf. 6 (2014) 13115–13128. doi:10.1021/am502980m.
[23] J. Salgado, J.J. Parajó, J. Fernández, M. Villanueva, Long-term thermal stability of some 1-butyl-1-methylpyrrolidinium ionic liquids, J. Chem. Thermodyn. 74 (2014) 51–57.
[24] A. Seeberger, A.-K. Andresen, A. Jess, Prediction of long-term stability of ionic liquids at elevated temperatures by means of non-isothermal thermogravimetrical analysis., Phys. Chem. Chem. Phys. 11 (2009) 9375–81. doi:10.1039/b909624h.
[25] R. Liang, M. Yang, X. Xuan, Thermal stability and thermal decomposition kinetics of 1-butyl-3-methylimidazolium dicyanamide, Chinese J. Chem. Eng. 18 (2010) 736–741. doi:10.1016/S1004-9541(09)60122-1.
[26] K.J. Baranyai, A.G.B. Deacon, A.D.R. Macfarlane, J.M. Pringle, J.L. Scott, Thermal degradation of Ionic liquids at elevated temperatures, Aust. J. Chem. 57 (2004) 145–147.
[27] M. Erceg, T. Kovačić, S. Perinović, Kinetic analysis of the non-isothermal degradation of poly(3-hydroxybutyrate) nanocomposites, Thermochim. Acta. 476 (2008) 44–50. doi:10.1016/j.tca.2008.07.009.
[28] Z. Ullah, M.A. Bustam, Z. Man, A.S. Khan, Thermal stability and kinetic study of benzimidazolium based ionic liquid, Procedia Eng. 148 (2016) 215–222. doi:10.1016/j.proeng.2016.06.577.
[29] P. Rajeshwari, Kinetic analysis of the non-isothermal degradation of high-density polyethylene filled with multi-wall carbon nanotubes, J. Therm. Anal. Calorim. 123 (2016) 1523–1544. doi:10.1007/s10973-015-5021-2.

M. Bendová, Z. Wagner, J. Rotrekl

2 Liquid–liquid equilibria in systems of ionic liquids: A guide to experiments and data analysis

Abstract: Experimental methods used to determine liquid–liquid equilibria (LLE) in systems containing ionic liquids (ILs) are summarized. While these methods are essentially the same as in studies of LLE in systems of molecular liquids, systems containing ILs show some specificities that must be taken into account. The methods addressed are therefore compared and assessed as to their suitability, advantages and drawbacks.

In the second part of the chapter, data analysis is addressed to demonstrate the wealth of information that can be obtained by means of using appropriate methods. An example of multivariate calibration using the partial least-squares method is given to show the means of separating overlapping UV–Vis spectra. Most importantly, though, a brief introduction to mathematical gnostics is given. This nonstatistical approach to data uncertainty is a powerful tool in critical assessment of a number of types of thermodynamic data, including LLE, and in a robust linear as well as nonlinear regression even of small samples of scattered data.

Keywords: liquid–liquid equilibria, experimental methods, mathematical gnostics, data analysis, multivariate calibration

2.1 Introduction

Studies of liquid–liquid equilibria (LLE), both in terms of experimental measurements and data treatment, require great care in general. In systems of ionic liquids (ILs), the experiments have to be designed and carried out even more carefully than in conventional systems of molecular compounds. In this chapter, an overview of the experimental possibilities and issues to watch out for in systems containing ILs will be briefly summarized.

Similarly, attention should be paid to a relevant data analysis of the experimental values that, in systems of ILs, may tend to show higher uncertainties or larger data scattering. In this chapter, data analysis by means of methods based on mathematical gnostics will be discussed. Indeed, high-quality and advanced data analysis is extremely important in critical assessment of all experimental data in general. In LLE data, the necessity for a reliable description of the data by means of appropriate thermodynamic

M. Bendová, Z. Wagner, J. Rotrekl, Department of Aerosol Chemistry and Physics, Institute of Chemical Process Fundamentals of the CAS, Prague, Czech Republic

https://doi.org/10.1515/9783110583632-002

equations arises. This often means using nonlinear regression methods in cases of complex shapes of objective functions.

2.2 Experimental determination of liquid–liquid equilibria

Experimental methods used to determine LLE in multicomponent systems containing ILs are essentially the same as in the conventional systems of molecular compounds. However, some specificities related to, for example, their high viscosity or an increased interfacial tension between the studied IL and the remaining components of the mixture may require special attention.

There are, in general, three types of methods to be used in these measurements. The direct analytical (static) method involves taking samples of phases of a carefully equilibrated mixture and analyzing them using a suitable analytical method. The main advantage of this experimental setup is that compositions of the equilibrium phases and consequently tie lines are obtained. However, this method is time- and material-consuming and requires a good knowledge of the analytical methods at hand. The volumetric method is based on measurements of volumes of equilibrium phases from which their composition is obtained by means of mass balance. It allows for measurements of tie lines for a range of temperatures, however, only in binary mixtures and mostly with a lower precision than other available methods. The cloud-point (synthetic) method then provides the possibility of measuring the points of the binodal curve, but not the compositions of the equilibrium phases.

2.2.1 Direct analytical method

In the direct analytical (or static) method, samples of carefully equilibrated phases are taken and analyzed by a suitable analytical method [1]. In a thermostated equilibrium cell, a heterogeneous mixture of a global composition corresponding roughly to the midpoint on the tie line is prepared and thoroughly mixed for a sufficiently long time to reach equilibrium. After another sufficiently long period of time of settling during which the equilibrium phases clear out the samples of both phases are taken. Both the stirring and settling times should be found experimentally for each studied system; this holds particularly for systems containing ILs. Indeed, in systems of ILs with molecular compounds, large differences in viscosity of the studied components are often found, the viscosity of ILs at room temperature often being of the order of tens to hundreds of mPa·s [2]. Also, values of the IL–air surface tension are lower than that of water, but higher than those of conventional

organic solvents (see, e.g., [3, 4]). This may lead to a poorer mass transfer on mixing; however, the phase separation on settling is facilitated [5].

Equilibration times indeed have to be determined quite carefully. In systems showing poor solubility of the IL in the molecular solvent starting measurements at a temperature higher than 25 °C with up to several days of stirring may be needed to reach the equilibrium [6]. Shorter times may lead to values of the measured solubility of IL in water that may be significantly lower than the equilibrium value.

Not least importantly, cross-contamination of equilibrium samples should carefully be avoided. To a large extent, using an equilibrium cell design proposed by Řehák et al. [7] (see Figure 2.1) allows for taking of non-contaminated samples. This setup allows for a thorough mixing of the entire mixture while at the same time ensuring that the sample of the lower phase is taken without the need to puncture the phase boundary. However, the formation of emulsion after settling can occur. In such cases, taking samples of the equilibrium phases is very difficult and even nearly impossible. Moreover, even if the equilibrium phases seem homogeneous, small droplets of one phase can be trapped in the second phase. This can lead to erroneous results, for instance, in systems of hydrophilic ILs with water in which the solubility of ILs in the aqueous phase is near the infinite dilution [6].

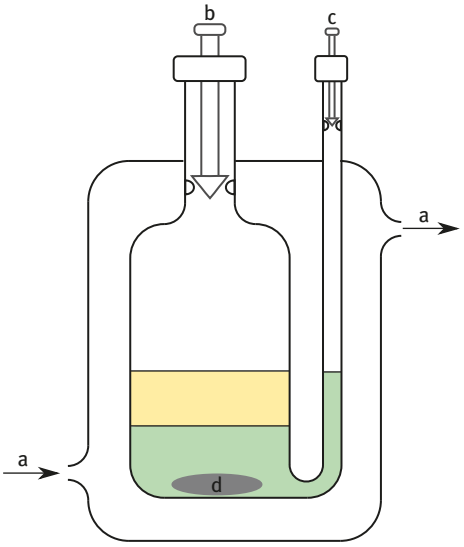

Figure 2.1: Measuring cell for the direct analytical method designed by Řehák et al. [7]: (a) thermostat in/out, (b) inlet for filling and taking of the upper-phase sample, (c) inlet for taking of the lower-phase sample, (d) magnetic stirrer.

A large range of analytical methods can then be applied to analyze the samples of the equilibrium phases. To analyze lower-boiling molecular compounds, gas chromatography is often applied [8–10]; however, care must be taken to add a guard column [8] to the experimental setup, to avoid the contamination of the measurement column by the nonvolatile ILs. NMR spectroscopy is a method of choice in some older works [11] due to its relative simplicity and small amount of sample required. It should

nevertheless be noted that the uncertainty of the NMR analyses is rarely better than 2%, and that as a consequence such measurements should only be used as a screening step and is not acceptable for measuring solubilities lower than 3% (mass). Often, data with "zero" solubility values are published when those only mean that the value is below the detection limit of the device. Such data should only be considered with some doubt, as screening values rather than reliable equilibrium data. Should they be published, detection limits of the analytical method should always be given. In addition, such data should be analyzed as censored, which to the best of our knowledge has never been done in literature till today. Measurements of physical properties, such as density or refractive index, can also be used in indirect determination of the composition of the equilibrium phases [12, 13], provided a homogeneous sample can be taken in sufficient quantity without disturbing the overall equilibrium.

2.2.2 Volumetric method

The volumetric method can be used for measurements of LLE in binary systems and consists of measuring volumes of the equilibrium phases in two mixtures of known compositions. Calculation of the equilibrium compositions is then carried out from mass balance [1, 14, 15]. The main advantage of this method is that even if a relatively large amount of sample is required (of the order of tens of milliliters), the prepared mixture can be used in repeated measurements over a large range of temperatures. After that, the IL can be readily recycled for further experiments. On the other hand, the uncertainty in the determined composition strongly depends on the difference between the molar masses of the studied components.

2.2.3 Cloud-point method

The cloud-point (or dynamic, turbidimetric) method allows for measurements of the points of the binodal curve [1, 16]. As a consequence, it does not provide information on the composition of the equilibrium phases, only the extent of the miscibility gap can be obtained. The measurements can be carried out in two modalities. The first one consists in titrating a pure liquid or a homogeneous mixture of known composition with another component at constant temperature until the appearance of the second phase [8]. Besides other, it requires excellent mixing, which makes this setup problematic for use with ILs. In the second modality, that may also be called a polythermal arrangement, a binary mixture of a known composition is heated or cooled at a defined rate to obtain the so-called solution temperature, that is, the temperature at which the phase change occurs [17]. An example of experimental setup for cloud-point measurement is shown in Figure 2.2.

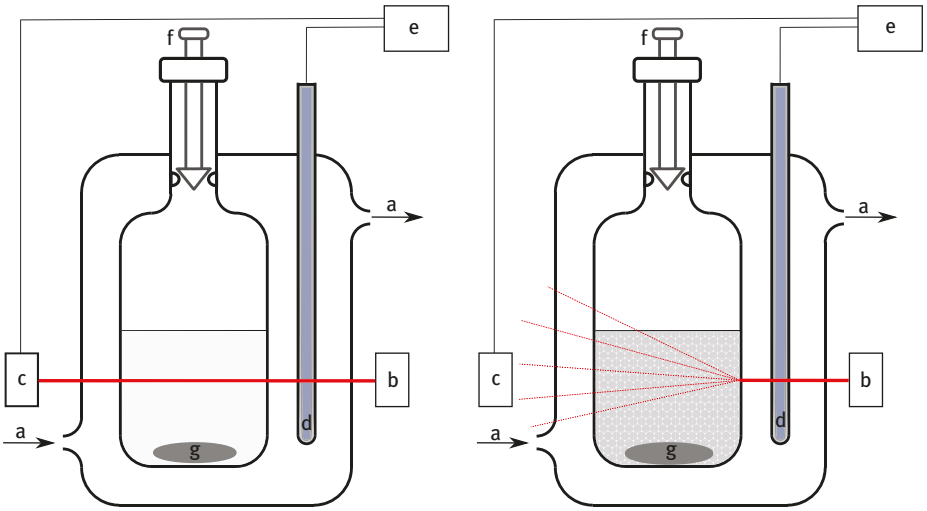

Figure 2.2: Measuring cell for the cloud-point method. Left – homogenous system, right – heterogenous system: (a) thermostat in/out, (b) laser source, (c) photodiode, (d) thermometer, (e) control unit (computer), (f) inlet for filling, (g) magnetic stirrer.

As in both previous cases, some specificities should be borne in mind that are related to studies of systems containing ILs. As in the direct analytical method, the large difference in viscosity of the ILs and molecular compounds lead to poorer mixing. In the polythermal arrangement the mixture usually has to be overheated to a temperature significantly higher (approximately 10–20 °C) than the solution temperature to obtain a homogeneous mixture. The values of the surface tension of ILs [5] also make the appearance of turbidity difficult to detect owing to its instability. Even if optical methods of detection that significantly improve the accuracy of the cloud-point method are used [17, 18], small droplets can go undetected unless a careful visual inspection is also used. As discussed in Section 2.2.1, in systems of ILs with molecular solvents poor mass transfer and quick phase separation may occur, which may lead to irreproducible results if repeated measurements with the same mixture are carried out without a sufficient equilibration times between the individual measurements.

2.3 Data analysis

The purpose of data analysis in general is to inspect available data and extract as much information as possible. A measured value is never exact. Each measurement is always disturbed. Having a single measured value we cannot in principle judge how much the value is shifted from the exact value and whether the shift is positive or negative. In order to estimate uncertainty, either a series of repeated measurements is needed or a dependence of one quantity on another and its mathematical model must be known.

Methodology of such calculations can be traced back to the books of a Persian scholar in the House of Wisdom in Baghdad, Muhammad Ibn Musa al-Khwarizmi, who was inspired by mathematics described by Brahmagupta in ancient India, especially the fundamental rules of algebra[1] and the concept of zero, which is now naturally used as a neutral element of an additive Abelian group. The basis of data analysis is rooted in the theory of measurement where a measured value is considered a sum of a true value and an error. A multiplicative model is also possible but there is a simple transformation between them, hence both models are mathematically equivalent. Additivity of measured quantities is a natural concept, therefore the measured values are mathematically modeled by means of an Abelian group. The theory of measurement further classifies measurement errors, briefly to systematic errors that can be corrected by calibration and random errors that cannot be avoided. The theory of measurement does not further analyze the random errors and leaves this task to statistics.

Two paradigms of measuring uncertainty are nowadays most widely used. The first approach has already been introduced, namely mathematical statistics. Most frequently the random error is considered to have normal distribution with zero mean and known variance, and the errors of individual measurements are uncorrelated. Violations of some of these assumptions can also be admitted, and such cases are described both from theoretical and practical point of view in the book of Beck and Arnold [19], and requirements for statistical expression of uncertainty are specified by NIST [20]. Without further theoretical explanation this approach will be described in Section 2.3.2.

Mathematical gnostics presents the second paradigm of measurement uncertainty. Its brief explanation with one application relevant to the topic of this chapter will be given in Section 2.3.2.1.

2.3.1 Partial least-squares regression in multivariate analysis

In some cases, a straightforward chemical analysis of samples of the equilibrium phases is difficult or nearly impossible. This is particularly the case in multicomponent mixtures in which complex matrices are involved, leading for instance to overlapping spectra in UV–Vis spectrophotometric analysis. Chemometric methods of multivariate analysis based on principal components analysis (PCA) or partial least-squares regression (PLS) can then be applied to separate the interfering signals [21, 22]. These full-spectrum methods not only allow for a decomposition of complicated spectra, but may also help tackle nonlinearities or colinearity of the measured data.

The partial least-squares method is a covariance-based method of projection of large sets of data into their latent structures, that is, it finds a regression of data by

1 The word *algebra* was invented by al-Khwarizmi in his book entitled *al-Kitāb al-mukhtaṣar fī ḥisāb al-jabr wal-muqābala (The Compendious Book on Calculation by Completion and Balancing).*

projecting both the observed and the predicted variables into a new space. Several algorithms can be applied with a general model expressed as

$$\mathbf{X} = \mathbf{TP}^{\mathbf{T}} + \mathbf{E}$$
$$\mathbf{Y} = \mathbf{UQ}^{\mathbf{T}} + \mathbf{F}$$

In this model, **X** is an $n \times m$ matrix of predictors (independent variables); **Y** is an $n \times p$ matrix of responses (dependent variables); n is the number of samples; m is the number of measurements; **T** and **U** are $n \times$ l matrices that are, respectively, projections of **X** (the X score, component or factor matrix) and projections of **Y** (the Y scores); **P** and **Q** are, respectively, $m \times$ l and $p \times$ l orthogonal loading matrices and matrices **E** and **F** are the error terms, assumed to be independent and identically distributed random normal variables. The decompositions of **X** and **Y** are made so as to maximize the covariance between **T** and **U**.

In determination of LLE in systems of ILs, the multivariate partial least-squares regression algorithm (PLS2) was successfully used to separate overlapping spectra of 1-methylimidazole and 1-butyl-3-methylimidazolium hexafluorophosphate in their ternary system with 1-chlorobutane [8]. However, the method presents a disadvantage in that the number of factors to be used in the spectra decomposition is not easy to optimize.

2.3.2 Advanced data analysis by mathematical gnostics

Mathematical gnostics is a nonstatistical approach toward data uncertainty. Based on the theory of measurement, the Abelian group of ideal values is considered a numerical image of the true values of the measured quantity and an Abelian group of uncertainties is considered a numerical image of disturbances. Their Cartesian product forms an Abelian group of numerical images of measured values. The fundamental equation is written as

$$A = A_0 + S\Phi$$

where A is the measured value, A_0 is the ideal value, S is the scale parameter and the whole term $S\Phi$ means uncertainty. Having in mind that the terms are numerical images of entities from three different sets, their properties can be analyzed as shown in the book of Kovanic and Humber [23]. For each data item A, a data weight f and an irrelevance h can be calculated as

$$f = \frac{2}{q^2 + q^{-2}}$$

$$h = \frac{q^2 - q^{-2}}{q^2 + q^{-2}}$$

where

$$q = exp\left(\frac{A - A_0}{S}\right)$$

The data weight measures the quality of a measured value, it is equal to one for a value equal to the ideal value and decreases to zero for imprecise values. The irrelevance is limited between minus and plus one and reaches zero for a value equal to the ideal value. It is used to measure the departure of a measured value from the ideal value. Both these properties ensure robustness.

Using an alternative algebraic expression, the link to thermodynamics is obtained as shown in the abovementioned book. The energy and Boltzmann's entropy of a single datum can be calculated. Knowing the relations from the theory of information we can also calculate probability for each individual data point. This is the first difference from statistics.

The fundamental equation can also be rewritten using matrix calculus. Examination of this form reveals the link to Lorentz transformations from special theory of relativity. It thus follows that an additive quantity cannot be the measurement error as used in statistics but the data weight *f* and irrelevance *h* should be used as additive measures. This is the basis for a gnostic aggregation law that allows us to find the relation for the gnostic distribution function from the properties of individual measurements.

Mathematical gnostics thus differs from statistics in three principle features:

1. Based on thermodynamics of a single data point, probability can be calculated and the aggregated properties are thus valid even for small data sets, extrapolation from an infinite to finite data set is not used.
2. All properties are derived by using fundamental laws of nature.
3. The gnostic estimators are naturally robust.

2.3.2.1 Robust nonlinear regression along a gnostic influence function in thermodynamic description of liquid–liquid equilibria

An experimentalist always takes care to prevent gross errors. However, larger experimental errors may occur, and measurement methods may in principle be difficult owing to the physico-chemical nature. If a dependence between two or more quantities is measured, repeated measurements are not always available because repetition at exactly the same conditions is impossible. In such cases, outliers may remain undetected if proper data analysis is not employed.

In the presence of errors of different magnitudes, statisticians usually assign different weights. Such assignment is rather arbitrary based on judgement of an experimentalist or set pragmatically to improve overall agreement of a model and data. This idea is utilized in robust statistics where such weights are calculated *a*

posteriori based on data analysis, and the data are iteratively reweighted by regression along an influence function [24]. The influence function is derived from the model of outliers.

The statistical regression along an influence function is a useful tool but it has a hidden pitfall. The number of outliers is always small, therefore it is impossible to verify the validity of a selected model by statistical tests. The method can thus unpredictably fail. Mathematical gnostics adds an influence function based on the principles outlined above [25]. No matter which influence function is used, the points conforming well to the model are characterized by the values of the *a posteriori* weights close to one while the weights close to zero signal outliers.

We have extended the linear robust regression along an influence function to nonlinear regression. In principle, it is a combination of regular maximum likelihood regression explained in [26] enriched with application of iterative reweighting using a gnostic influence function. The method was used not only for regression of LLE data [18] but also for regression of data on diffusion through a porous membrane [27] and temperature dependence of viscosities [28]. The latter application showed that it was possible to detect a problem with a measuring device although it is not visible in the graphical representation.

As mentioned in [26], nonlinear regression is difficult because several local minima can exist. The gnostic influence function does not help to solve the problem. On the contrary, if regression along an influence function is used, several local minima can exist even in the linear case. Careful analysis is therefore needed and these two typical situations can be observed:

1. The majority of data agree with the model and only a few outliers are detected. In such a case we can assume that the model was found and we should try to find differences occurring in these few measurements in the logbook.
2. A large amount of outliers are found. This usually signals separation of data into two or more clusters. The result need not be the desired one. Instead we have to continue with analysis of the outliers. They can conform to a model with different parameters. If data are split into clusters according to an author or a method or a batch of chemicals used or any other common condition, it is evident that we have discovered a systematic error in at least one of the clusters.

Robust regression along an influence function has, however, a disadvantage and it is its higher computation cost. It is not such a problem in simple regression if a function value can be obtained by direct evaluation. The method becomes computationally expensive in case of regression of phase equilibrium data where a set of nonlinear equations must be solved for each data point in each iteration over model parameters. Robust regression adds another level of iterative reweighting. If a large data set has to be analyzed, creative approach to data pretreatment is inevitable.

References

[1] Weir RD, De Loos TW, Eds. Measurement of the Thermodynamic Properties of Multiple Phases, VII. Elsevier: Amsterdam, 2005.

[2] Wasserscheid P, Welton T, Eds. Ionic Liquids in Synthesis; Wiley-VCH Verlag GmbH & Co. KGaA: Weinheim, Germany, 2007.

[3] Almeida HFD, Carvalho PJ, Kurnia KA, Lopes-da Silva JA, Coutinho JAP, Freire MG. Surface tensions of ionic liquids: Non-regular trend along the number of cyano groups. Fluid Phase Equilib, 2016, 409, 458–465.

[4] Heintz A. Recent developments in thermodynamics and thermophysics of non-aqueous mixtures containing ionic liquids. A review. J Chem Thermodyn 2005, 37, 525–535.

[5] Huddleston JG, Visser AE, Reichert WM, Willauer HD, Broker GA, Rogers RD. Characterization and comparison of hydrophilic and hydrophobic room temperature ionic liquids incorporating the imidazolium cation Green Chem. 2001, 3, 156–164.

[6] Rotrekl J, Storch J, Velíšek P et al. Liquid phase behaviour in systems of 1-Butyl-3-Alkylimidazolium bis(trifluoromethyl) sulfonylimide ionic liquids with water: Influence of the structure of the C5 Alkyl substituent. J Solut Chem, 2017, 46, 1456–1474.

[7] Řehák K, Matouš J, Novák JP, Bendová M. (Liquid+liquid) equilibrium for (dimethyl phthalate + water), (diethyl phthalate + water), and (dibutyl phthalate + water). J Chem Thermodyn, 2000, 32, 393–400.

[8] Bendová M, Sedláková Z, Andresová A, Wagner Z. Using partial least-squares regression in multivariate UV spectroscopic analysis of mixtures of imidazolium-based ionic liquids and 1-methylimidazole for measurements of liquid-liquid equilibria. J Solut Chem, 2012, 41, 2164–2172.

[9] Meindersma GW, Podt AJG, de Haan AB. Ternary liquid-liquid ekvilibria for mixtures of toluene + n-heptane + an ionic liquid. Fluid Phase Equilib, 2006, 247, 158–168.

[10] Rodríguez-Cabo B, Soto A, Arce A. Desulfurization of fuel-oils with $[C_2mim][NTf_2]$: A comparative study. J Chem Thermodyn, 2013, 57, 248–255.

[11] Arce A, Rodríguez H, Soto A. Use of green and cheap ionic liquid to purify gasoline octane boosters. Green Chem 2007, 9, 247–253.

[12] Deenadayalu N, Ngcongo KC, Letcher TM, Ramjugernath D. Liquid-liquid Equilibria for ternary mixtures (an Ionic Liquid + Benzene + Heptane of Hexadecane) at T = 298.2 K and Atmospheric Pressure. J Chem Eng Data 2006, 51, 988–991.

[13] Letcher TM, Reddy P. Ternary (liquid + liquid) ekvilibria for mixtures of 1-hexyl-3-methylimidazolium (tetrafluoroborate of hexafluorophosphate) + benzene + an alkane at T = 298.2 K and p = 0.1 Mpa. J Chem Thermodyn 2005, 37, 415–421.

[14] Řehák K, Voňka P, Dreiseitlová J. Revision of the volumetric method for measurements of liquid–liquid equilibria in binary systems. Fluid Phase Equilib 2005, 230, 109–120.

[15] Bendová M, Wagner Z. Liquid-liquid Equilibria in binary system [bmim][PF_6] + 1-Butanol. J Chem Eng Data 2006, 51, 2126–2131.

[16] Hefter GT, Tomkins RPT, Eds. The Experimental Determination of Solubilities; John Wiley & Sons, Ltd.: Chichester, 2003.

[17] Ochi K, Saito T, Kojima K. Measurement and Correlation of Mutual Solubilities in 2-Butanol + Water. J Chem Eng Data, 1996, 41, 361–364.

[18] Bendová M, Wagner Z, Moučka M. Liquid-liquid Equilibrium in a Binary Systém 1-butyl-3-methylimidazolium Hexafluorophosphate + Water: Experiment and data correlation. Int J Ther 2008, 11, 109–114.

[19] Beck JV, Arnold KJ. Parameter estimation in engineering and science. J. Wiley and Sons, New York 1977.

[20] Taylor BN, Kuyatt C., Guidelines for evaluating and expressing the uncertainty of NIST measurement results, NIST Technical Note 1297, 1994.
[21] Trygg J, Wold S. Orthogonal projections to latent structures (O-PLS). J Chemom, 2002, 16, 119–128.
[22] Martens H, Naes T. Multivariate Calibration, Wiley, 1992.
[23] Kovanic P, Humber MB. The Economics of Information-Mathematical Gnostics for Data Analysis, book 717 pp [on-line], 2015. available online at http://www.math-gnostics.eu/books, [cit 2017-12-28] (5 September 2015).
[24] Heiberger RM, Becker RA. Design of an S function for robust regression using iteratively reweighted least squares. J Comput Graph Stat, 1992, 1, 181–196.
[25] Kovanic P. A new theoretical and algorithmical basis for estimation, identification and control. Automatica, 1986, 22 (6), 657–674.
[26] Voňka P, Novák JP, Matouš J. Application of the maximum likelihood method to the parameter evaluation in heterogenous systems. Collect Czech Chem Commun, 1989, 54, 2823–2839.
[27] Setničková K, Wagner Z, Noble R, Uchytil P. Semi-Empirical Model of toluene transport in polyethylene membranes based on the data using a new type of apparatus for determining gas permeability, diffusivity and solubility. J Membr Sci, 2011, 66(22), 5566–5574.
[28] Andresova A, Storch J, Traïkia M, Wagner Z, Bendova M, Husson P. Branched and cyclic alkyl groups in imidazolium-based ionqic liquids: Molecular organization and physico-chemical properties. Fluid Phase Equilib, 2014, 371, 41–49.

Teresa B.V. Dinis, Catarina M.S.S. Neves, Luís Barbosa,
João A.P. Coutinho and Mara G. Freire

3 Aqueous biphasic systems formed by cholinium-based ionic liquids and mixtures of polymers

Abstract: In the past years, the relevance of introducing ionic liquids (ILs) has been shown as phase-forming components of aqueous biphasic systems (ABS), which allow the tailoring of polarity differences between the coexisting phases. Although investigations on the IL chemical structure and polymer molecular weight have been carried out, the use of mixtures of polymers can also be seen as a way of tailoring their two-phase formation ability and separation performance, which was not attempted earlier. In this work, we investigate novel ABS composed of cholinium-based ILs and mixtures of polymers, namely polyethylene glycol (PEG) of 400 and 2,000 $g \cdot mol^{-1}$, at different mole fractions, as a way of tailoring the formation of ABS and their separation performance. The respective liquid–liquid phase diagrams were determined, and their ability to separate a set of alkaloids (caffeine, theophylline and theobromine) appraised. An increase on the PEG 2000 mole fraction favors the formation of ABS. However, this does not follow a monotonous trend, where mole fractions of PEG 400 up to 0.3 do not display significant impact on the two-phase separation capability. Among the studied alkaloids, nicotine preferentially partitions to the IL-rich phase, while the remaining alkaloids majorly partition to the polymer-rich phase. Different selectivity patterns were verified, depending on the cholinium-based IL used and water content at the IL-rich phase. Overall, by using mixtures of polymers it is possible to decrease the viscosity of the coexisting phases and their toxicity impact, without losing their formation and separation capacities, by the addition of PEGs of lower molecular weight.

Keywords: aqueous biphasic systems, ionic liquids, polymers, partition coefficients, alkaloids, selectivity

3.1 Introduction

The research on more sustainable solvents and processes for replacing the largely applied volatile organic solvents (VOCs) fits within the green chemistry principles [1] In this field, liquid–liquid extraction processes based on aqueous biphasic systems (ABS) are seen as an alternative and promising route to replace the use of VOCs [2, 3].

Teresa B.V. Dinis, Catarina M.S.S. Neves, Luís Barbosa, João A.P. Coutinho, Mara G. Freire,
Department of Chemistry, University of Aveiro, Portugal

https://doi.org/10.1515/9783110583632-003

These systems are formed by combining at least two water-miscible nonvolatile compounds that, above specific concentrations, undergo phase separation [4]. The most common ABS are those composed of polymer–polymer [2, 3] and polymer–salt [2, 3] pairs dissolved in aqueous media, in which polyethylene glycol (PEG) has been one of the most investigated polymers due to its low cost and low toxicity [5] However, the narrow hydrophilic–hydrophobic range associated with these more conventional polymer-based ABS limits their applicability when selective extractions or separations from more complex matrices are envisaged. More recently, the use of ionic liquids (ILs) has been suggested to create ABS, [6] and a large number of IL–salt [4, 6], IL–polymer [4, 7] and IL–carbohydrate [4, 8] combinations have been reported. Due to the innumerous combinations between IL cations and anions[9], IL-based ABS allow the tailoring of polarity differences between the coexisting phases [4]. Accordingly, it has been demonstrated that the introduction of ILs leads to ABS with high extraction performance and selectivity for a large plethora of compounds [4].

Several PEG-IL-based ABS have been studied [4, 7, 10, 11], with selective separations achieved with these systems [12]. Moreover, the presence of ILs in ABS offers additional advantages over traditional polymer–polymer ABS, such as lower viscosities and faster phase separation [4] Besides the tunability of ILs, most reported ABS are formed by ILs based on imidazolium and pyridinium cations and/or composed of fluorinated anions, raising several toxicity and biodegradability concerns [13]. More recent studies have proposed a new class of natural-derived cholinium-based salts or ILs as more sustainable alternatives to the conventional IL structures [5, 14–16]. Most cholinium-based ILs are easier to synthesize and are of lower cost [11, 24–26]. Furthermore, some present enhanced biocompatibility [17–20] and low toxicity profiles [21–24]. This type of ILs also has demonstrated a high capability to undergo phase separation or to create ABS in the presence of aqueous solutions of inorganic/organic salts [16, 25–27] or aqueous solutions of polymers [5, 11, 14, 28, 29].

For ternary systems composed of ILs, high charge density salts and water, it has been demonstrated that the two-phase separation occurs due to the competition of the ions to form hydration complexes and to induce the salting-out [4, 16]. However, when dealing with ternary systems composed of polymers, such as PEG, a more complex scenario was reported [4]. It has been demonstrated that the formation of ABS composed of ILs and PEG depends on the balance of interactions of all components in equilibrium (IL ions, PEG and water) [5, 14, 30], that largely depend on the ternary system composition. In addition to these works that allow to better understand the formation of IL-PEG ABS, the molecular-level mechanisms driving the partitioning of biomolecules in these systems were also investigated. Pereira et al. [11] evaluated the partitioning of three alkaloids (caffeine, theophylline and theobromine) in a series of ABS formed by cholinium-based compounds and PEG 600 (PEG with a molecular weight of 600 $g.mol^{-1}$). The authors [11] concluded that the biomolecules preferentially migrate to the most hydrophobic phase, as addressed by the phases' water content, also allowing the use of this type of data to characterize the relative hydrophobicity of the coexisting phases.

Up to date, most reports on ABS formed by cholinium-based ILs and polymers focused on the IL ions chemical structure and polymer molecular weight to manipulate their two-phase formation ability and extraction performance [5, 11, 14, 28, 29] Nevertheless, the polymer molecular weight and its weight can be tailored by attempting the use of mixtures of polymers. In this work, we investigated ABS composed of cholinium-based ILs and mixtures of two PEGs with distinct molecular weights, namely PEG 400 and PEG 2000 with 400 and 2,000 g·mol^{-1}, respectively, as a way of tailoring the formation of ABS and the partitioning coefficients of a series of alkaloids (caffeine, theophylline, theobromine and nicotine). The ternary phase diagrams were determined at 298 K, for different ILs and mixtures of polymers at different mole fraction compositions, to infer their two-phase formation aptitude, followed by their evaluation to separate alkaloids through the determination of the respective partition coefficients and selectivity.

3.2 Experimental section

3.2.1 Chemicals

PEGs of molecular weights of 400 and 2,000 g mol^{-1} (PEG 400 and PEG 2000), acquired from Fluka and Alfa Aesar, respectively, were used. The studied cholinium ([$N_{111(2OH)}$]$^+$)-based ILs to form ABS with mixtures of polymers were commercially acquired, namely cholinium dihydrogen phosphate [$N_{111(2OH)}$][DHP] (>98 wt% from Iolitec) and cholinium bitartarate [$N_{111(2OH)}$][Bit] (97 wt% from Acros Organics). It should be remarked that cholinium dihydrogen citrate, [$N_{111(2OH)}$][DHC], cholinium bicarbonate, [$N_{111(2OH)}$][Bic], cholinium chloride, [$N_{111(2OH)}$]Cl, cholinium acetate, [$N_{111(2OH)}$][Ac], and cholinium butanoate, [$N_{111(2OH)}$][But], were also tested; however, they are not able to form ABS with PEG 2000 or with the mixtures of polymers investigated. The alkaloids studied as partitioning solutes were caffeine (99 wt%) and nicotine (99 wt%) from Fluka, and theophylline (99 wt%) and theobromine (99 wt%) from Sigma-Aldrich. The chemical structures of the cholinium-based ILs able to form ABS, polymers and alkaloids are depicted in Figure 3.1. The water used was double distilled, passed through a reverse osmosis system and further treated with a Milli-Q plus 185 apparatus.

3.3 Experimental procedure

3.3.1 Phase diagrams

The binodal curves, that is, the solubility curves that separate the monophasic and biphasic regions, were determined through the cloud point titration method [31–35]

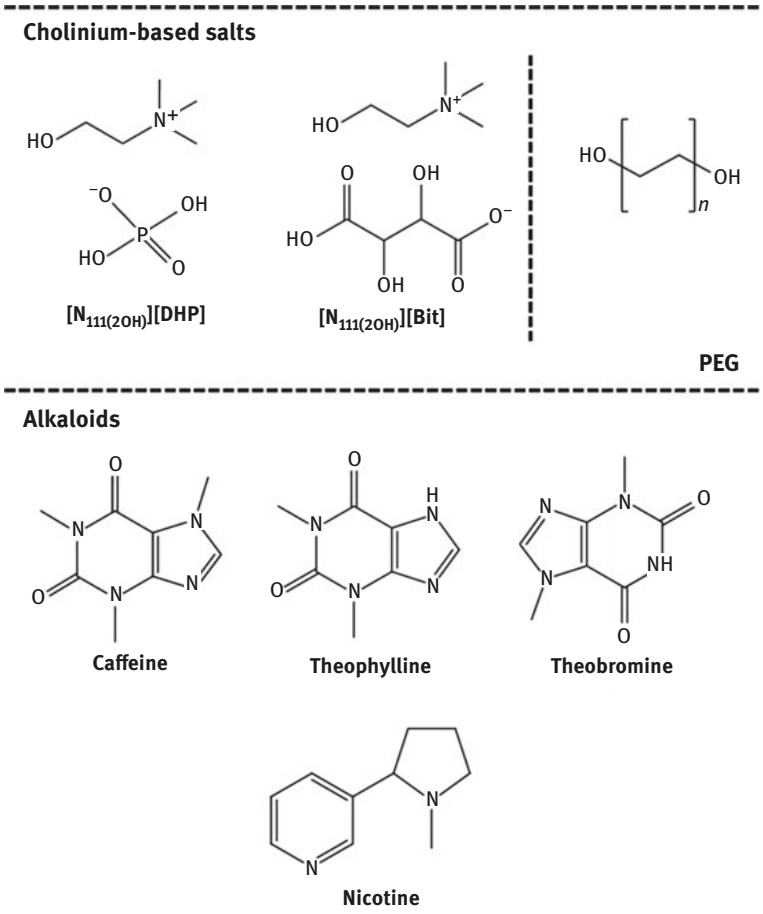

Figure 3.1: Chemical structures of the investigated ABS phase-forming components and alkaloids.

at (298 ± 1) K and atmospheric pressure. Aqueous solutions of polymers at approximately 60 wt% and aqueous solutions of the different cholinium-based IL ranging from 60 to 70 wt% were prepared and used for the determination of the binodal curves. Repetitive dropwise addition, under constant stirring, of the aqueous solution of cholinium-based salts to the aqueous solutions of PEGs, or vice versa, was carried out until the detection of a cloudy (biphasic) solution, followed by the dropwise addition of water until observing a monophasic region (clear and limpid solution). Pure PEG 400 and PEG 2000 and mixtures of both polymers at several mole fractions of PEG 400 (0.9, 0.75, 0.5, 0.25 and 0.1) were used. The systems formed by pure PEGs correspond to ternary systems, whereas those formed by mixtures of polymers are quaternary systems, although they are treated in this work as pseudo-ternary systems in order to simplify the evaluation of their impact toward the behavior of phase diagrams. All the investigated cholinium-based salts were

previously demonstrated to induce the formation of ABS with PEG 400, with the exception of $[N_{111(2OH)}][But]$ [5] On the other hand, only $[N_{111(2OH)}][DHP]$ and $[N_{111(2OH)}]$ [Bit] were able to form ABS with PEG 2000 and mixtures of polymers. For the remaining ILs only solid–liquid equilibrium was observed when PEG 2000 was added. The chemical structures of the cholinium-based ILs able to form ABS with PEG 2000 and mixtures of PEG 400 + PEG 2000 are given in Figure 3.1.

3.3.2 Composition of the coexisting phases (tie-lines)

The coexisting phases of the ABS investigated in this work were characterized by the quantification of the phase-forming components. The cholinium cation, and thus the IL content, in each phase was quantified by ^1H nuclear magnetic resonance (NMR) using a Bruker Avance 300 at 300.13 MHz, with dimethyl sulfoxide-d6 (DMSO-d6) as solvent and 0.03 vol% of tetramethylsilane as the internal reference. Approximately 3 vol% of benzene was added to each sample as internal standard. Examples of the obtained spectra for the PEG-rich and IL-rich phases are provided in the Supplementary Material – Figure 3.S.1. The water amount in each phase was gravimetrically determined ($\pm 10^{-4}$ g) by evaporation, using an air oven at ~100 °C, until a constant weight of the nonvolatile mixture (PEG + IL) was achieved. The amount of PEG in each phase was determined by mass balance. This process was carried out in triplicate to ascertain the associated standard deviations.

3.3.3 Partitioning and selectivity of alkaloids

Aqueous solutions of each alkaloid at the following concentrations were prepared: 4.7×10^{-3} mol·dm^{-3} for nicotine, caffeine and theophylline, and 1.1×10^{-3} mol·dm^{-3} for theobromine. At these concentrations all molecules can be considered at infinite dilution and completely solvated in aqueous media avoiding thus specific alkaloid–alkaloid interactions. For the partitioning studies, ternary mixture compositions were chosen based on the determined phase diagrams. All the partitioning studies were performed at a constant mixture composition for $[N_{111(2OH)}][DHP]$-based ABS (25.7 wt% of PEG + 35.7 wt% of IL) and at variable compositions for $[N_{111(2OH)}][Bit]$-based ABS (21–42 wt% of PEG + 33–37 wt% of IL). This last IL leads to phase diagrams that largely depend on the PEG mixture used, thus requiring to work with different mixture compositions able to form liquid-liquid systems (instead of monophasic or solid-liquid mixtures). Each mixture was vigorously stirred and left to equilibrate for at least 12 h (period established in previous optimizing experiments) in order to achieve a complete partitioning of each alkaloid between the two phases. After careful separation of both phases, the alkaloids in each phase were quantified by UV-spectroscopy, using a SHIMADZU UV-1700, Pharma-Spec Spectrometer, at a

wavelength of 260 nm for nicotine, 272 nm for theophylline and 273 nm for caffeine and theobromine, using calibration curves previously established. At least three ABS for each set of conditions and three individual samples of each phase were quantified in order to determine the average partition coefficients and corresponding standard deviations. Blank control samples were always used.

The partition coefficients of the studied alkaloids, K_{Alk}, are defined as the ratio of the concentration of each biomolecule in the PEG- to that in the IL-rich phase, according to eq. (3.1):

$$K_{Alk} = \frac{[Alk]_{PEG}}{[Alk]_{salt}} \tag{3.1}$$

The selectivity of the studied ABS to extract caffeine, theophylline and theobromine with respect to nicotine to the PEG-rich phase was determined according to eqs. (3.2)–(3.4), respectively,

$$S_{caf/nic} = \frac{K_{caf}}{K_{nic}} \tag{3.2}$$

$$S_{theof/nic} = \frac{K_{theop}}{K_{nic}} \tag{3.3}$$

$$S_{theob/nic} = \frac{K_{theob}}{K_{nic}} \tag{3.4}$$

3.3.4 pH and conductivity measurements

After the phase separation, the pH values (± 0.02) and conductivities (± 0.01 $mS{\cdot}cm^{-1}$) of each phase were determined at (298 ± 1) K using a SevenMulti (METTLER TOLEDO Instruments). The PEG- and IL-rich phases were identified by conductivity values.

3.4 Results and discussion

3.4.1 Phase diagrams

Several cholinium-based ILs or salts, composed of anions $[DHC]^-$, $[Bic]^-$, $[DHP]^-$, $[Bit]^-$, Cl^-, $[Ac]^-$ and $[But]^-$, were tested with regard to their ability to form ABS when combined with water and PEGs of two different molecular weights, namely 400 and 2,000 $g{\cdot}mol^{-1}$, or their mixtures. All the investigated cholinium-based salts were previously demonstrated to induce the formation of ABS with PEG 400, with the exception of $[N_{111(2OH)}][But]$ [5]. According to these data, PEG 2000 and mixtures of PEG 400 and PEG 2000 (different mole fractions, namely 0.9, 0.75, 0.5, 0.25 and 0.1 of

PEG 400) were investigated in order to evaluate the impact of mixtures of polymers with different molecular weights on the ABS formation ability. From all ILs tested, only $[N_{111(2OH)}][DHP]$ and $[N_{111(2OH)}][Bit]$ form liquid–liquid systems with PEG 2000 and mixtures of PEG 400 and PEG 2000 in water. For the remaining cholinium-based salts, only solid–liquid equilibrium was observed when PEG 2000 or mixtures comprising PEG 2000 were added. In a previous work, the existence of favorable interactions was demonstrated between PEG 600 and the IL anions, and that the strength of these interactions increase in the following order: $[DHP]^- < [Bit]^- < [Bic]^- < [Lac]^- \approx [Gly]^- \approx [Ac]^- < [DHC]^- \approx Cl^-$.[5] The authors [5] concluded that IL–polymer interactions play a significant role in the formation of respective ABS and that ILs with weaker interactions with the polymer are those that more easily form two-phase systems, being in agreement with the data gathered in this work where only $[N_{111(2OH)}][DHP]$ and $[N_{111(2OH)}][Bit]$ are able to induce the two-phase formation with mixtures of PEG 2000 and PEG 400. Similar findings were provided by Cláudio and coworkers [36] in the formation of ABS composed of protic alkylammonium-based ILs and PEG, demonstrating that the formation of protic IL–PEG-based ABS is dependent on the strength of the IL–PEG interactions [36].

The liquid–liquid phase diagrams of ABS composed of $[N_{111(2OH)}][DHP]$ or $[N_{111(2OH)}][Bit]$, PEG 400, PEG 2000 or their mixtures, and water, are depicted in Figure 3.2. For all phase diagrams, the biphasic region is located above the binodal curve, whereas the monophasic region is below the solubility curve. All data are shown in molality units to avoid effects derived from the phase-forming components molecular weights. The detailed experimental weight fraction data are provided in the Supplementary Material – Tables 3.S.1 to 3.S.12.

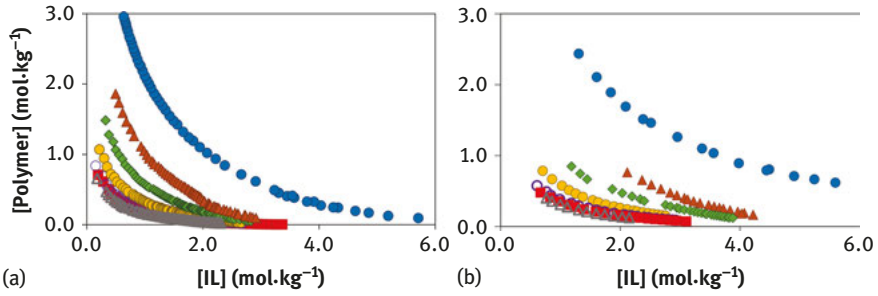

Figure 3.2: Phase diagrams of ABS at (298 ± 1) K and atmospheric pressure, composed of (A) $[N_{111(2OH)}][DHP]$ or (B) $[N_{111(2OH)}][Bit]$, and PEG 400 at different mole fractions in PEG 400 + PEG 2000 mixtures: 1.0[5] (●), 0.90 (▲), 0.75 (◆), 0.50 (●), 0.25 (○), 0.10 (■) and 0.0 (△).

Comparing the phase diagrams of the PEG-based ABS composed of $[N_{111(2OH)}][DHP]$ against those involving $[N_{111(2OH)}][Bit]$ for a given PEG or polymer mixture, the first are positioned at lower polymer/IL concentrations, meaning that $[N_{111(2OH)}][DHP]$ is more able to form two-phase systems and consequently require lower amounts of polymer

or IL to undergo liquid–liquid demixing. This result is in good agreement with the trend discussed earlier and with literature data, [5] where the authors [5] showed that [$N_{111(2OH)}$][DHP] establishes weaker interactions with PEG, and therefore has the highest ability to promote ABS, followed by [$N_{111(2OH)}$][Bit]. This trend occurs with PEG 400, PEG 2000 and their mixtures.

Figure 3.2 allows to evaluate the influence of different contents of PEG 400 and PEG 2000 in the formation of ABS. For the two cholinium-based ILs investigated, ABS are more easily formed using polymers of higher molecular weight (PEG 2000 versus PEG 400). This behavior is in accordance with previous studies on PEG–salt [5, 37] and PEG–IL [5, 36, 38] ABS. Pereira et al. [5] demonstrated the effect of PEG molecular weight on the ABS formation ability with cholinium-based salts, increasing in the order: PEG 400 < PEG 600 < PEG 1000. Furthermore, an increase in the PEG 2000 mole fraction in the polymer mixtures, resulting in an increase of the polymer hydrophobicity, leads to an easier ABS formation, that is, lower amounts of phase-forming components are required to form two-phase systems. Still, the effect of the addition of PEG 2000 does not follow a monotonous trend based on its mole fraction (Figure 3.3).

In Figure 3.3 it is shown that it is possible to improve the performance of ABS formation by continuously increasing the PEG 2000 amount for the systems containing [$N_{111(2OH)}$][DHP] or [$N_{111(2OH)}$][Bit]. However, for higher PEG 2000 contents (up to ca. 0.3 of PEG 400), PEG 400 has no major relevance on the phase diagram formation ability, being close to the performance displayed by systems composed of PEG 2000 alone. This trend can be seen as a major advantage when envisaging large-scale applications since PEGs of lower molecular weight, such as PEG 400, allow to decrease both the phases' viscosity and toxicity impact [39, 40], while keeping the two-phase formation ability.

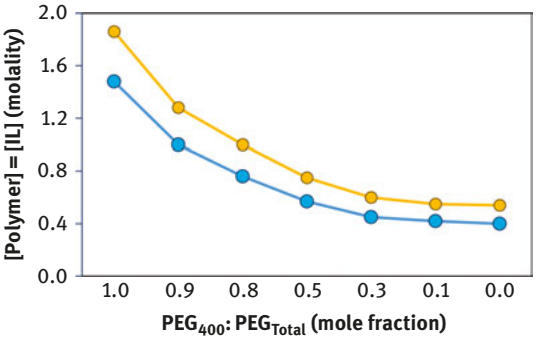

Figure 3.3: Correlation between the capability of cholinium-based compounds to create ABS (addressed by the values at each binodal curve at which the molality of polymer is equal to the molality of IL) and the mole fraction of PEG 400 in the PEG 400 + PEG 2000 mixture: [$N_{111(2OH)}$][DHP] (●) and [$N_{111(2OH)}$][Bit] (●) .

3.4.2 Partitioning and selectivity of alkaloids

ABS composed of ILs and polymers, such as PEG, have demonstrated interesting applications due to their wide polarity at the coexisting phases and separation performance [5, 11, 14]. Although large efforts have been placed on the interpretation of the molecular-level mechanisms that rule the formation of such type of systems [7, 11, 14, 36], research works on the use of these systems for the separation of biomolecules are more scarce [11, 12]. In order to better understand the mechanisms that govern the partitioning of biomolecules in ABS formed by ILs and polymers, as well as to identify the potential of these systems as platforms of extraction and purification, in this work we investigated the partitioning of several alkaloids, namely caffeine, theophylline, theobromine and nicotine, between the two phases.

The logarithmic values of the partition coefficients of all alkaloids at (298 ± 1) K are depicted in Figure 3.4. Detailed data on the partition coefficients and extraction efficiencies are given in the Supplementary Material – Table 3.S.13. It should be stressed that similar compositions of the phase-forming components in all systems were considered to evaluate the partitioning behavior of four alkaloids – cf Section 3.2.

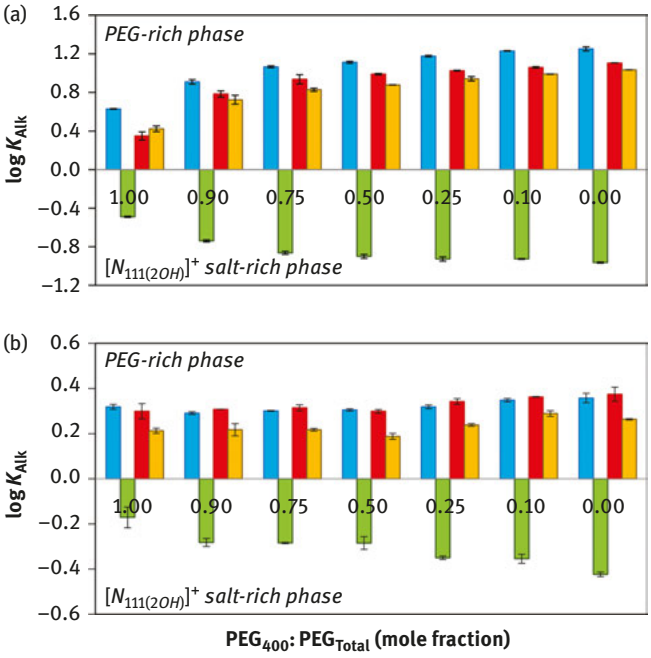

Figure 3.4: Logarithm of partition coefficients of alkaloids (logK_{Alk}) in ABS composed of cholinium-based ILs ((A) $[N_{111(2OH)}][DHP]$ and (B) $[N_{111(2OH)}][Bit]$) and PEG 400 at different mole fractions in PEG 400 + PEG 2000 mixtures (PEG total = PEG 400 + PEG 2000): caffeine (●), theophylline (●), theobromine (●), and nicotine (●).

Moreover, in all the investigated systems, the top phase corresponds to the polymer-rich phase, whereas the bottom phase is chiefly composed of IL and water, as identified by conductivity (experimental data given in the Supplementary Material).

With the exception of nicotine that favorably partitions to the IL-rich phase, the results obtained indicate that all alkaloids preferentially migrate to the polymer-rich phase, independently of the PEG 400 mole fraction. The pH values of both phases range between 3.5 and 5.0, as given in the Supplementary Material. Taking into account the alkaloids speciation as a function of the pH, [20] caffeine, theophylline and theobromine are mainly present as neutral molecules, while positively charged species are the predominant form for nicotine. These results reinforce the relevance of electrostatic interactions between the charged solute and the IL ions, in line with previous works addressing the partitioning of alkaloids [11, 12].

As already stated, and according to the data shown in Figure 3.4, all alkaloids migrate to the polymer-rich phase, while nicotine preferentially migrates to the IL-rich phase. However, the increase in the PEG 2000 mole fraction seems to favor the partition of all biomolecules for the corresponding phases, with the highest partition coefficient values obtained with ABS composed of IL and pure PEG 2000. Furthermore, ABS constituted by $[N_{111(2OH)}][Bit]$ present lower partition coefficients when compared with those containing $[N_{111(2OH)}][DHP]$, and for which the PEG 2000 addition or content has a less significant influence. Overall, the obtained results suggest that it is possible to tailor the separation performance of IL-PEG-based ABS by applying mixtures of PEGs.

The selective character of the studied ABS was further investigated by the determination of selectivity of systems to extract caffeine, theophylline and theobromine over nicotine. The corresponding results are shown in Figure 3.5. The increase in PEG 2000 mole fraction influences the selective separation of nicotine from the remaining alkaloids, and for which different selectivity patterns are observed depending on the IL used. The increase in PEG 2000 mole fraction in $[N_{111(2OH)}][DHP]$-based systems favors the separation of nicotine from the remaining alkaloids, whereas an inverse behavior is observed in systems composed of $[N_{111(2OH)}][Bit]$.

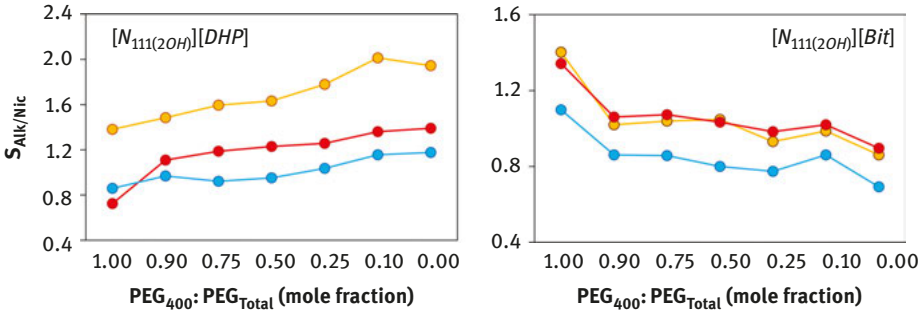

Figure 3.5: Selectivity of the studied ABS for caffeine/nicotine (●), theophylline/nicotine (●) and theobromine/nicotine (●).

The coexisting phases of the studied ABS were additionally characterized in order to better understand the partitioning profiles observed for the four alkaloids. The phase compositions were analytically determined, whose results are given in Table 3.1.

Table 3.1: Weight fraction composition (wt%) of the polymer-rich phase (PEG), initial mixture point (M) and IL-rich phase (IL) of systems composed of IL + PEG 400 + PEG 2000 + H_2O.

PEG 400: PEG_{Total} (mole fraction)	Weight fraction composition/(wt%)					
	$[PEG]_{PEG}$	$[IL]_{PEG}$	$[PEG]_M$	$[IL]_M$	$[PEG]_{IL}$	$[IL]_{IL}$
			$[N_{111(2OH)}][DHP]$			
1.00	49.66	5.38	24.71	34.39	9.56	43.34
0.90	53.83	5.37	24.54	34.71	0.00	55.77
0.50	46.10	2.09	24.54	34.88	0.00	62.86
0.00	58.44	0.93	24.54	34.79	0.00	61.88
			$[N_{111(2OH)}][Bit]$			
1.00	49.63	25.83	44.35	32.28	8.38	65.81
0.90	48.10	21.47	29.94	37.10	4.83	60.26
0.50	29.46	30.62	21.00	37.06	0.00	60.38
0.00	40.07	21.75	20.95	37.09	0.00	72.28

The average uncertainty of all parameters is within ± 10%.

Along with the increase in PEG 2000 mole fraction, there is an increase in the IL content and a decrease in the water and PEG contents in the IL-rich phase. Figure 3.6 represents the correlation between the selectivity of the studied ABS, discussed in Figure 3.5, as a function of the water content in the IL-rich phase – phase for which nicotine preferentially migrates. Detailed experimental data for alkaloids selectivity available in Supplementary Material – Table 3.S.15. Different patterns are observed between $[N_{111(2OH)}][DHP]$ and $[N_{111(2OH)}][Bit]$, although close linear correlations have been found in both situations. The higher/lower water-affinity profiles of the IL-rich phases follow the selective partitioning tendencies observed with the two cholinium-based salts.

Among the studied alkaloids, nicotine presents the lowest affinity for water, as predicted by its higher octanol–water partition coefficient (log K_{ow} = 1.17[20]), while caffeine, theophylline and theobromine display higher affinities for water, with log K_{ow} values of –0.07,[20] –0.04[20] and –0.78,[20] respectively. Moreover, and as stated earlier, nicotine is positively charged at the studied conditions and preferentially partitions to the IL-rich phase, whereas the remaining alkaloids are in their neutral state and preferentially migrate to the PEG-rich phase. According to Figure 3.6, for ABS composed of $[N_{111(2OH)}][DHP]$, the increase in the water content in the cholinium-rich phase, accompanied by the decrease of PEG 2000 in the system, leads to a favorable selective

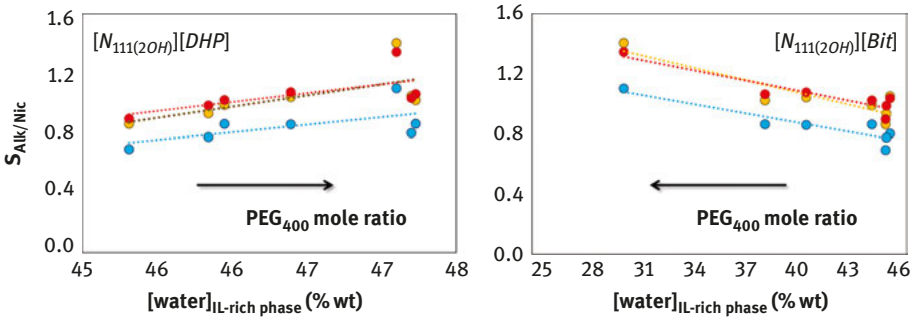

Figure 3.6: Correlation between the selectivity of the studied ABS for caffeine/nicotine (●), theophylline/nicotine (●) and theobromine/nicotine (●), as a function of water content determined in the $[N_{111(2OH)}]^+$-rich phase.

separation of nicotine from the remaining alkaloids, reflected by the increase in selectivity values. On the other hand, for ABS composed of $[N_{111(2OH)}][Bit]$, the increase of water content in cholinium-rich phase, together with the increase of PEG 2000 in the system, leads to a less favorable selective separation of nicotine from the remaining alkaloids, as shown by the decrease in selectivity values. In summary, these results show that it is possible to tailor the partition coefficients and selectivity of target biomolecules using ABS composed of ILs and mixtures of polymers, in which the IL and polymer type, and their content, play a significant role on the partition profile.

The novel ABS here determined, formed by ILs and mixtures of PEGs, allow us to obtain novel insights on their two-phase formation ability and on the selective partitioning of biomolecules. Although a deeper understanding on the relative hydrophilic/hydrophobic balance in these systems is still needed in order to better understand the mechanisms behind their separation performance, it was demonstrated that the studied systems allow the tailoring on the two-phase formation ability and separation performance by using mixtures of polymers. Furthermore, it is possible to decrease the viscosity of the coexisting phases and toxicity impact of these systems [39, 40], without losing their formation and separation capacities, by the addition of PEGs of lower molecular weight (up to some extents; in this work, up to ca. 0.3 mole fraction of PEG 400).

3.5 Conclusions

Novel ABS composed of cholinium-based ILs and mixtures of PEG 400 and PEG 2000 (at several mole fractions of PEG 400, namely 1.0, 0.90, 0.75, 0.50, 0.25, 0.10 and 0.0) were investigated. The determined liquid–liquid phase diagrams show that it is possible to improve the ability of two-phase separation by continuously increasing the PEG 2000 amount. However, up to ca. 0.30 mole fraction of PEG 400, there is no significant impact on the liquid–liquid demixing ability, which means that it is

possible to decrease the viscosity of the coexisting phases and toxicity impact of these systems, without losing their formation aptitude, by the addition of PEGs of lower molecular weight. The investigated ABS were further evaluated as separation techniques for biomolecules, using a set of alkaloids (caffeine, theophylline, theobromine and nicotine). The selectivity of the ABS to separate nicotine over the remaining alkaloids was also determined. Different selectivity patterns were verified, depending on the cholinium-based IL used and water content at the IL-rich phase. ABS formed by ILs and mixtures of polymers allow the tailoring of their formation ability and separation performance, while bringing additional advantages in terms of viscosity and toxicity impact when large-scale applications are envisaged.

Acknowledgments: This work was developed within the scope of the project CICECO-Aveiro Institute of Materials, POCI-01-0145-FEDER-007679 (FCT Ref. UID/CTM/50011/2013), financed by national funds through FCT/MEC and FEDER under the PT2020 Partnership Agreement. C. M. S. S. Neves and T. B. V. Dinis acknowledge FCT for the postdoctoral and doctoral grants SFRH/BDP/109057/2015 and SFRH/BD/130958/2017, respectively. M. G. Freire acknowledges the European Research Council under the European Union's Seventh Framework Programme (FP7/2007-2013)/ERC grant agreement no. 337753.

References

[1] P. Anastas and N. Eghbali, *Chemical Society Reviews*, 2010, **39**, 301–312.
[2] R. Hatti-Kaul, *Molecular Biotechnology*, 2001, **19**, 269–277.
[3] B. Y. Zaslavsky, *Aqueous Two-Phase Partitioning: Physical Chemistry and Bioanalytical Applications*, Taylor & Francis, Boca Raton, 1994.
[4] M. G. Freire, A. F. M. Claudio, J. M. M. Araujo, J. A. P. Coutinho, I. M. Marrucho, J. N. Canongia Lopes and L. P. N. Rebelo, *Chemical Society Reviews*, 2012, **41**, 4966–4995.
[5] J. F. B. Pereira, K. A. Kurnia, O. A. Cojocaru, G. Gurau, L. P. N. Rebelo, R. D. Rogers, M. G. Freire and J. A. P. Coutinho, *Physical Chemistry Chemical Physics*, 2014, **16**, 5723–5731.
[6] K. E. Gutowski, G. A. Broker, H. D. Willauer, J. G. Huddleston, R. P. Swatloski, J. D. Holbrey and R. D. Rogers, *Journal of the American Chemical Society*, 2003, **125**, 6632–6633.
[7] J. F. B. Pereira, L. P. N. Rebelo, R. D. Rogers, J. A. P. Coutinho and M. G. Freire, *Physical Chemistry Chemical Physics*, 2013, **15**, 19580–19583.
[8] M. G. Freire, C. L. S. Louros, L. P. N. Rebelo and J. A. P. Coutinho, *Green Chemistry*, 2011, **13**, 1536–1545.
[9] N. V. Plechkova and K. R. Seddon, *Chemical Society Reviews*, 2008, **37**, 123–150.
[10] Z. P. Visak, J. N. C. Lopes and L. P. N. Rebelo, *Monatshefte Fur Chemie*, 2007, **138**, 1153–1157.
[11] J. F. B. Pereira, A. Magri, M. V. Quental, M. Gonzalez-Miquel, M. G. Freire and J. A. P. Coutinho, *Acs Sustainable Chemistry & Engineering*, 2016, **4**, 1512–1520.
[12] J. F. B. Pereira, S. P. M. Ventura, F. A. e Silva, S. Shahriari, M. G. Freire and J. A. P. Coutinho, *Separation and Purification Technology*, 2013, **113**, 83–89.
[13] M. Petkovic, K. R. Seddon, L. P. N. Rebelo and C. S. Pereira, *Chemical Society Reviews*, 2011, **40**, 1383–1403.
[14] J. F. B. Pereira, K. A. Kurnia, M. G. Freire, J. A. P. Coutinho and R. D. Rogers, *Chemical Physics Chemistry*, 2015, **16**, 2219–2225.

[15] M. Petkovic, J. L. Ferguson, H. Q. N. Gunaratne, R. Ferreira, M. C. Leitao, K. R. Seddon, L. P. N. Rebelo and C. S. Pereira, *Green Chemistry*, 2010, **12**, 643–649.
[16] S. Shahriari, L. C. Tome, J. M. M. Araujo, L. P. N. Rebelo, J. A. P. Coutinho, I. M. Marrucho and M. G. Freire, *RSC Advances*, 2013, **3**, 1835–1843.
[17] H. Garcia, R. Ferreira, M. Petkovic, J. L. Ferguson, M. C. Leitao, H. Q. N. Gunaratne, K. R. Seddon, L. P. N. Rebelo and C. S. Pereira, *Green Chemistry*, 2010, **12**, 367–369.
[18] Z. Y. Li, X. X. Liu, Y. C. Pei, J. J. Wang and M. Y. He, *Green Chemistry*, 2012, **14**, 2941–2950.
[19] R. Vijayaraghavan, B. C. Thompson, D. R. MacFarlane, R. Kumar, M. Surianarayanan, S. Aishwarya and P. K. Sehgal, *Chemical Communications*, 2010, **46**, 294–296.
[20] Chemspider, The Free Chemical Database, http://www.chemspider.com/, (accessed 15th December, 2016).
[21] K. D. Weaver, H. J. Kim, J. Z. Sun, D. R. MacFarlane and G. D. Elliott, *Green Chemistry*, 2010, **12**, 507–513.
[22] P. Nockemann, B. Thijs, K. Driesen, C. R. Janssen, K. Van Hecke, L. Van Meervelt, S. Kossmann, B. Kirchner and K. Binnemans, *Journal of Physical Chemistry B*, 2007, **111**, 5254–5263.
[23] M. Petkovic, J. Ferguson, A. Bohn, J. Trindade, I. Martins, M. B. Carvalho, M. C. Leitao, C. Rodrigues, H. Garcia, R. Ferreira, K. R. Seddon, L. P. N. Rebelo and C. S. Pereira, *Green Chemistry*, 2009, **11**, 889–894.
[24] S. P. M. Ventura, F. A. E. Silva, A. M. M. Goncalves, J. L. Pereira, F. Goncalves and J. A. P. Coutinho, *Ecotoxicology and Environmental Safety*, 2014, **102**, 48–54.
[25] R. Wang, Y. Chang, Z. Tan and F. Li, *Journal of Molecular Liquids*, 2016, **222**, 836–844.
[26] C.-X. Zeng, R.-P. Xin, S.-J. Qi, B. Yang and Y.-H. Wang, *Journal of Separation Science*, 2016, **39**, 648–654.
[27] T. E. Sintra, R. Cruz, S. P. M. Ventura and J. A. P. Coutinho, *The Journal of Chemical Thermodynamics*, 2014, **77**, 206–213.
[28] M. V. Quental, M. Caban, M. M. Pereira, P. Stepnowski, J. A. P. Coutinho and M. G. Freire, *Biotechnology Journal*, 2015, **10**, 1457–1466.
[29] C. P. Song, R. N. Ramanan, R. Vijayaraghavan, D. R. MacFarlane, E. S. Chan and C. W. Ooi, *Acs Sustainable Chemistry and Engineering*, 2015, **3**, 3291–3298.
[30] L. I. N. Tome, J. F. B. Pereira, R. D. Rogers, M. G. Freire, J. R. B. Gomes and J. A. P. Coutinho, *Physical Chemistry Chemical Physics*, 2014, **16**, 2271–2274.
[31] C. Neves, S. P. M. Ventura, M. G. Freire, I. M. Marrucho and J. A. P. Coutinho, *Journal of Physical Chemistry B*, 2009, **113**, 5194–5199.
[32] S. P. M. Ventura, C. Neves, M. G. Freire, I. M. Marrucho, J. Oliveira and J. A. P. Coutinho, *Journal of Physical Chemistry B*, 2009, **113**, 9304–9310.
[33] T. B. V. Dinis, H. Passos, D. L. D. Lima, V. I. Esteves, J. A. P. Coutinho and M. G. Freire, *Green Chemistry*, 2015, **17**, 2570–2579.
[34] J. C. Merchuk, B. A. Andrews and J. A. Asenjo, *Journal of Chromatography B*, 1998, **711**, 285–293.
[35] H. Passos, D. J. P. Tavares, A. M. Ferreira, M. G. Freire and J. A. P. Coutinho, *ACS Sustainable Chemistry and Engineering*, 2016, **4**, 2881–2886.
[36] A. F. M. Claudio, J. F. B. Pereira, P. D. McCrary, M. G. Freire, J. A. P. Coutinho and R. D. Rogers, *Physical Chemistry Chemical Physics*, 2016, **18**, 30009–30019.
[37] R. D. Rogers and J. Zhang, *Journal of Chromatography B: Biomedical Sciences and Applications*, 1996, **680**, 231–236.
[38] M. G. Freire, J. F. B. Pereira, M. Francisco, H. Rodriguez, L. P. N. Rebelo, R. D. Rogers and J. A. P. Coutinho, *Chemistry-a European Journal*, 2012, **18**, 1831–1839.
[39] B. Ellis and R. Smith, *Polymers: A Property Database, Second Edition*, CRC Press, 2008.
[40] E. Chiellini and P. Giusti, *Polymers in Medicine: Biomedical and Pharmacological Applications*, Springer US, 2013.

Supplementary Material

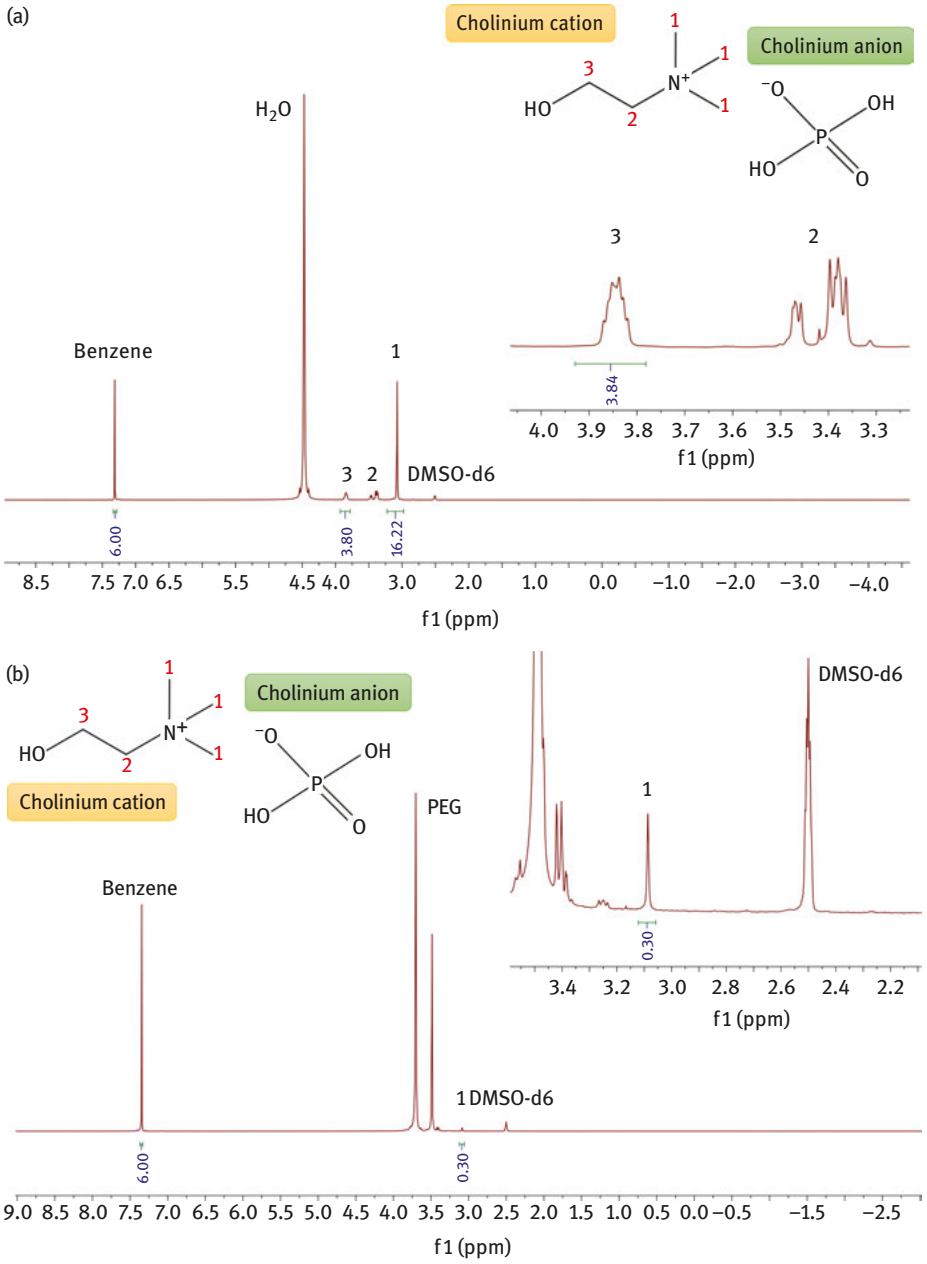

Figure 3.S.1: ^{1}H NMR spectra of ABS composed of $[N_{111(2OH)}][DHP]$ + PEG 400 + PEG 2000 + H_2O (PEG 400 mole fraction at 0.5) in DMSO-d6. A, IL-rich phase; B, polymer-rich phase.

Table 3.S.1: Experimental weight fraction data for the ABS composed of [$N_{111(2OH)}$][DHP] (1) + PEG 400 (2) at a mole fraction of 0.90 at (298 ± 1) K and atmospheric pressure.

100 w_1	100 w_2	100 w_1	100 w_2	100 w_1	100 w_2
0.495	1.862	1.551	0.609	2.092	0.308
0.553	1.735	1.586	0.589	2.109	0.296
0.617	1.593	1.633	0.566	2.121	0.289
0.681	1.464	1.678	0.546	2.131	0.275
0.758	1.362	1.703	0.527	2.188	0.264
0.813	1.261	1.747	0.508	2.204	0.256
0.932	1.115	1.761	0.494	2.231	0.248
0.985	1.052	1.803	0.477	2.255	0.240
1.034	0.995	1.819	0.464	2.279	0.233
1.069	0.945	1.839	0.451	2.356	0.218
1.130	0.903	1.859	0.441	2.406	0.204
1.164	0.862	1.878	0.431	2.470	0.192
1.232	0.830	1.913	0.418	2.553	0.174
1.281	0.794	1.904	0.409	2.602	0.160
1.314	0.762	1.946	0.399	2.610	0.149
1.357	0.731	1.964	0.387	2.719	0.139
1.399	0.705	1.953	0.376	2.735	0.127
1.447	0.679	1.986	0.358	2.810	0.117
1.483	0.653	2.021	0.340	2.854	0.107
1.510	0.632	2.023	0.329	2.911	0.097

Table 3.S.2: Experimental weight fraction data for the ABS composed of $[N_{111(2OH)}][DHP]$ (1) + PEG 400 (2) at a mole fraction of 0.75 at (298 ± 1) K and atmospheric pressure.

100 w_1	100 w_2	100 w_1	100 w_2	100 w_1	100 w_2
0.324	1.484	1.453	0.358	1.952	0.200
0.381	1.280	1.467	0.349	1.970	0.195
0.454	1.181	1.492	0.339	1.979	0.191
0.497	1.066	1.551	0.328	1.988	0.186
0.554	0.993	1.557	0.319	2.009	0.181
0.611	0.934	1.576	0.313	2.026	0.177
0.660	0.854	1.593	0.306	2.081	0.170
0.716	0.805	1.607	0.300	2.092	0.164
0.767	0.763	1.608	0.293	2.097	0.159
0.809	0.724	1.625	0.288	2.124	0.154
0.845	0.678	1.647	0.282	2.140	0.149
0.883	0.648	1.664	0.278	2.180	0.144
0.924	0.621	1.666	0.271	2.218	0.136
0.966	0.595	1.681	0.267	2.220	0.130
1.004	0.574	1.698	0.263	2.239	0.126
1.033	0.552	1.715	0.258	2.268	0.122
1.070	0.532	1.725	0.253	2.298	0.117
1.143	0.504	1.774	0.247	2.359	0.112
1.175	0.488	1.783	0.243	2.415	0.105
1.209	0.470	1.790	0.239	2.449	0.097
1.243	0.455	1.803	0.235	2.487	0.092
1.269	0.438	1.815	0.232	2.492	0.087
1.303	0.425	1.826	0.229	2.544	0.082
1.329	0.413	1.843	0.226	2.631	0.076
1.350	0.400	1.874	0.219	2.712	0.068
1.370	0.389	1.896	0.213	2.723	0.062
1.399	0.378	1.894	0.210	2.765	0.058
1.427	0.368	1.938	0.205	2.820	0.052

Table 3.S.3: Experimental weight fraction data for the ABS composed of $[N_{111(2OH)}][DHP]$ (1) + PEG 400 (2) at a mole fraction of 0.50 at (298 ± 1) K and atmospheric pressure.

100 w_1	100 w_2	100 w_1	100 w_2	100 w_1	100 w_2
0.216	1.071	1.480	0.191	2.119	0.084
0.300	0.945	1.492	0.188	2.139	0.080
0.350	0.824	1.543	0.181	2.176	0.077
0.417	0.720	1.563	0.174	2.225	0.074
0.475	0.673	1.587	0.169	2.245	0.070
0.521	0.610	1.586	0.165	2.250	0.066
0.582	0.571	1.599	0.163	2.287	0.064
0.633	0.529	1.606	0.161	2.284	0.063
0.679	0.505	1.621	0.158	2.286	0.061
0.713	0.467	1.647	0.154	2.315	0.059
0.798	0.434	1.669	0.150	2.333	0.057
0.818	0.411	1.697	0.146	2.355	0.056
0.854	0.395	1.727	0.142	2.370	0.054
0.895	0.382	1.751	0.137	2.377	0.052
0.921	0.363	1.770	0.133	2.403	0.051
0.956	0.352	1.776	0.132	2.404	0.049
0.976	0.341	1.798	0.128	2.425	0.048
1.001	0.331	1.827	0.125	2.440	0.047
1.028	0.321	1.829	0.122	2.453	0.045
1.053	0.311	1.880	0.119	2.466	0.044
1.069	0.302	1.892	0.116	2.490	0.043
1.117	0.286	1.897	0.114	2.516	0.042
1.136	0.275	1.909	0.112	2.511	0.040
1.196	0.265	1.904	0.110	2.541	0.039
1.210	0.258	1.924	0.108	2.567	0.037
1.226	0.252	1.943	0.106	2.608	0.035
1.275	0.244	1.944	0.105	2.584	0.034
1.276	0.233	1.962	0.102	2.604	0.033
1.301	0.228	1.978	0.101	2.659	0.031
1.321	0.224	1.997	0.099	2.672	0.030
1.343	0.219	2.029	0.096	2.688	0.028
1.371	0.214	2.034	0.093	2.722	0.027
1.383	0.210	2.039	0.091	2.755	0.025
1.400	0.206	2.070	0.089	2.768	0.024
1.463	0.199	2.076	0.087	2.768	0.023
1.468	0.194				

Table 3.S.4: Experimental weight fraction data for the ABS composed of $[N_{111(2OH)}][DHP]$ (1) + PEG 400 (2) at a mole fraction of 0.25 at (298 ± 1) K and atmospheric pressure.

100 w_1	100 w_2	100 w_1	100 w_2	100 w_1	100 w_2
0.154	0.839	1.507	0.131	2.158	0.053
0.293	0.687	1.521	0.128	2.171	0.052
0.331	0.574	1.528	0.125	2.187	0.050
0.368	0.514	1.557	0.120	2.201	0.049
0.424	0.469	1.589	0.116	2.211	0.048
0.468	0.438	1.593	0.114	2.223	0.047
0.513	0.421	1.642	0.110	2.235	0.046
0.548	0.396	1.661	0.106	2.254	0.044
0.585	0.376	1.686	0.102	2.279	0.043
0.625	0.354	1.717	0.099	2.282	0.042
0.662	0.334	1.750	0.096	2.299	0.041
0.700	0.317	1.762	0.094	2.324	0.040
0.736	0.307	1.793	0.091	2.333	0.039
0.769	0.295	1.804	0.088	2.346	0.038
0.796	0.284	1.836	0.086	2.356	0.037
0.831	0.273	1.843	0.084	2.367	0.036
0.868	0.263	1.860	0.082	2.390	0.035
0.897	0.251	1.869	0.079	2.403	0.034
0.936	0.240	1.913	0.077	2.422	0.033
1.001	0.229	1.954	0.075	2.440	0.032
1.029	0.222	1.952	0.073	2.455	0.031
1.049	0.215	1.962	0.071	2.454	0.031
1.076	0.208	1.984	0.070	2.480	0.030
1.100	0.202	1.985	0.068	2.500	0.028
1.125	0.196	2.009	0.067	2.542	0.027
1.180	0.187	2.013	0.065	2.514	0.026
1.238	0.179	2.028	0.064	2.534	0.025
1.244	0.171	2.033	0.063	2.577	0.024
1.302	0.166	2.054	0.062	2.590	0.023
1.355	0.157	2.074	0.060	2.605	0.022
1.405	0.150	2.094	0.059	2.635	0.021
1.406	0.145	2.108	0.057	2.651	0.020
1.426	0.142	2.127	0.055	2.656	0.020
1.477	0.137	2.140	0.054	2.678	0.019

Table 3.S.5: Experimental weight fraction data for the ABS composed of $[N_{111(2OH)}][DHP]$ (1) + PEG 400 (2) at a mole fraction of 0.10 at (298 ± 1) K and atmospheric pressure.

100 w_1	100 w_2	100 w_1	100 w_2	100 w_1	100 w_2
0.194	0.711	1.419	0.119	2.059	0.053
0.282	0.613	1.443	0.117	2.060	0.051
0.387	0.502	1.452	0.115	2.084	0.050
0.419	0.429	1.477	0.112	2.043	0.054
0.488	0.388	1.560	0.107	2.048	0.051
0.505	0.364	1.565	0.104	2.071	0.049
0.541	0.345	1.573	0.102	2.116	0.048
0.597	0.325	1.591	0.100	2.137	0.046
0.633	0.306	1.604	0.098	2.212	0.043
0.672	0.293	1.624	0.097	2.168	0.041
0.708	0.277	1.669	0.094	2.181	0.040
0.725	0.266	1.672	0.092	2.203	0.038
0.736	0.257	1.683	0.090	2.215	0.037
0.782	0.247	1.658	0.087	2.283	0.035
0.812	0.236	1.661	0.085	2.308	0.033
0.841	0.224	1.667	0.084	2.353	0.031
0.866	0.219	1.693	0.083	2.365	0.029
0.908	0.212	1.698	0.081	2.376	0.027
0.936	0.204	1.709	0.080	2.419	0.025
0.956	0.198	1.731	0.079	2.420	0.024
0.996	0.193	1.820	0.075	2.468	0.022
1.056	0.182	1.839	0.074	2.519	0.021
1.070	0.176	1.851	0.072	2.578	0.019
1.099	0.168	1.840	0.070	2.646	0.018
1.130	0.164	1.845	0.068	2.702	0.016
1.163	0.159	1.870	0.067	2.729	0.014
1.181	0.154	1.886	0.065	2.807	0.012
1.232	0.147	1.886	0.064	2.955	0.010
1.250	0.142	1.908	0.063	2.930	0.009
1.282	0.139	1.919	0.062	2.969	0.008
1.295	0.136	1.928	0.060	3.038	0.007
1.319	0.133	1.969	0.059	3.094	0.007
1.333	0.131	1.991	0.058	3.168	0.006
1.349	0.128	2.006	0.057	3.253	0.005
1.399	0.125	2.027	0.055	3.280	0.004
1.408	0.121	2.042	0.054	3.365	0.004

Table 3.S.6: Experimental weight fraction data for the ABS composed of [$N_{111(2OH)}$][DHP] (1) + PEG 400 at a mole fraction of 0.0 at (298 ± 1) K and atmospheric pressure.

100 w_1	100 w_2	100 w_1	100 w_2	100 w_1	100 w_2
0.177	0.659	1.442	0.095	1.970	0.045
0.333	0.471	1.462	0.093	1.969	0.044
0.370	0.429	1.487	0.091	1.983	0.043
0.415	0.389	1.518	0.088	1.998	0.043
0.472	0.354	1.546	0.085	1.999	0.042
0.509	0.327	1.582	0.081	2.003	0.041
0.550	0.311	1.607	0.079	2.017	0.041
0.590	0.290	1.629	0.076	2.028	0.040
0.599	0.277	1.650	0.074	2.033	0.040
0.624	0.266	1.663	0.072	2.039	0.039
0.642	0.258	1.681	0.071	2.051	0.038
0.660	0.249	1.698	0.069	2.055	0.038
0.726	0.235	1.707	0.068	2.073	0.037
0.782	0.217	1.735	0.066	2.081	0.036
0.793	0.208	1.760	0.065	2.084	0.036
0.858	0.193	1.778	0.063	2.102	0.035
0.877	0.188	1.771	0.062	2.122	0.034
0.921	0.177	1.795	0.061	2.152	0.033
0.936	0.171	1.797	0.060	2.168	0.032
0.954	0.168	1.832	0.057	2.165	0.031
0.976	0.163	1.849	0.056	2.184	0.030
1.027	0.154	1.861	0.054	2.197	0.030
1.042	0.150	1.855	0.054	2.209	0.029
1.068	0.145	1.855	0.053	2.230	0.028
1.122	0.138	1.862	0.052	2.232	0.028
1.171	0.133	1.872	0.052	2.243	0.027
1.193	0.127	1.889	0.051	2.254	0.027
1.239	0.122	1.888	0.050	2.271	0.026
1.271	0.117	1.901	0.050	2.274	0.026
1.301	0.113	1.908	0.049	2.283	0.025
1.344	0.106	1.913	0.049	2.296	0.025
1.364	0.104	1.928	0.048	2.310	0.024
1.384	0.102	1.932	0.047		
1.416	0.098	1.943	0.046		

Table 3.S.7: Experimental weight fraction data for the ABS composed of $[N_{111(2OH)}][Bit]$ (1) + PEG 400 (2) at a mole fraction of 0.90 at (298 ± 1) K and atmospheric pressure.

100 w_1	100 w_2	100 w_1	100 w_2
2.117	0.766	3.478	0.305
2.366	0.657	3.570	0.285
2.519	0.591	3.658	0.267
2.681	0.531	3.724	0.253
2.835	0.480	3.834	0.231
2.949	0.441	3.963	0.210
3.072	0.405	4.072	0.192
3.127	0.384	4.027	0.186
3.227	0.357	4.221	0.166
3.332	0.332		

Table 3.S.8: Experimental weight fraction data for the ABS composed of $[N_{111(2OH)}][Bit]$ (1) + PEG 400 (2) at a mole fraction of 0.75 at (298 ± 1) K and atmospheric pressure.

100 w_1	100 w_2	100 w_1	100 w_2
1.185	0.850	3.168	0.223
1.330	0.746	3.234	0.211
1.446	0.667	3.296	0.201
1.868	0.528	3.357	0.192
2.034	0.471	3.419	0.183
2.196	0.425	3.445	0.177
2.332	0.386	3.521	0.168
2.400	0.362	3.565	0.161
2.757	0.304	3.613	0.155
2.841	0.285	3.662	0.150
2.946	0.265	3.698	0.144
2.988	0.252	3.743	0.136
3.069	0.238	3.797	0.131

Table 3.S.9: Experimental weight fraction data for the ABS composed of $[N_{111(2OH)}][Bit]$ (1) + PEG 400 (2) at a mole fraction of 0.50 at (298 ± 1) K and atmospheric pressure.

100 w_1	100 w_2	100 w_1	100 w_2
0.705	0.786	1.999	0.263
0.861	0.668	2.118	0.243
1.025	0.575	2.227	0.225
1.145	0.514	2.284	0.214
1.258	0.465	2.377	0.200
1.375	0.419	2.465	0.188
1.540	0.369	2.552	0.178
1.635	0.341	2.627	0.169
1.760	0.311	2.693	0.160
1.893	0.283	2.758	0.153

Table 3.S.10: Experimental weight fraction data for the ABS composed of $[N_{111(2OH)}][Bit]$ (1) + PEG 400 (2) at a mole fraction of 0.25 at (298 ± 1) K and atmospheric pressure.

100 w_1	100 w_2	100 w_1	100 w_2
0.612	0.573	2.073	0.166
0.769	0.488	2.182	0.153
0.841	0.439	2.282	0.142
0.990	0.381	2.407	0.130
1.182	0.325	2.484	0.122
1.304	0.291	2.603	0.112
1.468	0.258	2.704	0.104
1.605	0.231	2.791	0.098
1.739	0.208	2.874	0.092
1.896	0.186		

Table 3.S.11: Experimental weight fraction data for the ABS composed of $[N_{111(2OH)}][Bit]$ (1) + PEG 400 (2) at a mole fraction of 0.10 at (298 ± 1) K and atmospheric pressure.

100 w_1	100 w_2	100 w_1	100 w_2
0.670	0.480	2.056	0.150
0.828	0.407	2.216	0.134
0.968	0.353	2.343	0.123
1.141	0.305	2.469	0.113
1.244	0.276	2.586	0.104
1.395	0.242	2.714	0.095
1.592	0.210	2.831	0.088
1.734	0.188	2.939	0.082
1.934	0.164	3.104	0.072

Table 3.S.12: Experimental weight fraction data for the ABS composed of $[N_{111(2OH)}][Bit]$ (1) + PEG 400 (2) at a mole fraction of 0.0 at (298 ± 1) K and atmospheric pressure.

100 w_1	100 w_2	100 w_1	100 w_2
0.765	0.404	1.601	0.186
0.856	0.358	1.741	0.167
0.997	0.311	1.892	0.149
1.116	0.277	2.033	0.135
1.303	0.237	2.151	0.124
1.439	0.210		

Table 3.S.13: Partition coefficients (K_{Alk}) and extraction efficiencies (EE_{Alk}%) of caffeine, theophylline, theobromine and nicotine in ABS composed of $[N_{111(2OH)}][DHP]$ or $[N_{111(2OH)}][Bit]$ + PEG 400 at different mole fractions of PEG 400, at (298 ± 1) K and atmospheric pressure.

PEG 400 mole fraction	K_{Caf}	EE_{Caf}%	K_{Theop}	EE_{Theop}%	K_{Theob}	EE_{Theob}%	K_{Nic}	EE_{Nic}%
				$[N_{111(2OH)}][DHP]$				
1.00	4.26	60.1	2.24	39.8	2.65	42.0	0.32	87.3
0.90	8.15	76.8	6.10	74.7	5.32	69.0	0.18	92.1
0.75	11.65	84.2	8.67	80.4	6.73	77.4	0.14	93.4
0.50	12.98	87.5	9.78	83.7	7.56	79.5	0.13	94.1
0.25	15.05	89.2	10.64	84.1	8.76	86.0	0.12	93.9
0.10	17.02	90.3	11.50	84.3	9.77	84.3	0.12	93.9
0.00	17.88	90.9	12.78	84.2	10.83	85.4	0.11	93.8
				$[N_{111(2OH)}][Bit]$				
1.00	2.08	77.3	2.00	76.6	1.63	72.0	0.51	47.4
0.90	1.95	53.7	2.03	52.6	1.65	47.0	0.47	76.9
0.75	2.00	58.0	2.06	59.7	1.65	54.4	0.46	69.6
0.50	2.02	60.3	1.99	59.2	1.54	54.8	0.45	68.1
0.25	2.08	64.1	2.20	63.6	1.73	58.6	0.42	71.9
0.10	2.23	66.5	2.31	66.7	1.95	62.7	0.41	70.3
0.00	2.28	66.9	2.37	67.6	1.83	60.6	0.38	72.4

The average uncertainty associated with the partition coefficients and extraction efficiencies of the alkaloids is within ±10%. The percentage extraction efficiency (EE_{Alk}%) of each alkaloid corresponds to the ratio between the weight of the alkaloid in the PEG-rich phase to the total weight of alkaloid.

Table 3.S.14: Conductivities, water content and pH values of the coexisting phases of the ABS composed of $[N_{111(2OH)}][DHP]$ or $[N_{111(2OH)}][Bit]$ + PEG 400 at different mole fractions of PEG 400, at (298 ± 1) K and atmospheric pressure.

PEG 400 mole fraction	Bottom phase	Top phase	Conductivity (μS·cm^{-1})		Water content (wt %)		pH	
			Bottom phase	Top phase	Bottom phase	Top phase	Bottom phase	Top phase
				$[N_{111(2OH)}][DHP]$				
1	Salt	PEG	805	180	49.9	64.7	4.80	4.87
0.9	Salt	PEG	(—)	(—)	49.0	84.2	4.70	5.00
0.75	Salt	PEG	(—)	(—)	46.9	86.2	4.70	5.00
0.5	Salt	PEG	1,099	44	47.2	86.0	4.62	4.64
0.25	Salt	PEG	(—)	(—)	46.1	87.5	4.55	4.66
0.1	Salt	PEG	(—)	(—)	46.4	87.6	4.60	4.65
0	Salt	PEG	1,084	34	45.5	86.1	4.56	4.63
				$[N_{111(2OH)}][Bit]$				
1	Salt	PEG	391	177	30.1	34.5	4.65	4.77
0.9	Salt	PEG	(—)	(—)	38.1	40.9	4.27	4.60
0.75	Salt	PEG	(—)	(—)	40.4	44.6	4.50	4.26
0.5	Salt	PEG	372	196	45.1	48.4	4.20	4.16
0.25	Salt	PEG	(—)	(—)	44.9	47.4	4.03	3.90
0.1	Salt	PEG	(—)	(—)	44.0	48.1	4.30	4.18
0	Salt	PEG	365	140	44.8	47.1	4.00	3.50

The average uncertainty associated with all parameters is within ± 10%.

Table 3.S.15: Selectivity parameters for caffeine/nicotine ($S_{caf/nic}$), theophylline/nicotine ($S_{theof/nic}$) and theobromine/nicotine ($S_{theob/nic}$) pairs in ABS composed of ILs and PEG 400 at different mole fractions.

	$[N_{111(2OH)}][DHP]$			$[N_{111(2OH)}][Bit]$		
PEG 400 mole fraction	$S_{caf/nic}$	$S_{theof/nic}$	$S_{theob/nic}$	$S_{caf/nic}$	$S_{theof/nic}$	$S_{theob/nic}$
1.00	1.38	0.73	0.86	1.40	1.34	1.10
0.90	1.48	1.11	0.97	1.02	1.06	0.86
0.75	1.60	1.19	0.92	1.04	1.07	0.86
0.50	1.63	1.23	0.95	1.05	1.03	0.80
0.25	1.78	1.26	1.04	0.93	0.98	0.77
0.10	2.01	1.36	1.16	0.99	1.02	0.86
0.00	1.94	1.39	1.18	0.86	0.90	0.69

Yong-Lei Wang, Sten Sarman, Mikhail Golets, Francesca Mocci,
Zhong-Yuan Lu and Aatto Laaksonen

4 Multigranular modeling of ionic liquids

Abstract: Ionic liquids (ILs) are a special category of molten salts with melting points near ambient temperatures (or by convention below 100 °C). Owing to their numerous valuable physicochemical properties as bulk liquids, solvents, at surfaces and in confined environments, ILs have attracted increasing attention in both academic and industrial communities in a variety of application areas involving physics, chemistry, material science and engineering. Due to their nearly limitless number of combinations of cation–anion pairs and mixtures with cosolvents, a molecular level understanding of their hierarchical structures and dynamics, requiring strategies to connect several length and time scales, is of crucial significance for rational design of ILs with desired properties, and thereafter refining their functional performance in applications. As an invaluable compliment to experiments from synthesis to characterization, computational modeling and simulations have significantly increased our understanding on how physicochemical and structural properties of ILs can be controlled by their underlying chemical and molecular structures. In this chapter, we will give examples from our own modeling work based on selected IL systems, with focus on imidazolium-based and tetraalkylphosphonium-orthoborate ILs, studied at several spatio-temporal scales in different environments and with particular attention to applications of high technological interest. We start by describing studies performed using *ab initio* methods on force field development for tetraalkylphosphonium-orthoborate ILs, and computational studies on thermal decomposition of these ILs. The delicate interplay between hydrogen bonding and π-type interactions in an imidazolium-orthoborate IL was studied by performing *ab initio* molecular dynamics simulations. On the atomistic level, atomistic simulations were performed with constructed force field parameters to study intrinsic molecular interactions between residual water molecules and tetraalkylphosphonium-orthoborate ionic species. For a typical trihexyltetradecylphosphonium bis(oxalato) borate IL at varied concentrations, microstructures and dynamics were systematically analyzed as water concentration increases. The liquid viscosities of typical trihexyltetradecylphosphonium-based ILs were estimated through equilibrium atomistic simulations using Green–Kubo relation with charge scaling factors on ionic species.

Yong-Lei Wang, Department of Materials and Environmental Chemistry, Stockholm University, Sweden; Department of Chemistry, Stanford University, The United States
Sten Sarman, Aatto Laaksonen, Department of Materials and Environmental Chemistry, Stockholm University, Sweden
Mikhail Golets, AkzoNobel Surface Chemistry AB, Stenungsund, Sweden
Francesca Mocci, Department of Chemical and Geological Sciences, University of Cagliari, Italy
Zhong-Yuan Lu, Institute of Theoretical Chemistry, Jilin University, China

https://doi.org/10.1515/9783110583632-004

Additionally, atomistic simulations were combined with X-ray scattering experiments to investigate phase behavior and ionic structures in IL mixtures with varied concentrations. Peculiar features of X-ray scattering spectra of IL mixtures with organic solvent are also discussed with an example dealing with ethyl ammonium nitrate and acetonitrile mixtures. On the mesoscopic level, a united-atom model for trihexyltetradecylphosphonium cation and coarse-grained models for butylmethy-limidazolium hexafluorophosphate were proposed, and effective interactions between coarse-grained beads were validated against experimental and computational data. Concluding remarks on multiscale strategies in understanding and predictive capabilities of ILs and IL mixtures are addressed in the final section. An outlook is provided to highlight future challenges and opportunities associated with IL materials in multiscale modeling community.

Keywords: Multi-scale modelling, *ab initio* calculations, tribology, ionic liquids, solid–liquid interfaces

4.1 Introduction

Ionic liquids (ILs) refer to a special category of molten salts, entirely consisting of complex, sterically mismatched molecular ions with their melting points at or close to room temperature [1–3]. The first room temperature IL was reported already more than 100 years ago by Pauls Valdens (Paul Walden) who presented the synthesis of ethylammonium nitrate (EAN) by neutralizing ethylamine with concentrated nitric acid in 1914 [4]. EAN is clear, colorless, odorless and has a melting point of 13–14 °C and a rather low viscosity [4, 5]. However, this early report did not receive much attention from the scientific community, and it was not foreseen that such salt materials would become of widespread interest decades later. In 1951, Hurley and Wier reported the synthesis of organic chloroaluminates by mixing alkylpyridinium chlorides with aluminium compounds, which is now considered as the first generation of ILs [6]. Unfortunately, these organic chloroaluminates are not stable in the presence of moisture because of their rapid hydrolysis. Additionally, their acidity and basicity are not easy to regulate [6, 7], and more detailed studies on these compounds started from 1970s [2, 8]. In 1992, Wilkes and Zaworotko prepared moisture/water-stable ILs consisting of imidazolium cations and tetrafluoroborate ($[BF_4]$) anion [9, 10]. It became clear that many ion combinations could form air- and water-stable ILs [2, 10–12]. Immediate scientific research on synthesis, characterizations and applications of ILs got an upswing in academia and industry communities [12–21].

The most frequently studied cationic structures have organic moieties, such as imidazolium, guanidinium, morpholinium, piperidinium, pyrazolium, pyridinium, pyrrolidinium, thiazolium, sulfonium, tetraalkylammonium and tetraalkyl-phosphonium ions. The anionic parts can be either organic or inorganic entities including acetate, halogens, hexafluorophosphate ($[PF_6]$), $[BF_4]$, orthoborate, nitrate ($[NO_3]$),

alkylsulfonate, alkylsulfate, bis(trifluoromethanesulfonyl)imide ([NTF_2]), alkylphosphate, trifluoromethylsulfonate ([TFO]), etc. [1, 8, 12–14, 16, 22, 23]. ILs have remarkable and multifaceted physicochemical characteristics, such as negligible volatility, low flammability, reasonable viscosity-conductivity feature, acceptable biocompatibility, high thermal-oxidative stability, wide electrochemical window, as well as outstanding ability to dissolve solutes of diverse polarities [1, 3, 7, 22, 24, 25]. An additional feature of ILs is that their physicochemical properties and microstructural organization can be widely tuned in a controllable fashion through judicious combinations of different cation–anion moieties in a general way, and by mutating specific atoms in constituent cations or anions [3, 22, 25, 26]. These characteristics make ILs exceptionally attractive and reliable candidates as environmentally benign alternative to conventional molecular solvents in synthetic chemistry to offer precise control over growth rate, particle size and morphology of nanomaterials [8, 11, 18, 23]; useful reaction media in catalytic chemistry to optimize yield, selectivity, substrate solubility, product separation and enantioselectivity [8, 11, 18, 27]; valuable working fluids in separation technology through selective absorption of gas molecules [13, 16, 19, 23, 28]; promising versatile electrolytes in electrochemical energy devices with tunable electrical conductivities and varied electrochemical stability windows [7, 13, 17, 20, 21, 29–31]; suitable lubricants in tribology to reduce wear and frictions between solid sliding contacts [14, 15, 32, 33].

Due to the existence of an enormous number of possible cation–anion combinations, there are also nearly limitless opportunities to produce neat ILs and their multicomponent mixtures with distinct molecular structures and physical properties [3, 22, 23]. However, it is not feasible to systematically pick up ion combinations to synthetize, purify and characterize them as they are simply too many. An efficient and reliable predictive tool is needed to obtain a molecular level understanding of the many competing intermolecular interactions between and within ionic species to guide the development cycle by providing expedient predictions of physicochemical properties for neat ILs and IL mixtures as well as providing an improved fundamental understanding of ILs and thereby obtain data to develop fast structure–property relationship models [2, 25].

Computer simulations, in close interplay with experiments, can provide much fundamental understanding of complicated phenomena on molecular level, which is particularly useful for ILs because of their large diversities and their complicated landscape of interactions. Various simulation methods are available to use at different spatio-temporal scales depending on specific targets requested from studied model IL systems [2, 31, 34–48]. Multiscale modeling approach generally involves several simulation techniques, including quantum chemical calculations, *ab initio*, atomistic and coarse-grained (CG) molecular dynamics simulations, to study specific model systems. The advantages and drawbacks of various methods in different spatio-temporal scales coexist and are often interchangeable [35, 42–45]. For quantum chemical methods, that is, wave-function-based (Hartree–Fock) calculations or density functional theory (DFT), the detailed physical insight into electronic structures of ILs is limited to small systems containing only a few ion pairs. The advantage of these quantum

chemical methods stems from their inherent accuracies through the electronic structure and can be systematically improved until predetermined target accuracy is achieved but on an increasing cost of computing time. Static properties of molecular clusters can be typically calculated even if some of these properties are not exclusively representatives of bulk systems [38, 39, 49–51]. Using DFT-based (Born–Oppenheimer or Car–Parrinello) molecular dynamics simulations it is now possible to set up a system up to 100 ion pairs and cover a time scale of a few nanoseconds. However, this is still far from being sufficient to sample any dynamical properties of ILs as they require much bigger systems and simulation times of hundreds of nanoseconds.

To reach much longer time scales, classical atomistic simulations are carried out to obtain dynamical and transport properties of ILs while treating systems consisting of hundreds of thousands of atoms and simulating over nano or even microsecond time scales [24, 34, 35, 41–45, 47, 52, 53]. Since the accuracy of thermodynamics, microstructures and transport properties of model systems depend ultimately on appropriate force field parameters, one can iteratively fine-tune interaction parameters and validate them at each refinement stage through underlying *first-principles* calculations and comparison of computed properties against experimental data when available. Additionally, one can further construct CG models allowing for large systems to be simulated for long times, thus revealing liquid structural and dynamical features of IL systems that are difficult to predict through conventional atomistic simulations [31, 35, 36, 41–46, 54–56].

In this chapter, we will highlight our work done during the lifetime of the COST action EXIL. We have studied many systems on butylmethylimidazolium- ([BMIM]), EAN- and tetraalkylphosphonium-orthoborate-based ILs. Typical molecular structures of these studied ILs are shown in Figure 4.1. We did start with force field development and validation for tetraalkylphosphonium-orthoborate ILs. Quantum chemical

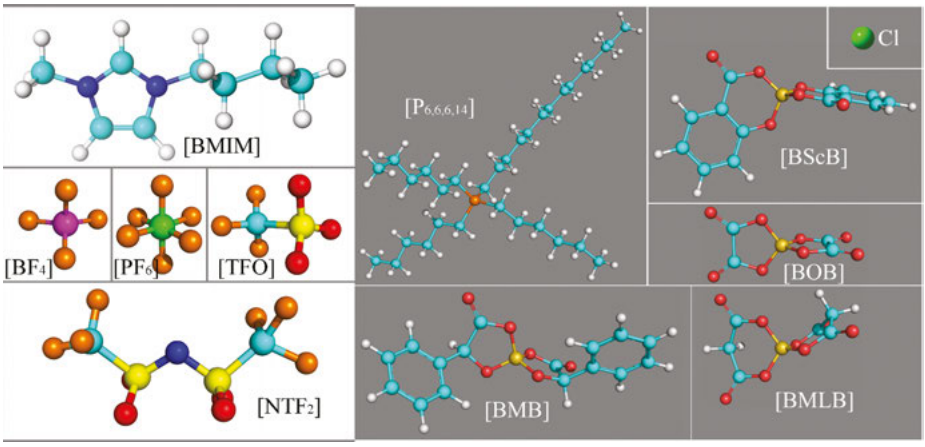

Figure 4.1: Representative ion structures of cations and anions discussed in this contribution.

calculations were performed to study thermal decomposition mechanism of typical tetraalkylphosphonium-orthoborate ILs. *Ab initio* molecular dynamics (AIMD) simulations were performed to investigate the complex interplay between hydrogen bonding (HB) characteristics and π-type stacking features in dimethylimidazolium bis(oxalato) borate ([MMIM][BOB]) IL. With constructed force field parameters, atomistic simulations were performed to study thermodynamics, microstructural and dynamical properties of tetraalkylphosphonium-orthoborate ILs, as well as the dependence of these properties on residual water contents in typical trihexyltetradecylphosphonium ($[P_{6,6,6,14}]$)-orthoborate ILs. We wanted to find out why it is difficult to remove residual water from a hygroscopic IL by studying four $[P_{6,6,6,14}]$-orthoborate ILs through calculations of solvation free energy of dissolving water from gas phase into bulk ILs and followed the coordination of dissolved water molecules among ions in IL matrices. Atomistic simulations were carried out to elucidate microscopic interfacial structures and ordering arrangement of [BMIM]-based ILs and $[P_{6,6,6,14}]$ bis(mandelato)borate ([BMB]) IL in confined environment characterized by different surface charge densities. The liquid viscosities and rheological properties of $[P_{6,6,6,14}]$-orthoborate ILs were computed using nonequilibrium shear flow simulations and equilibrium atomistic simulations using Green–Kubo relations. Atomistic simulations were combined with X-ray scattering technique to reveal striking scattering patterns of various IL mixtures. Additionally, we developed CG models for $[P_{6,6,6,14}]$ cation and $[BMIM][PF_6]$ IL to perform simulations at extended spatio-temporal scales. In addition to a benefit of computational efficiency, it is expected that these proposed CG models can reveal essential structural and dynamical properties of ILs at mesoscopic level by integrating over less important degrees of freedom at atomic level.

4.2 Quantum chemical calculations

4.2.1 Force field development

First-principles quantum chemical calculations and *ab initio* molecular dynamics simulations of ILs can provide accurate microstructural information without any experimental or empirical input. However, being computationally demanding, these methods are mainly applied to study chemical reactions and to derive effective interactions between ion pairs and to determine their delicate interactions with solute molecules in small systems and at short time scales [38, 39, 46, 57].

Since 2000, there have been continuous efforts to develop and refine force field parameters for IL systems. The first force field development for [MMIM] and ethylmethylimidazolium ([EMIM]) cations coupled with chloride (Cl) and $[PF_6]$ anions were carried out by Hanke and coworkers [58]. A Buckingham repulsion dispersion term was included in nonbonded repulsion–dispersion interactions between atomic sites in

cationic models to reproduce experimental crystal structures. Subsequent atomistic simulations were performed at high temperatures due to the high melting points of [MMIM]Cl and [MMIM][PF_6] ILs and limited computational resources. In a following study, the excess chemical potentials of hydroxyl, ether and alkane solutes in these ILs were calclated using thermodynamic integration method [59]. This is the first example of free energy calculation within an IL system, and it confirmed the importance of HB and charge–charge interactions for the solvation behavior of ILs.

These early works were followed by several groups who came up with force field developments either for specific ILs [24, 34, 60–64] or for an entire class of ILs [52, 53, 65–69]. These proposed interaction parameters for ILs were established by extending and refining the well-developed force fields, such as AMBER, CHARMM, OPLS and GROMOS, and thereafter were validated against available experimental properties, including liquid densities, spectroscopic, neutron scattering and diffraction data and X-ray crystallographic data on imidazolium-, pyridinium-, tetraalkylammonium- and guanidinium-based ILs.

Following a similar procedure, we developed an atomistic force field [70] for a new class of tetraalkylphosphonium-orthoborated ILs observed to have high friction-reducing and antiwear properties in tribological applications [33]. This force field is based on the AMBER framework employing the following functional forms to describe intra- and inter-molecular interactions between ionic species:

$$U_{total} = \sum_{bonds} K_r\left(r - r_{eq}\right)^2 + \sum_{angles} K_\theta\left(\theta - \theta_{eq}\right)^2 + \sum_{dihedrals} K_\phi 2[1 + \cos(n\phi - \gamma)] + \sum_{i<j}\left\{4\varepsilon_{ij}\left[\left(\sigma_{ij}r_{ij}\right)^{12} - \left(\sigma_{ij}r_{ij}\right)^{6}\right] + q_i q_j 4\pi\varepsilon_0\varepsilon_r r_{ij}\right\}$$

The first three terms represent the bonded interactions, that is, (harmonic) bond and angle, and dihedral potentials, and corresponding potential parameters have their usual meaning. The nonbonded interactions are described in the last term, including van der Waals (vdW, here in the Lennard-Jones 12-6 form) and Coulombic interactions between atom-centered point charges. The vdW interaction parameters between different atoms are obtained from the Lorentz-Berthelot combining rules with $\varepsilon_{ij} = \sqrt{\varepsilon_{ii}\varepsilon_{jj}}$ and $\sigma_{ij} = \left(\sigma_{ii} + \sigma_{jj}\right)/2$.

In the force field development, the optimized molecular geometries of isolated tetraalkylphosphonium cations, orthoborate anions, as well as the bounded tetraalkylphosphonium-orthoborated ion pair structures were obtained from quantum chemical calculations. The optimized tributyloctylphosphonium ([$P_{4,4,4,8}$]) [BOB] ion pair is characterized by a piggy-back structure with [BOB] anion riding on octyl chain in [$P_{4,4,4,8}$] cation, as shown in Figure 4.2. Atomic partial charges were obtained using standard restraint electrostatic potential methodology to fit molecular electrostatic potential generated from *ab initio* calculations. The vdW parameters were taken from the AMBER force field, and the bond stretching and angle bending force constants available

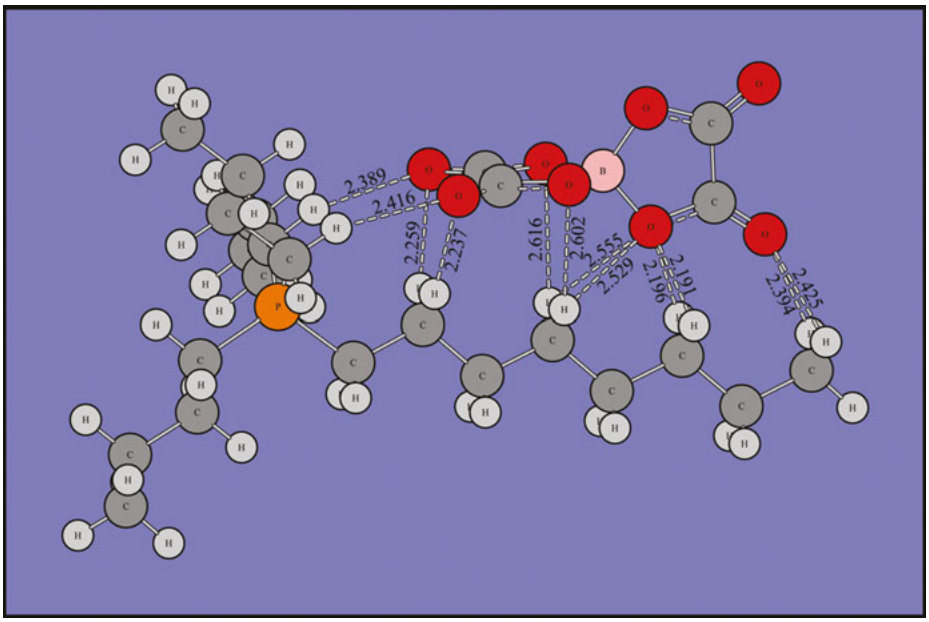

Figure 4.2: Optimized $[P_{4,4,4,8}]$[BOB] ion pair structure obtained from quantum chemical calculations at B3LYP/6-311++G(d) level of theory. The unit of O...H distance is Å.

in AMBER framework were subsequently adjusted to reproduce vibration frequency data derived from both experimental measurements and *ab initio* calculations. The missing bond, angle and dihedral terms in AMBER framework were obtained by fitting torsion energy profiles deduced from *ab initio* calculations.

In order to validate the proposed force field parameters, extensive atomistic simulations were performed for 12 tetraalkylphosphonium-orthoborate ILs [70]. The predicted densities for neat ILs and the $[P_{6,6,6,14}]$[BOB] sample with a water content of approximately 2.3–2.5 wt% are in excellent agreement with available experimental data [33]. The calculated diffusion coefficients of tetraalkylphosphonium cations and orthoborate anions are qualitatively consistent with available experimental viscosity data. The spatial distributions of boron (B) and oxygen (O) in four orthoborate anions ([BOB], bis(malonato)borate ([BMLB]), [BMB] and bis(salicylato)borate ([BScB])) around a $[P_{4,4,4,8}]$ cation, as shown in Figure 4.3, indicate that there are mainly four high probability domains for orthoborate anions in coordinating a $[P_{4,4,4,8}]$ cation in the first solvation shell. The B atom in [BOB] anion exhibits dispersed tetrahedral distributions around a central $[P_{4,4,4,8}]$ cation. An increase in anionic group size from [BOB] to [BMLB], [BMB] and [BScB] leads to the expansion of spatial distribution domains for B atoms (meshed yellow contour surfaces) around $[P_{4,4,4,8}]$ cation. The spatial distributions of O atoms (solid red contour surfaces) in orthoborate anions are characterized by trefoil-like structures, and follow a similar tendency as those for boron atoms as anionic size increases.

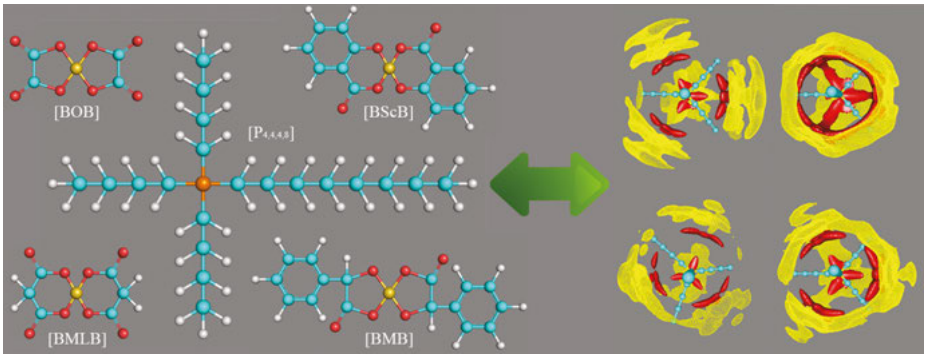

Figure 4.3: Spatial density distribution functions of boron atom (meshed yellow surface) and oxygen atoms (solid red surface) in four orthoborate anions around a $[P_{4,4,4,8}]$ cation obtained from atomistic simulations. The yellow and red contour surfaces correspond to 4.0 and 5.5 times of the average number densities of the corresponding atoms in bulk system.

4.2.3 Quantum chemical calculations on ionic liquid thermal decomposition

Understanding thermal decomposition of ILs on the nascent metal surface is important for the explanation of lubrication mechanisms in the presence of IL lubricants. In a recent work, a combined quantum chemical modeling and experimental approach was utilized to explain thermal decomposition of $[P_{4,4,4,8}]$[BOB] and $[P_{4,4,4,8}]$Cl ILs [57]. Quantum chemical calculations (i.e., vibration analysis and potential energy scans) revealed ionic structural changes of $[P_{4,4,4,8}]$ cation and [BOB] anion during thermal decomposition. The $[P_{4,4,4,8}]$ cation is rigid due to its stable central polar segments, and [BOB] anion exhibits high structural and energetic symmetry properties. The cleavage of B—O bond in [BOB] anion initiates the thermal decomposition in neat $[P_{4,4,4,8}]$[BOB] IL, as shown in Figure 4.4. The activation barrier in the beginning of reaction is 246.3 kJ mol^{-1}. The resulting monocyclic anions further react with $[P_{4,4,4,8}]$ cation in which P—O bonds are least stable. Three butyl chains in $[P_{4,4,4,8}]$ cation are oriented toward [BOB] anion with activation barriers ranging from 268.1 to 310.9 kJ mol^{-1}, and the octyl chain is isolated with higher activation barrier of 377.9 kJ mol^{-1}. The reaction products between butyl chains and anionic fragments include trialkylphosphines, alkenes, CO and CO_2. In contrast, the stable octyl radical reacts with anionic fragment and forms alkyl-boranes. The calculated structural features and product distributions are in agreement with experimental data obtained from Fourier transform infrared spectroscopy, thermal gravimetric analysis (TGA) and mass spectrometry (MS) experiments.

According to quantum chemical calculations, the compact $[P_{4,4,4,8}]$Cl IL is less stable since the activation barriers with accessible butyl chains are around 167.0 kJ mol^{-1}. Meanwhile, the isolated octyl chain in $[P_{4,4,4,8}]$ cation does not react with Cl anion demonstrating weaker nucleophilicity than that for [BOB] anion. These computational

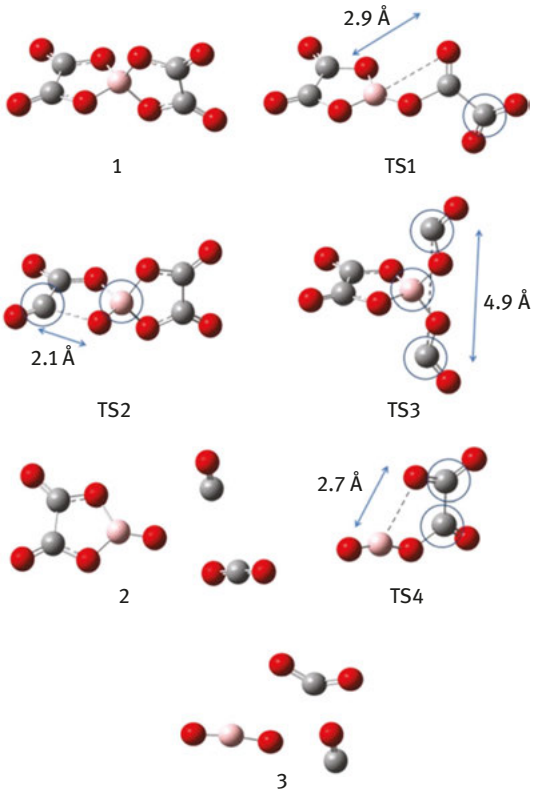

Figure 4.4: Optimized ionic structures of stationary points and transition states observed for thermal decomposition of an isolated [BOB] anion. The scanned coordinates in transition states are marked with dotted line. Atomic distances are presented by Å. Blue circles are attributed to imaginary frequencies: TS_1 (–1381.61 cm^{-1}), TS_2 (–270.30 cm^{-1}), TS_3 (–494.31 cm^{-1}) and TS_4 (–1924.23 cm^{-1}) as asymmetrical stretching around circled atoms.

results are contradicted with TGA measurements where $[P_{4,4,4,8}]$Cl IL is more stable at high temperature. Although, the sample of $[P_{4,4,4,8}]$[BOB] lost less weight at initial stage of test, it was shown that [BOB] anion is more stable at the initial stage of reaction. Presumably, nucleophilic anionic fragments are initially accumulated and further cause rapid thermal decomposition of $[P_{4,4,4,8}]$ cation in related ILs.

4.2.4 *Ab initio* molecular dynamics simulations of ionic liquid clusters

With developed force field parameters, the structural and dynamical properties of ILs that are balanced by Coulombic and dispersive forces can be investigated

on a molecular scale. For imidazolium-based ILs, the delicate intermolecular coordinations, like HB and π-type interactions that are rarely occurring simultaneously in traditional molten salts [1, 2, 10], are critical for the formation of rich ionic structures in bulk liquid and confined environment [1–3, 26, 39, 40, 49, 50, 71]. However, the nature of these interactions is distinctive and complex, and additionally, the delicate interplay among these interactions is complicated and depends on specific ion types [38–40, 51, 72, 73].

For imidazolium cations coupled with small anions, such as Cl, thiocyanate ([SCN]) and [NO_3] [38–40, 49, 51], HB and π-type interactions simultaneously occur between ionic species. Their cooperative effect promotes the formation of prominent ordered microstructures in bulk liquids. However, when imidazolium cations are associated with large anionic groups, like [NTF_2] [50, 72], both HB and π-type interactions are considerably weakened in IL phase. Large anions typically have multiple HB interaction sites and exhibit reduced HB strength and directionality in liquid environment. Additionally, these large anions take preferential *on-top* distribution above and below imidazolium rings, leading to π-type interactions being partially blocked due to anionic size effect. The delicate interplay of HB and π-type interactions among ionic species, either competitive or cooperative, becomes more complicated than this intuitive explanation implies if anions are featured with ring structures, like the chelated orthoborate families [33, 57, 70, 74–76].

We performed AIMD simulations to study the complex interplay between HB characteristics and π-type stacking features in the [MMIM][BOB] IL [77]. This IL is selected because of the relative simplicity of [MMIM] cation and [BOB] anion, but essential intermolecular interactions, like HB and π-type interactions between [MMIM] cations and [BOB] anions, are included. AIMD simulation results indicated that interactions between [MMIM] cations are stabilized by distinctive parallel π–π stacking interactions between imidazolium rings at short distance, which overtake repulsive electrostatic interactions and other weak intermolecular interactions in determining the relative distribution of neighboring imidazolium rings characterized by preferential *on-top* parallel orientations. The spatial orientations of imidazolium to neighboring oxalato rings are characterized by π–π stacking and parallel displaced offset stacking configurations at short distance and by sharp perpendicular distributions at intermediate distance, respectively. The former is stabilized by directional HB interactions between hydrogen atoms of [MMIM] cations and oxygen atoms of [BOB] anions, while the latter is dominated by attractive electrostatic interactions between ionic species. The spatial coordination pattern between intermolecular oxalato rings in [BOB] anions is balanced by repulsive Coulombic interactions and steric hindrance effect, leading to their tilted orientation in coordinating neighboring imidazolium cations in local ionic environment. Representative imidazolium-imidazolium, imidazolium-oxalato and oxalate-oxalato ionic structures are presented in Figure Figure 4.5.

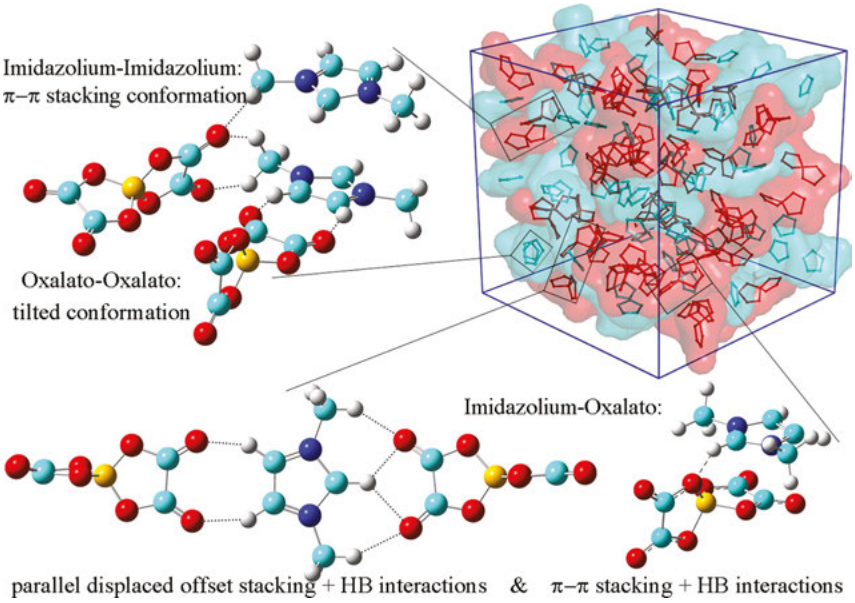

Figure 4.5: Representative molecular structures and orientations among close contact ionic groups. The imidazolium-imidazolium pair is featured with π–π stacking distribution. The imidazolium-oxalato pair is characterized by π–π stacking and parallel displaced offset stacking distributions, as well as HB interactions between hydrogen atoms in [MMIM] cations and oxygen atoms in [BOB] anions. The oxalato-oxalato pair is described by tilted molecular distribution that promotes HB interactions with neighboring [MMIM] cations.

4.3 Atomistic Molecular Dynamics Simulations

4.3.1 Tetraalkylphosphonium-orthoborate ionic liquid–water mixtures

For IL-related research and applications in laboratory and in industrial community, an inevitable and critical issue is the presence of impurities in IL samples [8, 59, 78–80]. As an omnipresent compound, water is one of the most common contaminators found in ILs, on one hand due to the intrinsic hygroscopic nature of some ILs, and on the other hand because many chemical processes (synthesis, extraction, etc.) involve water [33, 38, 79–86]. It has been well documented in experimental studies that even small traces of water can dramatically alter microstructures in an IL matrix, and thereafter result in significant changes in ILs' physicochemical properties, such as liquid densities [79, 83–85], diffusion coefficients [33, 82, 84–86], viscosities and rheological quantities [80–84, 86], as well as reactivity and selectivity of chemical reactions taking place in ILs [2, 3, 8, 12, 16, 18].

It was found in a recent work that the functionalization of orthoborate anions has obvious effect on residual water content in tetraalkylphosphonium-orthoborate ILs [33]. The retained water molecules are quite difficult to remove from these IL samples even after iterative purifications including vacuum drying for a few hours at 85–90 °C. The intrusion of water molecules may disturb microstructural organization in local environment, leading to a distinct change in thermodynamic properties, transport quantities and even macroscopic functional performance of ILs in practical applications. Thus, a molecular level understanding of the critical effect of residual water molecules on phase behavior of tetraalkylphosphonium-orthoborate ILs is necessary, not only because water is inevitably present in many practical applications, but also because it provides a new opportunity to tune various properties of tetraalkylphosphonium-orthoborate ILs by introducing a controllable amount of water molecules.

In order to understand why it is difficult to remove water molecules from IL matrices, we, from a thermodynamic point of view, calculated the solvation free energy of transferring one water molecule from gas phase into bulk $[P_{6,6,6,14}]$-orthoborate ILs as a function of temperature [76]. The calculated solvation free energies are positive and exhibit linear dependence on temperature, indicating that such a solvation procedure is a thermodynamically non-spontaneous process. The larger the solvation free energy the harder it is to dissolve water into IL matrix, that is, the easier it is to remove water from IL sample, which is exactly the experimental procedure to purify freshly synthesized IL sample through degassing it in a vacuum oven at elevated temperature. At given temperatures, the solvation free energy of dissolving one water molecule in four $[P_{6,6,6,14}]$-orthoborate ILs follows an order of [BMLB]>[BScB]>[BMB]>[BOB], indicating a similar possibility of removing water from IL samples. These thermodynamic simulation results are qualitatively consistent with the experimentally determined water content in four $[P_{6,6,6,14}]$-orthoborate IL samples [33]. Additionally, it takes less energy to dissolve the second water molecule within solvation shells of the first dissolved one into $[P_{6,6,6,14}]$-orthoborate IL matrices. This is attributed to an energetically favorable pairwise interaction between two water molecules, and preferential multibody interactions between water molecules and neighboring anionic groups at short distances.

The dissolution procedure does not only depend on thermodynamics but also on kinetic effects due to cooperative interactions between residual water molecules in IL matrices. In order to characterize how these dissolved water molecules behave in IL matrices, and the particular association/dissociation patterns of water molecules in coordinating neighboring $[P_{6,6,6,14}]$ cations, orthoborate anions and even water molecules nearby, we calculated the potential of mean force (PMF) between two dispersed water molecules in different $[P_{6,6,6,14}]$-orthoborate ILs as a function of water–water separation distance [76]. The water–water PMF profiles shown in Figure 4.6 indicate complex interactions of water molecules with neighboring ionic species depending on local ionic environment in IL matrices. A characteristic deep

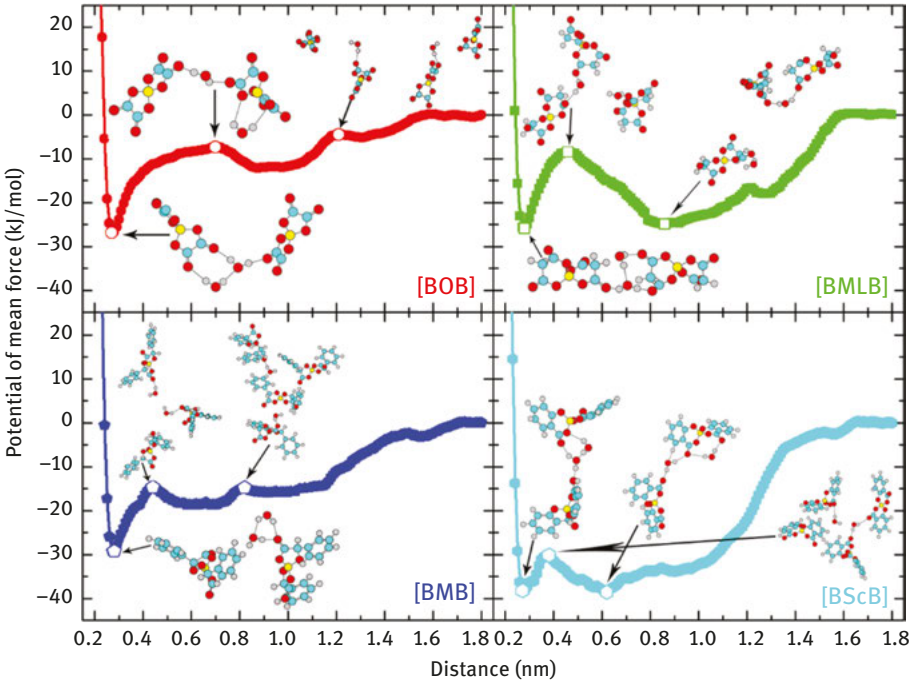

Figure 4.6: Potential of mean force results between two dispersed water molecules, and three key intermediate configurations of dispersed water molecules in coordinating neighboring orthoborate anions in four [$P_{6,6,6,14}$]-orthoborate IL matrices obtained from atomistic simulations at 333 K.

potential minimum located at around 0.28 nm is observed in four PMF profiles, indicating that intermolecular attractive interactions dominate PMF profile at short distance and favor the formation of a close contact water dimer complex through HB interactions. Additionally, this water dimer complex strongly coordinates with neighboring anionic species and forms stable ring structures through HB interactions. It takes approximately 28 kJ/mol in [$P_{6,6,6,14}$][BOB], [$P_{6,6,6,14}$][BMLB] and [$P_{6,6,6,14}$][BMB] ILs, and around 38 kJ/mol in [$P_{6,6,6,14}$][BScB] IL, respectively, to break these ring structures before pulling water molecules to larger distances. As separation distance between two water molecules slightly increases, there is still not enough space between water molecules for one ion to squeeze in due to its relatively large ionic size. This leads to unstable intermediates contributing to gradually increased water–water intermolecular potential energies until the formation of an ion-separated metastable water association structure at a larger distance.

The water–water association/dissociation patterns at larger separation distances are characterized by particular features depending on intrinsic molecular structures of orthoborate anions and delicate interactions of dispersed water molecules with surrounding ionic species. On the one hand, the hydrogen atoms in water molecules

are exclusively coordinated with oxygen atoms in hydrophilic C=O groups in orthoborate anions. The multiple hydrogen bonding acceptor sites (oxygen atoms) in orthoborate anions blur some insignificant metastable ion-separated potential minimum in corresponding PMF profiles. On the other hand, the introduction of either small methylene groups or large aromatic rings to [BOB] anion leads to distinct spatial coordination pattern of dispersed water molecules around neighboring orthoborate anions, as shown in Figure 4.7. In [BOB] and [BMLB] systems, the dispersed water molecules are preferentially coordinated with anions in equatorial region of oxalato ring planes due to directional HB interactions. However, in [BMB] and [BScB] ILs, water molecules are specifically localized around central polar segments to avoid direct contact with hydrophobic phenyl rings in [BMB] and [BScB] anions. Such a distinct spatial distribution of water molecules embedded in cavities between neighboring ionic species contributes to the formation of intermolecular hydrogen bonds between water molecules and anionic groups, and further mediates local ionic structures through ion water ion multiple complexes. By pulling two water molecules further away, the PMF oscillation becomes weak, indicating that interactions between dispersed water molecules are partially or totally screened by intervening multiple ionic species in between.

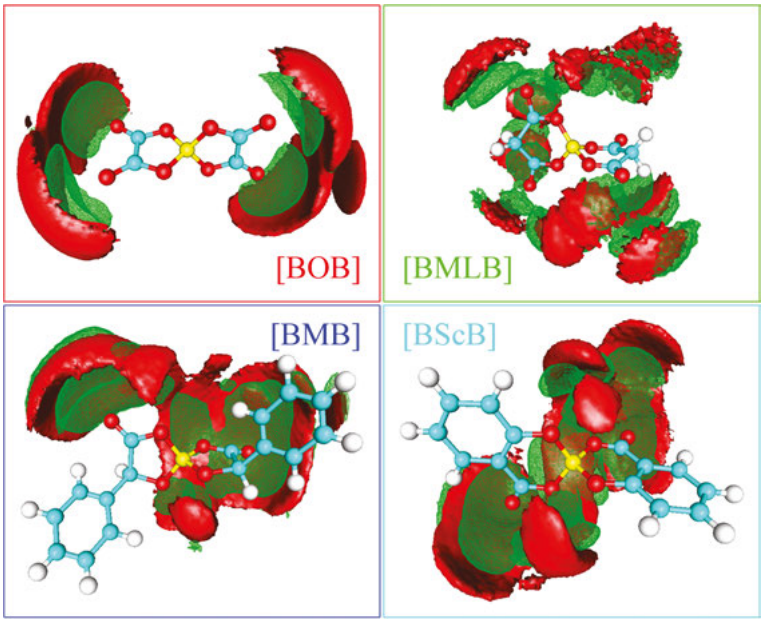

Figure 4.7: Spatial probability distribution functions of oxygen (solid red surface) and hydrogen (meshed green surface) atoms in water molecules around orthoborate anions in the first solvation shell obtained from atomistic simulations at 333 K. The red and green contour surfaces are drawn at 4.0 times of the average number density of the corresponding atoms in bulk system.

Comparing the potential depth of metastable ion-separated water association structure and the corresponding water–water separation distance in respective PMF profile, as well as the activation energy barrier from stable water dimer complex to metastable ion-separated water association structure, it can be further identified that the introduction of hydrophobic groups, either the small methylene unit or the large aromatic moiety, can essentially decrease the potential depth of ion-separated water association structure and the corresponding activation energy barrier, as well as shift the latter configurations to short separation distances. Integrating the activation energy barriers, solvation free energies and the residual water contents in four $[P_{6,6,6,14}]$-orthoborate ILs, we proposed that the removal of water molecules from IL matrices follows a two-step procedure. The separation of coupled water molecules within a heterogeneous IL matrix is the primary pathway, and the subsequent removal of water from bulk ILs is the secondary procedure in purification process. From a structural point of view, the introduction of hydrophobic units into central polar segments and the resulting conjugated structures in orthoborate anions can decrease the activation energy barrier for the separation of bounded water molecules, and hence can effectively reduce water content in the corresponding IL samples. This provides a valuable guidance for future design and synthesis of new orthoborate anions with different chemical polarities and possibly varied functional performance in practical applications.

In these four $[P_{6,6,6,14}]$-orthoborate ILs, the $[P_{6,6,6,14}]$[BOB] IL holds special significance. It was found that the residual water content in freshly synthesized $[P_{6,6,6,14}]$[BOB] IL sample is 2.3–2.5 wt% [33], which corresponds to a water mole fraction of approximately 0.5 in this sample. That is, the ratio of $[P_{6,6,6,14}]$[BOB] ion pairs and water molecules is 1:1, which might suggest interesting ionic structures like water molecules residing between close contact ion pair structures. By performing extensive atomistic simulations, four distinct compositional regimes were identified concerning the evolution of microscopic liquid organization, local ionic structures, volumetric quantities and translational and rotational mobilities of ionic species in $[P_{6,6,6,14}]$[BOB] IL–water mixtures as water concentration increases [74, 75]. The variations of liquid densities and translational diffusion coefficients of ionic species in $[P_{6,6,6,14}]$[BOB] IL–water mixtures as water concentration increases are illustrated in Figure 4.8.

– In neat ILs and IL–water mixtures with water mole fractions $x_{water} \leq 0.5$, the $[P_{6,6,6,14}]$ cations and [BOB] anions are closely coupled together via strong electrostatic interactions. The microscopic liquid organization is characterized by a connected apolar network consisting of volume-occupying alkyl substituents in $[P_{6,6,6,14}]$ cations and isolated polar domains composed of central polar segments of $[P_{6,6,6,14}]$ cations, [BOB] anions and water molecules. Such a heterogeneous local ionic environment leads to an exponential increase in translational diffusion of ionic species in $[P_{6,6,6,14}]$[BOB] IL–water mixtures as water concentration increases. Most of the added water molecules are dispersed and preferentially

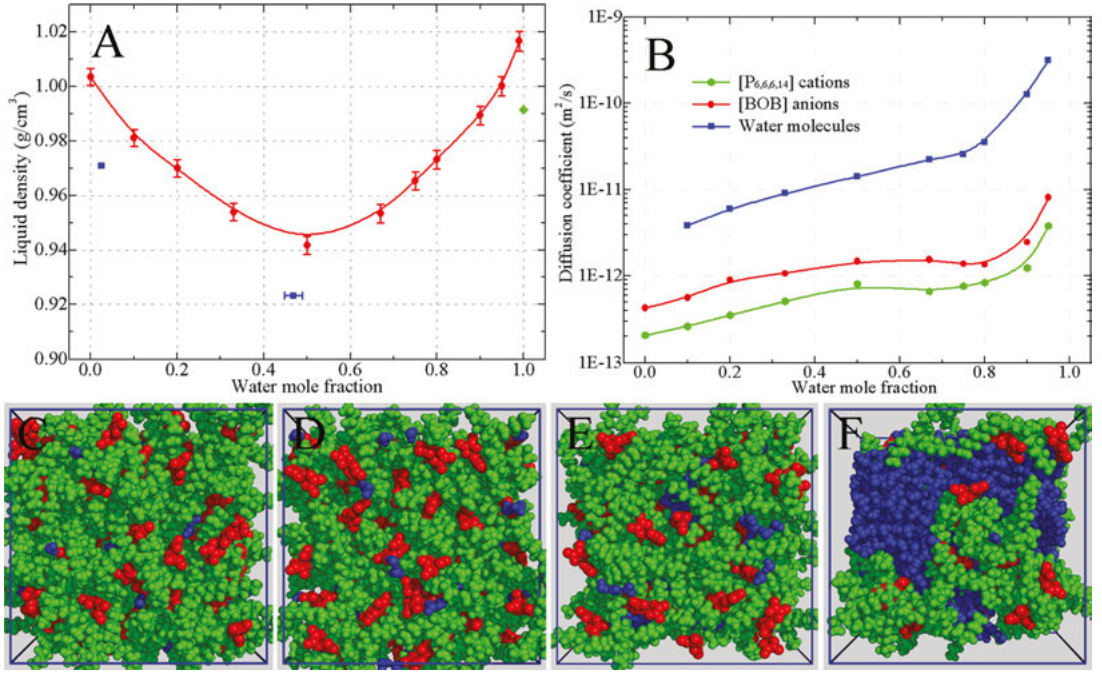

Figure 4.8: (A) Liquid densities of [$P_{6,6,6,14}$][BOB] ILwater mixtures with different water mole fractions at 333 K obtained from atomistic simulations (solid red circles) and determined from experimental measurements (solid blue squares) of two representative [$P_{6,6,6,14}$][BOB] IL samples with residual water contents of 0.06 and 2.30–2.50 wt%, respectively. The solid green diamond corresponds to an experimental density of neat water at 333 K. (B) Translational diffusion coefficients of [$P_{6,6,6,14}$] cations, [BOB] anions and water molecules in [$P_{6,6,6,14}$][BOB] IL–water mixtures with different water mole fractions at 333 K obtained from atomistic simulations. Representative snapshots of [$P_{6,6,6,14}$][BOB] IL–water mixtures with water mole fractions of x_{water} = 0.33 (C), 0.5 (D), 0.8 (E), and 0.95 (F). The [$P_{6,6,6,14}$] cations, [BOB] anions and water molecules in these mixtures are represented by green, red and blue beads, respectively.

associated with neighboring ionic species, leading to the local ionic environment characterized by solvent-shared ion pairs through cation–water–anion triple complexes. The restricted distribution of water molecules in local ionic environment results in a constrained reorientation of water molecules on a cone surface due to their dual nature in coordinating neighboring ionic species through HB interactions.

- In IL–water mixtures with intermediate water mole fractions of $0.5 < x_{water} \leq 0.8$, large water clusters appear and dominate size distribution of water aggregates since there is no sufficient void space to accommodate more water molecules. A distinct chain-like aggregate characterized by anion$\cdots(H_2O)_n\cdots$anion structure serves as bridge connecting more anionic species between isolated polar domains, as well as mediating their relative distribution and orientation in IL–water mixtures. The local ionic organization of these mixtures is characterized by solvent-mediated ion pairs. This leads to enhanced spatial correlations between ionic species, and thus considerably slows down translational and orientational mobilities of ionic species in IL–water mixtures.
- In IL–water mixtures with water mole fractions of $0.8 < x_{water} \leq 0.95$, water molecules are dynamically percolated throughout the entire simulation box and constructing a water network, leading to microscopic liquid environment described by interpenetrating polar and apolar networks. The percolation of polar domains within apolar framework promotes a rapid increase in translational diffusion of ionic species in these water-concentrated mixtures. Albeit there is a large amount of water in these mixtures, the central polar segments of $[P_{6,6,6,14}]$ cations and [BOB] anions remain in close proximity to each other through sharing one or more water molecules. This complex structure is rationalized by strong electrostatic interactions and favorable HB interactions between ionic species.
- In water concentrated mixtures with water mole fractions of $x_{water} > 0.95$, a further progressive dilution of IL–water mixtures leads to a percolation limit of IL in water, that is, upon further dilution, the connected apolar network (already stretched to its limit) starts to break up and loses its continuous nature. The local ionic environment is characterized by loose micelle-like aggregates in a highly branched water network.

The striking evolution of microstructures, local ionic environment, translational and orientational diffusion of ionic species in $[P_{6,6,6,14}]$[BOB] IL–water mixtures indicate that these mixtures are characterized by particular microstructural and dynamical heterogeneities. Such a spatio-temporal heterogeneity can be attributed to a competition between favorable HB interactions and strong Coulombic interactions between central polar segments in ionic species, and persistent dispersion interactions between hydrophobic alkyl chains in $[P_{6,6,6,14}]$ cations.

4.3.2 Neat ionic liquids in confined environment

4.3.2.1 [BMIM][PF_6] on neutral graphene surface

Either ILs used as lubricants between sliding contacts in tribology [12, 14, 15, 32, 33], as electrolytes in electrochemical energy devices [1, 7, 12, 16, 17, 21, 29, 31, 71, 87] or as liquid absorbents for CO_2 capture from fossil-fuel burning power plants [12, 13, 19, 20, 28], a common feature is the presence of interfaces between ILs and solid, gas phases [1, 7, 12–17, 19, 20, 26, 28–30, 32, 71, 87–93]. Experimental investigations of ILs under confinement indicate that physicochemical properties (melting points, surface tensions, chemical reactivities, etc.) and microstructures of ILs in interfacial regions are different to those in bulk phase [1, 7, 12, 14, 15, 17, 19, 23, 26, 28–30, 32, 71, 87–89, 93]. The direct recoil spectrometry measurements indicated a perpendicular distribution of imidazolium ring planes and a parallel orientation of butyl chains in [BMIM] cations in IL–gas interfacial region [94]. However, experimental characterizations based on sum frequency generation (SFG), high-resolution Rutherford backscattering spectroscopy and X-ray reflectivity observations [95–98] suggested that imidazolium rings prefer to take flat orientations along IL–gas interface, whilst butyl chains are loosely packed together and protruded from liquid phase into gas phase with a certain tilt. Additionally, in IL–solid interfacial region, nuclear magnetic resonance experiments showed that interfacial ionic structures of supported [BMIM][PF_6] IL depend strongly on solid surface types and the thickness of the confined IL film [93].

For absorbed [BMIM][PF_6] IL on neutral graphene surface with finite film thickness, it was observed in atomistic simulations that the confined IL film thickness has a significant effect on interfacial ionic structures and ordering orientational distributions of [BMIM][PF_6] ion pairs in IL–graphene and IL–gas interfaces [99]. Interfacial monolayers are formed in IL–gas interfacial region with ordering ionic structures. With an increase in IL film thickness, the orientations of [BMIM] cations in interfacial monolayers change gradually from dominant flat distributions along IL–gas interface to that characterized with several favorable orientations with different proportions, as shown in Figure 4.9. In these favorable orientations, the main distribution of imidazolium rings is their parallel distributions along IL–gas interface beneath the exposed outermost layer and perpendicular orientations with tilted angles toward IL–gas interface at the exposed outermost layer. The outmost layer is populated with alkyl groups and is imparted with hydrophobic feature. Distinct ionic layers with well-regulated interpenetrating polar and nonpolar networks are formed in the vicinity of IL–graphene interfacial region. The imidazolium rings lie preferentially flat on IL–graphene interfacial region, with the methyl and butyl chains in [BMIM] cations stretched out along graphene surface.

The presence of solid surface and formation of dense interfacial layers further complicate ILs' dynamical properties compared with those in bulk regions. It is

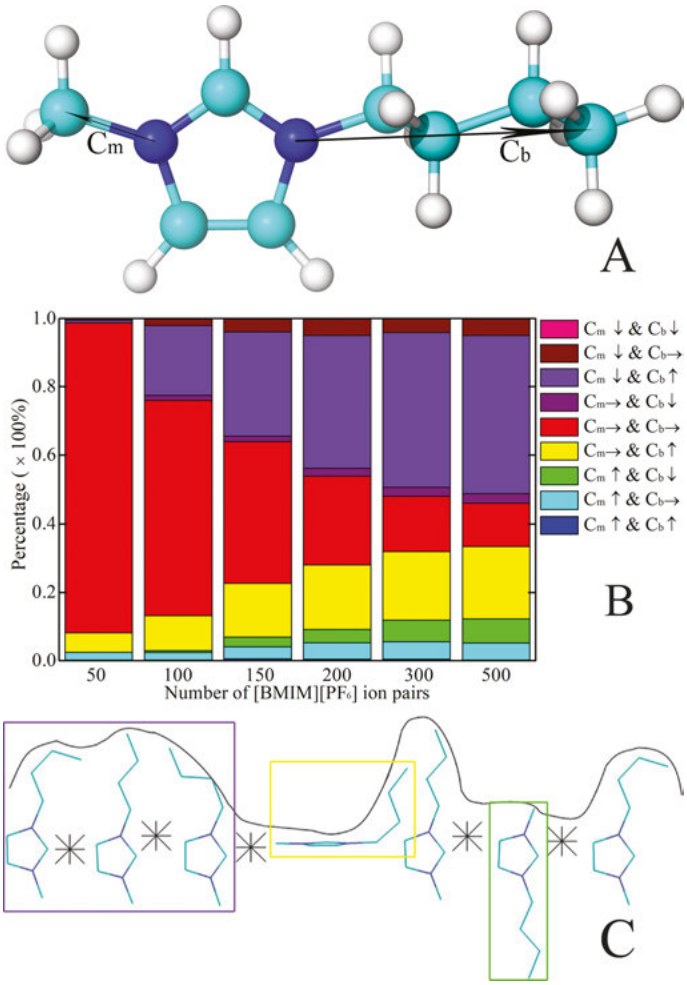

Figure 4.9: (A) Definition of C_m and C_b vectors in [BMIM] cationic framework and (B) probability distributions of these two vectors in the same ion for [BMIM] cations in IL–gas interfacial region in simulation systems consisting of varied numbers of [BMIM][PF_6] ion pairs on graphene surface. The notations →, ↓ and ↑ indicate that C_m or C_b vectors being parallel or perpendicular to the IL–gas interface with terminal carbon atoms projected into bulk region or protruded into gas phase, respectively. (C) Representative configurations of [BMIM] cations in IL–gas interfacial region.

shown that the dynamical quantities of the confined [BMIM][PF_6] ionic groups are highly heterogeneous depending on their relative positions in confined IL film, as characterized by mean square displacements of specific groups [100] shown in Figure 4.10. In IL–gas interfacial region, the relaxation and diffusion of terminal carbon atoms in butyl chains of [BMIM] cations are much faster than that in other layers of confined IL film and that in bulk region of simulation system without

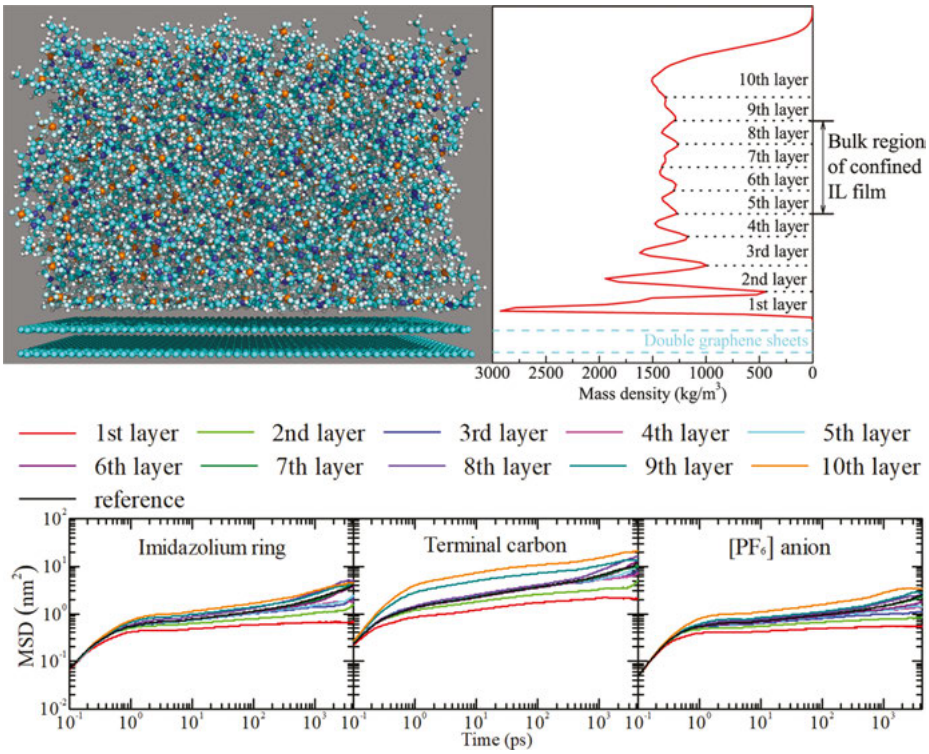

Figure 4.10: Representative snapshot of confined IL film consisting of 500 [BMIM][PF_6] ion pairs on a neutral graphene surface and the division of this IL film into ten layers based on mass density profile. Mean square displacements of imidazolium rings and terminal carbon atoms of butyl chains in [BMIM] cations and of [PF_6] anions in different layers of confined IL film, as well as that in simulation system without confinement.

confinement, due to their liberated motion in this interfacial region. In IL–graphene interface region, the dynamical heterogeneities of ionic groups are embodied both in their overall diffusions and in the diffusive components in parallel plane along solid surface and in perpendicular direction to solid surface, respectively. The overall translational mobility of [BMIM][PF_6] ionic species is characterized with slaved diffusion, and it takes much longer time for them to leave the cage formed by surrounding counterions before reaching the true diffusive regime than that without confinement.

The particular dynamical heterogeneity of confined [BMIM][PF_6] ionic groups is intrinsically related to their orientational preference and microscopic ionic structures in IL–graphene and IL–gas interfacial regions. The confinement effect induced by neutral graphene surface and formation of two-dimensional interpenetrating meso-phase contribute to the slaved diffusion of [BMIM][PF_6] ion pairs in IL–graphene interfacial region. However, such a confinement effect is short-ranged, and its

influence on dynamical properties is limited in bottom layers of confined IL film and becomes negligible with the increase of film thickness. For IL film with enough thickness, such as larger than 3 nm, the exposed outmost layer is populated with alkyl groups, mainly terminal carbon atoms of butyl chains of [BMIM] cations, which facilitates their liberated motion and hence contributes to their fast diffusion in IL–gas interfacial region. Beneath such exposed layer in IL–gas interface, the microscopic ionic structure resembles that in bulk region of confined IL film, and hence exhibits similar dynamical properties. It is the spatial structural heterogeneity of confined ion pairs in interfacial region that contributes directly to the striking dynamical heterogeneity. Both spatial and temporal heterogeneities of confined [BMIM][PF_6] ion pairs experiencing in interfacial regions are important for understanding the interfacial phenomena occurring in IL–solid and IL–gas interfacial regions before advancing their applications in related areas.

4.3.2.2 [BMIM]-based ionic liquids on charged quartz surfaces

The confined ionic species, however, exhibit distinct microstructures and ordering orientations in IL–solid interfacial region if solid surfaces are characterized by positive or negative charges [1, 7, 17, 30, 71, 87]. On charged quartz surfaces, the atomic force microscope (AFM) measurements revealed that the formation of interfacial layers of solvated ILs is strongly related to quartz surface charge and roughness [1, 26, 101]. The SFG spectroscopic signature indicated that imidazolium rings prefer to lie on quartz surface with the attached alkyl chains taking on tilted orientations [89, 90, 92]. However, this qualitative conclusion was summarized based on a simple assumption that each confined cation behaves as a rigid entity, and on limited orientational information of "reporter" groups, such as the vibrational frequency of C—H bonds on imidazolium rings.

Due to the lack of specific spectroscopic signatures for aliphatic chains, the distribution and orientation of alkyl chains in [BMIM] cations are not directly investigated. Therefore, we designed two chemically different quartz surface models to mimic the adsorption of [BMIM]-based ILs on synthesized and catalytic quartz surfaces [90–92, 102]. The dangling silicon atoms in one bare quartz surface are saturated with silanol $Si(OH)_2$ groups, whereas those in the other one are fully hydrogenated and covered by silane SiH_2 groups, respectively [103], as shown in Figure 4.11. Such an intrinsic difference in local chemical composition leads to the quartz surfaces saturated with $Si(OH)_2$ and SiH_2 groups characterized by negative and positive charges, respectively, which result in distinct stacking behavior of absorbed [BMIM]-based ILs on these two quartz surfaces.

Atomistic simulation results revealed that dense ionic layers, characterized by distinct mass, number, charge and electron densities, are formed in quartz interfacial region. The orientational preferences of confined ionic groups are characterized with

different features depending on quartz surface charges, ionic sizes and molecular geometries of anionic groups. In positively charged SiH_2 interfacial region, the anionic groups are particularly absorbed on solid surface due to strong electrostatic interactions. The main axes of asymmetric [TFO] and [NTF_2] anions are perpendicular and parallel to SiH_2 surface, respectively. However, an opposite effect is observed in negatively charged $Si(OH)_2$ interfacial region. The [BMIM] cations, either coupled with spherical ([BF_4] and [PF_6]) or aspherical ([TFO] and [NTF_2]) anions, are exclusively absorbed onto negatively charged $Si(OH)_2$ surface. The imidazolium rings lie predominantly perpendicular to $Si(OH)_2$ surface, with the corresponding methyl and butyl chains elongated along $Si(OH)_2$ surface, respectively. The anions exhibit random orientations in subsequent anionic layer, due to the partially screened intermolecular interactions between anions and atoms on $Si(OH)_2$ surface. Typical configurations of absorbed [BMIM] cations and their coupled [BF_4], [PF_6], [TFO] and [NTF_2] anions in $Si(OH)_2$ and SiH_2 interfacial regions are shown in Figure 4.11.

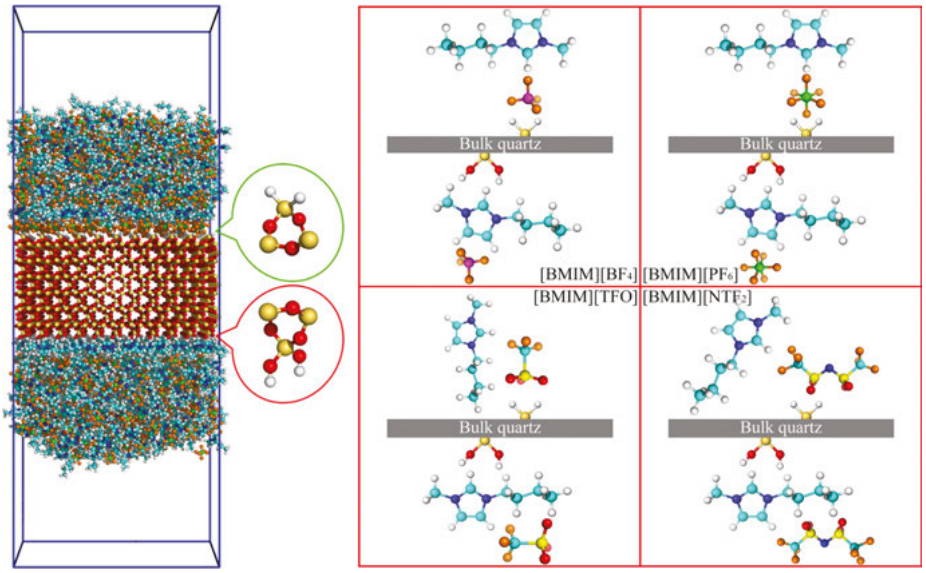

Figure 4.11: Representative configurations of [BMIM] based ILs confined in charged SiH_2 (top) and $Si(OH)_2$ (bottom) quartz interfacial region.

The distinct structural and orientational preferences of confined [BMIM] cations, and their coupled anions in IL–quartz interfacial regions are intrinsically related to quartz surface charge densities, molecular ionic sizes and geometries, as well as preferential intermolecular interactions between ionic groups and atoms constituting quartz solid surfaces. Given that ILs serve as both charged species and solvent molecules in confined environment, large ion concentration corresponds to small Debye length,

indicating that electrostatic interactions are partially screened, and thus other factors, like crowding effect originated from solid surface templating issue, become important. The subtle interplay between screening and crowding effects contributes to the formation of electric double-layer structures in charged interfacial region, which may provide an opportunity to unveil intrinsic ionic structures in controlling macroscopic functional performance of electric supercapacitors [7, 16, 20, 29, 30, 71, 87].

4.3.2.3 $[P_{6,6,6,14}]$[BMB] ionic liquid on charged gold electrodes

For all the confined [BMIM]-based ILs in solid interfacial regions, either on neutral graphene surface or on charged quartz surfaces, the charge density on solid surfaces is constant. In these confined systems, it is straightforward to study interfacial structures of confined ionic species on solid surfaces with specific charge densities, but not convenient to investigate the dependence of microstructural ordering distributions and orientations of confined ionic species on surface charge densities in IL–solid interfacial region. The application of external electric fields on solid surfaces with different interfacial charge densities, as verified in AFM and surface force apparatus (SFA) experimental characterizations [1, 26, 71, 104–107], is an effective way to induce molecular position fluctuations in confined environment, leading to the accumulation of specific ionic species in interfacial region and finally resulting in reconstruction of interfacial layering structures.

In order to understand the dependence of interfacial structures of confined ionic species on solid surface charge densities, we performed intensive atomistic simulations to probe interfacial ionic structures and molecular arrangements of $[P_{6,6,6,14}]$[BMB] IL (chosen owing to its excellent tribochemical properties in mechanical engineering contacts [33, 108]) confined between neutral and charged gold electrodes with controllable surface charge densities [109]. Detailed analyses of simulation results indicate that the interfacial chemical compositions, molecular arrangements of $[P_{6,6,6,14}]$[BMB] IL are different depending on surface charge densities to gold electrodes. For $[P_{6,6,6,14}]$[BMB] IL confined between neutral electrodes, due to the interfacial layer and a subsequent intermediate layer are formed before reaching bulk region of confined IL film. The innermost layer consists of both $[P_{6,6,6,14}]$ cations and [BMB] anions, which take compact ionic structures and checkerboard molecular arrangement in interfacial region. In this mixed innermost layer, both hexyl and tetradecyl chains in $[P_{6,6,6,14}]$ cations lie preferentially parallel along electrodes, and the most probable configuration of oxalato and phenyl rings in [BMB] anions is characterized by consecutive parallel and perpendicular arrangement adjacent to neutral electrodes, respectively.

As gold electrodes get electrified but with low surface charge densities (<20 $\mu C/cm^2$), the mixed innermost layer thickness gradually increases as that in surface charge density, due to a gradual accumulation of $[P_{6,6,6,14}]$ cations and [BMB]

anions, and their counterions being squeezed out from the innermost layer adjacent to negatively and positively charged electrodes, respectively. The effect of charging electrodes has little influence on the molecular alignment of hexyl and tetradecyl chains in $[P_{6,6,6,14}]$ cations along negatively charged electrodes due to their delocalized charge distribution within cationic framework and their saturated distribution in the innermost cationic layer. However, charging gold electrodes results in new orientational patterns for oxalato rings in the same [BMB] anions from parallel–perpendicular orientation to that characterized by constraint molecular arrangement with a tilted angle of 45° from positively charged electrode. In the meantime, the molecular distributions of phenyl rings are alerted accordingly due to their direct bonding to oxalato rings through flexible C—C bonds in [BMB] anions. Upon further charging gold electrodes with surface charge densities equal or higher than 20 $\mu C/cm^2$, distinctive innermost interfacial layers exclusively consisting of $[P_{6,6,6,14}]$ cations and [BMB] anions are formed adjacent to negatively and positively charged electrodes, respectively. This implies a templating effect in producing compact and tightly bounded innermost layers closest to charged electrodes as surface charge density increases. Such an interfacial effect will in turn alter packing ionic structures in subsequent layers, and so forth, resulting in enhanced compact interfacial structures in confined environment. It is expected that more energies are needed for a probe to rupture, to penetrate and to displace the innermost ionic layer due to the absorbed ionic species being strongly bounded to oppositely charge electrodes, as indicated from previous AFM and SFA measurements [104–107]. The orientations of oxalato and phenyl rings in [BMB] anions are described by broad and featureless characteristics before distinctive coordination pattern observed for [BMB] anions adjacent to positively charged electrodes with surface charge density of 100 $\mu C/cm^2$.

It is noteworthy that $[P_{6,6,6,14}]$ cations and [BMB] anions exhibit different responses to changes in external electric field generated from charged electrodes, which will have a profound effect on interfacial friction when this IL is used to lubricate gold engineering surfaces in technical applications. These atomistic simulation results are helpful in elucidating interfacial changes in ionic structures and molecular arrangements of $[P_{6,6,6,14}]$[BMB] IL confined between gold electrodes, and may provide more physical insight in further investigation of ILs' electrotunable friction response and lubrication mechanism in mechanical engineering systems.

4.3.3 Simulation algorithms for calculation of ionic liquid viscosity

The most immediate way to calculate the liquid viscosity is to perform a shear flow simulation. This can be done by using SLLOD equations of motion [110]. They have been used since 1980s to calculate the liquid viscosities of alkanes, Lennard-Jones liquids and liquid crystals [111–113]. When these equations are

used, a planar Couette velocity field, $\mathbf{u} = \dot{\gamma} z \mathbf{e}_x$, that is, a velocity in the x-direction varying linearly in the z-direction, is added to the ordinary Hamiltonian equations of motion

$$\dot{\underset{i\alpha}{q}} = \frac{p_{i\alpha}}{m_\alpha} + \dot{\gamma} e_x z_{i\alpha} \tag{4.1a}$$

and

$$\mathbf{p}_{i\alpha} = \mathbf{F}_{i\alpha} - \dot{\gamma} \mathbf{e}_x p_{i\alpha z} - \varsigma \mathbf{p}_{i\alpha} \tag{4.1b}$$

where $\mathbf{p}_{i\alpha}$and $\mathbf{q}_{i\alpha}$ are the linear momentum relative to streaming velocity, the position of atom α of molecule i, $\dot{\gamma}$ is the velocity gradient or shear rate, m_α is the mass of atom α and ζ is a thermostatting multiplier removing the excess heat generated by the shear field. The algebraic expressions for this multiplier can be selected in a few different ways depending on the desired ensemble. The edge effect vanishes by applying Lees–Edwards sliding brick boundary conditions. The viscosityη, in the Newtonian or linear regime is obtained as the zero field limit of ratio of the zx-component of shear stress, σ^s_{zx}, and the velocity gradient

$$\eta = \lim_{t\to\infty} {}^{s}_{zx}(t)/\dot{\gamma}. \tag{4.2}$$

According to linear response theory, the zero shear rate limit of the viscosity thus obtained should be exactly the same as the one given by the Green–Kubo relation for the viscosity

$$\eta = \frac{V}{10 k_B T} \int_0^\infty dt < \bar{\sigma}^s(t) : \bar{\sigma}^s(0) >_{eq}, \tag{4.3}$$

where V is the volume of the system, k_B is Boltzmann constant, T is the absolute temperature, $\bar{\sigma}^s = \frac{1}{2}\left(\bar{\sigma} + \bar{\sigma}^T\right) - \frac{1}{3} Tr(\bar{\sigma})$ is the symmetric traceless part of stress tensor and the subscript "*eq*" denotes that the average is evaluated in an equilibrium ensemble. Since shear flow simulations and the Green–Kubo relation should give the same results, they provide an important cross-check of atomistic calculations, that is, the shear rates in eq. (2) fall into a linear regime and that the correlation functions in eq. (3) have decayed. It is also a consistency test of the computer program used to perform simulations.

The shear flow algorithm and equilibrium Green–Kubo method have recently been adopted to calculate the liquid viscosities of $[P_{6,6,6,14}]$[BMB] and $[P_{6,6,6,14}]$[BOB] ILs. The selection of these two IL systems is due to their potential technological applications such as lubricants and electrolytes for fuel cells and others. It should be noted that it is still a challenge in a proper sense of word to calculate liquid viscosities

of $[P_{6,6,6,14}]$[BMB] and $[P_{6,6,6,14}]$[BOB] ILs owing to their complex molecular structures. Since these ionic molecules are rather large, there are polarization and charge transfer phenomena that can be explicitly handled in classical molecular dynamics simulations [114, 115]. However, this is also time consuming in practice for the abovementioned tetraalkylphosphonium-orthoborate ILs, because very long simulations are needed to evaluate their liquid viscosities. Therefore, we adopted a feasible procedure by using charge scaling factors between ionic species to calculate the liquid viscosities of these ILs.

The preliminary results of atomistic simulations on these ILs have shown that the viscosities of $[P_{6,6,6,14}]$[BMB] IL system do not change within statistical uncertainty when system size is increased from 96 to 735 ion pairs [116]. This is advantageous when the Green–Kubo relation is evaluated since thermal fluctuations are larger in smaller systems, which means that the time correlation functions converge faster. It has also been established that the viscosities obtained using the Green–Kubo method from equilibrium atomistic simulations agree with those obtained from shear flow simulations in the linear regime, which is in accordance with linear response theory. This provides a significant consistency test of simulation algorithm and shows that the computation time is long enough to obtain reliable values for the viscosity. As an example of computational results, we show the viscosities of an equimolar mixture of $[P_{6,6,6,14}]$[BMB] and $[P_{6,6,6,14}]$[BOB] ILs as a function of temperature between 363 and 423 K in Figure 4.12. These viscosities have been evaluated using Green–Kubo relation (eq. (3)) with a charge scaling factor of 0.8. It is obviously shown that the liquid viscosity of this mixture can be described by a rather simple Arrhenius expression over the studied temperature range, despite the complexity of this simulation system consisting of $[P_{6,6,6,14}]$ cations and [BMB] and [BOB] anions.

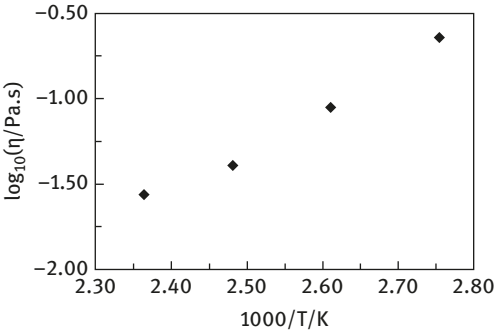

Figure 4.12: Liquid viscosities of an equimolar mixture of $[P_{6,6,6,14}]$[BMB] and $[P_{6,6,6,14}]$[BOB] ILs at different temperatures evaluated using Green–Kubo relations with a charge scaling factor of 0.8 for ionic species.

4.3.4 Atomistic simulations and small-angle X-ray scattering studies of alkylammonium nitrate with cosolvents

EAN was studied already in the year of 1914 by Paul Walden in a pioneering study, which is considered to mark the beginning of investigation on ILs [4, 12]. After more than 100 years, many features of EAN, and more in general of alkyl ammonium nitrate, and their mixtures with other solvents, are still attracting considerable interest.

We have recently investigated both experimentally and by means of molecular modeling the mixtures of this class of IL with important cosolvents such as N-methyl-2-pyrrolidone (NMP) and acetonitrile (ACN) [79, 81, 117, 118]. IL mixtures with cosolvents are macroscopically homogeneous but are typically characterized by microheterogeneity at nanoscale level. Small-angle X-ray scattering experiments (SAXS) on some IL mixtures with some cosolvents have revealed a pronounced scattered intensity in low q region of SAXS pattern [119–121]. Such phenomenon, termed as low q excess (LqE), is higher at low concentration of IL. In a recent investigation, some of us found that the mixtures of EAN with ACN display the same phenomenon. Furthermore, the LqE phenomenon observed at low concentration of EAN is the highest reported to date [118].

A combined experimental (volumetric measures, wide and small-angle X-ray scattering) and computational study performed on the whole concentration range of this EAN–ACN mixture allows to understand the microscopic origin of this finding. The partial molar volumes suggest that addition of small amount of EAN to ACN does not lead to a homogenous solution at molecular level, and that EAN molecules self-associate. The isobaric thermal expansivity data pointed to a similar conclusion concerning the lack of homogeneity at molecular scale. The nonhomogeneity of local structure leads to density fluctuations, and this is the origin of LqE observed at EAN molar fraction (x_{EAN}) lower than 0.5. Through the calculation of entity of density fluctuation at different EAN molar fractions, it can clearly be seen that the highest fluctuations occur at the lowest EAN concentration and that they decrease exponentially with increasing EAN molar fraction.

Atomistic simulations of these mixtures in the whole concentration range allowed reaching an understanding of these EAN–ACN systems at molecular level. The general Amber force field was used for bonded and vdW parameters [122], while partial charges were calculated at B3LYP/aug-cc-pVTZ level of theory, using a restricted electrostatic potential procedure. The initial simulation boxes for atomistic simulations were prepared using the same molar fraction as that in experimental samples. A dielectric constant of 1.8 was used in simulation with EAN, which is equivalent to charge scaling of 0.75.

Analysis of atomistic simulation trajectories at $x_{EAN} = 0.1$ reveals that EAN molecules organize in wormlike structure surrounded by ACN molecules. These molecular structures are constituted mainly by EAN, and their density is higher than that of neat IL due to a solvophobic effect and is much denser than ACN. Similar organization,

although less pronounced, is observed for x_{EAN} molar fraction of 0.3 and 0.5, while at higher EAN content the mixtures are homogeneous at molecular level, with ACN molecules dissolved in EAN matrix. The structural heterogeneity is observed in atomistic simulations only for mixtures that display LqE in SAXS patterns. This clearly indicates that the physical objects generating density variations that induce LqE are wormlike structures formed mainly by EAN ionic species.

4.4 Coarse-Grained molecular dynamics simulations

4.4.1 United-atom model for [$P_{6,6,6,14}$] cation

Compared with traditional molten salts, one fascinating feature of ILs is that they exhibit distinct heterogeneous nanostructural ordering [41]. The nanoscopic liquid organization in bulk ILs is characterized by either spongelike interpenetrating polar and apolar networks or segregated polar domains within apolar framework depending on the number of hydrophobic alkyl units in ionic species. The characteristic size of nanoscopic structural heterogeneity is found to scale linearly with aliphatic chain length in imidazolium and pyrrolidinium cations, as indicated by both SAXS experiments and atomistic simulations [36, 54, 123–127].

However, the dependence of nanoscopic liquid morphology on aliphatic chain length in tetraalkylphosphonium cation is complicated since there are four aliphatic chains in tetraalkylphosphonium cation, and each one can be tuned with varied aliphatic substituents [68, 70, 74, 75, 128] and mutated with different polar and apolar groups [34, 124]. Additionally, tetraalkylphosphonium cations can be associated with various anions and molecular liquids [33, 68, 70, 74–76, 108, 109, 129], leading to spectacular ionic structures and distinct liquid morphologies in IL matrices. The liquid organizational morphologies of [$P_{6,6,6,14}$]-based ILs, as indicated from X-ray scattering experiments and atomistic simulations conducted by Castner and Margulis groups, are dominated by three distinct landscapes at different length scales associated with short range adjacency correlations, positive–negative charge alternations at intermediate range and long-ranged polarity ordering correlations [34, 123, 124, 130].

Since aliphatic chain length is a sensitive handle to microstructural ionic environment in IL matrix, we performed atomistic simulations to elucidate the effect of linear aliphatic substituents in tetraalkylphosphonium cations on liquid landscapes, microstructures and dynamical properties of ionic species in local ionic environment [131]. Simulation results indicated that bulk tetraalkylphosphonium chloride ILs are characterized by distinct microscopic ionic structures and heterogeneous liquid morphologies depending on aliphatic chain length in tetraalkylphosphonium cations. For ILs consisting of small tetraalkylphosphonium cations, like in triethylbutylphosphonium chloride ([$P_{2,2,2,4}$]Cl) IL, microstructural liquid morphologies are

characterized by bicontinuous spongelike interpenetrating polar and apolar networks. Lengthening aliphatic chains in tetraalkylphosphonium cations leads to the polar network consisting of Cl anions and central polar groups in cations being partially broken or totally segregated within apolar framework.

The liquid morphology variations and heterogeneous microstructural changes in six tetraalkylphosphonium chloride ILs are qualitatively verified by prominent polarity alternation peaks and adjacency correlation peaks observed at low and high q range in total X-ray scattering structural functions, respectively, and their peak positions gradually shift to lower q values with lengthening aliphatic chains in tetraalkylphosphonium cations, as shown in Figure 4.13. The charge alternation peaks registered in intermediate q range exhibit complicated dependence on aliphatic chain length in tetraalkylphosphonium cations due to the complete cancellations

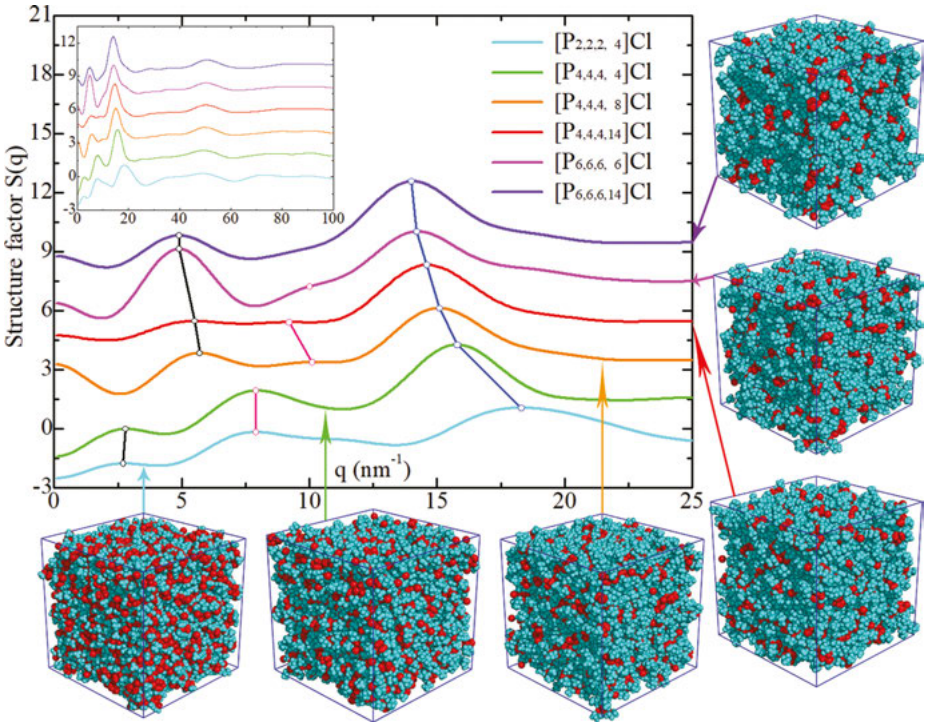

Figure 4.13: Structural functions $S(q)$ in the range of $q \leq 25$ nm^{-1} and $q \leq 100$ nm^{-1} (inset graph) for six tetraalkylphosphonium chloride ILs obtained from atomistic simulations at 323 K. These structural functions are vertically shifted by 2 units based on previous curves for clarity. The peak symbols in low, intermediate and high q values correspond to polar–apolar alternations, positive–negative charge alternations and close contact adjacency correlations, respectively. Representative liquid morphologies of six tetraalkylphosphonium chloride ILs at 323 K are illustrated, in which polar domains (red) consist of Cl anions and central P$(CH_2)_4$ groups in tetraalkylphosphonium cations, and apolar entity (cyan) is composed of the remaining alkyl units in tetraalkylphosphonium cations, respectively.

of positive contributions of same charge ions and negative contributions of ions of opposing charge.

The particular liquid morphologies and heterogeneous ionic structures in tetraalkylphosphonium chloride ILs are intrinsically manifested in dynamical properties characterized by mean square displacements, translational mobilities, van Hove correlation functions and non-Gaussian parameters of tetraalkyl-phosphonium cations and chloride anions in bulk systems [75, 100]. The terminal carbon atoms in aliphatic chains exhibit overall higher diffusivity than central phosphorus (P) atoms in tetraalkylphosphonium cations, and their cooperative effect contributes to the medium diffusion coefficients of the whole tetraalkylphosphonium cations. The P and Cl atoms exhibit comparable translational diffusivities due to their strong Coulombic coordination feature in polar domains, highlighting the existence of strongly correlated ionic structures in IL matrices. Lengthening aliphatic chains in tetraalkylphosphonium cations leads to concomitant shift of van Hove correlation functions and non-Gaussian parameters to larger radial distances and longer timescales, respectively, indicating the enhanced translational dynamical heterogeneities of tetraalkylphosphonium and chloride ions in constrained local environment.

In typical IL matrices, the liquid structural heterogeneity generally spans over an order of a few nanometers and is mainly derived from principle interactions involving different molecular moieties in ILs. The atomistic modeling of nanoscopic liquid organization of ILs over length scales beyond intermolecular distance requires that simulation system size should be several times larger than characteristic length scale of nanostructural organization of model ILs, and long time simulations should be performed to properly sample molecular conformations of ionic species in liquid organization [35, 41–44]. The latter, in particular, should be excruciatingly long due to the slow relaxation of ionic groups in bulk liquid matrix. Additionally, the lengthening aliphatic chains or increasing the number of hydrophobic alkyl units in ionic species leads to their voluminous characteristics, which further slows their reorientations in bulk region. This proposes a severe fundamental challenge for atomistic simulations despite of their initial successes in identifying the existence of nanostructural ordering phenomena in bulk ILs.

In this regard, CG models and simulations become imperative, and open a possibility to sample over large length and long time scales with a modest computational cost. The main aim of coarse-grained Molecular Dynamics (CGMD) simulations is to make this problem tractable with minimal diluting chemical rigor [35, 36, 41–43]. The CG strategy starts with a choice of specific length scale for coarsening and then subsumes all atoms presented within that length scale into one superatom or bead. These beads are then connected to one another by “bonds” to reproduce an overall architecture of CG molecule. The connected beads interact with each other via bond stretching and bending forces with similar interaction forms as that used in atomistic

models but with different interaction parameters. The speedup in mimicking model IL systems using CG models is achieved, on the one hand, due to manyfold reduction in total number of degrees of freedom and the usage of softer interaction potentials, and on the other hand, due to the utilization of a larger time step than that used in atomistic simulations. These benefits make CGMD simulation a powerful way to capture slow processes that occur in complex fluids.

Due to the voluminous characteristics of tetraalkylphosphonium cations, we proposed an united-atom (UA) model for $[P_{6,6,6,14}]$ cation through a multiscale modeling protocol in which the force field parameters derived at high-resolution scale are transferred to low-resolution level in a self-consistent computational scheme using a bottom-up approach bridging different length and time scales [129]. Quantum chemical calculations were first performed to obtain the optimized molecular geometries of an isolated $[P_{6,6,6,14}]$ cation and a tightly bounded $[P_{6,6,6,14}]$ Cl ion pair structure, the latter of which is characterized by strong electrostatic interactions and moderate HB interactions between Cl anion and $[P_{6,6,6,14}]$ cation, respectively, as shown in Figure 4.14. The procedure to develop effective force field parameters and atomic partial charges for atomistic $[P_{6,6,6,14}]$ cation is the same as that used in previous works [64, 66, 68, 70]. Furthermore, an economical and nonpolarizable UA model is constructed for the $[P_{6,6,6,14}]$ cation. The hydrogen atoms in four methylene groups that are directly connected to central P atom in atomistic $[P_{6,6,6,14}]$ cation are retained in the UA model due to their preferences to form hydrogen bonds with Cl anion. Other methylene and methyl units in aliphatic chains in $[P_{6,6,6,14}]$ cation are represented as single interaction sites. The interaction parameters for UA sites are carefully tuned based on the transferable potentials for phase equilibria force field [132] to qualitatively match bond and angle distributions as that obtained from atomistic simulations, as shown in lower panels in Figure 4.14. A reduced partial charge of +0.8e is used in UA $[P_{6,6,6,14}]$ cationic model as an effective way to account for the average electrostatic polarization effect in condensed liquid state.

Atomistic and CG simulations were performed over a wide temperature range of 273–393 K to validate the proposed UA model against available experimental and computational data. The predicted volumetric quantities, including liquid density, volume expansivity and isothermal compressibility, of bulk $[P_{6,6,6,14}]$Cl IL agree well with experimental measurements. The proposed UA $[P_{6,6,6,14}]$ cationic model can essentially depict intrinsic local ionic structures and thermodynamics predicted by *ab initio* calculations and atomistic simulations, and nonlocal transport properties against corresponding experimental characterizations of $[P_{6,6,6,14}]$Cl IL over a wide temperature range. From a perspective point of view, the proposed multiscale modeling protocol to construct atomistic and UA models from *ab initio* calculations is useful and can be extended to other classes of ILs.

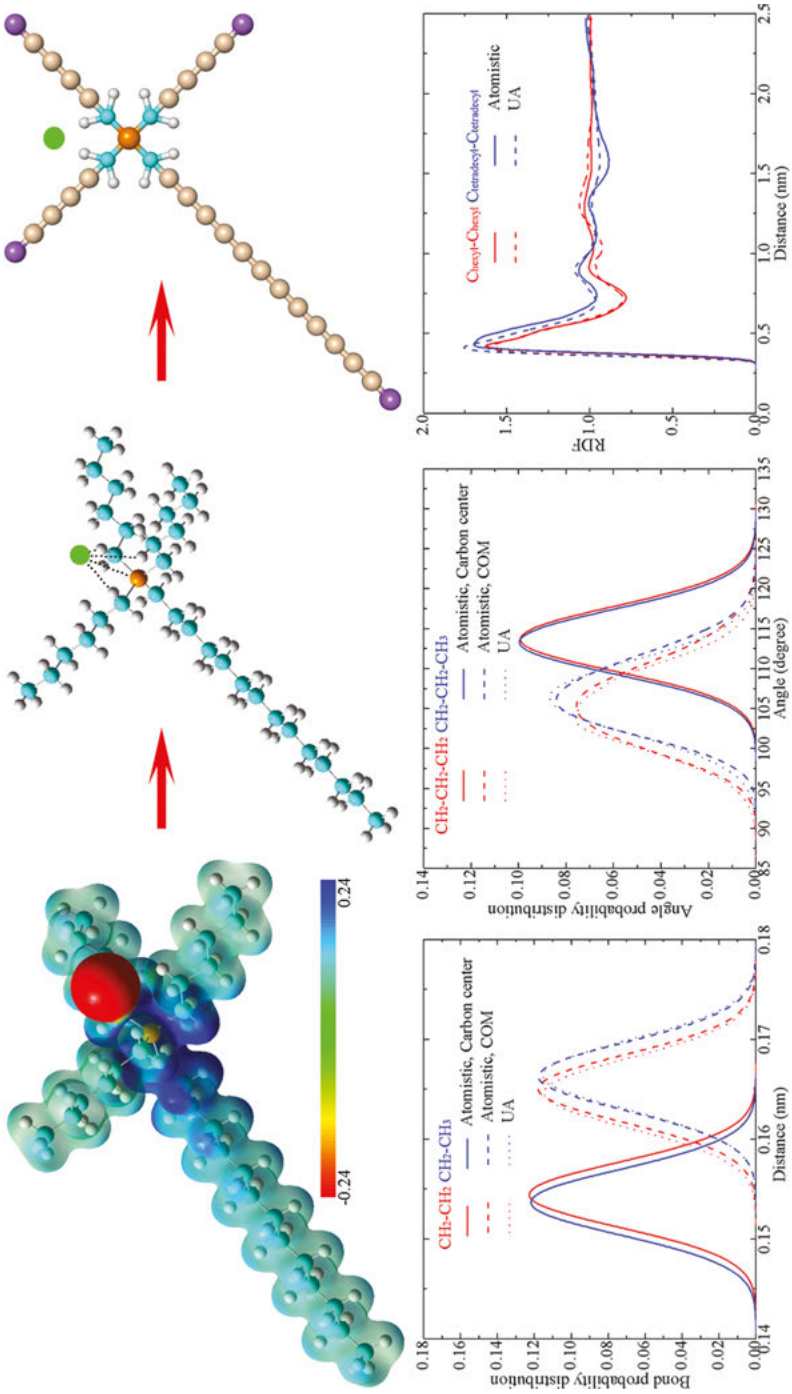

Figure 4.14: Molecular electrostatic potential surface and the corresponding atomistic ionic models with close contact atom pairs in a tightly bounded $[P_{6,6,6,14}]Cl$ ion pair obtained from quantum chemical calculations. The bond length and angle probability distributions and radial distribution functions of terminal carbon atoms in aliphatic chains calculated from the constructed UA $[P_{6,6,6,14}]$ cationic model are compared with those determined from atomistic simulations to validate proposed interaction parameters.

4.4.2 Coarse-grained model for [BMIM][PF_6] ionic liquid

By further coarse-graining of the proposed UA models to an upper level, like lumping three UA beads into a new one, one can continuously reduce computational time relative to atomistic and UA models and facilitate computational studies of solute-based dynamics on microsecond scale. Of course, this computational saving comes at an expense of some realism of real ionic models. There is an inevitable trade-off between computational cost and physical accuracy inherent to any CG model development. Additionally, CG models can reveal essential structural properties and qualitatively describe transport properties of model IL systems at mesoscopic level by integrating over less important degrees of freedom at atomic scale [31, 35, 36, 55, 56, 133, 134].

Wang and Voth first developed a generic CG model for ILs consisting of imidazolium cations coupled with [NO_3] anion to study their nanoscopic ionic structures with varied aliphatic chains attached to imidazolium rings [35, 36, 54, 125]. A multiscale coarse-graining approach based on the force matching method was adopted to reproduce the effective forces acting on CG beads to match with those calculated from atomistic simulations. The subsequent CGMD simulations demonstrate that charged imidazolium rings and anions organize into continuous ionic network due to strong electrostatic interactions, and the neutral aliphatic chains in cations form nonpolar domains separated from ionic framework, respectively [35, 36, 54, 125]. The geometrical constraints of head and tail groups in cations result in a novel balanced liquid crystal-like structure at low temperatures. This physical picture can qualitatively explain the experimentally observed IL crystal structure, the transition from IL to isotropic liquid crystal and changes in physicochemical and structural properties of ILs with varied aliphatic chains. In subsequent work, several coarse-graining schemes were proposed for imidazolium cations [31, 41, 55, 134]. Interaction potentials between CG beads are either obtained from specific coarse-graining approaches, like iterative Boltzmann inversion (IBI) method [134], or described by generic interaction potentials [55]. CGMD simulations show that these CG models exhibit different efficiency in describing microstructural organizations of [BMIM][PF_6] ILs at varied thermodynamic conditions depending on the detailed coarse-graining strategy [35–37, 41, 55, 125, 129, 134].

It should be noted that in the effective potentials derived specifically for [BMIM][PF_6] IL in above studies, electrostatic interactions are either explicitly calculated with Ewald summation-based methods [35, 36, 55, 125, 133], or implicitly included in interaction potentials [134]. In order to evaluate the different treatment of electrostatic interactions in CGMD simulations, we proposed a CG model for [BMIM][PF_6] IL based on following principles [37]: (i) Three methylene units in aliphatic chains are treated as single CG bead. This is one of the most popular coarse-graining schemes widely used in other CG simulations [55, 134]; (ii) Imidazolium ring and two remaining methyl units are symmetrically divided into two CG beads; (iii) The anionic group

is described by one CG bead, which is the normal scheme in other CG models for IL system [35, 55, 133, 134]. With these guiding principles, the CG prototype for [BMIM][PF_6] IL was constructed and is illustrated in Figure 4.15.

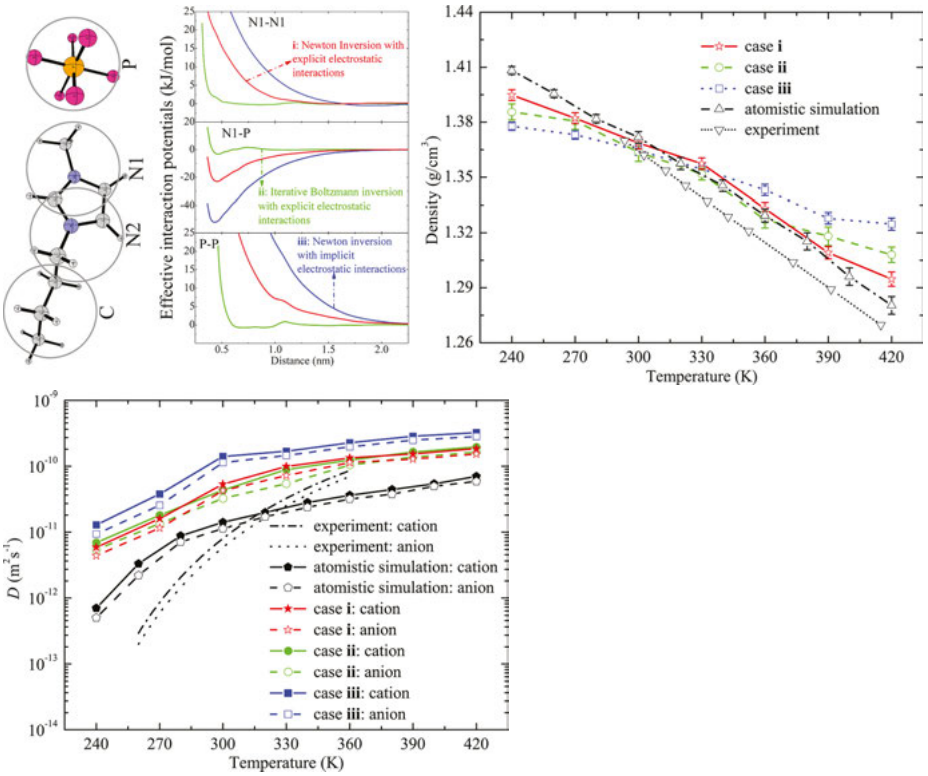

Figure 4.15: The CG model for [BMIM][PF_6] IL and typical effective interaction potentials derived from the NI and IBI methods with different treatment procedure of electrostatic interactions. Liquid densities and diffusion coefficients of [BMIM][PF_6] IL calculated from CG simulations using three sets of interaction potentials are compared with experimental and atomistic simulation results.

Three sets of effective interaction potentials between CG beads were derived from two iteration procedures, that is, the Newton inversion (NI) [135] and IBI methods [134], respectively, with different treatment fashion of electrostatic interactions based on radial distribution functions (RDFs) calculated from atomistic simulations. It is shown in Figure 4.15 that even the forms of effective interaction potentials derived from the NI and IBI procedures with varied treatment of electrostatic interactions are different, three sets of effective potentials can reproduce RDFs as that obtained from atomistic reference simulations with statistical uncertainty. With three sets of constructed CG potentials, we performed CG simulations on [BMIM][PF_6] IL over large spatial and long temporal scales and thereafter the obtained CG simulation results

were comprehensively compared with experimental and atomistic simulation results on thermodynamics, microstructures, charge density distributions, scattering and dynamical properties to validate the proposed CG protocols. The interaction potentials deduced from two methods with explicit treatment of electrostatic interactions provide results that are most consistent with atomistic simulation results, whereas simulation results obtained from the effective potentials with implicit inclusion of electrostatic interactions show noticeable deviations for thermodynamic, structural and dynamical properties. In addition, the translational diffusion coefficients of ionic groups obtained from CGMD simulations are larger than that calculated from atomistic simulations, which is attributed to the simple description of [BMIM] cation and $[PF_6]$ anion. This discrepancy becomes small as temperature increases, which is rationalized by the fact that force field details become unimportant and just short-ranged bead connectivity prevails at high temperatures [134]. In the development of effective potentials with the NI and IBI methods, the electrostatic interactions should be explicitly incorporated in iteration processes. In subsequent CGMD simulations, the long range electrostatic interactions should also be calculated explicitly with proper methods [136–138] to improve the reliability of dynamical properties of model IL systems at wide temperature range.

4.5 Conclusions and outlook

We have given several examples on how computer modeling and simulations at different length and time scales can provide valuable insight to better understand these very complex IL systems. It is clear that molecular modeling should be always closely combined with experiments as seen in the above investigations to study microstructural and dynamical properties of ILs in bulk region and in confined environment. It is fortunate that this relatively "new" class of materials has appeared at a time when simulation methodologies and computing power have converged to enable sophisticated modeling on these materials. The research field of ILs has reached an astonishing level enriched by computational knowledge gained from quantum chemical calculations, *ab initio*, atomistic and CG simulations. Had extensive interest in ILs blossomed 17 years earlier, it is unlikely that molecular simulations would be able to address all critical questions that are being tackled today. Lots of spectacular phenomena taking place at bulk region and in confined environment are still mysterious. Molecular simulations, in a long period of time in future, will be on an equal footing with experimental investigations on these striking properties of ILs in varied applications.

In future work, molecular simulations will be generally adopted in two modes within IL community. The first mode is the accurate prediction of physicochemical and microstructural quantities of model IL systems. Simulations have already been

shown to make quantitative predictions of thermodynamics, microstructures, liquid morphologies and dynamics of neat ILs and IL mixtures, and this area will continue to be an important area in future investigation. The predictions of molecular properties, especially for ILs under harsh conditions where experimental characterizations are difficult to conduct, such as at high temperatures and pressures, will be of special significance. Additionally, the thermodynamic property predictions for IL mixtures, either for binary, ternary or multicomponent mixtures, should be paid more attention as these multicomponent mixtures are characterized with desirable properties that are absent in single IL sample [8, 18, 23, 34, 49]. However, care should be taken before making broad generalization. The current data set is quite restricted and some properties have been investigated for one set of ILs and other properties have been studied for others. Most IL mixtures exhibit nonideality in thermodynamics, but this does not imply that it will always be the case. Near ideal mixing is possible and has been observed in experiments [23, 49]. For IL mixtures used as absorbents for CO_2 capture, a critical parameter is the gas solubility of CO_2 in IL mixtures [19, 28]. Mixture solubility measurements are much harder to carry out experimentally than those for pure species solubility, but are in principle no more difficult to conduct in a simulation. The predicted thermodynamic properties can be further used as input parameters to test, develop and validate molecular theories, such as the statistical associating fluid theory and regular solution theory.

The second mode is providing qualitative insight into the structure–property relationship, which is even more important than calculating detailed physicochemical properties. Either IL or IL mixtures used as electrolytes in electrochemical devices [7, 17, 20, 21, 29], as absorbents for gas separation [16, 19, 28], as solvents for material synthesis or as lubricants in tribology [14, 15, 32], the overall goal is to maximize their functional performance in macroscopic applications. Clearly, such a goal is ambitious, but achievable in the long term. As discussed in previous sections, multiscale modeling simulations have already been adopted to elucidate the delicate interactions between HB and π-type interactions, to describe striking coordination pattern between residual water molecules and ionic species in IL matrices and distinct structural ordering quantities of ionic species in confinement, and to unveil nanosized polar and apolar domains within heterogeneous ionic environment. Future studies aimed to interpret the effect of molecular ionic structures on their functions in varied applications will become increasingly important. In this manner, multiscale modeling simulations may help suggest new application areas and experiments.

Despite the fact that impressive progresses have been made over the last decades, many problems still remain. Quantum chemical calculations have been invaluable in understanding the complex interplay of intermolecular forces in ILs and relationship to their thermodynamic properties. However, the proper description of transport properties is still not sufficient to generate reliable statistical data and to compute ion mobility due to limitations in computational resources. Accurate atomistic force fields must be further developed and validated for a much larger range of

ionic compounds. Many force fields have been published, especially for imidazolium-based ILs [24, 46, 52, 58, 61, 62, 65, 66]. Lopes and Padua have produced a large set of force field parameters based on OPLS format [52, 67, 69], and several other groups have been active in developing force fields as well. Despite these efforts, there is a huge number of cation and anion types for which force field parameters do not yet exist. Moreover, many of the proposed force fields have not been subjected to a rigorous validation procedure. In most of these proposed force fields, liquid density is the first choice to compute and thereafter to compare with experimental measurements. This is not a good choice for force field validation since force fields having widely varying parameters can give essentially the same liquid density. This is because liquid density is essentially a mean-field property that is insensitive to specific interactions and energies [42]. It has been argued that enthalpies of vaporization, melting point and crystal structure might be better experimental quantities to compare against as these quantities are often available and extremely sensitive to the quality of force field parameters [42]. Additionally, dynamics and transport properties, which might be extremely demanding as long time simulations should be performed due to ILs' viscous feature, should be used to validate IL interaction parameters. Furthermore, as it is validated for conventional molecular liquid, one can compute liquid vapor equilibria and critical points and compare these with available experimental data. The inclusion of polarizability into constructed force fields will be an interesting topic, which can considerably increase the accuracy of the estimation of dynamics and transport properties of ILs. The computational effort for such simulations is quite large; however, with the increased computing power, the number of polarizable force fields just recently started to grow. Besides validating existing force fields, new force field parameters, or some modifications on available force field parameters, are needed for different cation and anion classes. Generating new force fields is tedious and time consuming, but must be done if molecular simulations are to be used to help guide the design of new ILs. Without new force fields that permit exploration of the diverse range of potential ILs, the relevance of molecular simulations will wane.

Another major area where opportunities for improvement exist is the development of new methods to conduct long-time simulations. CG approach is a feasible way, and it uses large time step, thereby enabling larger systems to be simulated for long times. The development of an UA model for [$P_{6,6,6,14}$] cation and a CG model for [BMIM] cation at a higher level, as discussed in this contribution, is the typical example of this approach. It is noteworthy that the downside of CG methods is that there is an inevitable loss of some nonessential degrees of freedom at the level in which CGMD simulations are performed, and so these methods are best used when qualitative information is sought or when the desired properties are insensitive to these omitted degrees of freedom. It is shown that CG models tend to overestimate transport properties such as diffusivities. The dynamical inconsistency in CG models and its transferability are interesting topics for future research. New concepts,

theories and computational tools need to be developed in the future to make truly seamless multiscale modeling a reality.

Last but not least, collaborations between simulations and experiments are crucial in order to achieve the longstanding goal of predicting particle–structure–property relationship in material design and optimization of IL systems. It is the time to carry out sophisticated computational and experimental characterizations on these materials. What could be better?

Abbreviations

ACN	acetonitrile
AFM	atomic force microscope
AIMD	*ab initio* molecular dynamics
B	boron
BF_4	tetrafluoroborate
BMB	bis(mandelato)borate
BMIM	butylmethylimidazolium
BMLB	bis(malonato)borate
BOB	bis(oxalato)borate
BScB	bis(salicylato)borate
CG	coarse-grained
Cl	chloride
DFT	density functional theory
EAN	ethylammonium nitrate
EMIM	ethylmethylimidazolium
HB	hydrogen bonding
IBI	iterative Boltzmann inversion
IL	ionic liquid
LqE	low q excess
MMIM	dimethylimidazolium
MS	mass spectrometry
NI	Newton inversion
NMP	N-methyl-2-pyrrolidone
NO_3	nitrate
NTF_2	bis(trifluoromethanesulfonyl)imide
O	oxygen
P	phosphorus
$[P_{2,2,2,4}]$	triethylbutylphosphonium
$[P_{4,4,4,8}]$	tributyloctylphosphonium
$[P_{6,6,6,14}]$	trihexyltetradecylphosphonium
PF_6	hexafluorophosphate
PMF	potential of mean force
RDF	radial distribution function
SAXS	small-angle X-ray scattering
SCN	thiocyanate
SFA	surface force apparatus

SFG	sum frequency generation
TFO	trifluoromethylsulfonate
TGA	thermos gravimetric analysis
UA	united-atom
vdW	van der Waals

References

[1] R. Hayes, G. G. Warr, R. Atkin, Structure and Nanostructure in Ionic Liquids, *Chem. Rev.*, **115**, 6357–6426 (2015).

[2] H. Weingärtner, Understanding Ionic Liquids at the Molecular Level: Facts, Problems, and Controversies, *Angew. Chem. Int. Ed.*, **47**, 654–670 (2008).

[3] E. W. Castner Jr, C. J. Margulis, M. Maroncelli, J. F. Wishart, Ionic Liquids: Structure and Photochemical Reactions, *Annu. Rev. Phys. Chem.*, **62**, 85–105 (2011).

[4] P. Walden, Molecular Weights and Electrical Conductivity of Several Fused Salts, *Bull. Acad. Imper. Sci. (St. Petersburg)*, 1800 (1914).

[5] V. N. Emelyanenko, G. Boeck, S. P. Verevkin, R. Ludwig, Volatile Times for the Very First Ionic Liquid: Understanding the Vapor Pressures and Enthalpies of Vaporization of Ethylammonium Nitrate, *Chem. Eur. J.*, **20**, 11640–11645 (2014).

[6] F. H. Hurley, T. P. Wier, The Electrodeposition of Aluminum from Nonaqueous Solutions at Room Temperature, *J. Electrochem. Soc.*, **98**, 207–212 (1951).

[7] M. V. Fedorov, A. A. Kornyshev, Ionic Liquids at Electrified Interfaces, *Chem. Rev.*, **114**, 2978–3036 (2014).

[8] T. Welton, Room-Temperature Ionic Liquids. Solvents for Synthesis and Catalysis, *Chem. Rev.*, **99**, 2071–2084 (1999).

[9] J. S. Wilkes, M. J. Zaworotko, Air and Water Stable 1-Ethyl-3-methylimidazolium Based Ionic Liquids, *J. Chem. Soc., Chem. Commun.*, 965–967 (1992).

[10] J. S. Wilkes, A Short History of Ionic Liquids—From Molten Salts to Neoteric Solvents, *Green Chem.*, **4**, 73–80 (2002).

[11] Y. Chauvin, L. Mussmann, H. Olivier, A Novel Class of Versatile Solvents for Two-Phase Catalysis: Hydrogenation, Isomerization, and Hydroformylation of Alkenes Catalyzed by Rhodium Complexes in Liquid 1,3-Dialkylimidazolium Salts, *Angew. Chem. Int. Ed.*, **34**, 2698–2700 (1996).

[12] N. V. Plechkova, K. R. Seddon, Applications of Ionic Liquids in the Chemical Industry, *Chem. Soc. Rev.*, **37**, 123–150 (2008).

[13] R. J. Soukup-Hein, M. M. Warnke, D. W. Armstrong, Ionic Liquids in Analytical Chemistry, *Annu. Rev. Anal. Chem.*, **2**, 145–168 (2009).

[14] F. Zhou, Y. Liang, W. Liu, Ionic Liquid Lubricants: Designed Chemistry for Engineering Applications, *Chem. Soc. Rev.*, **38**, 2590–2599 (2009).

[15] I. Minami, Ionic Liquids in Tribology, *Molecules*, **14**, 2286–2305 (2009).

[16] J. F. Wishart, Energy Applications of Ionic Liquids, *Energy Environ. Sci.*, **2**, 956–961 (2009).

[17] H. Liu, Y. Liu, J. Li, Ionic Liquids in Surface Electrochemistry, *Phys. Chem. Chem. Phys.*, **12**, 1685–1697 (2010).

[18] J. P. Hallett, T. Welton, Room-Temperature Ionic Liquids: Solvents for Synthesis and Catalysis. 2, *Chem. Rev.*, **111**, 3508–3576 (2011).

[19] Z. Lei, C. Dai, B. Chen, Gas Solubility in Ionic Liquids, *Chem. Rev.*, **114**, 1289–1326 (2014).

[20] S. Zhang, J. Sun, X. Zhang, J. Xin, Q. Miao, J. Wang, Ionic Liquid-based Green Processes for Energy Production, *Chem. Soc. Rev.*, **43**, 7838–7869 (2014).
[21] D. R. MacFarlane, M. Forsyth, P. C. Howlett, M. Kar, S. Passerini, J. M. Pringle, H. Ohno, M. Watanabe, F. Yan, W. Zheng, Ionic Liquids and Their Solid-State Analogues as Materials for Energy Generation and Storage, *Nat. Rev. Mater.*, **1**, 15005 (2016).
[22] S. Zhang, N. Sun, X. He, X. Lu, X. Zhang, Physical Properties of Ionic Liquids: Database and Evaluation, *J. Phys. Chem. Ref. Data*, **35**, 1475–1517 (2006).
[23] H. Niedermeyer, J. P. Hallett, I. J. Villar-Garcia, P. A. Hunt, T. Welton, Mixtures of Ionic Liquids, *Chem. Soc. Rev.*, **41**, 7780–7802 (2012).
[24] J. de Andrade, E. S. Böes, H. Stassen, A Force Field for Liquid State Simulations on Room Temperature Molten Salts: 1-Ethyl-3-methylimidazolium Tetrachloroaluminate, *J. Phys. Chem. B*, **106**, 3546–3548 (2002).
[25] N. Wood, G. Stephens, Accelerating the Discovery of Biocompatible Ionic Liquids, *Phys. Chem. Chem. Phys.*, **12**, 1670–1674 (2010).
[26] R. Hayes, G. G. Warr, R. Atkin, At the Interface: Solvation and Designing Ionic Liquids, *Phys. Chem. Chem. Phys.*, **12**, 1709–1723 (2010).
[27] J. W. Lee, J. Y. Shin, Y. S. Chun, H. B. Jang, C. E. Song, S. G. Lee, Toward Understanding the Origin of Positive Effects of Ionic Liquids on Catalysis: Formation of More Reactive Catalysts and Stabilization of Reactive Intermediates and Transition States in Ionic Liquids, *Acc. Chem. Res.*, **43**, 985–994 (2010).
[28] X. Han, D. W. Armstrong, Ionic Liquids in Separations, *Acc. Chem. Res.*, **40**, 1079–1086 (2007).
[29] M. Armand, F. Endres, D. R. MacFarlane, H. Ohno, B. Scrosati, Ionic-Liquid Materials for the Electrochemical Challenges of the Future, *Nat. Mater.*, **8**, 621–629 (2009).
[30] C. Merlet, B. Rotenberg, P. A. Madden, M. Salanne, Computer Simulations of Ionic Liquids at Electrochemical Interfaces, *Phys. Chem. Chem. Phys.*, **15**, 15781–15792 (2013).
[31] B. Li, K. Ma, Y.-L. Wang, M. Turesson, C. E. Woodward, J. Forsman, Fused Coarse-Grained Model of Aromatic Ionic Liquids and Their Behaviour at Electrodes, *Phys. Chem. Chem. Phys.*, **18**, 8165–8173 (2016).
[32] A. E. Somers, P. C. Howlett, D. R. MacFarlane, M. Forsyth, A Review of Ionic Liquid Lubricants, *Lubricants*, **1**, 3–21 (2013).
[33] F. U. Shah, S. Glavatskih, D. R. MacFarlane, A. Somers, M. Forsyth, O. N. Antzutkin, Novel Halogen-Free Chelated Orthoborate-Phosphonium Ionic Liquids: Synthesis and Tribophysical Properties, *Phys. Chem. Chem. Phys.*, **13**, 12865–12873 (2011).
[34] C. Margulis, H. Stern, B. Berne, Computer Simulation of a "Green Chemistry" Room-Temperature Ionic Solvent, *J. Phys. Chem. B*, **106**, 12017–12021 (2002).
[35] Y. Wang, S. Izvekov, T. Yan, G. A. Voth, Multiscale Coarse-Graining of Ionic Liquids, *J. Phys. Chem. B*, **110**, 3564–3575 (2006).
[36] Y. Wang, S. Feng, G. A. Voth, Transferable Coarse-Grained Models for Ionic Liquids, *J. Chem. Theory Comput.*, **5**, 1091–1098 (2009).
[37] Y.-L. Wang, A. Lyubartsev, Z.-Y. Lu, A. Laaksonen, Multiscale Coarse-Grained Simulations of Ionic Liquids: Comparison of Three Approaches to Derive Effective Potentials, *Phys. Chem. Chem. Phys.*, **15**, 7701–7712 (2013).
[38] C. Spickermann, J. Thar, S. Lehmann, S. Zahn, J. Hunger, R. Buchner, P. Hunt, T. Welton, B. Kirchner, Why are Ionic Liquid Ions Mainly Associated in Water? A Car-Parrinello Study of 1-Ethyl-3-methyl-imidazolium Chloride Water Mixture, *J. Chem. Phys.*, **129**, 104505 (2008).
[39] Y.-L. Wang, Competitive Microstructures Versus Cooperative Dynamics of Hydrogen Bonding and π-Type Stacking Interactions in Imidazolium Bis(oxalato)borate Ionic Liquids, *J. Phys. Chem. B*, **122**, 6570–6585 (2018).

[40] P. A. Hunt, C. R. Ashworth, R. P. Matthews, Hydrogen Bonding in Ionic Liquids, *Chem. Soc. Rev.*, **44**, 1257–1288 (2015).
[41] B. Bhargava, S. Balasubramanian, M. L. Klein, Modelling Room Temperature Ionic Liquids, *Chem. Commun.*, 3339–3351 (2008).
[42] E. J. Maginn, Molecular Simulation of Ionic Liquids: Current Status and Future Opportunities, *J. Phys. Condens. Matter*, **21**, 373101 (2009).
[43] F. Dommert, J. Schmidt, C. Krekeler, Y. Y. Zhao, R. Berger, L. Delle Site, C. Holm, Towards Multiscale Modeling of Ionic Liquids: From Electronic Structure to Bulk Properties, *J. Mol. Liq.*, **152**, 2–8 (2010).
[44] K. Dong, X. Liu, H. Dong, X. Zhang, S. Zhang, Multiscale Studies on Ionic Liquids, *Chem. Rev.*, **117**, 6636–6695 (2017).
[45] M. Salanne, Simulations of Room Temperature Ionic Liquids: From Polarizable to Coarse-Grained Force Fields, *Phys. Chem. Chem. Phys.*, **17**, 14270–14279 (2015).
[46] J. G. McDaniel, E. Choi, C. Y. Son, J. Schmidt, A. Yethiraj, Ab Initio Force Fields for Imidazolium-Based Ionic Liquids, *J. Phys. Chem. B*, **120**, 7024–7036 (2016).
[47] G. Driver, Y. Huang, A. Laaksonen, T. Sparrman, Y.-L. Wang, P.-O. Westlund, Correlated/Non-correlated Ion Dynamics of Charge-Neutral Ion Couples: The Origin of Ionicity in Ionic Liquids, *Phys. Chem. Chem. Phys.*, **19**, 4975–4988 (2017).
[48] F. Mocci, A. Laaksonen, Y.-L. Wang, G. Saba, A. Lai, F. C. Marincola, CompChem and NMR Probing Ionic Liquids, *The Structure of Ionic Liquids*, Springer, 97–126 (2014).
[49] M. Brüssel, M. Brehm, A. S. Pensado, F. Malberg, M. Ramzan, A. Stark, B. Kirchner, On the Ideality of Binary Mixtures of Ionic Liquids, *Phys. Chem. Chem. Phys.*, **14**, 13204–13215 (2012).
[50] H. Weber, O. Hollóczki, A. S. Pensado, B. Kirchner, Side Chain Fluorination and Anion Effect on the Structure of 1-Butyl-3-methylimidazolium Ionic Liquids, *J. Chem. Phys.*, **139**, 084502 (2013).
[51] R. P. Matthews, T. Welton, P. A. Hunt, Hydrogen Bonding and π-π Interactions in Imidazolium-Chloride Ionic Liquid Clusters, *Phys. Chem. Chem. Phys.*, **17**, 14437–14453 (2015).
[52] J. N. Canongia Lopes, J. Deschamps, A. A. Pádua, Modeling Ionic Liquids Using a Systematic All-atom Force Field, *J. Phys. Chem. B*, **108**, 2038–2047 (2004).
[53] S. V. Sambasivarao, O. Acevedo, Development of OPLS-AA Force Field Parameters for 68 Unique Ionic Liquids, *J. Chem. Theory Comput.*, **5**, 1038–1050 (2009).
[54] Y. Wang, G. A. Voth, Tail Aggregation and Domain Diffusion in Ionic Liquids, *J. Phys. Chem. B*, **110**, 18601–18608 (2006).
[55] D. Roy, N. Patel, S. Conte, M. Maroncelli, Dynamics in an Idealized Ionic Liquid Model, *J. Phys. Chem. B*, **114**, 8410–8424 (2010).
[56] H. Lu, B. Li, S. Nordholm, C. E. Woodward, J. Forsman, Ion Pairing and Phase Behaviour of an Asymmetric Restricted Primitive Model of Ionic Liquids, *J. Chem. Phys.*, **145**, 234510 (2016).
[57] M. Golets, M. Shimpi, Y.-L. Wang, O. Antzutkin, S. Glavatskih, A. Laaksonen, Understanding the Thermal Decomposition Mechanism of a Halogen-Free Chelated Orthoborate-based Ionic Liquid: A Combined Computational and Experimental Study, *Phys. Chem. Chem. Phys.*, **18**, 22458–22466 (2016).
[58] C. Hanke, S. Price, R. Lynden-Bell, Intermolecular Potentials for Simulations of Liquid Imidazolium Salts, *Mol. Phys.*, **99**, 801–809 (2001).
[59] R. Lynden-Bell, N. Atamas, A. Vasilyuk, C. Hanke, Chemical Potentials of Water and Organic Solutes in Imidazolium Ionic Liquids: A Simulation Study, *Mol. Phys.*, **100**, 3225–3229 (2002).
[60] J. K. Shah, J. F. Brennecke, E. J. Maginn, Thermodynamic Properties of the Ionic Liquid 1-n-Butyl-3-methylimidazolium Hexafluorophosphate from Monte Carlo Simulations, *Green Chem.*, **4**, 112–118 (2002).
[61] T. I. Morrow, E. J. Maginn, Molecular Dynamics Study of the Ionic Liquid 1-n-Butyl-3-methylimidazolium Hexafluorophosphate, *J. Phys. Chem. B*, **106**, 12807–12813 (2002).

[62] B. Bhargava, S. Balasubramanian, Refined Potential Model for Atomistic Simulations of Ionic Liquid [BMIM][PF_6], *J. Chem. Phys*., **127**, 114510 (2007).
[63] F. Dommert, C. Holm, Refining Classical Force Fields for Ionic Liquids: Theory and Application to [MMIM][Cl], *Phys. Chem. Chem. Phys*., **15**, 2037–2049 (2013).
[64] X. Liu, S. Zhang, G. Zhou, G. Wu, X. Yuan, X. Yao, New Force Field for Molecular Simulation of Guanidinium-based Ionic Liquids, *J. Phys. Chem. B*, **110**, 12062–12071 (2006).
[65] J. de Andrade, E. S. Böes, H. Stassen, Computational Study of Room Temperature Molten Salts Composed by 1-Alkyl-3-methylimidazolium Cations Force-Field Proposal and Validation, *J. Phys. Chem. B*, **106**, 13344–13351 (2002).
[66] Z. Liu, S. Huang, W. Wang, A Refined Force Field for Molecular Simulation of Imidazolium-based Ionic Liquids, *J. Phys. Chem. B*, **108**, 12978–12989 (2004).
[67] J. N. Canongia Lopes, A. A. Pádua, Molecular Force Field for Ionic Liquids Composed of Triflate or Bistriflylimide Anions, *J. Phys. Chem. B*, **108**, 16893–16898 (2004).
[68] X. Liu, Y. Zhao, X. Zhang, G. Zhou, S. Zhang, Microstructures and Interaction Analyses of Phosphonium-based Ionic Liquids: A Simulation Study, *J. Phys. Chem. B*, **116**, 4934–4942 (2012).
[69] J. N. Canongia Lopes, A. A. Pádua, K. Shimizu, Molecular Force Field for Ionic Liquids IV: Trialkylimidazolium and Alkoxycarbonyl-imidazolium Cations; Alkylsulfonate and Alkylsulfate Anions, *J. Phys. Chem. B*, **112**, 5039–5046 (2008).
[70] Y.-L. Wang, F. U. Shah, S. Glavatskih, O. N. Antzutkin, A. Laaksonen, Atomistic Insight into Orthoborate-based Ionic Liquids: Force Field Development and Evaluation, *J. Phys. Chem. B*, **118**, 8711–8723 (2014).
[71] G. Xie, J. Luo, D. Guo, S. Liu, Nanoconfined Ionic Liquids Under Electric Fields, *App. Phys. Lett*., **96**, 043112 (2010).
[72] K. Fumino, A. Wulf, R. Ludwig, Strong, Localized, and Directional Hydrogen Bonds Fluidize Ionic Liquids, *Angew. Chem. Int. Ed*., **47**, 8731–8734 (2008).
[73] S. Zahn, G. Bruns, J. Thar, B. Kirchner, What Keeps Ionic Liquids in Flow?, *Phys. Chem. Chem. Phys*., **10**, 6921–6924 (2008).
[74] Y.-L. Wang, S. Sarman, S. Glavatskih, O. N. Antzutkin, M. W. Rutland, A. Laaksonen, Atomistic Insight into Tetraalkylphosphonium-bis(oxalato)borate Ionic Liquid/Water Mixtures. I. Local Microscopic Structure, *J. Phys. Chem. B*, **119**, 5251-5264 (2015).
[75] Y.-L. Wang, M. R. Shimpi, S. Sarman, O. N. Antzutkin, S. Glavatskih, L. Kloo, A. Laaksonen, Atomistic Insight into Tetraalkylphosphonium Bis(oxalato)borate Ionic Liquid/Water Mixtures. 2. Volumetric and Dynamic Properties, *J. Phys. Chem. B*, **120**, 7446–7455 (2016).
[76] Y.-L. Wang, S. Sarman, L. Kloo, O. N. Antzutkin, S. Glavatskih, A. Laaksonen, Solvation Structures of Water in Trihexyltetradecylphosphonium-Orthoborate Ionic Liquids, *J. Chem. Phys*., **145**, 064507 (2016).
[77] Y.-L. Wang, A. Laaksonen, D. M. Fayer, Hydrogen Bonding versus π-π Stacking Interactions in Imidazolium-Oxalatoborate Ionic Liquid, *J. Phys. Chem. B*, **121**, 7173–7179 (2017).
[78] P. Nockemann, K. Binnemans, K. Driesen, Purification of Imidazolium Ionic Liquids for Spectroscopic Applications, *Chem. Phys. Lett*., **415**, 131–136 (2005).
[79] M. Usula, F. Mocci, F. C. Marincola, S. Porcedda, L. Gontrani, R. Caminiti, The Structural Organization of N-methyl-2-pyrrolidone+Water Mixtures: A densitometry, X-ray Diffraction, and Molecular Dynamics Study, *J. Chem. Phys*., **140**, 124503 (2014).
[80] H. Ohno, K. Fujita, Y. Kohno, Is Seven the Minimum Number of Water Molecules Per Ion Pair for Sssured Biological Activity in Ionic Liquid-Water Mixtures?, *Phys. Chem. Chem. Phys*., **17**, 14454–14460 (2015).
[81] M. Usula, S. Porcedda, F. Mocci, L. Gontrani, R. Caminiti, F. Cesare Marincola, NMR, Calorimetry, and Computational Studies of Aqueous Solutions of N-methyl-2-pyrrolidone, *J. Phys. Chem. B*, **118**, 10493–10502 (2014).

[82] W. Shi, K. Damodaran, H. B. Nulwala, D. R. Luebke, Theoretical and Experimental Studies of Water Interaction in Acetate Based Ionic Liquids, *Phys. Chem. Chem. Phys*., **14**, 15897–15908 (2012).
[83] O. Borodin, W. A. Henderson, E. T. Fox, M. Berman, M. Gobet, S. Greenbaum, Influence of Solvent on Ion Aggregation and Transport in PY_{15}TFSI Ionic Liquid-Aprotic Solvent Mixtures, *J. Phys. Chem. B*, **117**, 10581–10588 (2013).
[84] H. E. Bailey, Y.-L. Wang, M. D. Fayer, The Influence of Hydrophilicity on the Orientational Dynamics and Structures of Imidazolium-based Ionic Liquid/Water Binary Mixtures, *J. Chem. Phys*., **149**, 044501 (2018).
[85] M. Moreno, F. Castiglione, A. Mele, C. Pasqui, G. Raos, Interaction of Water with the Model Ionic Liquid [BMIM][BF_4]: Molecular Dynamics Simulations and Comparison with NMR Data, *J. Phys. Chem. B*, **112**, 7826–7836 (2008).
[86] H. E. Bailey, Y.-L. Wang, M. D. Fayer, The Impact of Hydrogen Bonding on the Dynamics and Structure of Protic Ionic Liquid/Water Binary Mixtures, *J. Phys. Chem. B*, **121**, 8564–8576 (2017).
[87] S. Baldelli, Surface Structure at the Ionic Liquid-Electrified Metal Interface, *Acc. Chem. Res*., **41**, 421–431 (2008).
[88] K. R. Lovelock, Influence of the Ionic Liquid/Gas Surface on Ionic Liquid Chemistry, *Phys. Chem. Chem. Phys*., **14**, 5071–5089 (2012).
[89] C. S. Santos, S. Baldelli, Gas-Liquid Interface of Room-Temperature Ionic Liquids, *Chem. Soc. Rev*., **39**, 2136–2145 (2010).
[90] C. Romero, H. J. Moore, T. R. Lee, S. Baldelli, Orientation of 1-Butyl-3-methylimidazolium Based Ionic Liquids at a Hydrophobic Quartz Interface Using Sum Frequency Generation Spectroscopy, *J. Phys. Chem. C*, **111**, 240–247 (2007).
[91] S. Chen, Y. Liu, H. Fu, Y. He, C. Li, W. Huang, Z. Jiang, G. Wu, Unravelling the Role of the Compressed Gas on Melting Point of Liquid Confined in Nanospace, *J. Phys. Chem. Lett*., **3**, 1052–1055 (2012).
[92] J. B. Rollins, B. D. Fitchett, J. C. Conboy, Structure and Orientation of the Imidazolium Cation at the Room-Temperature Ionic Liquid/SiO_2 Interface Measured by Sum-Frequency Vibrational Spectroscopy, *J. Phys. Chem. B*, 111, 4990–4999 (2007).
[93] M. R. Castillo, J. M. Fraile, J. A. Mayoral, Structure and Dynamics of 1-Butyl-3-methylimidazolium Hexafluorophosphate Phases on Silica and Laponite Clay: From Liquid to Solid Behavior, *Langmuir*, **28**, 11364–11375 (2012).
[94] T. J. Gannon, G. Law, P. R. Watson, A. J. Carmichael, K. R. Seddon, First Observation of Molecular Composition and Orientation at the Surface of a Room-Temperature Ionic Liquid, *Langmuir*, **15**, 8429–8434 (1999).
[95] Y. Jeon, J. Sung, W. Bu, D. Vaknin, Y. Ouchi, D. Kim, Interfacial Restructuring of Ionic Liquids Determined by Sum-Frequency Generation Spectroscopy and X-Ray Reflectivity, *J. Phys. Chem. C*, **112**, 19649–19654 (2008).
[96] S. Rivera-Rubero, S. Baldelli, Influence of Water on the Surface of Hydrophilic and Hydrophobic Room-Temperature Ionic Liquids, *J. Am. Chem. Soc*., **126**, 11788–11789 (2004).
[97] A. Ohno, H. Hashimoto, K. Nakajima, M. Suzuki, K. Kimura, Observation of Surface Structure of 1-Butyl-3-methylimidazolium Hexafluorophosphate Using High-Resolution Rutherford Backscattering Spectroscopy, *J. Chem. Phys*., **130**, 204705 (2009).
[98] E. Sloutskin, B. M. Ocko, L. Tamam, I. Kuzmenko, T. Gog, M. Deutsch, Surface Layering in Ionic Liquids: An X-Ray Reflectivity Study, *J. Am. Chem. Soc*., **127**, 7796–7804 (2005).
[99] Y.-L. Wang, A. Laaksonen, Z.-Y. Lu, Influence of Ionic Liquid Film Thickness on Ion Pair Distributions and Orientations at Graphene and Vacuum Interfaces, *Phys. Chem. Chem. Phys*., **15**, 13559–13569 (2013).

[100] Y.-L. Wang, Z.-Y. Lu, A. Laaksonen, Heterogeneous Dynamics of Ionic Liquids in Confined Films with Varied Film Thickness, *Phys. Chem. Chem. Phys*., **16**, 20731–20740 (2014).
[101] S. Bovio, A. Podesta, P. Milani, P. Ballone, M. Del Pópolo, Nanometric Ionic-Liquid Films on Silica: A Joint Experimental and Computational Study, *J. Phys.: Condens. Matter*, **21**, 424118 (2009).
[102] M. P. Singh, R. K. Singh, S. Chandra, Studies on Imidazolium-Based Ionic Liquids Having A Large Anion Confined in a Nanoporous Silica Gel Matrix, *J. Phys. Chem. B*, **115**, 7505–7514 (2011).
[103] Y.-L. Wang, A. Laaksonen, Interfacial Structure and Orientation of Confined Ionic Liquids on Charged Quartz Surfaces, *Phys. Chem. Chem. Phys*., **16**, 23329–23339 (2014).
[104] Y.-X. Zhong, J.-W. Yan, M.-G. Li, X. Zhang, D.-W. He, B.-W. Mao, Resolving Fine Structures of the Electric Double Layer of Electrochemical Interfaces in Ionic Liquids with an AFM Tip Modification Strategy, *J. Am. Chem. Soc*., **136**, 14682–14685 (2014).
[105] H. Li, R. J. Wood, M. W. Rutland, R. Atkin, An Ionic Liquid Lubricant Enables Superlubricity to be "switched on" in situ Using an Electrical Potential, *Chem. Commun*., **50**, 4368–4370 (2014).
[106] A. M. Smith, K. R. Lovelock, N. N. Gosvami, P. Licence, A. Dolan, T. Welton, S. Perkin, Monolayer to Bilayer Structural Transition in Confined Pyrrolidinium-Based Ionic Liquids, *J. Phys. Chem. Lett*., **4**, 378–382 (2013).
[107] A. M. Smith, M. A. Parkes, S. Perkin, Molecular Friction Mechanisms Across Nanofilms of a Bilayer-Forming Ionic Liquid, *J. Phys. Chem. Lett*., **5**, 4032–4037 (2014).
[108] J. Wu, X. Lu, X. Feng, Y. Shi, Halogen-Free Ionic Liquids as Excellent Lubricants for PEEK-Stainless Steel Contacts at Elevated Temperatures, *Tribol. Int*., **104**, 1–9 2016).
[109] Y.-L. Wang, M. Golets, B. Li, S. Sarman, A. Laaksonen, Interfacial Structures of Trihexyltetradecylphosphonium-Bis(mandelato)borate Ionic Liquid Confined between Gold Electrodes, *ACS App. Mater. Interfaces*, **9**, 4976–4987 (2017).
[110] D. Evans, G. P. Morriss, Statistical Mechanics of Nonequilibrium Liquids, *Cambridge University Press* (2008).
[111] S. Sarman, Y.-L. Wang, A. Laaksonen, Non-Newtonian Rheological Properties of Shearing Nematic Liquid Crystal Model Systems Based on the Gay-Berne Potential, *Phys. Chem. Chem. Phys*., **17**, 16615–16623 (2015).
[112] S. Sarman, Y.-L. Wang, A. Laaksonen, Self-Diffusion in the Non-Newtonian Regime of Shearing Liquid Crystal Model Systems Based on the Gay-Berne potential, *J. Chem. Phys*., **144**, 054901 (2016).
[113] S. Sarman, Y.-L. Wang, A. Laaksonen, Thermomechanical Coupling in Coarse Grained Cholesteric Liquid Crystal Model Systems with Pitches of Realistic Length, *Phys. Chem. Chem. Phys*., **18**, 16822–16829 (2016).
[114] O. Borodin, Polarizable Force Field Development and Molecular Dynamics Simulations of Ionic Liquids, *J. Phys. Chem. B*, **113**, 11463–11478 (2009).
[115] R. Ishizuka, N. Matubayasi, Self-Consistent Determination of Atomic Charges of Ionic Liquid through a Combination of Molecular Dynamics Simulation and Density Functional Theory, *J. Chem. Theory Comput*., **12**, 804–811 (2016).
[116] S. Sarman, Y.-L. Wang, P. Rohlmann, S. Glavatskih, A. Laaksonen, Rheology of Phosphonium Ionic Liquids: A Molecular Dynamics and Experimental Study, *Phys. Chem. Chem. Phys*, **20**, 10193–10203 (2018).
[117] M. Usula, E. Matteoli, F. Leonelli, F. Mocci, F. C. Marincola, L. Gontrani, S. Porcedda, Thermo-Physical Properties of Ammonium-Based Ionic Liquid + N-methyl-2-pyrrolidone Mixtures at 298.15 K, *Fluid Phase Equilib*., **383**, 49–54 (2014).
[118] A. Mariani, R. Caminiti, F. Ramondo, G. Salvitti, F. Mocci, L. Gontrani, Inhomogeneity in Ethylammonium Nitrate-Acetonitrile Binary Mixtures: The Highest "Low q Excess" Reported to Date, *J. Phys. Chem. Lett*., **8**, 3512–3522 (2017).

[119] H. J. Jiang, P. A. FitzGerald, A. Dolan, R. Atkin, G. G. Warr, Amphiphilic Self-assembly of Alkanols in Protic Ionic Liquids, *J. Phys. Chem. B*, **118**, 9983–9990 (2014).
[120] O. Russina, A. Sferrazza, R. Caminiti, A. Triolo, Amphiphile Meets Amphiphile: Beyond the Polar-Apolar Dualism in Ionic Liquid/Alcohol Mixtures, *J. Phys. Chem. Lett.*, **5**, 1738–1742 (2014).
[121] A. Mariani, R. Dattani, R. Caminiti, L. Gontrani, Nanoscale Density Fluctuations in Ionic Liquid Binary Mixtures with Nonamphiphilic Compounds: First Experimental Evidence, *J. Phys. Chem. B*, **120**, 10540–10546 (2016).
[122] J. Wang, R. M. Wolf, J. W. Caldwell, P. A. Kollman, D. A. Case, Development and Testing of a General Amber Force Field, *J. Comput. Chem.*, **25**, 1157–1174 (2004).
[123] H. K. Kashyap, C. S. Santos, H. V. Annapureddy, N. S. Murthy, C. J. Margulis, E. W. Castner, Jr, Temperature-Dependent Structure of Ionic Liquids: X-Ray Scattering and Simulations, *Faraday Discuss.*, **154**, 133–143 (2012).
[124] H. K. Kashyap, C. S. Santos, R. P. Daly, J. J. Hettige, N. S. Murthy, H. Shirota, E. W. Castner Jr, C. J. Margulis, How Does the Ionic Liquid Organizational Landscape Change When Nonpolar Cationic Alkyl Groups Are Replaced by Polar Isoelectronic Diethers? *J. Phys. Chem. B*, **117**, 1130–1135 (2013).
[125] Y. Wang, G. A. Voth, Unique Spatial Heterogeneity in Ionic Liquids, *J. Am. Chem. Soc.*, **127**, 12192–12193 (2005).
[126] A. Triolo, O. Russina, H.-J. Bleif, E. Di Cola, Nanoscale Segregation in Room Temperature Ionic Liquids, *J. Phys. Chem. B*, **111**, 4641–4644 (2007).
[127] H. V. Annapureddy, H. K. Kashyap, P. M. De Biase, C. J. Margulis, What is the Origin of the Prepeak in the X-Ray Scattering of Imidazolium-Based Room-Temperature Ionic Liquids?, *J. Phys. Chem. B*, **114**, 16838–16846 (2010).
[128] J. N. Marták, S. T. Schlosser, New Mechanism and Model of Butyric Acid Extraction by Phosphonium Ionic Liquid, *J. Chem. Eng. Data*, **61**, 2979–2996 (2016).
[129] Y.-L. Wang, S. Sarman, B. Li, A. Laaksonen, Multiscale Modeling of the Trihexyltetradecylphosphonium Chloride Ionic Liquid, *Phys. Chem. Chem. Phys.*, **17**, 22125–22135 (2015).
[130] J. J. Hettige, J. C. Araque, H. K. Kashyap, C. J. Margulis, Communication: Nanoscale Structure of Tetradecyltrihexylphosphonium Based Ionic Liquids, *J. Chem. Phys.*, **144**, 121102 (2016).
[131] Y.-L. Wang, B. Li, S. Sarman, A. Laaksonen, Microstructures and Dynamics of Tetraalkylphosphonium Chloride Ionic Liquids, *J. Chem. Phys.*, **147**, 224502 (2017).
[132] K. A. Maerzke, J. I. Siepmann, Transferable Potentials for Phase Equilibria–Coarse-Grain Description for Linear Alkanes, J. *Phys. Chem. B*, **115**, 3452–3465 (2011).
[133] Y.-L. Wang, Y.-L. Zhu, Z.-Y. Lu, A. Laaksonen, Electrostatic Interactions in Soft Particle Systems: Mesoscale Simulations of Ionic Liquids, *Soft Matter*, **14**, 4252–4267 (2018).
[134] H. A. Karimi-Varzaneh, F. Müller-Plathe, S. Balasubramanian, P. Carbone, Studying Long-Time Dynamics of Imidazolium-based Ionic Liquids with a Systematically Coarse-Grained Model, *Phys. Chem. Chem. Phys.*, **12**, 4714–4724 (2010).
[135] A. Lyubartsev, A. Mirzoev, L. Chen, A. Laaksonen, Systematic Coarse-Graining of Molecular Models by the Newton Inversion Method, *Faraday Discuss.*, **144**, 43–56 (2010).
[136] Y.-L. Wang, A. Laaksonen, Z.-Y. Lu, Implementation of Non-Uniform FFT Based Ewald Summation in Dissipartive Particle Dynamics Method, *J. Comput. Phys.*, **235**, 666–682 (2013).
[137] Y.-L. Wang, F. Hedman, M. Porcu, F. Mocci, A. Laaksonen, Non-Uniform FFT and Its Applications in Particle Simulations, *Applied Mathematics*, **5**, 520–541 (2014).
[138] S.-C. Yang, Y.-L. Wang, G.-S. Jiao, H.-J. Qian, Z.-Y. Lu, Accelerating Electrostatic Interaction Calculations with Graphical Processing Units based on New Developments of Ewald Method Using Non-Uniform Fast Fourier Transform, *J. Comput. Chem.*, **37**, 378–387 (2016).

Renata Costa, Carlos M. Pereira, A. Fernando Silva

5 Ionic liquids at electrified interfaces for advanced energy/charge storage applications

Abstract: Energy storage topic becomes a critical element for smart grids to meet the goals of smart cities in supporting a sustainable energy management. The improvement of energy storage systems would be a milestone in the advancement and promotion of several technologies associated with a low carbon emission future: for instance, hybrid vehicles, renewable energy generation and distribution. One of the highest priorities in the European policy funding is focused on scientific and technological research accomplishments in the field of inventive energy storage solutions such as electric double-layer capacitors (EDLCs). The design and development of new energy/charge storage ionic liquid (IL)-based devices requires a deep understanding of the mechanisms governing the formation of the electric double layer between electrodes and IL electrolytes. This is far from being accomplished and more experimental evidence is required. It is known that the capacitive performance of electrochemical devices is greatly affected by the ion concentration profile at the electrode/electrolyte interface. IL mixtures associated with high surface area carbon materials begin to gain strength as a promising strategy to tune EDLC performance in charging/discharging processes (by controlling the ion concentration profile of the electrolyte near the electrode surface, surface roughness, temperature, among other factors).

Keywords: Electric double layer, Ionic liquids, Differential capacitance, Energy storage, Ionic Liquid/electrode interface, Temperature effect

5.1 Introduction

Human progress is dependent on the ubiquitous, unique and valuable resource – energy. The world's economy is driven by energy. Is energy the resource we still need most in the future? Should energy and sustainability be two concepts that should be balanced up [1, 2]? What can contribute scientific research for these two paradigms? The sustainability of energy supply has been one of the great challenges of our time to minimize the impact on the depletion of resources, and severe environmental effects resulted from the continuous use of fossil fuels [3, 4]. The changes required for the transition from an economy mainly focused on nonrenewable fuel source to one

Renata Costa, Carlos M. Pereira, A. Fernando Silva, Departamento de Química e Bioquímica, Universidade do Porto, Portugal

https://doi.org/10.1515/9783110583632-005

taking advantage of greener and sustainable energy resources will require significant scientific research, accompanied by the development of more efficient engineering systems, environmental-friendly approaches of chemical processes and the pursuit of sustainable energy policies [5, 6]. A symbiotic relationship between green chemistry and renewable energy is highly desirable not only in designing energy-efficient efforts, materials and chemical systems but also in harvesting those renewable energies [7].

Sources of renewable energy such as solar or the wind have an inherent problem because of their intermittent nature and their availability rarely matches the needs of the network [8, 9]. In order to use the unequivocal contribution of these energy sources to the sustainability of the energetic system, it is necessary to implement energy storage systems that can store and deliver the energy when required by the grid [10–13]. Albeit these procedures have been effectively accomplished with batteries on a low-power scale, new approaches for increasing the efficiency boost will require large amounts of power that can only be provided by alternative energy storage technologies such as supercapacitors [14, 15]. Thus, it is imperative to develop more efficient and diversified energy storage and distribution systems that meet multiple requirements, namely, transportation and grid storage will have strong commercial prospects. High charge and discharge rates, longer life cycles, reduced cost per cycle, the use of low toxicity and thermostable materials for both onboard and stationary applications make them a lucrative option as energy storage devices [16]. A recent trend is to integrate and optimize the performance of supercapacitors using ionic liquids (ILs) and IL mixtures. A demonstration of the relevance of this path shows the increase in research and scientific publications in these fields (Figure 5.1).

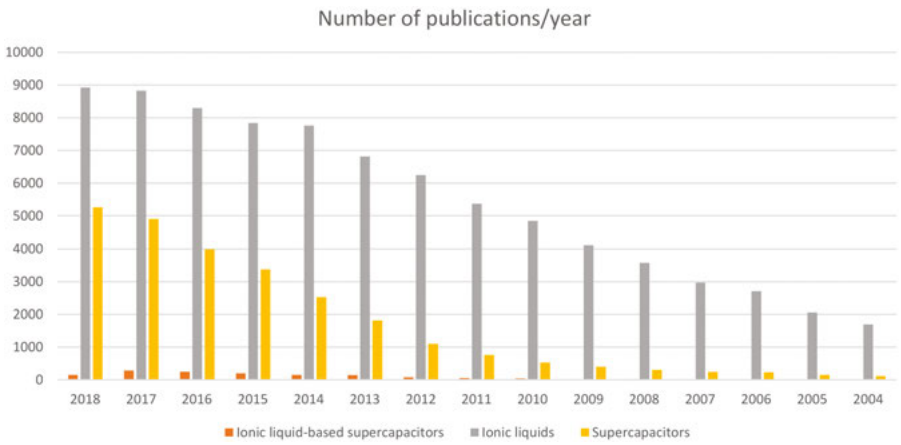

Figure 5.1: Number of peer-reviewed scientific publications in the field of supercapacitors, ionic liquids and in ionic liquid-based supercapacitors. Information gathered from the Web of Sciences.

The number of publications in supercapacitors and ILs follows a similar trend, although the number of registered publications under the thematic of "supercapacitors" is half the

number of publications that mention the subject of "ILs." However in a more modest number the publications that deal with "ILs" and "supercapacitors" have a continuous increase and have observed a 20-fold increase in the last 10 years (compared with a threefold increase in the number of papers dealing with "ILs").

5.1.1 Supercapacitors market forecast

In the last decade, the market for new energy and innovative storage solutions has been treated with increased attention. Suitable energy storage devices are core elements for highly required environmental-friendly and reliable resources for an appropriate response to the high energy demand (low carbon emission sustainable economy present in the EU 2020 policy targets). Industry forecasts and investments suggest that the future looks solid niche market potential in the field of supercapacitors, even in an unpredictable and unstable economy. The global supercapacitor market is segmented into consumer electronics (laptops, digital cameras, portable speakers and mobile computing), industrial automation (memory storage, uninterrupted power supply and automatic meter reading), power and energy (actuators, wind turbines and photovoltaic), medical (defibrillators), transport (trains, cranes, cars, buses, elevators, aircraft and hybrid electric vehicles) and robotics (autonomy) [16].

Supercapacitor sales are expected to more than double over the next five years, and automotive industry is permanent investing in supercapacitor research. The interest is even higher with the possibility of combining a fuel cell with a supercapacitor, which is more expensive than a battery but has a much longer life cycle and an extremely high power capacity providing higher stability, efficiency and reliability. Interestingly, new trends on future consumer electronics and portable devices (with $86 billion market by 2023) point out that they are becoming increasingly thinner and more power-demanding [17].

According to a new report published by Future Market Insights, the supercapacitor market is anticipated to increase over 20% annual growth rate (CAGR) for the next 10 years (2016–2026), with the supercapacitor market expected to worth $2.10 billion by 2020 (research report "Supercapacitor Market by Materials – Analysis & Forecast").

The number of companies dedicated to the production of supercapacitors and batteries has doubled in the last few years. Some companies had increased their production to 30% and others are also tripling their production capacity. The target market sharply increases when supercapacitors are also considered as supporting role, for example in conjunction with batteries and fuel-cell devices to enhance their performance and lifetime (hybrid devices). The remarkable market growth requires the reinforcement accompanied by a prompt improvement in energy and power density capability, in the available devices following the trend to lower its costs [18].

5.1.2 IL market forecast

The application of solvent-free electrolytes such as ILs to double-layer capacitors development may become a promising strategy to overcome some unsolved key challenges such as the quick charge drop when compared with conventional batteries. Since IL-based technologies are in the embryonic stage of development, the IL market global forecast is very large and promising, crossing various industrial sectors due to its capability for sustainable replacement of traditional organic solvents.

At 2016, Frost and Sullivan analysts estimated that the IL market has an estimated value of $1.3 billion dollars and in 2020 the market growth is expected to double to $2.77 billion dollars due to the IL expansion/global demand and eco-friendliness strategies (Frost and Sullivan, Technology Advancements in Ionic Liquids (TechVision), 2016).

Although there is a great opportunity to market the implementation on a large scale of ILs as promising solvents in energy storage devices, it is important to anticipate some economic and technical obstacles. A technoeconomic analysis was carried out to understand the cost drivers, economic potential and relative merits as well as challenges of each route.

- Capital requirements: Scientific progress and technological advances are important drivers of economic performance and require high capital investment and highly skilled researchers.
- The fast implementation of recent scientific advances to new products and processes.
- Barriers to entry new products into the market: legislation, patents, rights, safety, health, environmental data and so on.
- The interaction between science and industry varies greatly from country to country and the industrial research interests are not always in line with the R&D conducted in the academic environment.
- Being a very fast evolving area, the results emerged from the academia can be obsolete in a short time (before upscaling).
- A decrease in market demand: High product offer in the market.
- Cost and availability of ILs: To overcome this issue the synthesis processes should be redesigned based on a low-cost deconstruction process, thus taking advantage of the highly tunable properties of ILs.
- Stability of ILs in the final product: Failure in the scale-up, for example, the performance achieved in the fundamental research can be lost in the upscaling process.
- Compatibility of ILs with standard materials commonly used in niche application sectors.
- Cost upscaling from the laboratory to industrial scale: Long-term durability and costs represent barriers to upscaling from laboratory science to the next level of technological maturity and ultimately its introduction into the market.

Consequ-ently, the focus on improved materials processing could mean a breakthrough in the tailored structure of materials, enhancing its performance on energy storage devices that would dramatically decrease their costs.
- Manufacturing: Complex synthesis processes and difficulties in incorporating the ILs sensitive to air moisture.
- Recovery and recycling: Although small amounts of ILs will be used, a large-scale use of such devices will generate residues that recovery and recycling has to be considered [19].
- Some of the ILs ecotoxicity is not known, thus the increase in the biodegradability of ILs must be "built-in" in its design stage [20, 21].
- Technoeconomic risk: Threat of substitutes (the appearance in the market of a new technology with better prices and better performance that could put in risk the product). The commercial challenges are to orient the research centered on the fundamental applied understanding of the IL structure to its performance. The achievement of such goal is crucially dependent on the understanding of ILs behavior at charged surfaces and from a business perspective point of view includes the development of cheaper ILs through the redesign of synthetic pathways, fundamental versus applied research strategic lines, IL standardization and explicit IL-oriented products to business benefits.

5.2 IL application in electric double-layer capacitors

5.2.1 Revisit the recent past

Supercapacitors are high-power energy storage devices through fast surface processes based on the ion adsorption from the electrolyte (electric double-layer capacitors – EDLCs) or based on fast surface redox reactions (pseudocapacitors) by means of an electrolyte solution between two solid conductors [22–24]. The conventional EDLCs have operative voltages in the range of 2.3–2.7 V. The energy (E) stored within a supercapacitor is given by eq. (1), and the stored energy is proportional to both the capacitance of the device and the square of the cell potential:

$$E = \frac{1}{2} CV^2 \tag{5.1}$$

where E is the energy (J), C the capacitance (F) and V the cell voltage (V) [25].

Supercapacitors can be charged and discharged within seconds, displaying high power (up to 10 kW kg^{-1}) [26]. Supercapacitor devices include also a subtype of hybrid capacitors composed of a combination of an EDLC electrode with a pseudocapacitive or

battery joint electrode [27]. Generally, this setting allows an intermediate performance by combining the properties of both systems.

Table 5.1 summarizes and compares the characteristics estimated for supercapacitors and batteries.

Table 5.1: Comparison table between energy storage technologies: supercapacitors versus batteries.

Characteristics	Supercapacitor	Battery
Specific energy (W h kg^{-1})	1–10	10–100
Specific power (W kg^{-1})	500–10,000	<1,000
Discharge time	Seconds to minutes	0.3–3 h
Charge time	Seconds to minutes	1–5 h
Coulombic efficiency (%)	85–98	70–85
Life cycle	>500,000	About 1,000
Storage mechanism	Physical	Chemical
Power limitation	Electrolyte conductivity	Reaction kinetics, mass transport
Energy storage	Limited (surface area)	High (bulk)
Charge rate	High, same as discharge	Kinetically limited
Life cycle limitations	Side reactions	Mechanical stability, chemical reversibility

Adapted from Pandolfo and Hollenkamp [28], Miller and Simon [29].

This chapter focuses on double-layer capacitors, namely, in the mechanisms of formation of electric double-layer (EDL) structure at electrode/electrolyte (ILs) interface. In addition, the progress toward mechanisms, new materials and novel device designs requires the fundamental understanding of the mechanism centered on the relationship between the structural properties of electrolyte versus electrode materials and its impact on the interfacial properties such as the differential capacitance versus applied potential dependence.

Double-layer concept was first described in 1853 by a German physicist Helmholtz. The energy stored in double-layer capacitors is predominantly electrostatic in nature, and the differential capacitance of an EDL can be calculated as follows [25, 30]:

$$C = \frac{\varepsilon_r \varepsilon_0 A}{d} \tag{5.2}$$

where ε_r represents the dielectric constant of the electrolyte, ε_0 the permittivity of free space, A the area of the electrode and d the thickness of the layer. Subsequently, many authors have introduced the concept to improve the differential capacitance model taking into consideration the dependence on the ionic concentration and applied potential (Gouy–Chapman); however, the double layer would not be compact as described by Helmholtz, but of varying thickness – the ions being free to move (diffuse model). However, the model still present marked limitations since the model does not consider the polarizability of the ions and fails for highly charged double layers [25, 31]. Subsequently, Stern introduced

modifications to the theory of Gouy–Chapman, redefining the Helmholtz layer as the plane of maximum approximation of the ions – internal Stern layer. One of the limitations of this model is not to consider ion-specific adsorption phenomena [32]. Grahame et al. [33] and Whitney et al. [34] proposed a new model for the structure of the solution-side interface designated as the triple-layer model.

It would be foreseen that the metal/salt interface would provide a simpler model compared to aqueous electrolytic solutions due to the absence of solvent molecules; however, authors quickly realized that this was not the case. Although complex formulas have been deduced for the calculation of the double-layer capacitance in molten salt systems, the analytical models emerged do not describe yet accurately the experimental results, in particular, differential capacitance as a function of temperature [35]. The challenges in modeling such systems are closely related to the difficulty in assessing the interfacial properties that are extremely difficult to obtain experimentally.

For this reason, ILs with low melting points that remain in the liquid state at room temperature motivated a noticeable increase in interest in the scientific community. The requirement for development of an analytical model to describe ILs at charged surfaces become even more fundamental since any application would be dependent on its knowledge and understanding.

The interfacial capacitance of the first metal/IL model was presented in the Kornyshev seminal paper in 2007 [36]. The author concluded that the Gouy–Chapman–Stern model did not predict the maximum observed in the differential capacitance for dense ionic regimes and developed a model that took into account constraints imposed by the packaging of ions. The authors derived an analytical expression to describe the differential capacitance of IL-containing spherical ions considering the compressibility of the liquid and the volume occupied by the ions at the electrode. The shape of the differential capacitance was found to shift from camel shape ($y = 0.1$) to bell shape with the increase in the incompressibility of liquids ($y = 1$); for example, at this stage it is expected that the free voids in the liquid no longer exist. In 2016 the model was improved by adding "short-range correlation terms" in the free energy function [37].

Revisiting previous Kornyshev [36] and Fedorov et al.'s [38, 39] works, important conclusions were drawn by the prediction of U-shaped differential capacitance curves when small exclusion volume was considered allowing a more efficient packaging of the ions at the surface as the applied potential rises. Another important conclusion was for crowd regimes, for example, if the electrode surface becomes saturated with the ions, the volume exclusion effects decrease in capacitance values. Monte Carlo simulations for a dense set of Lennard–Jones spheres between charged interfaces also foreseen "camel shape" differential capacitance curves considering size of different anions and cations. Asymmetric "camel shape" profile for ions of equal size can also be obtained, however, for ions with different specific affinities to the electrode surface [40].

Many authors have also been dedicated to modeling the double-layer structure in particular with computational simulations to infer the profile of the capacitance curves and to determine the structure of the electrode/IL interface. The simulations also focused on the importance of the specific adsorption effects.

Experimental studies in parallel with theoretical studies have made it possible to considerable and important progress in understanding the effect of small modifications of the ion structure in the interfacial behavior of ILs.

The differential capacitance is of great interest in terms of physical chemistry since dQ/dV is the instantaneous capacitance of the interface at any given potential. Differential capacitance data have been extensively used to assess the structure of electrolyte solutions near charged interfaces and used as experimental validation of models for electrolyte structure. In parallel, from the application standpoint, the integral capacitance is used to assess and represent the capacitance of the double-layer device, for example, the integral of $dQ(V)/dV$ over the operational voltage range of the electrode [41].

Enhanced methods and devices to store energy are critical to improve the energy efficiency. One possible strategy for the advance in energy storage lies in both finding innovative materials and understanding how the existing and new materials behave [42–44]. There has been considerable research activity (particularly simulations [45–48]) in the last years on the charge storage mechanisms of ILs based mainly on imidazolium, pyrrolidinium and ammonium at electrode surfaces and several strategies have been proposed to modify the charging rate [49–51]. This may be very relevant to energy storage and the advances in this topic would have a major impact on its development. However, several topics remain unclear and further work is still needed to clarify some questions.

5.2.2 Present challenges

On the supercapacitors side, as well as for batteries, there are a lot of questions about the effect of ILs on the electrochemistry and transport properties [52]. How fast are the ions moving? How are the redox reactions affected by the confinement (for batteries especially)? The structure of the electrode/electrolyte interface and the effect of ILs in the shape of the capacitance curves? The kinetics of ions reorientation with an applied potential? The increasing demand for efficient, reliable and affordable energy storage devices has yet to overcome some issues such as low cycle durability in the high-temperature region, poor charge–discharge properties at low temperatures or the flammability of the electrolytes raise safety concerns [53]. In order to increase the energy density of EDLCs, it is necessary to increase its capacitance for the optimization of the performance of supercapacitors [54].

Higher ionic concentration in the electrolyte is required for the improvement of the capacitance value and ILs present properties that make them good candidates

for conventional electrolyte replacement [55]. Furthermore, ILs are less flammable when compared with the common molecular organic solvents and should be an attractive feature to improve the safety and durability at high temperatures of EDLCs [56, 57].

The use of organic electrolytes such as propylene carbonate and acetonitrile, although offers wide operating voltages, faces problems involving toxicity and depletion issues (due to the poor thermal stability) [58]; they present higher environmental impact and low ionic conductivity. Although H_2SO_4 and KOH aqueous electrolytes exhibit high ionic conductivity, they present a narrow electrochemical window (1.2 V) [59, 60].

Hence, the introduction of ILs as electrolytes in energy storage devices brought an increase in the operating voltage up to 6.0 V (although the working range often reported in the literature varies from 2.5 to 4.0 V). This fact is often connected to issues related to the electrochemical stability of ILs [61]. The use of mixtures of ILs with organic electrolyte has been shown as a suitable route for the tailorable electrolytes design. Depending on the IL/organic electrolyte ratio in the mixture, high conductivity, low viscosity and a large electrochemical stability window can be achieved [62].

Pure ILs are electrolytes consisting entirely of ions which, in the last two decades, have been subject to huge research activity with their ongoing introduction in industrial applications [63, 64]. These electrolytes became very attractive in the replacement of corrosive and low stable electrolytes used in several technological applications. This has been mainly due to their high charge density, solvent-free nature, tailored structure and also low vapor pressure and wide electrochemical windows [65]. Furthermore, ILs are less flammable when compared with the common molecular organic solvents and should be an attractive feature to improve the safety and durability at high temperatures of EDLCs.

ILs composed of bulky organic cations and inorganic anions show a large liquid phase range and also a wide electrochemical window; however, their high viscosity may reduce the ion migration [66]. One of the most desired properties presented by ILs is their capability to act as “designer solvents”; that is, by the independent selection of cation and anion their physicochemical properties can be fine-tuned for a specific task [67, 68]. The selection of the cation has a strong effect on IL properties and will often define the IL stability, and in general, the choice of the anion influence on the chemistry and functionality of the IL [69]. This “design solvent concept” and taking into account the broad variety of cations and anions, this may lead to a theoretically possible number of 1,018 ILs that are possible to synthesize. However, only approximately 300 are commercially available and approximately 1,000 ILs are described in the literature [70].

A better-off structural diversity is achieved by mixing ILs, becoming an alternative “tool” to design tailor-made solvents for required technologies. A new concept of “double salt ILs” or blended ILs is obtained through the combination of more than

one cation or anion in the mixture [71]. The remarkable advantage of using mixed ILs relies on a suitable anion–cation combination in order to accomplish more efficient electrochemical devices by designing task-specific IL mixtures.

5.2.3 ILs in capacitance enhancements

Stemming from the search for the understanding of the role of ionic species on the electrical double-layer structure and capacity, research efforts have been focused on increasing the energy and power densities of double layer by combining actions upon the electrode surface [51, 72] and tailoring the electrolyte composition by using IL mixtures [50, 73, 74]. Many excellent reviews have overviewed traditional electrode materials and electrolytes [75–79]; however, there is still a lack of systematic understanding of the IL application.

5.2.3.1 Electrolyte composition

ILs most studied for supercapacitor applications are based on imidazolium, pyrrolidinium and asymmetric aliphatic quaternary ammonium salts. The most studied anions are tetrafluoroborate, trifluoromethanesulfonate, bis(trifluoromethanesulfonyl)imide, (bis(fluorosulfonyl)imide and hexafluorophosphate with all featuring a wider electrochemical window compared with conventional organic electrolytes [80, 81]. ILs are part of the current advancement in research and upscaling of various electrochemical energy storage devices from the perspective of electrolytes. The energy (E) stored in an electric double layer (EDL)-based capacitor is proportional to its capacity, C, as well the applied potential. In order to increase the energy density of EDLCs, it is necessary to increase its capacitance for the optimization of its performance.

Since energy storage in supercapacitors relies on the electrolyte/electrode interface, its success is crucially dependent on the full insight into the EDL of an IL at a charged substrate. In Scheme 5.1, in a very simplified version, the interactions established between the electrically charged surfaces immersed with an electrolyte composed only of ions – ILs (e.g., ion–surface Coulombic interaction) are represented.

There are several interactions that can affect the structure of the IL/electrode interface. In fact, the great scientific interest in ILs results from the coexistence and interplay of van der Waals, Coulomb, dipole and hydrogen bond interactions. The interactions resulted from the contact of an IL with an electrically charged surface are obviously modulated by the applied electric field resulting in the establishment of other interactions (vertical interactions). To understand and evaluate the relevance of some of these interactions, particularly those resulting from the nature of the ions, for example, the presence or absence of aromatic rings in the cation, the

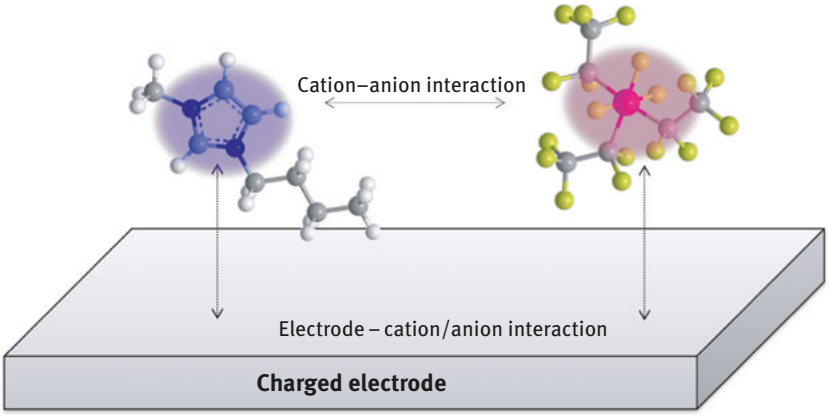

Scheme 5.1: Lateral interactions (ion–ion) and vertical interactions (ion–electrode) at the ionic liquid/electrode interface. Reprinted from Electrochimica Acta, 167, Renata Costa,Carlos M. Pereira, A. Fernando Silva, Charge Storage on Ionic Liquid Electric Double Layer: The Role of the Electrode Material, 421-428, Graphical Abstract, Copyright (2018), with permission from Elsevier.

temperature and the nature of the surface, a set of ILs was selected. To reconcile the data gathered for the most representative systems, the most relevant data and their particular EDL structures proposed to describe the IL/electrode interface are summarized in Scheme 5.2.

Despite controversy in the literature in considering deep eutectic solvents (DES) or not in the class of ILs, the structure of electrode/deep eutectic interfaces illustrated in Scheme 5.2(A) was recognized in the literature to bring important steps toward understanding the complexities of DES structures at electrified surfaces [82]. Similar to what has been reported in the literature for aqueous or organic electrolytes, at large negative potentials the structure of the adjacent layer to the electrode comprises a layer of choline cations separated from the electrode surface by a layer of hydrogen bond donor (HBD) molecules. As the potential becomes less negative, the differential capacitance rises sharply suggesting the replacement of choline cations by the adsorption of anions, specifically attributed to the increasing adsorption of Cl^- anion possibly non-coordinated to the HBD (as illustrated in the cartoon of the insert of Scheme 5.2(A)) [83].

As reported for pure ILs, the interfacial structure involving IL mixtures is also affected by the ion–substrate and ion–ion interactions (van der Waals, hydrogen bonding, π–π interactions, solvophobic and Coulombic), ion shape, size and ion packing constraints [84].

In the literature, several surface structures have been reported for the IL adjacent layers to the surface, ranging from self-assembled structures [85], checkerboard patterns [86], monolayer and bilayer [87, 88] or multilayer structures [89–91], lamellar [92–94], sponge-like morphologies [95], bicontinuous [96, 97], coil-like, worm-like, micelle-like adsorbed ion [84] to "island"-type arrangements [98]. The

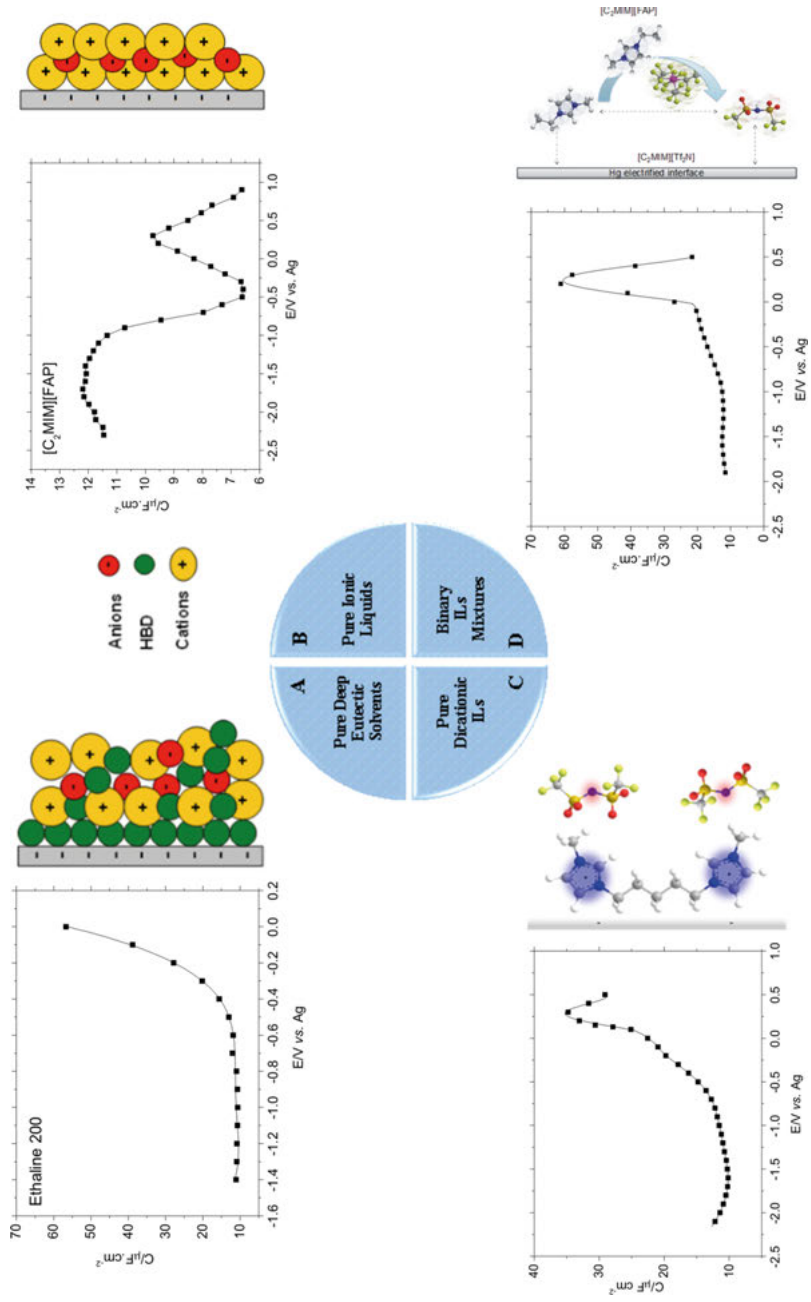

Scheme 5.2: Summary of the interfacial properties measured at ionic liquid/electrode interface: chemical composition of the surface, the strength of ion–ion interactions, that is, the IL molecular structure and surface nature and potential.

degree of propagation into the bulk of the ordering/layering is attributed to a combination of multiple effects, which includes the rich structural diversity present in ILs, molecular flexibility, coulombic and solvophobic interactions, packing geometry, hydrogen bonding interactions, conformations, IL–surface interactions, temperature and electrode material nature. Confronting all the EDL models that have been proposed, one aspect is consensual: the structure of the first more or less ordered layer of counterions adjacent to the electrode is induced in a high degree and accompanied by a template effect of the surface structure. From the physical chemistry point of view, the data gathered by using a nonstructured mercury electrode allows not only to decouple any templating effect induced from electrode surface but also it allows the independent determination of the potential of zero charge values.

The pure IL/electrode interface "architecture" reported is based on the assumption of a multilayer structure with interpenetrating layers of cations and anions with their distance to the electrode being modulated by the applied potential (Scheme 5.2 (B)). Depending on the composition and structure of the IL and the electrode nature of the surface, the results point out to the possible formation of a multilayer checkboard-type model (Scheme 5.2(C)) [90, 99–102].

The use of ILs with ions of different sizes became recently a strategic tool of tuning of the composition of the liquid which could lead to an increase in the charge accumulated at a specific potential (Scheme 5.3(D)). Despite the interfacial properties are fairly studied for pure ILs, the interfacial properties of the IL mixtures are less thoroughly studied [73, 99, 103–107].

Recent results reported by Costa et al. [73, 74, 99] using the nonstructured mercury/IL interface revealed that for a specific composition, the IL mixtures outperform their pure original components, for example, the IL mixtures present higher capacitance when compared with their respective pure liquids. Accordingly, a certain deviation to the degree of the monotonic behavior was found in a specific interval of polarization, representing an enhancement of the capacitance in the presence of both anions present in the mixture. This deviation was not only found in the differential capacitance as a function of the applied potential but also on the potential at zero charge (p.z.c.) as a function of the IL mixture composition trend.

This trend allows to predict that there is an optimal composition range for the IL mixtures that maximizes the differential capacitance. This nonmonotonic behavior resulted from the replacement of the biggest anion by the smaller ones. This effect may be interpreted as a result of a more effective and efficient packing of more counterions in the adjacent layer relative to the electrode. This may be favored by the balance between the volume-excluded effects and by the simultaneous enhancement of electrostatic interactions promoted by the smaller and charge-concentrated anion.

Scheme 5.3(A) represents the enhancement in differential capacitance observed when a pure IL ([C_4MIMFAP]) is mixed with an IL with a common cation and a smaller

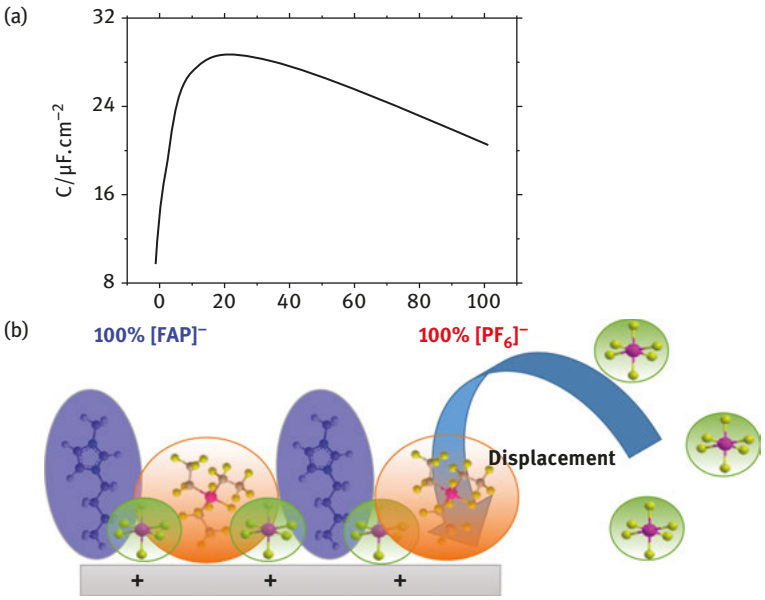

Scheme 5.3: Mechanism proposed for the enhancement of the differential potential reported mixtures composed by anions with large asymmetry and size.

and symmetrical anion ($[PF_6]^-$). Scheme 5.3(B) also presented the proposed mechanism to describe the double layer structure in mixtures of ILs with a common cation and two dissimilar anions at large rational positive potentials.

The interpretation that can be offered at this stage for the increase in the interfacial charge accumulation is based on current models of the EDL of ILs. The mechanism proposed to describe the enhancement reported in the differential capacitance corroborates those models, where the accumulation of large ions leaves voids which can be occupied by smaller ions. The imidazolium alkyl chain seems to play an important role in the formation of voids and also in the charge compensation. For shorter alkyl chains (ethyl), the enhancement reported at positive rational potentials in the capacitance (for lower content on the smaller anion in the mixture) is accompanied by an abrupt change in the EDL structure arrangement (structural ordering transitions were reported). Increasing two carbons in the imidazolium chain length, the increase in the differential capacitance is not a consequence of a potential-driven structural transition of the monolayer adjacent to the electrode but from an increase in the ionic packing efficiency promoted by the anionic different sizes present in the mixture. The interfacial surface void occupation occurs, thus allowing the accumulation of more counterions with simultaneous displacement of larger anions by the smaller ones in the mixture. However, for longer alkyl chains (hexyl), the enhancement effect on the differential capacitance

reported for shorter chains is lost (at least for the accessible electrochemical window). EDL studies at the interface of mercury–binary IL mixtures with different lengths of alkyl side chains revealed stronger hydrophobic interactions with the surface of longer imidazolium alkyl side chains at negative charge densities [108]. The interaction of the alkyl chain with the electrode surface and the tail reorientation as the potential becomes less negative seems to impede the accumulation of the same sum of charges as reported for the analogue mixtures with shorter chains. The enhancement obtained in the differential reported is greatly affected by parameters such as ion concentration, temperature, applied potential, substrate nature and structure of ions.

This finds support in the recent work published by Siimenson et al. [104]. The authors report remarkably higher capacitance values for three-component IL mixtures with a common cation which differ in the size of the anion at Bi(111) electrode when compared with the corresponding binary mixture EMImOTF + 1 wt% EMImI (three-component mixture composition: EMImOTF (trifluoromethanesulfonate) + $EMImBF_4$ (tetrafluoroborate) + 1 wt% EMImI (iodide)). The authors interpret the results as the EDL structure being determined by the chemical nature and geometric structure of the anions. In a subsequent work considering the same electrode surface (Bi(111)), however, the iodide was replaced by the bromide anion. The authors expect that for the binary mixtures composed of $EMImBF_4$ + *x*% EMImBr mixtures, the stored charge value in a supercapacitor cell is twice higher than expected for pure $EMImBF_4$ [106]. Lian et al. [50] assessed to the capacitance performance by formulating IL mixtures ($[C_2MIM][Tf_2N]$ + $[C_2MIM][BF_4]$) at the onion-like carbon electrode interfaces using classical density functional theory (DFT) based on coarse-grained models. The results point to the existing of a mixture composition that yields the integral capacitance. This enhancement is interpreted as being caused by the balance between the reduction of the excluded volume effects and the enhancement of electrostatic interaction resulted in the disruption of the alternating layering structure.

Formulation of IL mixtures at charged surfaces with a common cation and varying the molar fraction of anions different in size and geometry seems to favor the accumulation of smaller counterions on the adjacent layer of electrode with simultaneous displacement of the bigger counterparts. The charge accumulation mechanism proposed may also lead to the coions exclusion from the electrode surface, which is also proposed to play an important role in the stabilization of the double-layer structure.

The possibility of accumulating more charge per unit area opens new possibilities for the design of ion structures leading to original routes in the IL synthesis. The reshaping of a new generation of more performative electrochemical energy storage and generation devices is a long-term commitment between experimental developments and theoretical modeling and interface designs [109].

5.2.3.2 Temperature effect on *C*(*E*) curves

The absence of solvent molecules in salts with high melting temperatures and ILs poses the challenge for the development of models capable of describing interfacial structures composed only of ions. Perhaps due to the degree of complexity in the interpretation of results, minor attention has been given to the effect of temperature on the double-layer studies involving ILs. Nevertheless, any model developed to accurately describe and accommodate the interfacial dependence of the EDL structure–IL properties relationship needs necessarily to accommodate the experimentally observed temperature coefficients of the differential capacitance.

It is expected that the rise in temperature influences the organization of the solvent at the interface, and consequently causes variations not only in the lateral interactions of ions but also in the vertical solvent interaction established between ions and the electrode surface. In the literature, positive and negative effects of increasing temperature on the differential capacitance have been reported. So far there has been not an acceptable explanation for the effects observed, and the temperature effect on the *C*(*E*) curves is still a controversial picture.

Generally, differential capacitance curves increase with increasing temperature. The magnitude of the increase sometimes is not significant and it is not uniform throughout the whole accessible potential range as evidenced in Figure 5.2.

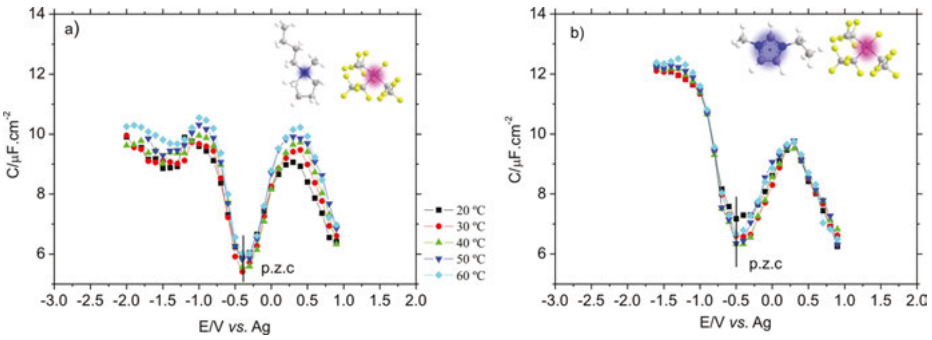

Figure 5.2: Temperature dependence on the differential capacitance curves measured at Hg/[$C_{1,4}$Pyr][FAP] and [C_2MIM][FAP] interface.

The effect of temperature increase on the *C(E)* curves measured at the interface of Hg/[C_2MIM][FAP] and [$C_{1,4}$Pyr][FAP] is represented in Figure 5.2. The temperature dependence measured at the Hg/[$C_{1,4}$Pyr][FAP] interface increases with increasing temperature over the entire range of the accessible potential range (Figure 5.2(a)). In contrast, the *C(E)* curves measured at the Hg/[C_2MIM][FAP] interface show a positive temperature coefficient at large negative

potentials and a slight negative coefficient in the vicinity of the p.z.c. and it is almost insensitive to temperature variation at large positive rational potentials (Figure 5.2(b)).

The effect of increasing the temperature was found to increase the differential capacitance of Pt, GC and Hg/[C_4MIM][PF_6] interfaces in the whole accessible potential range [99, 110]. It was shown almost a factor of 2 increase in the differential capacitance across a wide potential range within approximately 55 °C temperature window. Later, it was estimated the Cp.z.c. temperature coefficients which were found to range between 0.01 and 0.02 μF cm^{-2} K^{-1} depending on the liquid structure. Strong electrostatic coupling counterion–coion at the interface based on Monte Carlo simulations were invoked to explain the anomalous positive temperature coefficient of the capacitance at the p.z.c. for molten inorganic salts [111].

Despite being considered an anomalous trend, positive temperature dependence of differential capacitance for ILs has been reported by Zistler et al. [112] for IL blends and has also been found in double-layer capacitor studies [113, 114]. Positive temperature coefficients of the differential capacitance have also been reported for high-temperature molten salts [115–117].

This led to the suggestion of a possible valid interpretation of the charge reorganization at the interface for ILs following similar mechanism as reported for highly concentrated ionic electrolytes. The increase in the differential capacitance with the rise of temperature leads to the possible decrease of the double-layer thickness as a consequence of the complex balance between the free volume structural heterogeneity of the liquid. The rise in temperature may lead to the increase in the free volume and thus to increase the interdispersion of ions (approaching their planes of charge to the electrode surface). Nevertheless, it is also reasonable to assume the probable breakdown of the structural heterogeneity of the liquid leading to the increase of simple "free" ions in the layer adjacent to the electrode.

Experimentally, Lockett et al. [118] and Kislenko et al. [119, 120] using molecular dynamic (MD) simulations attributed the growth and variation in the potential–capacitance curves with increasing temperature as a result of decrease in the association of ions in the double layer. The weakening of ionic association reported consequently causes more effective screening of electrode charge at high temperatures. The trend found in several studies is in contrast with the negative temperature coefficient reported by Alam et al. [121] for the Hg electrode surface and is also in contrast with the predictions of the classical Gouy–Chapman theory of dilute electrolytes. Druschler et al. [122] also found an overall small decrease of differential capacitance with increasing temperature, and the results were interpreted as a result of a fast relaxation process associated with electrolyte reordering in the EDL structure. The apparent increase of differential capacitance reported in the literature with temperature was attributed to a possible artifact caused by the single-frequency Electrochemical Impedance Spectroscopy (EIS) measurement used by some authors. Cannes et al. [123] have also reported an overall decrease of

differential capacitance curves as a function of the temperature for Pt and C electrode-based surfaces in $[C_4MIM][TFSI]$.

In the literature, there is an apparent contradiction on the trend of temperature-dependent capacitance in both experimental and theoretical simulations since there is no common agreement about the real trend that $C(E)$ curves should follow as the temperature becomes higher. This may arise not only from the complex interplay present in the IL-based interfacial EDL structure but also from the narrower potential window that is experimentally accessible when compared with the potential range achieved in simulations. The Hg surface has been elected as a metal model because its surface is easily renewable and it presents great repeatability and reproducibility in temperature dependence studies, in contrast to the studies reported for solid electrode surfaces. Solid electrodes are not only extremely sensitive to the presence of impurities but also very sensitive to the surface cleaning/preparation method, requiring strict control of the experimental conditions. The absence in the literature of a general agreement about the nature of the temperature dependence on the capacitance of EDL in IL media is affected by the difficulty in controlling the "quality of the interface."

Positive and negative coefficients of temperature, particularly in Hg electrode immersed in liquids constituted by the imidazolium dication are experimentally reported [102]. The $C(E)$ as a function of temperature reveals an apparent isosbestic point at +0.01 V (vs. Ag) which defines a transition between positive temperature coefficient to the negative temperature coefficient of capacitance. A reasonable explanation that can offer at the moment relies on the increase in the strengthening in the specific adsorption of $[C_5(MIM)_2]^+$ which allows a relatively lower packing density of $[Tf_2N]^-$, which causes less effective screening of the surface charge, and thereby decreasing the differential capacitance at large positive rational potentials.

Both $C(E)$ curves with negative and positive temperature dependences were predicted by DFT [124], Monte Carlo simulations [125] and mean spherical approximation [126] theory of concentrated electrolytes (molten salts). The authors report capacitance with a negative slope at high temperatures and a positive slope at low temperatures. Liu et al. [127] also found a similar trend using MD simulation for $[C_4MIM][PF_6]$. The maxima of Cd simulated at the negative polarization decreases monotonically with a rise in temperature, whereas at the positive polarization it gradually increases within the 450–550 K range and the trend inverts at the highest temperature simulated.

For mixtures containing a common cation and varying the content of the smaller anion in the binary mixture, sharp peaks in the differential capacitance curves were observed for a small range of mixture compositions at positive charge densities. The data obtained are consistent with potentially driven transition in the adsorbed layer of $[Tf_2N]^-/[FAP]^-$ anions at the interface and it was found to be dependent on the ion concentration, temperature and applied potential [73]. By increasing the temperature, a shift in the peak position is noted toward more positive potentials. For

temperature above 60 °C, no peak is observed within the accessible potential window.

The effect of increasing the temperature on differential capacitance in IL blends comprising a common anion and varying the alkyl chain of the imidazolium cation is very slight; however, the trend found is positive [108].

Recently, Kornyshev et al. [128] revisit the temperature dependence on the double layer of ILs. This was achieved by introducing concepts such as "ion pairs" and "neutral aggregates" in the developed mean-field theory of earlier work that may have opened a full voltage window. The authors report in the differential capacitance curves a shape transition from camel to bell shape with the rise of temperature attributed to thermal activation of ions leading to the disruption of "ion pairs" and "neutral aggregates."

Ivaništšev et al. [129] performed MD simulations of a generic coarse-grained IL confined between two oppositely charged surfaces in order to rationalize the IL double layer versus temperature dependence. The authors gave special focus on negative dC/dT gradient. Important conclusions were addressed to the impact of the temperature on the double-layer structure, such as the suppression of the overscreening phenomena as the temperature becomes higher (leading to negative $C(E)$ temperature coefficients). Depending on the potential regime, the vertical interactions (electrode–ions) may play a dominant role in determining the EDL structure while at lower potential regimes, the lateral interactions overcome the previous ones (e.g., cation–anion electrostatic interactions) and ion packing efficiency interplay will dominate the interfacial structure.

5.2.3.3 High surface area electrode materials

The configuration of a double-layer capacitor requires the confinement of the IL between two electrodes. The ions accumulate near the oppositely charged electrode in a nanometer-thick layer as a result of the applied potential, and the energy generated is stored across the electrified interface [130].

High surface area carbons including activated carbon, carbon nanotubes, carbon nanofibers, carbide-derived carbon, graphene and mesoporous carbon, have given promising results as being excellent electrode materials for this class of devices [131]. The nanoscale structural features of electrodes (nanopore size, surface roughness and curvature) have shown to be favorable for the capacitance enhancements [132].

The improvement of porous carbon-based capacitors can occur throughout two main strategic actions – on the electrode surface modification (increasing the capacitance and decreasing dielectric screening contribution) or by the electrode geometry/electrolyte adjustment [133].

The maximization of the capacity at the interface by increasing the interfacial area per volume has been the most pursuit route to boost supercapacitive energy. Larger

surface leads to greater capacitance and, consequently, a larger stored charge is accomplished for a given potential. This option will allow increasing the overall capacitance by several orders of magnitude. Increasing the roughness of the surface will not be sufficient to reach this objective. The strategy passes to fill the volumetric surface comprising the highly porous electrodes that have to be very well wetted by the electrolyte.

The pore structure of the active electrode material, the accessibility of these pores to the electrolyte and the wettability of the electrode have been considered as a key factor for good supercapacitor performance using IL electrolytes [134]. Nevertheless, the advance of this topic is crucially dependent on the knowledge emerged from the fundamental study of the IL/electrode interface. Key issues such as the understanding of how ILs screen the electrode potential, the shape of the differential capacitance versus applied potential, the vertical and lateral interactions of ions that form the electrode adjacent layer and how such structure reacts to the applied potential and molecular properties of ILs/double layer relationship are fundamental for any electrochemical practical application [135, 136]. Understanding the confinement, potential and IL structure effect on the structure and capacitance of the double layers inside nanopores is fundamental to the progress of capacitor optimization [137, 138].

Considering all the above-mentioned and discussed topics, it is evident that the electrolyte plays an important role on capacitive performance, safety, and lifetime of an EDLC.

Extensive research has been addressed to optimize the energy density of electric energy storage devices using ILs; however, no systematic study has been carried out.

McEwen et al. [139] used IL for the first time in supercapacitors acting as salts in solvent-based electrolytes to produce highly conducting electrolytes. Pyrrolidinium [140, 141] and imidazolium [142, 143] cations are the main two most promising and most often used families of aprotic ILs that have been considered as potential electrolytes for EDLCs.

The design of electrode materials and also innovative electrolytes with specific composition will require not only a complete understanding on the influence of ILs on the EDL structure and its capacitance, but also on the knowledge about how deep this effect is propagated into the IL bulk, especially in interfaces containing porous carbon materials.

5.3 Concluding remarks

Energy storage topic is a very broad field that encloses many types of energy harvesting/conversion/storage mechanisms. Electrolytes have been identified as one of the most important components contributing to the performance of electrochemical supercapacitors. Furthermore, it is very difficult for an electrolyte to meet all the requirements for an ideal electrolyte since each electrolyte has its own advantages and shortcomings and therefore mixtures of electrolytes can be used to overcome the

existing limitations and it is vital to increase the number of experimental and theoretical studies of mixtures in order to boost our understanding of the key factors governing the observed capacitance enhancement. The nature of the pure ionic liquids electrolytes and its mixtures along with their ionic strength, ion charge and ion size has pronounced influence on EDL formation, as well as on electrochemical reactions and adsorption of ions. In order to perform a realistic approach to the design of EDLCs, it is necessary to identify and control the factors affecting the ion transport and adsorption from pure and mixtures of the electrolytes in contact with the charged surface. Manipulating the electrolyte composition in combination with materials with a large specific surface area as electrodes is undoubtedly a significant way in advancing the emergence of a new generation of high-energy supercapacitors (even stable to operate over a large temperature range).

Acknowledgments: This work was financially supported by Fundação para a Ciência e Tecnologia (FCT/MEC) funds and cofinanced by the European Union (FEDER funds) under the Partnership Agreement PT2020, through project POCI/01/0145/FEDER/006980 with reference UID/QUI/UI0081/2013 (CIQUP – Physical Analytical Chemistry and Electrochemistry group) and IL4Energy project (with reference POCI-01-0145-FEDER-032294). Renata Costa acknowledges a Post-Doc scholarship awarded by FCT with reference SFRH/BPD/89752/2012 under the QREN – POPH – Advanced Training, subsidized by the European Union and national MEC funds. The authors also thank the COST Action CM1206 – EXIL (Exchange on Ionic Liquids).

References

[1] A. Grunwald, C. Rösch, Sustainability assessment of energy technologies: towards an integrative framework, Energy, Sustainability and Society 2011:3, 1–10.

[2] D. Parra, M. Swierczynski, D. Stroe, S. Norman, A. Abdon, J. Worlitschek, T. O'Doherty, L. Rodrigues, M. Gillott, X. Zhang, C. Bauer, M. Patel, An interdisciplinary review of energy storage for communities: Challenges and perspectives, Renewable and Sustainable Energy Reviews 2017, 79, 730–749.

[3] M. Li, Q. Wang, Will technology advances alleviate climate change? Dual effects of technology change on aggregate carbon dioxide emissions, Energy for Sustainable Development 2017, 41, 61–68.

[4] J. Markard, R. Raven, B. Truffer, Sustainability transitions: An emerging field of research and its prospects, Research Policy 2012, 955–967.

[5] Y. Kajikawa, J. Yoshikawa, Y. Takeda, K. Matsushima, Tracking emerging technologies in energy research: Toward a roadmap for sustainable energy, Technological Forecasting & Social Change 2008, 75, 771–782.

[6] R. Abotah, T. Daim, Towards building a multi perspective policy development framework for transition into renewable energy, Sustainable Energy Technologies and Assessments 2017, 21, 67–88.

[7] P. Anastas N. Eghbali, Green chemistry: Principles and practice, Chemical Society Reviews, 2010, 39, 301–312.
[8] E Hart, E Stoutenburg, M Jacobson, Potential of intermittent renewables to meet electric power demand, Proceedings of the IEEE 2012, 100, 322–334.
[9] H. Chen, T.N. Cong, W. Yang, C. Tan, Y. Li, Y. Ding, Progress in electrical energy storage system: A critical review, Progress in Natural Science 2009, 19, 291–312.
[10] S. Howell, Y. Rezgui, J. Hippolyte, B Jayan, H. Li, Towards the next generation of smart grids: Semantic and holonic multi-agent management of distributed energy resources, Renewable and Sustainable Energy Reviews 2017, 77, 193–214.
[11] O. Ellabbana, H. Rubb, F. Blaabjerg, Renewable energy resources: Current status, future prospects and their enabling technology, Renewable and Sustainable Energy Reviews 2014, 39, 748–764.
[12] M. Guney, Y. Tepe, Classification and assessment of energy storage systems, Renewable and Sustainable Energy Reviews 2017, 75, 1187–1197.
[13] B. Dunn, H. Kamath and J.-M. Tarascon, Electrical energy storage for the grid: A battery of choices, Science, 2011, 334, 928–935.
[14] A. Brouwer, M. Broek, A. Seebregts, André Faaij, Impacts of large-scale Intermittent Renewable Energy Sources on electricity systems, and how these can be modeled, Renewable and Sustainable Energy Reviews 2014, 33, 443–466.
[15] S. Faraji, F. Ani, The development supercapacitor from activated carbon by electroless plating—A review, Renewable and Sustainable Energy Reviews 2015, 42, 823–834.
[16] A. González, E. Goikolea, J. Barrena, R. Mysyk, Review on supercapacitors: Technologies and materials, Renewable and Sustainable Energy Reviews 2016, 58, 1189–1206.
[17] http://www.idtechex.com/research/reports/batteries-and-supercapacitors-in-consumer-electronics-2013-2023-forecasts-opportunities-innovation-000336.asp (accessed September 2017).
[18] X. Luo, J. Wang, M. Dooner, J. Clarke, Overview of current development in electrical energy storage technologies and the application potential in power system operation, Applied Energy 2015, 137, 511–536.
[19] A. Jordan, N. Gathergood Biodegradation of ionic liquids – A critical review, Chemical Society Reviews, 2015, 44, 8200–8237.
[20] A. Mehrkesh, A. Karunanithi, Life-cycle perspectives on aquatic ecotoxicity of common ionic liquids, Environmental Science & Technology 2016, 50, 6814–6821.
[21] T. Phuong, T. Phama, C. Choa, Y. Yun, Environmental fate and toxicity of ionic liquids: A review, Water Research 2010, 44, 352–372.
[22] P. Sharma, T. Bhatti, A review on electrochemical double-layer capacitors, Energy Conversion and Management 2010, 51, 2901–2912.
[23] A. Forse, C. Merlet, J. Griffin, C. Grey, New perspectives on the charging mechanisms of supercapacitors. Journal of the American Chemical Society 2016, 138, 5731–5744.
[24] F. Wang, X. Wu, X. Yuan, Z. Liu, Y. Zhang, L. Fu, Y. Zhu, Q. Zhou, Y. Wu, W. Huang, Latest advances in supercapacitors: From new electrode materials to novel device designs, Chemical Society Reviews 2017, Advance Article.
[25] A. Bard, L. Faulkner, Electrochemical Methods. Fundamentals and Applications, John Wiley & Sons, Inc. 2ª edição, 2001.
[26] H. Ibrahim, A. Ilinca, J. Perron, Energy storage systems characteristics and comparisons 2008, Renewable and Sustainable Energy Reviews, 12, 1221–1250.
[27] D. Dubal, O. Ayyad, V. Ruiz, P. Romero, Hybrid energy storage: The merging of battery and supercapacitor chemistries, Chemical Society Reviews, 2015, 44, 1777–1790.

[28] A. Pandolfo, A. Hollenkamp, Carbon properties and their role in supercapacitors, Journal of Power Sources 2006, 157, 11–27.
[29] J. Miller, P. Simon, Electrochemical capacitors for energy management. Science 2008, 321, 651–2.
[30] H. Helmholtz, Ueber einige Gesetze der Verlheiiung elektrischcr Strdme in kdrperlichen Leitern mit Anwendung auf die thierisch - elektrischen Versuche; oon H, Helmholtz. Ann. Phys. Chem. 1853, 89, 211
[31] M. Gouy, Sur la constitution de la charge électrique à la surface d'un electrolyte, Journal of Theoretical and Applied Physics 1910, 9, 457–468.
[32] O. Stern, Zur theorie der elektrolytischen doppelschicht, Zeitschrift für Elektrochemie . 1924, 30, 508–516.
[33] D. Grahame, The electrical double layer and the theory of electrocapillarity, Chemical Reviews. 1947, 41, 441–501.
[34] R. Whitney, D. Grahame, A modified theory of the electrical double layer, Chemical Reviews 1941, 9, 827–828.
[35] A. Frischknecht, D. Halligan, M. Parks, Electrical double layers and differential capacitance in molten salts from density functional theory, Journal of Chemical Physics 2014, 141, 054708 1–11.
[36] A. Kornyshev, Double-layer in ionic liquids: Paradigm change? Journal of Physical Chemistry B 2007, 111, 5545–5557.
[37] Z. Goodwin, G. Feng, A. Kornyshev, Electrochimica Acta 2017, 225, 190–197.
[38] M. Fedorov, A. Kornyshev, Ionic liquid near a charged wall: Structure and capacitance of electrical double layer. Journal of Physical Chemistry B 2008, 112, 11868–11872.
[39] M. Fedorov, A. Kornyshev, Towards understanding the structure and capacitance of electrical double layer in ionic liquids, Electrochimica Acta 2008, 53, 6835–6840.
[40] M. Fedorov, N. Georgi, A. Kornyshev, Double layer in ionic liquids: The nature of the camel shape of capacitance, Electrochem Commun. 2010, 12, 296–299.
[41] T. Fave, R. Tsu, Capacitance: A property of nanoscale materials based on spatial symmetry of discrete electrons, Microelectronics Journal 2008, 39, 617–623.
[42] G. Wang, L. Zhang, J. Zhang, A review of electrode materials for electrochemical supercapacitors, Chemical Society Reviews., 2012,41, 797–828.
[43] M. Lukatskay, B. Dunn, Y. Gogotsi, Multidimensional materials and device architectures for future hybrid energy storage, Nature Communications 2016, 7, 1–13.
[44] C. Liu, F. Li, L. Ma, H. Cheng, Advanced materials for energy storage, dv Mater. 2010, 22, E28–E62.
[45] M. Fedorov, A. Kornyshev, Ionic liquids at electrified interfaces, Chemical Reviews 2014, 114, 2978–3036.
[46] C. Merlet, D. Limmer, M. Salanne, R. van Roij, P.A. Madden, D. Chandler, B. Rotenberg, The electric double layer has a life of its own, Journal of Physical Chemistry Letters C2004, 118, 18291–18298.
[47] A.A. Kornyshev, R. Qiao, Three-dimensional double layers, Journal of Physical Chemistry C 2015, 118, 18285–18290.
[48] K. Breitsprecher, K. Szuttor, C. Holm, Electrode models for ionic liquid-based capacitors, Journal of Physical ChemistryC 2015, 119, 22445–22451.
[49] X. Kong, D. Lu, Z. Liu, J. Wu, Molecular dynamics for the charging behavior of nanostructured electric double layer capacitors containing room temperature ionic liquids, Nano Research 2015, 8, 931–940.
[50] C. Lian, K. Liu, K. Aken, Y. Gogotsi, D. Wesolowski, H. Liu, D. Jiang, J. Wu, Enhancing the capacitive performance of electric double-layer capacitors with ionic liquid mixtures, ACS Energy Letters 2016, 1, 21–26.

[51] R. Costa, C. Pereira, A. Silva, Insight on the effect of surface modification by carbon materials on the Ionic Liquid Electric Double Layer Charge Storage properties, Electrochimica Acta 2015, 176, 880–886.
[52] C. Merlet, M. Salanne, B. Rotenberg, P. Madden, Influence of solvation on the structural and capacitive properties of electrical double layer capacitors, Electrochimica Acta 2013, 101, 262–271.
[53] C. Zhong, Y. Deng, W. Hu, J. Qiao, L. Zhang, J. Zhang, Review of electrolyte materials and compositions for electrochemical supercapacitors, Chemical Society Review, 2015, 44, 7484–7539.
[54] P. Simon, Y. Gogotsi, Materials for electrochemical capacitors, Nature Materials 2008, 7, 845–54.
[55] A. Eftekhari, Supercapacitors utilising ionic liquids, Energy Storage Materials 2017, 9, 47–69.
[56] C. Wolff, S. Jeong, E. Paillard, A. Balducci, S. Passerini, High power, solvent-free electrochemical double layer capacitors based on pyrrolidinium dicyanamide ionic liquids, Journal of Power Sources 2015, 293, 65–70.
[57] S. Zhang, J. Sun, X. Zhang, J. Xin, Q. Miao, J. Wang, Ionic liquid-based green processes for energy production, Chemical Society Reviews, 2014, 43, 7838–7869.
[58] A. Forse, J. Griffin, C. Merlet, J. Carretero-Gonzalez, A. Raji, N. Trease, C. Grey, Direct observation of ion dynamics in supercapacitor electrodes using in situ diffusion NMR spectroscopy, Nature Energy 2, 16216 1–7.
[59] B. Mendoza-Sánchez, Y. Gogotsi, Synthesis of two-dimensional materials for capacitive energy storage, Advanced Materials 2016, 28, 6104–6135.
[60] D. Macfarlane, N. Tachikawa, M. Forsyth, J. Pringle, P. Howlett, Energy applications of ionic liquids, Energy & Environmental Science, 2014, 232–250.
[61] C. Liu, Z. Yu, D. Neff, A. Zhamu, B. Jang, Graphene-based supercapacitor with an ultrahigh energy density, Nano Letters 2010, 10, 4863–4868.
[62] A. Krause, A. Balducci, High voltage electrochemical double layer capacitor containing mixtures of ionic liquids and organic carbonate as electrolytes, Electrochemistry Communications 2011, 13, 814–817.
[63] S. Turosung, B. Ghosh, Application of ionic liquids in the upstream oil industry-A review, The International Journal of Peptide Research 2017, 1, 50–60.
[64] G. Durga, A. Mishra, Ionic liquids: Industrial applications. Encyclopedia of Inorganic and Bioinorganic Chemistry 2016, 1–13.
[65] P. Hunt, C. Ashworth, R. Matthews, Hydrogen bonding in ionic liquids, Chem. Chemical Society Reviews, 2015, 44, 1257–1288.
[66] B. Xua, F. Wu, R. Chen, G. Cao, S. Chen, Y. Yang, Mesoporous activated carbon fibers as electrode material for high performance electrochemical double layer capacitors with ionic liquid electrolyte, Journal of Power Sources 2010, 195, 2118–2124.
[67] K. Marsh, J. Boxal, R. Lichtenthaler, Room temperature ionic liquids and their mixtures—A review, Fluid Phase Equilibria 2004, 219, 93–98.
[68] N. Plechkova, K. Seddon, Applications of ionic liquids in the chemical industry. Chemical Society Reviews, 2008, 37, 123–150.
[69] G. Chatel, J. Pereira, V. Debbeti, H. Wang, R. Rogers, Mixing ionic liquids – “simple mixtures” or “double salts”?, Green Chemisrty, 2014, 16, 2051–2083.
[70] N. Plechkova, K. Seddon, Ionic Liquids: “Designer” Solvents for Green Chemistry, in Methods and reagents for green chemistry: An introduction (eds P. Tundo, A. Perosa and F. Zecchini), 2007, John Wiley & Sons, Inc., : Hoboken, NJ, USA. doi: 10.1002/9780470124086.ch5.
[71] H. Niedermeyer, J. Hallett, I. Garcia, P. Hunt, T. Welton, Mixtures of ionic liquids, Chemical Society Reviews 2012, 41, 7780–7802.

[72] J. Vatamanu, M. Vatamanu, D. Bedrov, Non-faradic energy storage by room temperature ionic liquids in nanoporous electrodes 2015, ACS Nano 9, 5999–6017.
[73] R. Costa, C. Pereira, A Silva Structural ordering transitions in ionic liquids mixtures, Electrochemistry Communications 2015, 57, 10–13.
[74] Renata Costa, Iuliia V Voroshylova, M. Cordeiro, C. Pereira, A. Silva, Enhancement of differential double layer capacitance and charge accumulation by tuning the composition of ionic liquids mixtures, submitted to Electrochimica Acta 2017.
[75] V. Augustyn, P. Simon, B. Dunn, Pseudocapacitive oxide materials for high-rate electrochemical energy storage, Energy & Environmental Science, 2014, 7, 1597–1614.
[76] M. R. Lukatskaya, B. Dunn and Y. Gogotsi, Multidimensional materials and device architectures for future hybrid energy storage, Nature Communications 2016, 7, 12647–12659.
[77] Y. Wang, Y. Song and Y. Xia, Electrochemical capacitors: Mechanism, materials, systems, characterization and applications, Chemical Society Reviews 2016, 45, 5925–5950.
[78] Y. Liu, B. Zhang, F. Wang, Z. Wen and Y. Wu, Nanostructured intercalation compounds as cathode materials for supercapacitors, Pure and Applied Chemistry 2014, 86, 593–609.
[79] H. Wu, G. Zhang, L. Yu, X. Lou, One-dimensional metal oxide–carbon hybrid nanostructures for electrochemical energy storage, Nanoscale Horiz., 2016, 1, 27–40.
[80] Z. Lei, B. Chen, Y. Koo, D. MacFarlane, Introduction: Ionic Liquids, Chemical Reviews, 2017, 117 (10), pp 6633–6635.
[81] T. Greaves, C. Drummond, Protic ionic liquids: Evolving structure–property relationships and expanding applications, Chemical Reviews 2015, 115, 11379–11448.
[82] Z. Chen, M. Ludwig, G. Warr, R. Atkin, Effect of cation alkyl chain length on surface forces and physical properties in deep eutectic solvents, Journal of Colloid and Interface Science 2017, 494, 373–379.
[83] R. Costa, M. Figueiredo, C. Pereira, A. Silva, Electrochemical double layer at the interfaces of Hg/choline chloride based solvents, Electrochimica Acta 2010, 55, 8916–8920.
[84] R. Hayes, G. Warr, R. Atkin, Structure and nanostructure in ionic liquids, Chemical Reviews. 2015, 115, 6357–6426.
[85] F. Buchner, K. Tonigold, M. Bozorgchenani, A. Gross, R. Behm, Interaction of a self-assembled ionic liquid layer with graphite(0001): A combined experimental and theoretical study. Chemical Reviews. 2016, 7, 226–233.
[86] L. Tamam, M. Ocko, H. Reichert, M. Deutsch, Checkerboard self-patterning of an ionic liquid film on mercury, Physical Review Letters 2011, 106, 197801 1–4.
[87] K. Kirchner, T. Kirchner, V. Ivaništšev, M. Fedorov, Electrical double layer in ionic liquids: Structural transitions from multilayer to monolayer structure at the interface, Electrochimica Acta 2013, 110, 761–771.
[88] A. Smith, K. Lovelock, S. Perkin, Monolayer and bilayer structures in ionic liquids and their mixtures confined to nano-films, Faraday Discussions, 2013, 167, 279–292.
[89] B. Rotenberg, M. Salanne, Structural transitions at ionic liquid interfaces, Journal of Physical Chemistry Letters 2015, 6, 4978–4985.
[90] R. Costa, C. Pereira, F. Silva, Double layer in room temperature ionic liquids: influence of temperature and ionic size on the differential capacitance and electrocapillary curves, Physical Chemistry Chemical Physics, 2010, 12, 11125–11132.
[91] Y. Liu, Y. Zhang, G. Wu and J. Hu, Coexistence of liquid and solid phases of Bmim-PF6 ionic liquid on mica surfaces at room temperature, Journal of the American Chemical Society, 2006, 128, 7456–7457.
[92] J. B. Rollins, B. D. Fitchett and J. C. Conboy, Structure and orientation of the imidazolium cation at the room-temperature ionic Liquid/SiO2 interface measured by sum-frequency vibrational spectroscopy, Journal of Physical Chemistry. B 2007, 111, 4990–4999.

[93] M. Mezger, S. Schramm, H. Schroder, H. Reichert, M. Deutsch, E. Souza, J. Okasinski, B. Ocko, V. Honkimaki, H. Dosch, Layering of [BMIM]+[BMIM]+-based ionic liquids at a charged sapphire interface, Journal of Physical Chemistry, 2009, 131, 094701 1–9.
[94] Y. Yokota, T. Harada, K. Fukui, Direct observation of layered structures at ionic liquid/solid interfaces by using frequency-modulation atomic force microscopy, Chemical Communications 2010, 46, 8627–8629.
[95] R. Hayes, G. Warr, R. Atkin, At the interface: solvation and designing ionic liquids, Physical Chemistry Chemical Physics 2010, 12, 1709–1723.
[96] C. Hardacre, J. Holbrey, M. Nieuwenhuyzen, T. Youngs, Structure and solvation in ionic liquids. Acc Chem Res. 2007; 40, 1146–1155.
[97] R. Atkin, G. Warr, The smallest amphiphiles: Nanostructure in protic room-temperature ionic liquids with short alkyl groups, Journal of Physical Chemistry B 2008, 112, 4164–4166.
[98] A. Uysal, H. Zhou, G. Feng, S. Lee, S. Li, P. Cummings, P. Fulvio, S. Dai, J. McDonough, Y. Gogotsi, P. Fenter, Interfacial ionic liquids: connecting static and dynamic structures . Journal of Physics: Condensed Matter 2015, 27, 032101–032108.
[99] F Silva, C Gomes, M. Figueiredo, R Costa, A Martins, C. Pereira, The electrical double layer at the [BMIM][PF6] ionic liquid/electrode interface – Effect of temperature on the differential capacitance, Journal of Electroanalytical Chemistry, 622, 153–160.
[100] R. Costa, C. Pereira, A. Silva, Role of the anion on the interfacial structure of ionic liquids binary mixtures at mercury interfaces, Electrochimica Acta 2016, 195, 150–157.
[101] R. Costa, C. Pereira, A. Silva, Charge storage on ionic liquid electric double layer: the role of the electrode material, Electrochimica Acta, 167, 2015, 421–428.
[102] R. Costa, C. Pereira, A. Silva, Dicationic ionic liquid: insight in the electrical double layer structure at mercury, glassy carbon and gold surfaces, Electrochimica Acta 2014, 116, 306–313.
[103] D. Santos, M. Cordeiro, Effect of replacing [NTf2] by [PF6] anion on the [BMIm][NTf2] ionic liquid confined by gold, Molecular Simulation. 2015, 41, 455–462.
[104] C. Siimenson, L. Siinor, K. Lust, E. Lust, Electrochemical characterization of iodide ions adsorption kinetics at Bi(111) electrode from three-component ionic liquids mixtures, ECS Electrochemistry Letters 2015, 4, H62–H65.
[105] S. Ramnarine, S. N. Suarez, N. V. Zmich, D. Ewko, S. Ramati, D. Cuffari, M. Sahin, Y. Adam, E. Rosario, D. Paterno, J. F. Wishart, Electrochemical characterization of iodide ions adsorption kinetics at Bi(111) electrode from three-component ionic liquids mixtures, ECS Transactions 2014, 64, 57–69.
[106] C Siimenson, M Lembinen, O. Oll, L. Läll, M. Tarkanovskaj, V. Ivaništšev, L. Siinor, T. Thomberg, K. Lust, E. Lust, Electrochemical investigation of 1-Ethyl-3-methylimidazolium bromide and tetrafluoroborate mixture at Bi(111) Electrode Interface, Journal of the Electrochemical Society 2016, 163, H723–H730.
[107] C. Siimenson, L. Siinor, K. Lust, E. Lust, Electrochemical characterization of iodide ions adsorption kinetics at Bi(111) electrode from three-component ionic liquids mixtures. ECS Electrochemistry Letters. 2015, 4, H62–H65.
[108] R. Costa, C. Pereira, A. Silva, Electric double layer studies at the interface of mercury–binary ionic liquid mixtures with a common anion, RSC Advance, 2013, 3, 11697–11706.
[109] S. Badwal, S. Giddey, C. Munnings, A. Bhatt, A. Hollenkamp, Emerging electrochemical energy conversion and storage technologies, Frontiers in Chemistry 2014, 2, 1–28.
[110] C. Gomes, R. Costa, C. Pereira, A. Silva, The electrical double layer at the ionic liquid/Au and Pt electrode interface, RSC Advances, 2014, 4, 28914–28921.
[111] D. Boda, D. Henderson, K. Chan, Monte Carlo study of the capacitance of the double layer in a model molten salt, The Journal of Chemical Physics 1999, 110, 5346–5350.

[112] M. Zistler, P. Wachter, C. Schreiner, M. Fleischmann, D. Gerhard, P. Wasserscheid, A. Hinsch, H. J. Gores, Temperature dependent impedance analysis of binary ionic liquid electrolytes for dye-sensitized solar cells, Journal of the Electrochemical Society, 2007, 154, B925–B930.
[113] M. Ue, M. Takeda, A. Toriumi, A. Kominato, R. Hagiwara, Y. Ito, Application of low-viscosity ionic liquid to the electrolyte of double-layer capacitors, Journal of the Electrochemical Society. 2003, 150, A499–A502.
[114] M. Ue, M. Takeda, T. Takahashi,M. Takehara, Electrochem. Ionic liquids with low melting points and their application to double-layer capacitor electrolytes, Electrochemical and Solid State Letters 2002, 5, A119–A121.
[115] M. Devanathan, B. Tilak, The structure of the electrical double layer at the metal-solution interface, Chemical Reviews 1965, 65, 635–684.
[116] A. Graves, The electrical double layer in molten salts: Part 1. The potential of zero charge, Journal of Electroanalytical Chemistry, 1970, 25, 349–356.
[117] A. Graves, D. Inman, The electrical double layer in molten salts: Part 2. The double-layer capacitance, Journal of Electroanalytical Chemistry 1970, 25, 357–372.
[118] V. Lockett, R. Sedev, J. Ralston, M. Horne, T. Rodopoulos, Differential capacitance of the electrical double layer in imidazolium-based ionic liquids: influence of potential, cation size, and temperature. Journal of Physical Chemistry . C 2008, 112, 7486–7495.
[119] S. Kislenko, R. Amirov, I. Samoylov, Influence of temperature on the structure and dynamics of the [BMIM][PF6] ionic liquid/graphite interface, Physical Chemistry Chemical Physics 2010, 12, 11245–11250.
[120] S. Kislenko, R. Amirov, I. Samoylov, Molecular dynamics simulation of the electrical double layer in ionic liquids, Journal of Physics: Conference Series 2013, 418, 012021–8.
[121] M.T. Alam, Md. M. Islam, T. Okajima, T. Ohsaka, Measurements of differential capacitance at, Mercury/Room-temperature ionic liquids interfaces, Journal of Physical Chemistry. C 2007, 111, 18326–18333.
[122] M. Druschler, N. Borisenko, J. Wallauer, C. Winter, B. Huber, F. Endresb and B. Roling, New insights into the interface between a single-crystalline metal electrode and an extremely pure ionic liquid: slow interfacial processes and the influence of temperature on interfacial dynamics, Physical Chemistry Chemical Physics, 2012, 14, 5090–5099.
[123] C. Cannes, H. Cachet, C. Chouvy, C. Deslouis, J. Sanoit, C. Naour, V. Zinovyeva, double layer at [BuMeIm][Tf2N] ionic liquid–pt or –c material interfaces, Journal of Physical ChemistryC, 2013, 117, 22915–22925.
[124] J. Zygmunt, S. Sokolowski, D. Henderson, D. Boda, Temperature dependence of the double layer capacitance for the restricted primitive model of an electrolyte solution from a density functional approach, Journal of Physical Chemistry, 2005, 122, 84504 1–6.
[125] L. Bhuiyan, C. Outhwaite, D. Henderson, A modified Poisson-Boltzmann analysis of the capacitance behavior of the electric double layer at low temperatures, Journal of Physical Chemistry, 2005, 123, 34704 1–5.
[126] M. Holovsko, V. Kapko, D. Henderson and D. Boda, On the influence of ionic association on the capacitance of an electrical double layer, Chemical Physics Letters, 2001, 341, 363–368.
[127] X. Liu, Y. Han, T. Yan, Temperature Effects on the Capacitance of an Imidazolium-based Ionic Liquid on a Graphite Electrode: A Molecular Dynamics Simulation, Chemistry Chemical Physics 2014, 15, 2503–2509.
[128] M. Chen, Z. Goodwin, G. Feng, A. Kornyshev, On the temperature dependence of the double layer capacitance of ionic liquids, Journal of Electroanalytical Chemistry. 2017, 10.1016/j. jelechem.2017.11.005.
[129] V. Ivaništšev, K. Kirchner, M. Fedorov, Xiv:1711.06854 [cond-mat.soft].

[130] R. Burt, G. Birkett, X. Zhao, A review of molecular modelling of electric double layer capacitors, Physical Chemistry Chemical Physics, 2014, 16, 6519–6538.
[131] A. Borenstein, O. Hanna, R. Attias, S. Luski, T. Brousse, D. Aurbach, Carbon-based composite materials for supercapacitor electrodes: a review. Journal of Materials Chemistry A, 2017, 5, 12653–12672.
[132] J. Vatamanu, O. Borodin, M. Olguin, G. Yushin, D. Bedrov, Charge storage at the nanoscale: understanding the trends from the molecular scale perspective, Journal of Materials Chemistry A 2017, DOI:10.1039/C7TA05153K.
[133] C. Zhan, C. Lian, Y. Zhang, M. Thompson, Y. Xie, J. Wu, P. Kent, P. Cummings, D. Jiang, D. Wesolowski, Computational insights into materials and interfaces for capacitive energy storage, Advanced Science 2017, 4 1700059 1–27.
[134] X. Wang, H. Zhou, F. Lou, Y. Li, M. Buan, X. Duan, J. Walmsley, E. Sheridan, D. Chen, Boosted Supercapacitive energy with high rate capability of a carbon framework with hierarchical pore structure in an ionic liquid, Chemical Sustainable Chemistry 2016, 9, 1–10.
[135] Y. Su, Y. Fu, J. Yan, Z. Chen, B. Mao, Double Layer of Au(100)/Ionic Liquid Interface and Its Stability in Imidazolium-Based Ionic Liquids, Angewandte Chemie 2009, 121, 5250–5253.
[136] S. Tazi, M. Salanne, C. Simon, P. Turq, M. Pounds, and P. Madden, Potential-induced ordering transition of the adsorbed layer at the ionic liquid/electrified metal interface, Journal of Physical Chemistry B 2010, 114, 8453–8459.
[137] S. Zhang, J. Zhang, Y. Zhang, Y. Deng, Nanoconfined ionic liquids, Chemical Reviews 2017, 117, 6755–6833.
[138] M. Singh, R. Singh, S. Chandra, Ionic liquids confined in porous matrices: Physicochemical properties and applications, Progress in Materials Science 2014, 64, 73–120.
[139] A. McEwen, H. Ngo, K. LeCompte, J. Goldman, Electrochemical properties of imidazolium salt electrolytes for electrochemical capacitor applications, Journal of the Electrochemical Society 1999, 146, 1687–1695.
[140] K. Liu, C. Lian, D. Henderson, J. Wu, Impurity effects on ionic-liquid-based supercapacitors, Molecular Physics 2017, 115, 454–464.
[141] A. Lewandowski, A. Olejniczak, M. Galinski, I. Stepniak, Performance of carbon supercapacitors based on organic, aqueous and ionic liquid electrolytes, Journal Power Sources 2010, 195, 5814–5819.
[142] R. Palm, H. Kurig, K. Tõnurist, A. Jänes, E. Lust, Is the mixture of 1-ethyl-3-methylimidazolium tetrafluoroborate and 1-butyl-3-methylimidazolium tetrafluoroborate applicable as electrolyte in electrical double layer capacitors?, Electrochemistry Communications. 2012, 2, 203–206.
[143] W. Liu, X. Yan, J. Lang, Q. Xue, Effects of concentration and temperature of EMIMBF_4/acetonitrile electrolyte on the supercapacitive behavior of graphene nanosheets, Journal of Materials Chemistry 2012, 22, 8853–8861.

Farid Taherkhani, Babak Minofar

6 Static and dynamical properties of colloidal silver nanoparticles in [EMim][PF6] ionic liquid

"Beauty is truth, truth beauty,"– that is all you know on earth, and all you need to know.
(*John Keats, May 1819*)

Abstract: Ionic liquids are used for many applications such as electrolytes for energy storage in electric double-layer capacitors and dye-sensitized solar cells for conversion of solar energy. The nonextensivity of entropy was investigated for different sizes of colloidal Ag nanoparticles (NPs) and it was shown that subextensivity of entropy occurs for colloidal Ag NPs. In small size of colloidal Ag NPs and at low temperature, nonextensivity is important. The pattern of configurational entropy for Ag NPs in terms of size in gas phase is completely different with colloidal Ag NPs in [EMim][PF6] ionic liquid as a solvent. Configurational entropy of colloidal silver NPs in terms of size of colloidal Ag NPs is nonmonotonic. There is a nonmonotonic behavior for mean collision time of vibrational mode of colloidal Ag NP size in IL; however, mean collision time of vibrational mode for Ag NP in gas phase decreases monotonically as the Ag NP size increases. The increase of the size of colloidal silver NP does not change [EMim] cation configuration around colloidal silver NP.

Keywords: Ionic liquid, colloidal silver nanoparticle, Molecular dynamics simulation

6.1 Introduction

The unique properties of ionic liquids (ILs) make them suitable candidates as superior solvents in both industry and academia. X-ray diffraction was used to investigate the effect of alkyl chain on bulk structure and properties of alkyl ammonium nitrate ILs and the effect of water on the surface structure of 1-butyl-1-methylpyrrolidinium trifluoromethyl sulfonylimide [C4mpyr][NTf2] IL [1, 2].

Molecular dynamic (MD) simulations have been performed for calculations of anomalous dependence of surface tension with concentration for aqueous solutions 1-butyl-3-methylimidazolium tetrafluoroborate and 1-butyl-3-methylimidazolium hexafluorophosphate ILs [3]. The investigation of surface tension

Farid Taherkhani, Department of Chemistry, Sharif University of Technology, Iran; Center for Nanobiology and Structural Biology, Academy of Sciences of the Czech Republic, Czech Republic
Babak Minofar, Faculty of Science, University of South Bohemia, Czech Republic

https://doi.org/10.1515/9783110583632-006

has been extended for aqueous solutions of magnesium acetate and magnesium nitrate at various concentrations [4].

It is of great interest to study nanoparticles (NPs) in ILs, especially metal NPs which attract significant attention because of their novel properties [5–7]. Many metal clusters and NPs are used as catalysts [8] for reactions that are used in sensors, electronics, photonics and solar cell applications.

Many researchers have been interested in studying NPs or small metal clusters [9–12]. The clusters that have been examined theoretically are of interest as models for larger systems or surfaces. The size-dependent properties of NPs are of interest in many areas [13]. In this chapter, sliver NPs have been chosen because of their utility in microelectronics, stereoselective catalysis [14–16] and electrochemical sensor properties [17, 18]. The properties of silver NPs with different sizes were also investigated in both gas phase and IL as solvent.

As some of the systems with different sizes were synthesized and experimentally investigated, we were able to compare computational findings with experimental data.

Several publications have been reported for high yield synthesis and theoretical investigations of metallic NPs in ILs [19–21]. In fact, metal NPs synthesized in ILs are reported to be monodispersed and nonagglomerated as a result of IL stabilization [22–24]. Active colloidal NP has significant effect on catalyzing the reduction of chemical reaction such as reduction of hydrogen peroxide to oxygen and water [25]. The stability of active colloidal NP can be controlled by positive or negative number of Soret coefficient [26].

Suspension of metal NPs into ILs has many applications such as in electrochemical devices based on high electrical conductivity [27, 28], lithium metal ion batteries [29, 30], lubricants, catalysis [31–33] and high-performance biosensors [34–37]. Metal NPs enhance the ability of ILs as heat transfer fluid for solar collector applications [38].

In order to prepare desired metallic NPs in ILs, the stability of the NP dispersion should be carefully controlled. NPs are kinetically very stable [39] and two main pathways are used to stabilize NP suspension in solution. The first is the stabilization where ions adsorb on the electrophilic metal surface [40, 41], which results in an electrostatic repulsive force between NPs [40, 42, 43]. The second is steric stabilization where large molecules of IL surround the NPs [44, 22, 7]. For imidazolium-based ILs, the long alkyl chains by altering the physicochemical properties of ILs as well as the interactions between ILs and NPs impact the NPs stability in ILs [23].

According to entropic stabilization theory when second surface approaches the absorbed layer, it is compressed and this causes a decrease in entropy because of the restricted movement of the molecules. This effect increases the ΔG and gives rise to an overall repulsion between the particles [45]. Many other factors that affect the stability of metallic NPs in ILs include cation–anion Coulomb attraction [46], metal polarizability [47, 48], coordination of anions of ILs [49, 25], temperature, viscosity of ILs and the diffusive velocities of the sputtered NPs [50, 51]. Thus, an improved understanding of the stability of NP dispersions in ILs may lead to the synthesis of

NPs with controlled size and morphology in ILs. As polarizability is important for large ions and metals, polarizable force field could be used for MD simulation which is used for ions at air/water interface [52].

The chemistry of NP–IL interfaces is often very different from that of bulk IL. The spatial distribution of solvent ions at NP–IL interfaces is thus a central problem. Metal surfaces are conducting, thus highly polarizable and their interactions with charged entities incorporate multiple effects that are expected to be nonnegligible even for small clusters of metal atoms [53, 54].

Several other reviews of structure at metal–IL interfaces have since emerged [55–57], including some focuses on the electrochemically active interface [58–60] that provide a good overview of the problems and challenges of resolving ion arrangements.

The mutual structural effects of the surface and the surrounding IL on each other determine the properties of the system [61]. IL–metal interfaces remain largely unexploited in chemical processes because their interfacial structure and dynamics have not yet been understood.

MD simulation is used to understand interfacial processes at a molecular level because it can describe the systems with atomistic detail. MD simulations have been used not only as a tool to study the interactions and ordering of ILs around metallic NPs but also as a method to directly predict the properties of ILs. A number of IL–metal systems have been modeled using classical MD simulations [53, 62–64].

Although many thermodynamic properties of ILs have been studied extensively [65], lack of information on the thermodynamic properties of colloidal metal NPs in ILs still exists.

The purpose of this molecular simulation study of Ag NPs in 1-ethyl-3-methylimidazolium hexafluorophosphate [EMim][PF6] is twofold. First, it tries to determine heat capacity and entropy of system, then an attempt is made to determine free energy and entropy of Ag NPs in terms of temperature and size range of Ag NPs.

6.2 Computational method

6.2.1 MD simulations

Three kinds of interaction could be defined in the study system: IL–IL, metal–metal (M–M) and M–IL. The potential function of the system (U) will have contributions from all of these interactions:

$$U = U_{\mathrm{IL-IL}} + U_{\mathrm{M-M}} + U_{\mathrm{M-IL}} \tag{6.1}$$

The force field used in our simulations includes the typical short-range Lennard–Jones and the long-range Coulomb interaction terms between atoms that are not

covalently bonded, and an intramolecular or bonded term that includes bond stretching, r, angle bending, θ, and dihedral torsions, ψ. $U_{\mathrm{IL-IL}}$ may be written as

$$U_{\mathrm{IL-IL}}(r_{ij}) = 4\varepsilon_{ij}\left[\left(\frac{\sigma_{ij}}{r_{ij}}\right)^{12} - \left(\frac{\sigma_{ij}}{r_{ij}}\right)^{6}\right] + \frac{q_i q_j}{4\pi\varepsilon_0 r_{ij}} + \sum_{\text{bonds}} k_b\left(r - r_{\mathrm{eq}}\right)^2 + \sum_{\text{angles}} k_\theta\left(\theta - \theta_{\mathrm{eq}}\right)^2 + \sum_{\text{dihedrals}} k_\psi[1 + \cos(n\psi - \delta]^2 \tag{6.2}$$

where r_{ij} is the distance between atoms i and j of different ions. The force field parameters are those previously proposed by Canongia Lopes et al. [66] based on the Assisted Model Building with Energy Refinement (AMBER) and Optimized Potentials for Liquid Simulations (OPLS) force fields [67]. The equilibrium values of bond angles θ_{eq} and bond lengths in the $[\mathrm{EMim}]^+$ and $[\mathrm{PF6}]^-$ are derived from the crystallographic X-ray structure of solid [EMim][PF_6] [68]. There is some progress for Canongia Lopes force field to get better value for transport properties such as viscosity, conductivity and diffusivity [69].

We have applied the quantum Sutton-Chen (Q-SC) potential to describe interatomic interaction for silver nanoclusters [70]. The $U_{\mathrm{M-M}}$ potential is given by [70]

$$\sum_{i=1}^{N} U_i = \sum_{i}^{N} \varepsilon\left[1/2\sum_{j\neq i}^{N} V\left(r_{ij}\right) - C\sqrt{\rho_i}\right] \tag{6.3}$$

where r_{ij} is the distance between atoms i and j, c is a positive dimensionless parameter and ε is a parameter with the dimensions of energy. $V(r_{ij})$ in eq. (6.3) is defined as

$$V(r_{ij}) = \left(\frac{a}{r_{ij}}\right)^n \tag{6.4}$$

where ρ_i in eq. (6.3) is a local electron density which is defined by the following equation:

$$\rho_i = \sum_{j\neq i}\left(\frac{a}{r_{ij}}\right)^m \tag{6.5}$$

where a is the length parameter, n and m are both positive integer parameters, that is $n > m$ [71].

Lennard-Jones has been included as estimation for M–IL potential interaction. Site–site potential functions of the type $n - m$ similar to Lennard-Jones potential has been applied for potential interaction of surface metal of iron nanoparticle with IL [72]. Interaction between silver metal with 108 atom and IL can be considered as a Lennard-Jones potential from fitting density functional theory (DFT) result as follows:

$$U_{\mathrm{M-IL}} = 4\varepsilon\left[\left(\frac{\sigma}{r}\right)^{12} - \left(\frac{\sigma}{r}\right)^{6}\right] + \frac{q_i q_j}{r} \tag{6.6}$$

Q-SC potential parameters for silver atom, which are used in this study, are taken from ref. [68]. Lennard-Jones potential parameter between silver and IL atom is taken from ref. [73]. In this study, Triple-zeta valence basis set, TZVP basis set for ionic fragmentation and LanL2DZ basis set for both metal and liquid have been used to get surface potential via firefly quantum chemistry package [74] for present MD simulations. Electrostatic forces of the point partial charges on the atomic sites of the ions and the Drude dipoles on the metal atoms caused the polarization of the surface. Ewald summation method has been applied for electrostatic interaction between all charged particles in MD simulations.

Fitting atomistic potential of surface metal NP with IL using DFT method or experimental data gives more reliable structural result for MD simulations [72]. BP86 level using Slater-type basis sets could be used for optimization of transition metal–carbonyl bond [75]. DFT has been used to investigate electronic structure and interaction between bare and hydrated first-row transition-metal ions [76]. All unit energies in our calculation are KJ/mol.

We used the periodic cubic box containing 128 $[EMim]^+$ and 128 $[PF6]^-$, where nanocluster of silver was inserted in the center of the simulation box within a cutoff distance of 12 Å at equilibrium pressure of 1.0 bar. The Berendsen thermostat was applied to control the temperature. The temperature range chosen for all simulations was 350–470 K. The DL_POLY program version 4.03 was used to perform all MD simulations in three steps. In the first step, pure [EMim][PF6] is simulated with NPT ensemble (NPT ensembles maintains constant temperature T and constant pressure P, as well as the number of particles) and application of Berendsen thermostat for 500 ps. Optimum silver nanocluster has been inserted in the center simulation box of optimum structure of IL from step 1 as an initial structure for MD simulation of step 2. At the second step, MD simulations have been done for 400 ps with time step of 0.4 fs and canonical ensemble with Berendsen thermostat. In the third step, MD simulations for 100 ps have been performed on optimum structure from the second step by applying NPT ensemble with relaxation time for thermostat and barostat 0.10 and 2 fs, respectively. As a result, 1 s has been performed for colloidal Ag NPs in IL.

The Verlet leapfrog scheme [77] was used for the integration of the equation of motions. The production runs lasted 500 ps for NPs in gas phase within NVE ensemble (NVE ensemble indicates constant number of particle, volume and energy N).

6.2.2 Methodology

The phonon DOS (density of states) function $S(\omega)$ was calculated using MD trajectories, in order to study the distribution of vibrational normal modes of the silver nanocluster in IL and in gas phase. The phonon DOS function can be obtained from the Fourier transform of the velocity autocorrelation function:

$$S(\omega) = \int \frac{\langle \vec{v}(t) \cdot \vec{v}(0) \rangle}{\langle \vec{v}(0)^2 \rangle} e^{-i\omega t} dt \tag{6.7}$$

where $\vec{v}(0)$ is the velocity vector of a particle at initial time, $\vec{v}(t)$ is the velocity at time t and ω is the frequency [78].

In previous studies, phonon investigation has been done on metallic and bimetallic nanostructures [71, 79]. The entropy (S) of NPs is obtained by utilizing calculated phonon DOS as follows [80]:

$$S = k_B \int_0^\infty S(\omega) \left\{ \left(\frac{\hbar\omega}{2k_B T} \right) \left[\coth\left(\frac{\hbar\omega}{2k_B T} \right) - 1 \right] - \ln\left[1 - \exp\left(\frac{\hbar\omega}{k_B T} \right) \right] \right\} d\omega \tag{6.8}$$

The free energy of nanocluster is calculated on the basis of phonon energy of the solid.

The vibrational contribution to the free energy $F(\omega)$ is given by [81, 82]

$$F(\omega) = 3Nk_B T \int_0^\infty \ln\left[2\sinh \frac{\hbar\omega}{2k_B T} \right] S(\omega) d\omega \tag{6.9}$$

where $S(\omega)$, $\hbar$ and k_B are phonon DOS, Planck's constant divided by 2π and Boltzmann's constant, respectively.

Configurational entropy $\Delta S(T)$ of the system can be calculated in the usual way by integrating over the measured heat capacity at constant pressure $C_p(T)$ as follows [83]:

$$\Delta S(T) = \int_{T_1}^{T_2} \frac{C_p(T)}{T} dT \tag{6.10}$$

C_p is given by

$$C_p(T) = \left(\frac{dU}{dT} \right)_P + P \left(\frac{dV}{dT} \right)_P \tag{6.11}$$

where U, P, V are configurational energy, pressure and volume, respectively.

Tsallis introduced the following generalized entropic form of nonextensive systems, S_q [84, 85]:

$$S_q = k \frac{1 - \sum_{i=1}^{W} p_i^q}{q - 1} \tag{6.12}$$

where k is a positive constant, p_i are the probabilities associated with the microscopic configurations, W is their total number and the parameter q is known as the nonextensive entropy index. This equation is indicative of the fact that the entropy is nonadditive. The entropy of the mixture $S(A + B)$ for two systems A and B described by independent probability distributions is given by [86–88]

$$S(A+B) = S(A) + S(B) + (1-q)S(A)S(B) \tag{6.13}$$

The cases $q < 1$, $q = 1$ and $q > 1$ are named as the cases of superextensivity, extensivity (Boltzmann–Gibbs statistics) and subextensivity, respectively.

6.3 Results and discussion

6.3.1 Entropy of silver nanoclusters in gas phase and in IL

On the basis of eq. (8), entropy of silver NPs in bulk structure has been calculated from MD simulations. Q-SC potential has been used for interatomic interaction in silver bulk structure [89, 90]. Colloidal silver NP with sizes of 108, 256 and 500 in

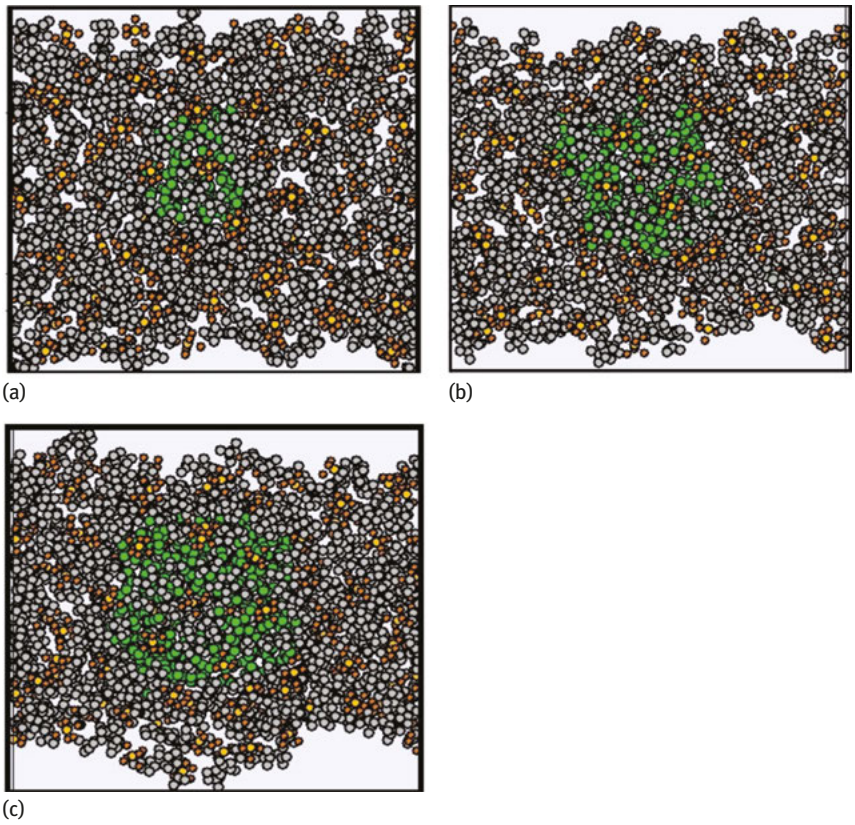

Figure 6.1: (a) Colloidal silver nanoparticle with size 108 in [EMim][PF6] ionic liquid at 350 K. (b) Colloidal silver nanoparticle with size 256 in [EMim][PF6] ionic liquid at 350 K. (c) Same as (b). Colloidal silver nanoparticle with size 500 in [EMim][PF6] ionic liquid at 350 K.

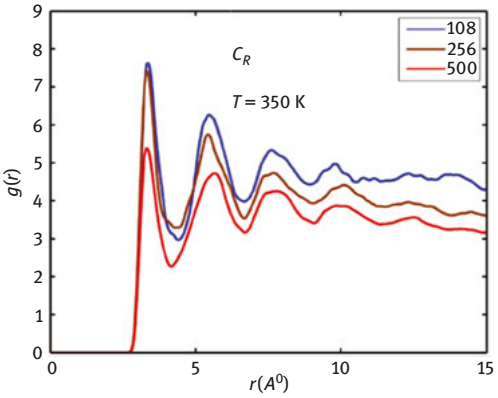

Figure 6.2: Radial distribution function of [EMim] cation versus distance from the center of [EMim] cation ring for colloidal silver nanoparticle with sizes 108, 256 and 500.

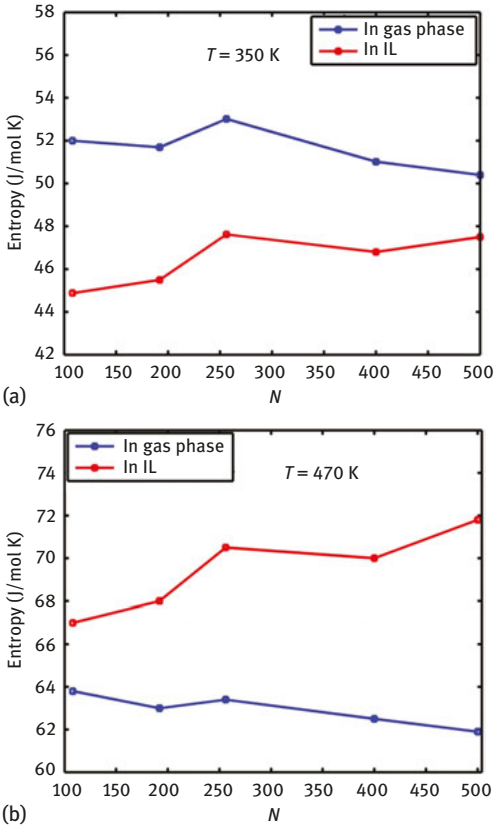

Figure 6.3: (a) Comparison entropy for Ag NPs in gas phase (blue) and colloidal Ag NPs in IL (red) in terms of size at temperature 350 K. (b) Comparison entropy for Ag NPs in gas phase (blue) and colloidal Ag NPs in IL (red) in terms of size at temperature 470 K.

[EMim][PF6] has been presented in Figure 6.1(a, b, c), respectively. Radial distribution function versus distance from cation ring for [EMim] for colloidal silver NP with sizes 108, 256, 500 has been shown in Figure 6.2. Based on Figures 6.1(a, b, c) and 6.2, the increase in size of colloidal silver NP does not change the [EMim] cation configuration around the colloidal silver NP.

Figure 6.3(a) shows the comparison of entropy result at temperature 350 K for Ag NPs and colloidal Ag NPs in terms of size.

At high temperature the entropy of colloidal Ag NPs is higher in ionic liquids than that of Ag NPs in gas phase, as seen in Fig. 6.3b. At high temperature kinetics energy removes electrostatic of charge in ionic liquid and same ions could encounter repeal each other and repulsion force between metal surface charges with ions in IL creates more entropy for colloidal silver NPs in comparison with entropy of silver NPs in gas phase. Therefore, the kinetic energy of system increases when temperature increases and repulsion force between metal surface charges with ions in IL creates more entropy for colloidal silver nanoparticles in comparison with entropy of silver nanoparticles in gas phase.

6.3.2 Free energy for colloidal silver NPs in IL and silver NPs in gas phase

By using eq. (9), free energy for Ag NPs in gas phase and colloidal Ag NPs has been calculated as a function of temperature and size. The result of free energy for Ag NPs in terms of temperature at different size range $108 \leq N \leq 500$ is shown in Figure 6.4(a). Based on Figure 6.4(a) with increasing temperature, free energy decreases and Ag NP becomes stable. Free energy of Ag NPs as a function of temperature is monotonic on the basis of Figure 6.4(a), and larger size of Ag NP in gas phase shows more negative free energy values. Therefore, as the size increases the Ag NP becomes more stable in gas phase. Free energy of colloidal Ag NPs in IL has been presented in Figure 6.4(b).

On the basis of Figure 6.4(b) there is monotonic behavior for free energy of colloidal Ag NPs as a function of temperature for all sizes of silver NPs. Free energy of colloidal Ag NPs in terms of size has been presented in Figure 6.5. On the basis of Figure 6.5 there is a regular trend for free energy of colloidal Ag NPs as a function of size. In small size of colloidal Ag NPs, the stability of NPs increases from energetic point of view due to strong electrostatic interaction of metal surface charge with the ion in IL. As a result, stabilization of colloidal Ag NPs decreases as the size of colloidal Ag NPs increases. The free energy of Ag NPs in gas phase is higher than that of colloidal Ag NPs and this difference increases as the size of NPs decreases (see Figure 6.5). As a result, the stability of colloidal Ag NPs increases in comparison with the Ag NPs in gas phase.

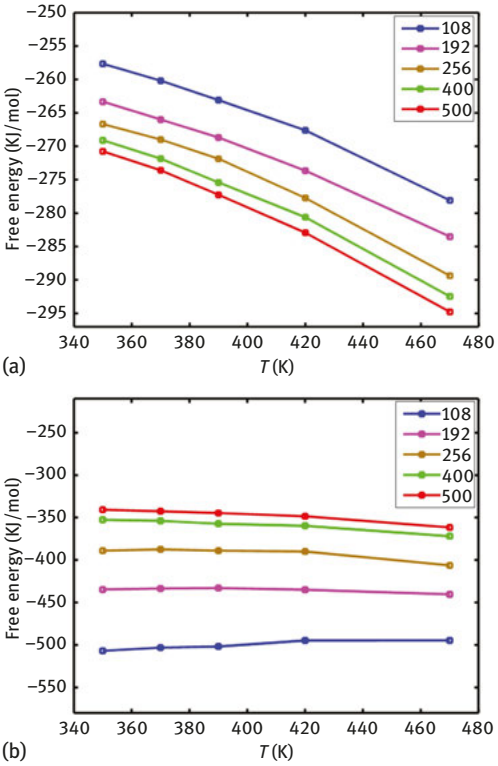

Figure 6.4: (a) The free energy of Ag NPs for sizes 108, 192, 256, 400 and 500 in gas phase in relation to temperature. (b) Free energy for colloidal Ag NPs in IL for sizes 108, 192, 256, 400 and 500 in relation to temperature.

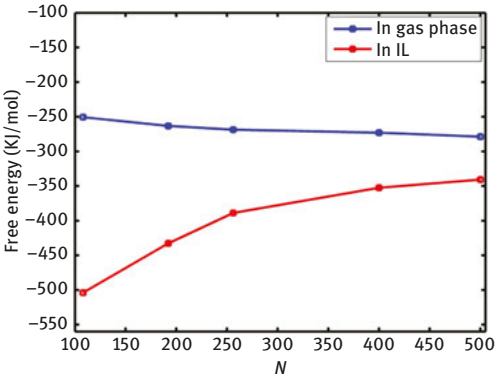

Figure 6.5: Comparison free energy for Ag NPs in gas phase (blue) and colloidal Ag NPs in IL (red) in terms of size at temperature 350 K.

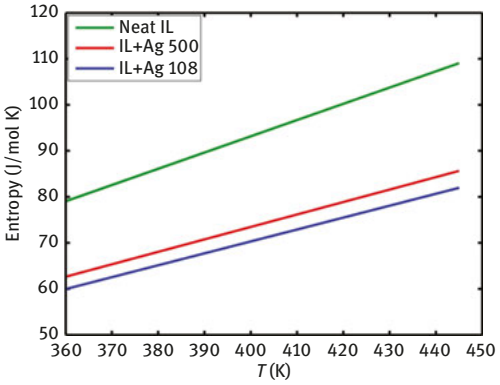

Figuer 6.6: Entropy for pure IL and total solution of colloidal Ag NPs in IL with the sizes 108 and 500.

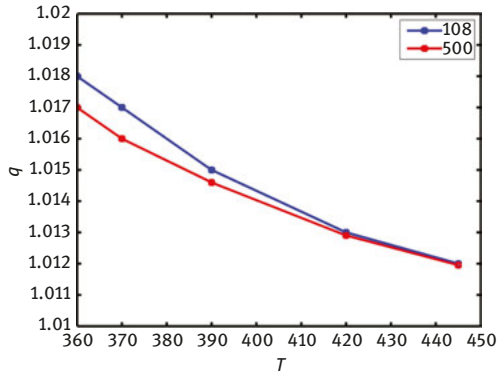

Figure 6.7: Nonextensive entropy index, q, for sizes 108 and 500 for colloidal Ag NPs in terms of temperature.

6.3.3 Entropy of colloidal silver NP solution and pure IL

The entropy of colloidal Ag NP solution at different sizes of 108 and 500 and pure IL in relation to temperature is presented in Figure 6.6. According to Figure 6.6, monotonic behavior in terms of temperature for entropy of colloidal Ag NPs solution and pure IL is observed. Nonextensive entropy of colloidal Ag NPs solution can be calculated via eq. (13). The result of nonextensive parameter, q, for colloidal Ag NP solution in relation to temperature has been shown in Figure 6.7. On the basis of Figure 6.7, nonextensive entropy for small size of colloidal Ag NPs is more than that of large size of colloidal Ag NPs. The results of nonextensive entropy of colloidal Ag NPs solution show that nonextensivity of entropy decreases when the temperature increases. In low temperature, nonextensivity of entropy in small size of colloidal Ag NP seems important. On the basis of Figure 6.7, the

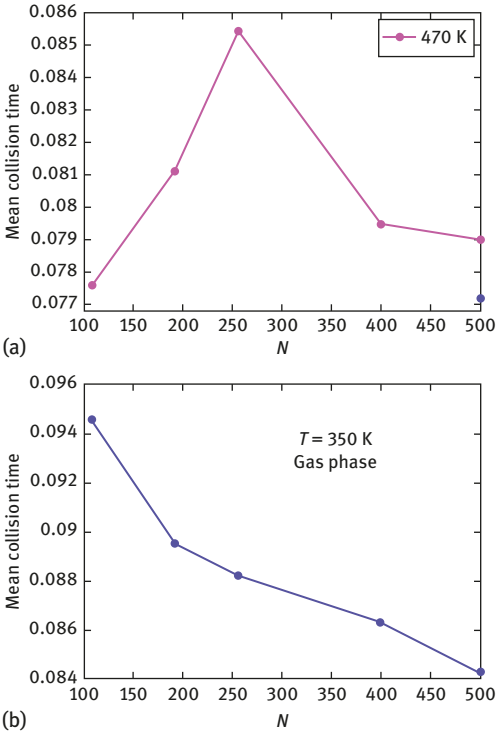

Figure 6.8: (a) Vibrational mean collision time of colloidal silver nanoparticle versus size silver nanoparticle. (b) Vibrational mean collision time for silver nanoparticle versus size in gas phase.

nonextensivity parameter, q, is $q>1$ so subextensivity from entropic point of view in colloidal Ag NPs solution occurs. Strong electrostatic interaction between dipole moment of surface metal with the ions in small colloidal Ag NP size yields large subextensivity of entropy. Mean collision time of vibrational mode for colloidal silver NP versus size at 470 K is presented in Figure 6.8(a). On the basis of Figure 6.8 (a) there is a peak for mean collision time of vibrational mode versus size of colloidal silver NP. Figure 6.8(b) shows that the trend of mean collision time of vibrational mode versus size for silver NP is monotonic and it decreases with increasing size of silver NP.

6.4 Conclusion

The effect of size and temperature on configurational entropy and free energy of colloidal Ag NPs in IL have been investigated. Configurational entropy of colloidal Ag NPs and Ag NPs in gas phase as a function of temperature has monotonic behavior for both colloidal Ag NP in IL and Ag NP configurational entropy versus size are not

completely monotonic. Configurational entropy regarding colloidal Ag NPs versus size is complex. The configurational entropy of colloidal Ag NPs in IL at low temperature is smaller than those in gas phase. However, at high temperature, the configurational entropy of colloidal Ag NPs is greater than the entropy of Ag NPs in gas phase. Monotonic behavior could be found for free energy for colloidal Ag NPs and Ag NPs in gas phase versus temperature and size. Free energy for colloidal Ag NPs increases as particle size increases. However, free energy in gas phase decreases as particle size increases. Energy and entropy can affect the stabilization of colloidal silver NPs. On the one hand, in small size of colloidal Ag NPs, the stability of NPs increases from energetic point of view due to the strong electrostatic interaction of metal surface charges with the ions in IL. On the other hand, in small size of colloidal Ag NPs, there is a small amount of entropy value. This is because there is a lack of degree of freedom with strong electrostatic interaction. Consequently, the stabilization of colloidal silver NPs increases as the size of colloidal Ag NPs decreases. The heat capacity of pure IL in our calculation increases as the temperature increases linearly, which confirms the available experimental data for heat capacity of pure IL. As the size of colloidal Ag NPs increases, heat capacity increases and there is a monotonic behavior for heat capacity of colloidal Ag NPs versus temperature. Total entropy of pure IL and colloidal Ag NPs solution monotonically increases as the temperature increases. Subextensivity of entropy for colloidal Ag NP solution is seen and nonextensive entropy index increases as the temperature and particle size decrease.

Acknowledgments: B.M. would like to acknowledge the support from Czech Science Foundation for grant 13-21053S. Access to instruments and other facilities was supported by the Czech Research Infrastructure for Systems Biology C4SYS (Project No. 756 LM2015055) which is acknowledged. Access to computing and storage facilities owned by parties and projects contributing to the National Grid Infrastructure MetaCentrum provided under the program "Projects of Large Research, Development, and Innovations Infrastructures" (CESNET LM2015042) is greatly appreciated. Also B.M. acknowledges the support from the Ministry of Education, Youth, and Sports of the Czech Republic (Project LTAUSA17163).

References

[1] X. Song, H. Hamano, B. Minofar, R. Kanzaki, K. Fujii, Y. Kameda, S. Kohara, M. Watanabe, Shinichi Ishiguro, Y. Umebayashi, J. Phys. Chem. C 116 (2012) 2801–2813.
[2] Y. Lauw, MD. Horne, T. Rodopoulos, NAS Webster, B. Minofar, A. Nelson, J. Phys. Chem. C 11 (2009) 11507–11514.
[3] J. Picálek, B. Minofar, J. Kolafa, P. Jungwirth, Phys.Chem. Chem. Phys. 10 (2008), 5765–5775.
[4] B. Minofar, R. Vácha, A. Wahab, S. Mahiuddin, W. Kunz, P. Jungwirth, J. Phys. Chem. 110 (2006), 15939–15944.

[5] P. K. Jain, X. Huang, I. H. El-Sayed, M. A. El-Sayed, Acc. Chem. Res. 41 (2008) 1578–1586.
[6] P. Alexandridis, Chem. Eng. Technol. 34 (2011) 15–28.
[7] Z. He, P. Alexandridis, Phys. Chem. Chem. Phys. 17 (2015) 18238–18261.
[8] D. Astruc, F. Lu, J. R. Aranzaes, Angew. Chem. Int. Ed. 44 (2005) 7852–7872.
[9] F. Taherkhani, P. F. Seresht, Prog. Theor. Exp. Phys. (2015) 043I01.
[10] F. Taherkhani, H. Akbarzadeh, H. Rezania, J. Alloys Compd. 617 (2014) 746–750.
[11] H. Akbarzadeh, M. Abbaspour, J. Mol. Liq. 222(2016) 648.
[12] F. Taherkhani, H. Rezania, J. Nanopart. Res. 14 (2012) 1–8.
[13] A. Fernando, K. D. M. Weerawardene, N. V. Karimova, C. M. Aikens, Chem. Rev. 115 (2015) 6112–6216.
[14] G. Pei, X. Liu, A. Wang, A. F. Lee, M. A. Isaacs, L. Li, X. Pan, X. Yang, X. Wang, Z. Tai, ACS Catal. (2015).
[15] A) F. Negreiros, F. Taherkhani, G. Parsafar, A. Caro, A. Fortunelli, J. Chem. Phys. 137 (2012) 194302. B) H. Rezania, F. Taherkhani, Applied Physics A 109 (2012) 343–347,C) H. Rezania, F. Taherkhani, H. Rezania, F. Taherkhani, Solid State Communications 152 (2012), 1776–1780
[16] F. Taherkhani, F. R. Negreiros, G. Parsafar, A. Fortunelli, Chem. Phys. Lett. 498 (2010) 312–316.
[17] M. Torkashvand, M. Gholivand, F. Taherkhani, Mater. Sci. Eng., C 55 (2015) 209–217.
[18] N. Karimian, M. Gholivand, F. Taherkhani, J. Electroanal. Chem. 740 (2015) 45–52.
[19] J. Dupont, M. R. Meneghetti, Curr. Opin. Colloid Interface Sci. 18 (2013) 54–60.
[20] D. O. Silva, L. Luza, A. Gual, D. L. Baptista, F. Bernardi, M. J. Zapata, J. Morais, J. Dupont, Nanoscale 6 (2014) 9085–9092.
[21] M. Abbaspour, H. Akbarzadeh, P. Yousefi, M. Razmkhah, Colloid Interface Sci. 504 (2017) 171.
[22] C. Vollmer, C. Janiak, Coord. Chem. Rev. 255 (2011) 2039–2057
[23] P. Migowski, G. Machado, S. R. Texeira, M. C. Alves, J. Morais, A. Traverse, J. Dupont, Phys. Chem. Chem. Phys. 9 (2007) 4814–4821.
[24] H.-C. Chang, S.-C. Chang, T.-C. Hung, J.-C. Jiang, J.-L. Kuo, S. H. Lin, J. Phys. Chem. C 115 (2011) 23778–23783.
[25] J. R. Howse, R. A. L. Jones, A. J. Ryan, T. Gough, R. Vafabakhsh, and R. Golestanian, Phys. Rev. Lett 99 (2007) 048102.
[26] R. Golestanian, Phys. Rev. Lett 108 (2012) 038303.
[27] P. S. Campbell, C. C. Santini, F. Bayard, Y. Chauvin, V. Collière, A. Podgoršek, M. F. C. Gomes, J. Sá, J. Catal. 275 (2010) 99–107.
[28] H. Bönnemann, K. S. Nagabhushana, Metal Nanoclusters in Catalysis and Materials Science The Issue of Size Contro, Elsevier BV, Amsterdam (2008) 21–48.
[29] Y. Lu, K. Korf, Y. Kambe, Z. Tu, L. A. Archer, Angew. Chem. 126 (2014) 498–502.
[30] Y. Lu, S. K. Das, S. S. Moganty, L. A. Archer, J. Adv. Mater. 24 (2012) 4430–4435.
[31] A. Banerjee, R. Theron, R. W. Scott, J. Mol. Catal. A: Chem. 393 (2014) 105–111.
[32] S. A. Stratton, K. L. Luska, A. Moores, Catal. Today 183 (2012) 96–100
[33] L. Qiu, B. Liu, Y. Peng, F. Yan, Chem. Commun. 47 (2011) 2934–2936.
[34] K. Kwak, S. S. Kumar, K. Pyo, D. Lee, ACS Nano 8 (2013) 671–679.
[35] S. C. Fernandes, S. K. Moccelini, C. W. Scheeren, P. Migowski, J. Dupont, M. Heller, G. A. Micke, I. C. Vieira, Talanta 79 (2009) 222–228.
[36] D. Brondani, C. W. Scheeren, J. Dupont, I. C. Vieira, Sens. Actuators, B: Chem. 140 (2009) 252–259.
[37] A. C. Franzoi, I. C. Vieira, J. Dupont, C. W. Scheeren, L. F. de Oliveira, Analyst 134 (2009) 2320–2328.
[38] T. C. Paul, A. Morshed, E. B. Fox, J. A. Khan, Int. J. Heat Mass Transfer 83 (2015) 753–761.
[39] J. D. Aiken, R. G. Finke, J. Mol. Catal. A: Chem. 145 (1999) 1–44.
[40] S. Özkar, R. G. Finke, J. Am. Chem. Soc. 124 (2002) 5796–5810.
[41] R. J. Hunter, Foundations of Colloid Science, vol II (1987) 992–1052.

[42] L. S. Ott, R. G. Finke, Coord. Chem. Rev. 251 (2007) 1075–1100.
[43] A. J. Bard, LR Faulkner Electrochemical Methods, Wiley, (1980).
[44] A. Kraynov, T. E. Müller, Concepts for the Stabilization of Metal Nanoparticles in Ionic Liquids, in Applications of Ionic Liquids in Science and Technology, ed. Scott Handy, (2011)
[45] H.-F. Eicke, Modern trends of colloid science in chemistry and biology. Springer, (1985).
[46] C.-H. Liu, B.-H. Mao, J. Gao, S. Zhang, X. Gao, Z. Liu, S.-T. Lee, X.-H. Sun, S.-D. Wang, Carbon 50 (2012) 3008–3014.
[47] S. Tazi, M. Salanne, C. Simon, P. Turq, M. Pounds, P. A. Madden, J. Phys. Chem. B 114 (2010) 8453–8459.
[48] M. Salanne, P. A. Madden, Mol. Phys. 109 (2011) 2299–2315.
[49] A. B. Patil, B. M. Bhanage, Phys. Chem. Chem. Phys. 16 (2014) 3027–3035.
[50] Y. Hatakeyama, S. Takahashi, K. Nishikawa, J. Phys. Chem. C 114 (2010) 11098–11102.
[51] T. Kameyama, Y. Ohno, T. Kurimoto, K.-i. Okazaki, T. Uematsu, S. Kuwabata, T. Torimoto, Phys. Chem. Chem. Phys. 12 (2010) 1804–1811.
[52] L. Vrbka, M. Mucha, B. Minofar, P. Jungwirth, E.C. Brown, D.J. Tobias. Curr. Opin. Colloid Interface Sci. 9 (2004) 67–73.
[53] A. S. Pensado, A. A. Pádua, Angew. Chem. 123 (2011) 8842–8846.
[54] B. Zhang, N. Yan, Catalysts 3 (2013) 543–562.
[55] E. A. Muller, M. L. Strader, J. E. Johns, A. Yang, B. W. Caplins, A. J. Shearer, D. E. Suich, C. B. Harris, J. Am. Chem. Soc. 135 (2013) 10646–10653.
[56] E. Schmidt, S. Shi, P. P. Ruden, C. D. Frisbie, ACS Appl. Mater. Interfaces, (2016).
[57] N. V. Plechkova, K. R. Seddon, Ionic Liquids further UnCOILed: Critical Expert Overviews. John Wiley & Sons, (2014)
[58] R. Atkin, N. Borisenko, M. Drüschler, F. Endres, R. Hayes, B. Huber, B. Roling, J. Mol. Liq. 192 (2014) 44–54.
[59] F. Endres, N. Borisenko, S. Z. El Abedin, R. Hayes, R. Atkin, Faraday Discuss. 154 (2012) 221–233.
[60] Y. Z. Su, Y. C. Fu, Y. M. Wei, J. W. Yan, B. W. Mao, Chem. Phys. Chem 11 (2010) 2764–2778.
[61] R. Hayes, G. G. Warr, R. Atkin, Chem. Rev. 115 (2015) 6357–6426.
[62] E. S. Ferreira, C. M. Pereira, M. N. D. Cordeiro, D. J. dos Santos, J. Phys. Chem. B 119 (2015) 9883–9892.
[63] T. Méndez-Morales, J. S. Carrete, O. s. Cabeza, O. Russina, A. Triolo, L. J. Gallego, L. M. Varela, J. Phys. Chem. B 118 (2014) 761–770.
[64] A. C. Mendonça, A. A. Padua, P. Malfreyt, J. Chem. Theory Comput. 9 (2013) 1600–1610.
[65] F. Taherkhani, B. Minofar, J. Phys. Chem. C 29 (2017), 15493–15508.
[66] J. N. Canongia Lopes, J. Deschamps, A. A. Pádua, J. Phys. Chem. B 108 (2004) 2038–2047.
[67] J. N. Canongia Lopes, A. A. Pádua, J. Phys. Chem. B 108 (2004) 16893–16898.
[68] H. C. áDe Long, J. Chem. Soc., Chem. Commun. (1994) 299–300.
[69] V. V. Chaban, I. V. Voroshylova, J. Phys. Chem. B 119 (2015) 6242–6249.
[70] Y. Qi, T. Çağın, Y. Kimura, W. A. Goddard III, Phys. Rev. B. 59 (1999) 3527.
[71] F. Taherkhani, Z. Parviz, H. Akbarzadeh, A. Fortunelli, J. Phys. Chem. C 119 (2015) 7922–7932.
[72] A. C. Mendonça, P. Malfreyt, A. A. Padua, J. Chem. Theory Comput. 8 (2012) 3348–3355.
[73] S. Kiani, F. Taherkhani, J. Mol. Liq. 230 (2017) 374–383.
[74] http://classic.chem.msu.su/gran/gamess/index.html; A. A. Granovsky, MW. Schmidt.
[75] A. Diefenbach, F M. Bickelhaupt, G. Frenking, JACS 122 (2000) 6449–6458.
[76] T. Marino, M. Toscano, N. Russo, A. Grand, J. Phys. Chem. B 110 (2006) 24666–24673.
[77] D. Frenkel, B. Smit, Comput. Sci. Ser. 1 (2002) 1–638.
[78] S.-T. Lin, M. Blanco, W. A. Goddard III, J. Chem. Phys. 119 (2003) 11792–11805.

[79] A. Rapallo, J. Olmos-Asar, O. Oviedo, M. Luduena, R. Ferrando, M. Mariscal, J. Phys. Chem. C 116 (2012) 17210–17218.
[80] Y. Zhang, X. Ke, C. Chen, J. Yang, P. Kent, Phys. Rev. B 80 (2009) 024304.
[81] O. Al-Mushadani, R. Needs, Phys. Rev. B 68 (2003) 235205.
[82] M. Sternik, K. Parlinski, J. Chem. Phys. 123 (2005) 204708.
[83] M. D. Ediger, C. Angell, S. R. Nagel, J. Phys. Chem. 100 (1996) 13200–13212.
[84] C. Tsallis, J. Stat. Phys. 52 (1988) 479–487.
[85] C. Tsallis, Solitons Fract. 13 (2002) 371–391.
[86] E. Vives, A. Planes, Phys. Rev. Lett. 88 (2001) 020601.
[87] G. A. Mansoori, Principles of nanotechnology: molecular-based study of condensed matter in small systems. World Scientific (2005).
[88] F. Taherkhani, H. Abroshan, H. Akbarzadeh, A. Fortunelli, Phase Trans. 85 (2012) 577–591.
[89] H. Akbarzadeh, H. Yaghoubi, A. N. Shamkhali, F. Taherkhani, J. Phys. Chem. C 118 (2014), 9187–9195.
[90] H. Akbarzadeh, H. Yaghoubi, A. N. Shamkhali, F. Taherkhani, J. Phys. Chem.C 117 (2013), 26287–26294.

P. Verpoort, J. De Strycker, A. De Cleene

7 Industrialisation of surface treatment with electrodeposition processes from deep eutectic solvents

Abstract: Methods for electrochemical deposition of a metal coating on a metal substrate are described. The method may use an ionic liquids or DESs. as electrolyte, and the substrate may comprise a first metallic element. In this paper, a first intensive technology evaluation of a trivalent chromium electrodeposition from DESs was reported as the upscaling process consisting in the designing and constructing a semi-industrial electrodeposition pilot line.

Keywords: electrodeposition process, deepeutectic, chromium, pilot line, ionic liquid recycling

7.1 Introduction

Electrodeposition processes from ionic liquids or deep eutectic solvents (DES) are not known yet at industrial scale. Most of the current research is performed on academic level and is mainly focusing on depositing new metals or alloys.

However, some of the obtained metallic coatings are industrially interesting since no comparable alternative from aqueous solutions is available at industrial scale.

The first example is electrodeposition of aluminum. Due to the electrochemical reduction potential of trivalent aluminum, this element cannot be electrodeposited from aqueous solutions because the water itself will be reduced first to hydrogen gas.

The second example is the electrodeposition of metallic chromium, which is electrodeposited from aqueous hexavalent chromium baths at present. Since hexavalent chromium baths are catalogued as being carcinogenic, mutagenic and toxic, the European Community decided to put these substances in the Annex XIV of the REACH regulation in April 2013 [1]. The sunset date, from which no further application is allowed unless an official authorisation is granted by the European Commission, was set in September 2017. Therefore, an international quest for alternative technologies is ongoing for already several years. Up to now, no alternative technology has been published which is being capable of replacing all the applications or markets where hexavalent chromium is used.

Industrial applications for chromium can be divided into two different segments, being the decorative chromium market and the functional, the so-called hard chromium market.

P. Verpoort, J. De Strycker, A. De Cleene, OCAS N.V., Pres. J.F. Kennedylaan 3, Belgium

https://doi.org/10.1515/9783110583632-007

The decorative application is typically used for surface appearance improvements, for example on sanitary equipment such as water taps in the bathroom or kitchen. This market typically only needs a thickness of a few micrometers. Since aqueous processes using trivalent chromium salts are limited to a few micrometer thick coatings (due to a self-passivating process), alternative technologies are being developed in the market.

The hard chromium market is focusing mainly on improving functional properties of an object, such as hardness, corrosion resistance and reduced friction coefficient. These improvements require thicknesses varying between 5 µm and several hundreds of micrometer. The existing aqueous trivalent chromium processes are not able to fulfill the needs of these industries. Therefore, the research center for the application of steel (OCAS) started to investigate the feasibility of electrodeposition from DESs using trivalent chromium salts [2].

One example of a hard chrome application is the cold rolling mill during steel production within ArcelorMittal, where the cold rolling is aimed at reducing the steel thickness of a steel plate. Cold rolling cylinders of up to about 6 m long need to be chrome plated in order to have an acceptable friction coefficient. Since huge forces are used in this process, the chrome coating plays also a role in preventing the formation of iron particles which could otherwise result in a bad cleanliness of the outgoing steel surface.

OCAS performed a first intensive technology evaluation of a trivalent chromium electrodeposition from DESs. This feasibility study was positive, so the next step was to start the upscaling process from lab scale to semi-industrial scale. This upscaling process consisted of designing and constructing a semi-industrial electrodeposition pilot line for being able to supply demo samples to interested parties on which they can perform their specific industrial qualification tests.

7.2 Challenges for upscaling from lab scale to semi-industrial scale

During the design phase of the semi-industrial pilot line for electrodeposition, a lot of attention has been spent on the multifunctionalities and the flexibility in order to have an acceptable compromise between the industrial needs and the R&D needs, where a lot of parameters can be adapted to the needs of the project under investigation. These multifunctionalities will be discussed later in more detail in this chapter.

Besides the functionalities of the electrodeposition line, a lot of attention needs to be given to safety. All actions that will be performed or all reactions that can be ongoing during the process need to be taken into account in such a way that the environment and the operators are not working in a dangerous environment. At the same time, the materials to be used for the design were also investigated.

So upscaling from lab scale toward (semi-)industrial scale is not just the installation of a pilot line, but it involves much more. Most of the involved actions or considerations are elaborated in this chapter.

7.2.1 Preparation of samples

The first step in electroplating is to prepare the samples. An important step is removing eventual contamination or protective oil from metallic samples. Depending on the industry segment, the needed degreasing step can be performed pure chemically (sometimes at higher temperatures than room temperature) or electrolytically. The consequence is that a pilot line should be able to cope with both systems and need a heater, but also the electrochemical hardware, that is anodes, rectifier and so on.

Figure 7.1 shows the degreasing bath as installed at OCAS N.V., where the anodes can be clearly observed. Since degreasing occurs typically in aqueous solutions, the conductivity will be high enough and the distance between anode and cathode is not that important. Therefore, anodes at the side wall of the bath are sufficient to have a reproducible degreasing process.

Figure 7.1: Degreasing bath.

7.2.2 Sample shapes and sizes

In an upscaling process one needs to consider also the different possible shapes that future customers might need. If complex structures are not taken during the start-up phase, two main shapes exist in steel industry, that is flat sheets or circular shapes such as cylinders and tubes. Those two formats influence the design of an electrodeposition line already drastically: a flat sheet requires a flat anode, while a cylinder requires a concentrical shape. This is definitely the case when the viscosity of the electrolyte will be high and the conductivity low, as it is the case with DESs. In these cases, the distance between the anode and the cathode should be rather small, in order to prevent too much ohmic heating in the electrolyte. At a certain distance, the throwing power might not be sufficient anymore to achieve the desired coating on the cathode part.

When performing electrodepositions at lab scale, several actions are performed manually. Samples are typically small and hence have a low weight. So, the handling can be done manually and can even be done in a fast way. On industrial level, however, the samples are much larger and heavier. In the OCAS pilot line cylinders can be processed up to about 1 m long and with a diameter of 0.25 m. If this part is a massive cylinder the weight can go up to about 400 kg. A lifting device is therefore needed for the transport of the part from bath to bath.

This not only includes the installation of a lifting device such as a crane, but the handling of it needs to be performed in a safe way and the operators also need to be trained for this activity.

For the process planning of the project afterward, one needs to realise that this preparation step might become the rate determining step in the full process. Depending on the thickness of the coating, the deposition process itself can take between some minutes up to about 1 h. The mounting of, for example, a cylinder involves several steps, which will finally take more time than the electrodeposition step itself:

- Mounting the cylinder into the lifting device (see further): the part need to be mounted in a secure way and the final electrical connections need to be checked to assure a successful electrodeposition process.
- On most of the pieces, only a part need to be coated. The parts that remain uncoated should be or out of the anode or protected with, for example, tape, which is a mainly manual operation.

7.2.3 Electrolyte

Performing research on lab scale has the benefit of using small volumes of electrolyte. This has the advantage that electrolyte parameters can be changed in a short time and at a relatively low cost. Typical electrolyte parameters are the composition

of the base materials and the use of additives. A small volume of even about 5 L can easily be prepared. If the final electrolyte does not result in acceptable deposited layers, another composition can easily be prepared.

If larger electrolyte volumes are prepared, those changes are not that convenient anymore, not only in preparation time but also in processing cost. It also needs to be taken into account that replacing a non-working electrolyte has also side-effects in cost. When the electrolyte of about 1,300 L, as in the OCAS pilot line, need to be replaced, the side-effects are the time to drain the old electrolyte out of the process bath, the time and the loss of electrolyte for cleaning the process bath and all connected tubings and the time to refill and heat-up the process bath with a new electrolyte. This entire process can even take up to several days to prevent cross-contamination between the two different electrolytes.

An important factor in maintaining an electrolyte as long as possible is the composition control. Analysis techniques for most aqueous-based liquids are well known. In the case of dense and viscous DESs or ionic liquids, this is not that obvious anymore. Most DESs are strongly concentrated. Diluting the solvents for analysis purposes cannot always be used, since diluting can cause an important shift in complexation or side-reactions, which would lead to an incorrect analytical value. Moreover, the DES used in this study for the hard chrome electrodeposition is very reactive to most metals (see also chapter 7.2.6 on material compatibility). Since most analytical equipment use metallic parts (like stainless steel), they cannot be used for some DES, since the DES will start dissolving or reacting with the metals. Adaptations to the apparatus or to the methodology are hence necessary.

7.2.4 Process parameters

A small-range rectifier can be enough to perform studies on lab scale. And if the range of the rectifier is not sufficient, one can easily change to another lab-scale rectifier. Before installing a rectifier on industrial scale, a clear view on both the current and the voltage range is needed.

This also accounts for the temperature. At lab scale, typically heating plates or double-walled cells can be used, where a large range of temperatures can be applied. However, during the design of a semi-industrial line, the final temperature range needs to be clear before starting the installation.

Since the conductivity of most DESs is low, ohmic heating during an electrodeposition process can occur, leading to uncontrolled heating close to the cathodic piece that needs to be plated. Since temperature can be one of the most important parameters affecting the plating efficiency, a good temperature control is mandatory. Due to this undesirable ohmic heating, one option is to install a heater/cooler unit. Another option is to use a larger volume of electrolyte as a buffering agent. The buffer tank in the OCAS pilot line is an example thereof (Figure 7.2). A total volume of about 1,300 L can be used in

Figure 7.2: Buffer tank.

the total system, while only about 400 L need to be present in the processing tank itself (Figure 7.4). Both tanks are in direct contact with each other via a pumping system or via a communicating vessel setup. Due to the controlled flow in the full system, the "ohmic heated" electrolyte is pumped toward the buffer tank, where it will represent only a relatively low volume with respect to the bath volume present in this buffer tank. It will therefore cool down rapidly to the temperature of the electrolyte in this tank.

The electrolyte flow, as mentioned earlier, is also an important process parameter, certainly in DES electrolytes. But due to the high viscosity (e.g. about 180 mPa·s) adapted pumps and/or filtering systems are needed, which can cope with these viscosities.

In the OCAS pilot line, the electrolyte flow can be controlled in two different ways or in a combination of both. On one hand, cylindrical parts can be mounted in a hanging/suspending device, as shown in Figure 7.4. A rotation system is mounted in this device. This rotation is not only taking care that the full diameter of the cylinder will be plated by using a semicircular anode (as shown in Figure 7.3), but it also creates an important and controlled movement of the electrolyte in the proximity of the cathodic piece. Since this line is built not only for cylindrical devices but also for other shapes, an extra flow regulating system is installed by using eductors. Different eductors are installed over the full length and height of the bath. They can be seen at the bottom of the plating tank in Figure 7.3. Each eductor can not only be changed in vertical position, but can also be rotated in each direction. Moreover, manual valves in each supply tubing can even be separately set to control the flow rate of each eductor (Figure 7.3)

Setting up the correct positions for a specific part, that need to be plated, can be time-consuming. The fact that OCAS also has a modeling department helps us to be

Figure 7.3: Plating bath.

Figure 7.4: Hanging device with rotation motor.

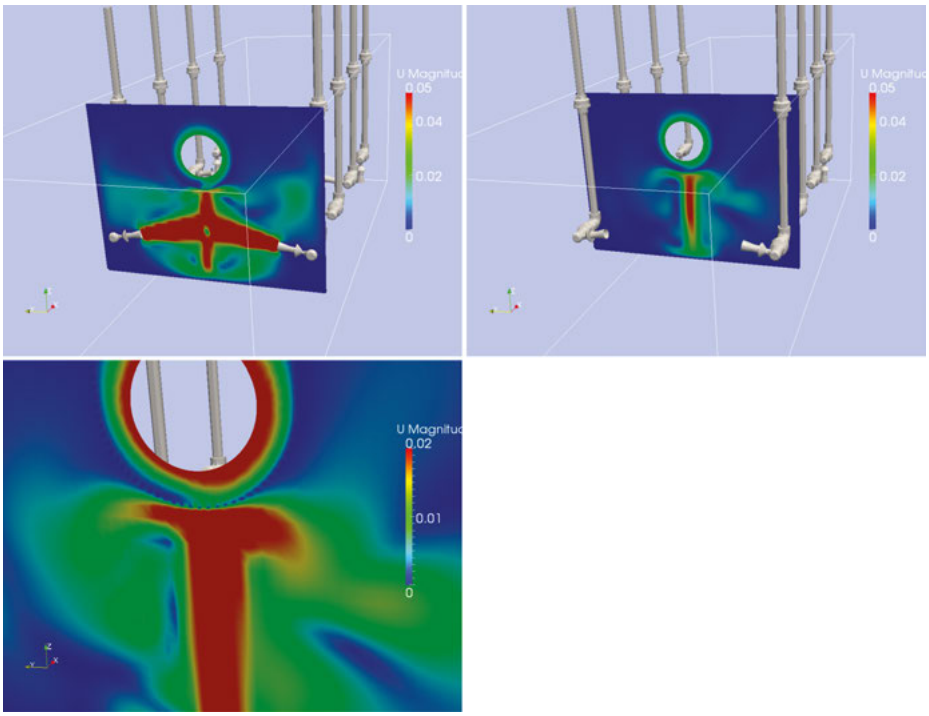

Figure 7.5: Modeling examples of a cylindrical part with specific eductor locations, directions and flowrate (left: at the position of an eductor, right: in between two eductors), bottom: detail at anode.

much more time efficient. Figure 7.5 is showing examples of the modeling performed for a typical cylindrical workpiece. The left image shows the physical flow rate of the electrolyte as a crosscut at the position of an eductor. By directing the eductors slightly upward, the flow coming from the left and right sides of the bath is bumping into each other, leading to a vertical upward flow toward the meshed anode. This mesh in the anode buffers the direct flowrate, but pushes it also through the meshes. This leads to a constant and controlled refreshment of the electrolyte between the anode and the cathodic piece. Also between two eductors a vertical upward flow is still existing due to the conical shape of the eductors (see top right image in Figure 7.5). The rotation of the cylinder itself will then allow to achieve a rather laminar flow on the cathode, with a constant refreshment of the electrolyte.

7.2.5 Environment, health and safety

Last, but not least, is the risk analysis that definitely needs to be performed concerning environment, health and safety. Since heavy weights are handled and parts are

moveable, all safety precautions need to be investigated and installed for human exposure.

Since gas evolution might always occur during the electrodeposition process, balancing the metal reduction by an oxidation at the anode, an exhaust system is installed. However, for each process the possible gases need to be determined or analysed, since exposure even to the outside environment is limited. Eventually a gas scrubber might be needed.

Due to the high electrolyte volume, a leak floor is mandatory under the full equipment which can contain more volume than the tank with the highest volume.

Waste management also need to be considered before starting a specific project. Depending on the content of the electrolyte, a waste treatment company should be contacted. This is not only for the electrolyte itself but also for the wastewater that needs to be collected after rinsing the electrolyte from the plated parts. Eventually a recycling process of the electrolyte might be considered, certainly if the electrolyte is expensive.

Another important factor to take into account is that in R&D centers such as OCAS, new industrial electrolytes might be designed. Before exposing this to the industrial market, an official registration of the product will be necessary.

7.2.6 Hardware

As mentioned earlier, DESs have the tendency to react quite aggressively toward metals. “Normal” industrial installations contain however a lot of metallic parts, due to their low price and their high strength. Pieces made from stainless steel are often used since they can also provide a rather good resistance towards corrosion in a lot of aqueous chemical solutions.

In a material compatibility study at OCAS, it was found that most typical metals, as used in industrial installations, are not compatible with the DES based on choline chloride and chromium chloride. Almost the only metal that was found to be resistant to this specific electrolyte is titanium. Therefore, all metallic parts that are in direct contact with the electrolyte or with eventual produced gases (e.g. bolts and support parts) are made of pure Ti.

In the same extensive study, most plastics and elastomers were investigated. For plastics, the commonly used ones are polypropylene (PP), polytetrafluorethylene (Teflon) and polyvinylidenefluoride (PVDF). These are typically used for bath materials and for tubings. The three mentioned plastics were compatible, although PP was more sensitive than the other ones. In order to cope with different chemicals that might be used in future projects, OCAS decided to use a PVDF liner material in the processing baths.

Elastomers are also a necessary part in installations, where they are typically used as sealing rings. The most known material is Viton®. This material is known as being resistant to most chemicals, and it was shown in our compatibility study that it is also resistant to the currently studied DES.

7.3 Process control at industrial scale

7.3.1 Bath control

In order to achieve an acceptable process control, one of the first challenges is to control the bath composition and hence to have a methodology to measure the base compounds.

In the specific case of the OCAS technology, the trivalent chromium content could be measured by using Inductively coupled plasma – optical emission spectrometry (ICP-OES). Since the raw materials (choline chloride and chromium chloride) are hydrated salts, the amount of hydrated water needs to remain controlled. A well-known technique is the Karl-Fischer titration method, which was also proven to be valid for this specific DES. For the determination of chloride ions, a standard $AgNO_3$ titration can be used.

The major issue was to measure the choline concentration in the highly concentrated DES. Although several advanced techniques were tried, they were without real success since several measurement techniques were interfered by the Cr(III) chloride complex. Finally, a gravimetric method was found to be valid for choline chloride. This technique is based on a quantitative precipitation of the choline cation by reaction with the so-called Reinecke salt (ammonium tetrathiocyanatodiaminechromate(III), see Figure 7.6).

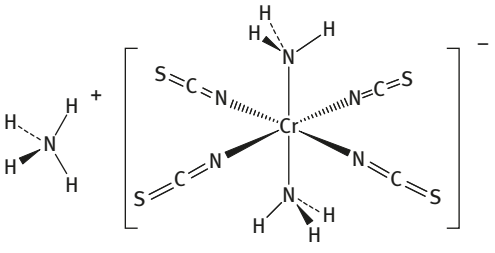

Figure 7.6: Reinecke salt.

A preliminary test with a chromium chloride solution showed no precipitation, proving that this salt will not interfere the measurement of the choline. When a theoretical mass fraction of 30.5% choline chloride was reacting with the Reinecke salt, a final mass fraction of 33.5% was obtained. Finally, four samples of the DES (freshly prepared) were measured. The results are shown in Table 7.1.

The conclusion is hence that the Reinecke salt gravimetric method can effectively be used for the quantification of choline chloride in choline chloride/chromium chloride mixtures, but a few percentage of deviation can be expected.

Table 7.1: Choline chloride quantification in DES.

Sample	Choline chloride (m%)
1	44.5
2	43.6
3	43.2
4	43.0
Average	*43.6 ± 0.7*

Table 7.2: Bath composition over lifetime.

	$[Cr^{3+}]$(m%)	$[H_2O]$(m%)	[Chol Cl](m%)	$[Cl^-]$(m%)
0 months	7.4	36.0 ± 0.27	40.6 ± 4.9	241
10 months	7.0	34.3 ± 0.20	57.4 ± 1.1	228
12 months	7.2	36.2 ± 0.42	41.0 ± 3.1	258
14 months	7.6	36.8 ± 0.14	40.3 ± 5.2	267
20 months	7.5	37.1 ± 0.26	38.9 ± 5.0	261
22 months	6.7	38.0 ± 0.08	31.8 ± 1.5	214

Table 7.2 is showing the results of the bath composition over a lifetime of almost 2 years in the OCAS pilot line. During these 2 years, the pilot line has been used for plating all kinds of samples (cylinders and flat sheets). Although this was not in a full-time production mode, the same DES was relatively stable over the 2 years, without the addition of any extra salt over this lifetime.

7.3.2 Process control

By having the ability to monitor the bath composition, better process control can finally be achieved. One of the studies that was performed hereafter was a controlled matrix study of the chromium coating hardness. Since the hardness has been specified by possible customers on 1,000 HV, the study consisted of a process optimisation of this hardness. Figure 7.7 shows the hardness of the electrodeposited Cr coating over the lifetime of the DES in the OCAS pilot line. An average hardness around 800 HV was obtained in the beginning of the project, with some extreme fluctuations in several points. At the end of the graph the obtained results from the controlled matrix study are depicted (in the red dashed circle), showing that reproducible higher hardness values can be achieved with controlled parameters and/or bath conditions. So this graph is showing the relevance of having a descent bath control before starting parameter studies.

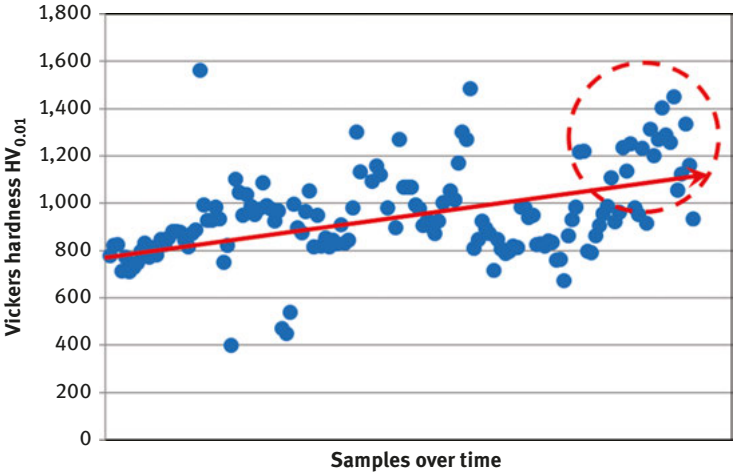

Figure 7.7: Vickers hardness of electrodeposited Cr coating over lifetime of DES.

7.3.3 Anodic reactions

The basic reactions that occur during the electrodeposition process are as follows:

– At cathode side:

$$Cr^{3+} + 3e^- \rightarrow Cr^0$$

$$2H_2O + 2e^- \rightarrow 2OH^- + H_2$$

– At anode side (with inert dimensionally stable anodes):

$$2Cl^- \rightarrow Cl_2 + 2e^-$$

$$2H_2O \rightarrow O_2 + 4H^+ + 4e^-$$

These basic reactions do not take into consideration the fact that the choline chloride might be reacting with any other side-product.

Chlorine gas is effectively formed during the electrodeposition process. In the OCAS pilot line, values of about 3,000–4,000 ppm are measured, but with the exhaust flow that is used, this is still under the emission limit. However, chlorine gas is considered as a negative side reaction. A possible solution is the use of soluble anodes, being chromium nuggets or a solid chromium anode. During lab-scale tests with soluble anodes, no chlorine evolution could be measured, which is a positive result. However, the chromium anodes are dissolving at the same time in a chemical way (so even without applying an external current to the Cr anodes). Figure 7.8 is indeed showing that the chemical dissolution rate of Cr cannot be disregarded since the

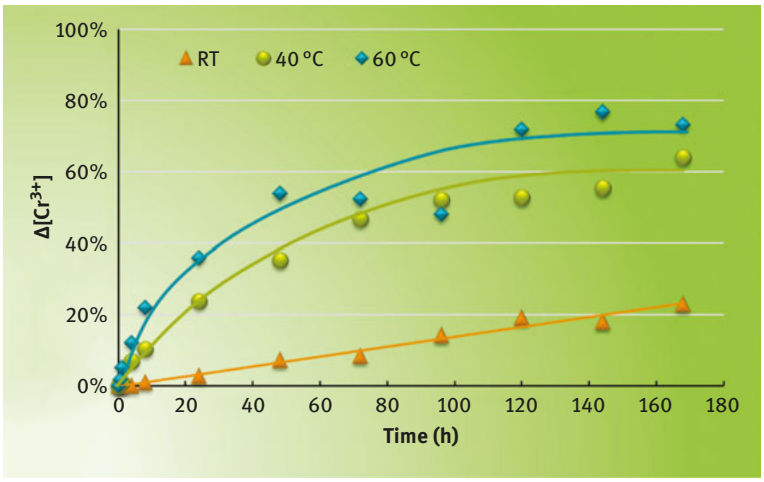

Figure 7.8: Chemical dissolution of Cr anodes versus time.

Cr^{3+} concentration is already increasing by 20% at room temperature and even up to 70–80% at more elevated process temperatures.

Also electrochemically the increase in Cr^{3+} concentration is too high, as shown in Figure 7.9. Due to the Cr^{3+} increase, both the conductivity and viscosity are changing too strong (see Figure 7.10).

In our specific case, the change in both parameters are even that high that the Walden rule is not valid anymore, which is shown in the inset of Figure 7.10. Figure 7.11 then shows that the increase in viscosity is mainly due to the Cr^{3+} increase in the electrolyte during deposition with soluble anodes.

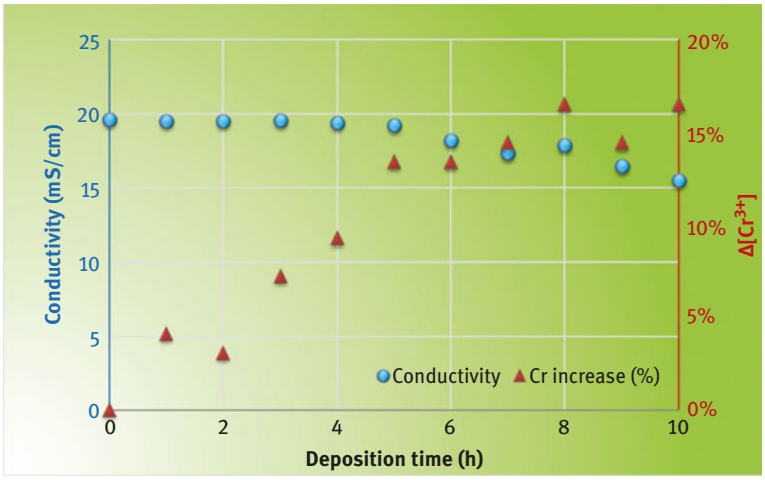

Figure 7.9: Change in conductivity and Cr^{3+} concentration versus deposition time.

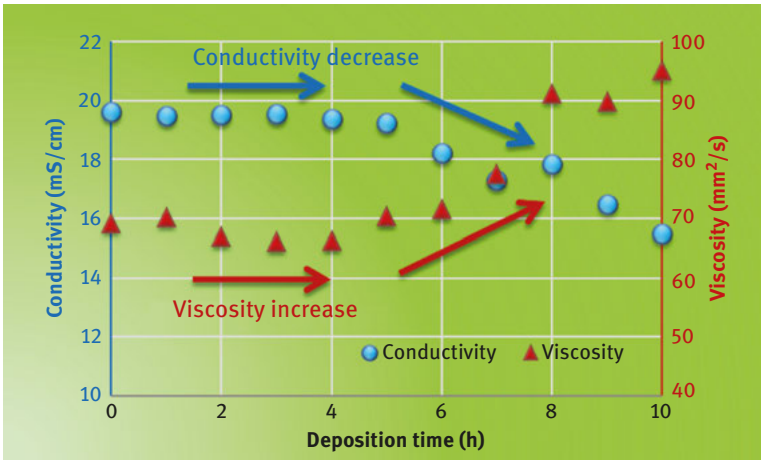

Figure 7.10: Change of conductivity and viscosity versus deposition time (same experiment set as in Figure 7.9).

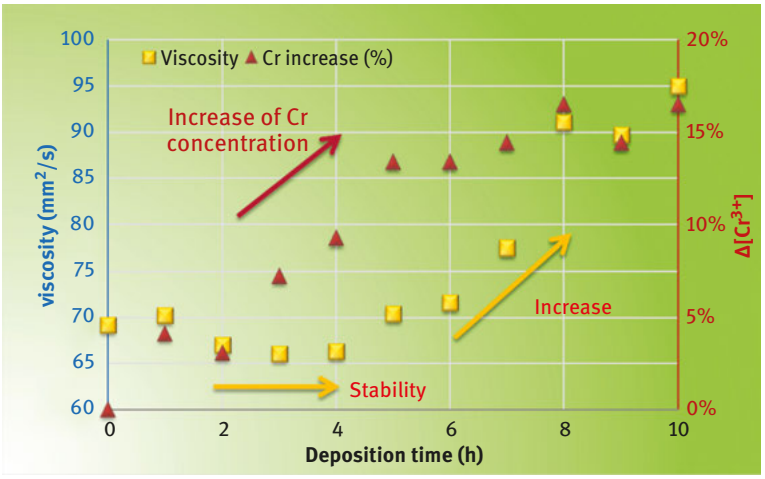

Figure 7.11: Change in viscosity and Cr^{3+} concentration versus deposition time.

The observation that soluble anodes are dissolving chemically and electrochemically at a higher rate than Cr^{3+} electrodeposited on the cathode means that the chemical ratio of the base materials (Cr^{3+} and choline chloride) is changing drastically, which makes the use of soluble anodes more difficult. Anyway, by engineering this dissolution versus deposition it still can give a solution in an industrial production environment.

References

[1] https://echa.europa.eu/authorisation-list
[2] A.P. Abbott, G. Capper, D. L. Davies and R. K. Rasheed, “Ionic liquid analogues formed from hydrated metal salts”, *Chem. Eur. J.* **10** 3769-3774 (2004).

Index

https://doi.org/10.1515/9783110583632-008